

ABSTRACT

YOKUS, MURAT A. Multiplexed Biochemical and Biophysical Sensing Systems for Monitoring Human Physiology. (Under the direction of Dr. Michael A. Daniele and Dr. Tushar Ghosh).

Noninvasive access to biochemical biomarkers of human physiology is one of the most challenging tasks in digital health. Today, measurement of the biomarkers of health, wellness, or even diseases requires frequent lab visits for routine blood or urine test panels for full-body screening. Treatment or medical prescription is usually provided based on the measured metrics and patient's recall of symptoms. However, some of these test panels are still deemed invasive, painful, or inconvenient, and most importantly, they do not offer real-time measurement physiological data. Thus, addressing these challenges requires the development of multiplexed wearable systems that converge biochemical and biophysical sensing functionalities into a single platform and provide real-time measurement of biomarkers of human physiology in daily settings.

In this dissertation, we provide wireless, wearable health monitoring systems that can noninvasively and continuously measure the biomarkers of human physiology. The developed systems can measure metabolites (glucose, lactate), pH, and other physical signals (skin temperature, heart rate, and tissue oxygenation) via electrochemical sweat analysis and optical methods. The dissertation introduces the fabrication of flexible sensing arrays, fabrication and characterization of biosensors, design and validation of the wearable electronic systems, and off-body multiplexed analysis of artificial and collected real sweat samples. The developed wearable systems provide multimodal, noninvasive analysis of biomarkers of metabolism and respiration, extending its applications from diet management and performance monitoring to the prolonged assessment of overall health and wellness in ambulatory settings.

© Copyright 2020 by Murat Abdurrahim Yokus

All Rights Reserved

Multiplexed Biochemical and Biophysical Sensing Systems for Monitoring Human Physiology

by
Murat A. Yokus

A dissertation submitted to the Graduate Faculty of
North Carolina State University
in partial fulfillment of the
requirements for the degree of
Doctor of Philosophy

Electrical Engineering & Fiber and Polymer Science

Raleigh, North Carolina
2020

APPROVED BY:

Dr. Michael A. Daniele
Committee Co-Chair

Dr. Tushar Ghosh
Committee Co-Chair

Dr. Alper Bozkurt

Dr. Veena Misra

DEDICATION

To my family for their endless support

BIOGRAPHY

Murat Yokus received a B.Sc. degree in Textile Engineering (summa cum laude) with a minor in Industrial Engineering in 2011 from Uludag University in Turkey. He completed the last year of his bachelor's degree at Polytechnic University of Valencia (Spain) and the University of Manchester (England). Later that year, he received Fulbright Scholarship from the U.S. Department of State's Bureau of Educational and Cultural Affairs to pursue his M.Sc. degree in Textile Engineering at North Carolina State University. Then, he pursued a Ph.D. program at North Carolina State University, majoring in Electrical Engineering and co-majoring in Fiber and Polymer Science. He initially worked in NEXT Research Group on wearable electronic textiles. Afterward, he joined BioInterface Lab under the direction of Dr. Michael Daniele. His research interests include wearable and implantable electronics, biosensors, and integrated circuit design for biomedical applications.

ACKNOWLEDGMENTS

First, I would like to thank my advisor and a close friend, Dr. Michael Daniele. Four and half years ago, you gave me the opportunity to join the BioInterface Lab and supported my ideas and research interest. I am very thankful for your help and guidance throughout my graduate studies. I am very grateful for your time and effort in transitioning me to an independent researcher.

I also would like to thank the rest of my advisory committee members for their guidance and support: Dr. Alper Bozkurt, Dr. Tushar Ghosh, Dr. Veena Misra, and Dr. Brendan O'Connor. Specifically, I would like to thank Dr. Ghosh for being my dissertation co-chair and Dr. Bozkurt for the helpful research discussions throughout my Ph.D.

This research has been possible with funding from the NSF Engineering Research Center for Advanced Self-Powered Systems of Integrated Sensors and Technologies (ASSIST). I would like to thank everyone in the ASSIST Center, Veena, Mehmet, Tom, Casey, Elena, Roy, Jason, Scott, Clay, for providing the students with the resources for professional and personal development. Special thanks to Dr. Rajinder Khosla and Dr. Mehmet Ozturk for the pleasant talks.

To staff and individuals of the NNF, AIF, ECE department, BME department, and College of Textiles, thank you for providing assistance and training for the tools and equipment. Your expertise allowed me to learn the required skills needed for the research in this dissertation.

I would like to extend my sincere thanks to my research collaborators, Talha Agcayazi, Tanner Songkakul, and Tamoghna Saha, for their great friendship and significant contribution to the work presented in this dissertation. I would like to thank the undergraduates who afforded me the chance to mentor them (Kristi, Nathan, Rachel, Grace, Cheyanne, Kendal, and Matt). Special thanks to Rachel Foote for her excitement and contribution to the research on stretchable printed interconnects.

To all of the BioInterface Lab, iBionics Lab, and NEXT Research Lab members, thanks for making the labs an exciting place to learn and explore. Your friendship and useful research discussions will not be forgotten. Special thanks to Ashlyn Young, Vladimir Pozdin, Parthiban Rajan, James Dieffenderfer, Talha Agcayazi, Tanner Songkakul, Peter Sotory, Evan Williams, Parvez Ahmmed, Tahmid Latif, Michael McKnight, Ryan Hodges, Halil Akyildiz, and Jonathan Halbur. All the students from the ASSIST Center, Francisco, Michael Lim, Abhishek, Tim, Saba, Amanda, Namita, Jose, Rita, Akhilesh, Xiao Zhang, Marzana, Michael Wilkins, Rafael Silva... and everyone else, thanks for the enjoyable moments and great memories. I also would like to thank to the Turkish community and friends, Alper, Safak, Rana, Halil, Ozkan, Emrah, Ramiz, Serdar, Mehmet, Nihat, Musab, Tugrul, Elif, and Cemile, for their friendship and great memories.

My concluding statement of the most profound gratitude is for my family. Thank you, dad, thank you, mom, and thank you, my dear sisters. I couldn't be here where I am today without your help, support, and guidance throughout my life.

Thank you.

TABLE OF CONTENTS

LIST OF TABLES	viii
LIST OF FIGURES	ix
CHAPTER 1: Introduction	1
1.1. Objective.....	1
1.2. Dissertation Outline.....	4
CHAPTER 2: Literature Review	7
2.1. Introduction	7
2.2. Wearable Biochemical Sensors	12
2.2.1. Sweat Extraction and Sampling Methods in Wearable Sensors.....	12
2.2.2. Biochemical Sensing in Current Wearable Devices.....	18
2.2.2.1. Metabolites	18
2.2.2.2. pH and Electrolytes	24
2.2.2.3. Oxygen	28
2.2.2.4. Other Chemical Biomarkers	33
2.3. Wearable Biophysical Sensors	35
2.3.1. Sweat Rate	35
2.3.2. Temperature.....	40
2.4. Wearable Systems with Multimodal Sensing.....	42
2.5. Summary and Outlook.....	46
2.6. References	50
CHAPTER 3: Wearable Multiplexed Biosensor System Toward Continuous Monitoring of Metabolites.....	61
3.1. Abstract.....	61
3.2. Introduction	62
3.3. Materials and Methods	66
3.3.1. Fabrication of Flexible Electrode Array.....	66
3.3.2. Functionalization of the Flexible Electrode Array	67
3.3.3. Characterization of the Flexible Sensor Array	69
3.4. Results and Discussion.....	72
3.4.1. Design of Flexible Sensor Array and Custom Multiplexing System	72
3.4.2. In-vitro Characterization of Glucose, Lactate, pH, and Temperature Sensors.....	76
3.4.3. System Validation of the Custom Multiplexing System	81

3.4.4. Simultaneous Measurement of Glucose, Lactate, pH, and Temperature	87
3.5. Conclusion	90
3.6. Supplementary Material	92
3.6.1. Supplementary Text.....	92
3.6.1.1. Comparison of wearable multimodal systems.....	92
3.6.1.2. Comparison of custom-built potentiostats.....	92
3.6.1.3. Fabrication of the flexible sensor array	92
3.6.1.4. Electrode functionalization and characterization	93
3.6.1.5. Selective functionalization of the electrodes	95
3.6.1.6. Comparison of the glucose and lactate sensors with previous studies	96
3.6.2. Supplementary Tables and Figures	97
3.7. References	121
CHAPTER 4: Conclusion and Future Work.....	128
4.1. Summary.....	128
4.2. Future Work: Multiplexed Electrochemical and Biophotonic Sensing.....	129
APPENDICES	135
Appendix A: Fabric-Based Wearable Dry Electrodes for Body Surface Biopotential Recording	136
Appendix B: Printed Stretchable Interconnects for Smart Garments: Design, Fabrication and Characterization	161
Appendix C: Skin Hydration Sensor for Customizable Electronic Textiles	191
Appendix D: Towards a Wearable Perspiration Sensor	202
Appendix E: Towards Wearable Electrochemical Lactate Sensing using Osmotic-Capillary Microfluidic Pumping	211
Appendix F: Wearable Sweat Rate Sensors.....	221
Appendix G: IRB Human Trials Document: Analysis of Sweat and Measurement of Local Tissue Oxygenation with a Wearable Device.....	231
Appendix H: List of Publications	255

LIST OF TABLES

Table 2.1.	List of biochemical and biophysical sensors with their health applications.	43
Supplementary Table S3.1.	Selected wearable sweat sensors.....	97
Supplementary Table S3.2.	Comparison of state-of-the-art custom-designed potentiostats.....	98
Supplementary Table S3.3.	Specifications of the custom-designed potentiostat.	104
Supplementary Table S3.4.	Bill of materials of the schematic in Figure S3.8.....	108
Supplementary Table S3.5.	Bill of materials of the schematic in Figure S3.9.....	109
Supplementary Table S3.6.	Effective electrochemically active surface area of gold nanoparticle deposited electrodes.	110
Supplementary Table S3.7.	Comparison of glucose sensors (benchtop potentiostat results)	112
Supplementary Table S3.8.	Comparison of lactate sensors (benchtop potentiostat results)	113
Supplementary Table S3.9.	Concentration of glucose and lactate in the collected and artificial sweat samples (n = 3).	117

LIST OF FIGURES

- Figure 1.1. Overview of wearable health monitoring systems. Multiplexing biochemical and biophysical sensors opens up new opportunities for health applications toward a comprehensive understanding of overall health and disease states. 1
- Figure 1.2. Chronological overview of the developed wearable health monitoring systems in this dissertation. The numbers on each figure (1 to 5) indicate the order of the developed systems..... 3
- Figure 2.1. A schematic illustration of the architecture of wearable multimodal health monitoring systems. The system consists of external sensors, a central processing unit, analog-to-digital converter (ADC), a wireless interface, battery, and energy management unit. The processing module acquires, processes, and transmits the signals from external biochemical and biophysical sensors. The wearable systems have the capability of sampling and analyzing biofluid of interest (sweat) via biochemical sensors and can wirelessly send the biochemical information with other physical, sensory data to a smartphone or a tablet. The medical data from these devices is sent to the medical servers (i.e., cloud) via cellular networks or Wi-Fi, where physicians and caregivers are connected through a network of health servers and databases to provide feedback, treatment, prognosis, and diagnosis based on the history of the clinically relevant data. 10
- Figure 2.2. Sweat extraction and sampling methods in wearable systems. a) An oil-membrane approach for sweat sampling. Reproduced with permission ⁴³. Copyright 2016, The Royal Society Chemistry. b) An absorbent porous substrate for sweat collection. Reproduced with permission ⁴⁴. Copyright 2014, WILEY-VCH Verlag GmbH & Co. c) A silicone headband for guiding sweat to the sensing device. Reproduced with permission ⁴⁵. Copyright 2017, American Chemical Society. d) Superwetttable flexible band for sweat sampling. Reproduced with permission ⁴⁶. Copyright 2019, American Chemical Society. e) A hexagonal network for transport and sampling of low sweat volumes. Reproduced with permission ⁴⁷. Copyright 2018, The Royal Society Chemistry. f) A paper microfluidic channel for continuous sweat transport and evaporation. Reproduced with permission ⁴⁸. Copyright 2017, Elsevier. g) 3D microfluidic channels for sweat sampling and measurement of sweat loss. Reproduced with permission ⁴⁹. Copyright 2019, The Royal Society Chemistry. h) A microfluidic patch with capillary bursting valves for chrono-sampling of sweat. Reproduced with permission ⁵⁰. Copyright 2017, WILEY-VCH Verlag GmbH & Co. i) A fully integrated platform for iontophoretic sweat stimulation and sensing. Reproduced with permission ⁵¹. Copyright 2017, National Academy of Sciences USA. 15
- Figure 2.3. Examples of electrochemical wearable metabolite sensors. a) A printed electrochemical temporary tattoo sensor for lactate sensing. Reproduced with permission ⁶¹. Copyright 2013, American Chemical Society. b) A printed tattoo

sensor with reverse iontophoresis option for glucose sensing. Reproduced with permission ⁶³. Copyright 2015, American Chemical Society. c) An epidermal microfluidic platform with sweat collection and glucose or lactate sensing capabilities. Reproduced with permission ⁶⁴. Copyright 2017, American Chemical Society. d) An epidermal sensor for lactate and electrocardiogram sensing. Reproduced with permission ⁶⁵. Copyright 2016, Creative Commons Attribution 4.0 International License. e) Eyeglasses with integrated electrochemical lactate and potassium sensors. Reproduced with permission ⁶⁶. Copyright 2017, The Royal Society of Chemistry. f) Self-powered lactate sensing with biofuel cells. Reproduced with permission ⁶⁷. Copyright 2016, The Royal Society of Chemistry. g) A self-powered and continuous glucose, Na⁺, and K⁺ sensing system based on NiCo₂O₄ micro-supercapacitors. Reproduced with permission ⁶⁸. Copyright 2019, Elsevier. h) A sweat biosensing device with integrated sweat stimulation for ethanol sensing. Reproduced with permission ⁷². Copyright 2018, The Royal Society of Chemistry. i) A self-powered electronic skin for measurement of uric acid, urea, glucose, and lactate with piezoelectric-enzymatic-reaction coupling. Reproduced with permission ⁷³. Copyright 2017, American Chemical Society.

..... 22

Figure 2.4. Examples of electrochemical, optical, and colorimetric wearable sensors for electrolyte sensing. a) A roll-to-roll printed electrode arrays for pH, K⁺, and Na⁺ sensing. Reproduced with permission ⁷⁸. Copyright 2018, American Chemical Society. b) An omniphobic paper-based smart bandage for pH sensing. Reproduced with permission ⁷⁹. Copyright 2018, Elsevier. c) A smart bandage for optical monitoring of pH. Reproduced with permission ⁸⁰. Copyright 2017, Elsevier. d) A wearable chemical barcode microfluidic platform for pH sensing. Reproduced with permission ⁸¹. Copyright 2012, Elsevier. e) An RFID patch for Na⁺ sensing. Reproduced with permission ⁸³. Copyright 2015, IEEE. f) SWEATCH wearable Na⁺ sensing device. Reproduced with permission ⁸⁴. Copyright 2016, John Wiley and Sons. g) A wearable patch for monitoring of Na⁺ and K⁺. Reproduced with permission ⁸⁵. Copyright 2018, The Royal Society of Chemistry. h) A thin elastomeric patch with open cellular designs for pH, K⁺, Ca²⁺ sensing. Reproduced with permission ⁸⁶. Copyright 2017, WILEY-VCH Verlag GmbH & Co. i) A microfluidic patch with superabsorbent valves for time-sequenced colorimetric monitoring of Cl⁻. Reproduced with permission ⁸⁷. Copyright 2018, WILEY-VCH Verlag GmbH & Co..... 26

Figure 2.5. Examples of wearable optical sensors for the detection of oxygen. a) Smart e-skin system comprising ultra-flexible polymer light-emitting diodes (PLEDs) and an organic photodetector (OPD). Reproduced with permission ⁹². Copyright 2016, Creative Commons Attribution 4.0 International License. b) A reflective oximeter with an array of red and NIR LEDs and OPDs. Reproduced with permission ⁹³. Copyright 2018, Creative Commons Attribution 4.0 International License. c) An ambient light oximeter (ALO) with printed OPDs. Reproduced with permission ⁹⁴. Copyright 2020, WILEY-VCH

Verlag GmbH & Co. d) A battery-free, wireless, epidermal optoelectronic system. Reproduced with permission ⁹⁵. Copyright 2016, Creative Commons Attribution 4.0 International License. e) A soft, wireless chest and limb units for physiological monitoring of neonatal and pediatric patients. Reproduced with permission ⁹⁶. Copyright 2020, Springer Nature. f) A miniaturized, wireless oximeter with microscale LEDs (μ -LEDs) and a microscale inorganic photodetector (μ -IPD). Reproduced with permission ⁹⁷. Copyright 2019, Creative Commons Attribution 4.0 International License. 32

Figure 2.6. Examples of wearable sensors for the detection of other analytes in sweat. a) A flexible multiplexed array for detection of Zn, Cd, Pb, Cu, and Hg. Reproduced with permission ¹⁰⁴. Copyright 2016, American Chemical Society. b) A flexible sweatband for caffeine monitoring. Reproduced with permission ¹⁰⁶. Copyright 2018, WILEY-VCH Verlag GmbH & Co. c) A laser-engraved graphene-based sensor for uric acid, tyrosine, temperature, and respiration rate monitoring. Reproduced with permission ¹⁰⁷. Copyright 2020, Springer Nature. d) An organic electrochemical transistor modified with molecularly imprinted polymer for cortisol sensing. Reproduced with permission ¹⁰³ Copyright 2018, Creative Commons Attribution Noncommercial License 4.0. 34

Figure 2.7. Examples of wearable sweat rate sensors. a) A wireless sweat volume and conductivity sensor. Reproduced with permission ¹¹³. Copyright 2016, Elsevier. b) A digital volume dispensing system for sweat rate measurement. Reproduced with permission ¹¹⁴. Copyright 2019, The Royal Society Chemistry. c) A wearable wireless sweat patch for Na⁺ and sweat rate sensing. Reproduced with permission ¹¹⁵. Copyright 2018, American Chemical Society. d) A multi-model sweat sensing patch for measurement of Na⁺, sweat rate, and total ionic concentration. Reproduced with permission ¹¹⁶. Copyright 2019, The Royal Society Chemistry. e) A battery-free, wireless microfluidic system for sweat rate and loss monitoring. Reproduced with permission ¹¹⁷. Copyright 2018, WILEY-VCH Verlag GmbH & Co. f) A waterproof, epidermal microfluidic sweat patch for virtual assessment of sweat loss in an aquatic environment. Reproduced with permission ¹¹⁸. Copyright 2019, Creative Commons Attribution 4.0 International License. g) A sweat volume monitoring patch with swellable hydrogels. Reproduced with permission ¹¹⁹. Copyright 2020, The Royal Society Chemistry. h) A wearable sweat rate sensor based on the diffusion of the water vapor evaporated from the skin. Reproduced with permission ¹²⁰. Copyright 2018, Elsevier. i) A wearable and wireless sweat rate monitoring system based on chemiresistors. Reproduced with permission ¹²¹. Copyright 2019, WILEY-VCH Verlag GmbH & Co. 39

Figure 2.8. Examples of wearable temperature sensors. a) A flexible healthcare patch with temperature and ECG sensing capabilities. Reproduced with permission ¹²⁶. Copyright 2017, WILEY-VCH Verlag GmbH & Co. b) A wearable, flexible sensor with pH and temperature sensors. Reproduced with permission ¹²⁷. Copyright 2017, American Chemical Society. c) A flexible wireless temperature-sensing platform with a printed temperature sensor. Reproduced

with permission ¹²⁹. Copyright 2020, Creative Commons Attribution 4.0 International License. d) A wireless wearable sensor patch for ECG and temperature sensing. Reproduced with permission ¹³⁰. Copyright 2016, WILEY-VCH Verlag GmbH & Co. e) An epidermal wireless thermal sensor (eWTS) with a thin and soft thermal sensing/actuating component. Reproduced with permission ¹³¹. Copyright 2018, WILEY-VCH Verlag GmbH & Co. f) A thermoresponsive colorimetric temperature sensor with plasmonic gold nanoparticles in PNIPAM hydrogels. Reproduced with permission ¹³². Copyright 2018, Creative Commons Attribution 4.0 International License..... 41

Figure 2.9. Examples of wearable and wireless systems illustrating the integration of biochemical and biophysical sensors on a single platform. a) A wearable multiplexed biosensor system with a flexible sensing array for glucose, lactate, pH, and skin temperature measurement. Reproduced with permission ¹⁵⁵. Copyright 2020, Elsevier. b) A disposable strip with a wrist-worn system for measurement of glucose, temperature, heart rate, SpO₂, and activity. Reproduced with permission ¹⁵⁶. Copyright 2018, WILEY-VCH Verlag GmbH & Co. c) A freestanding electrochemical system with an out-of-plane signal interconnection design for strain isolation in the signal pathway. Reproduced with permission ¹⁵⁷. Copyright 2020, Creative Commons Attribution 4.0 International License. d) A perspiration-powered soft electronic skin for urea, NH₄⁺, glucose, pH, and temperature measurement. Reproduced with permission ¹⁵⁸. Copyright 2020, The American Association for the Advancement of Science..... 46

Figure 3.1. Images and system block diagram of the custom multiplexing system along with a flexible sensor array. (a) Exploded view of the flexible sensor array showing the polyimide (bottom), metallization (intermediate), and encapsulation (top) layers. (b) *Left*: Picture of wrist-worn, wearable multiplexing system in a 3D printed watch enclosure for demonstration purposes only. *Right*: Picture of the flexible sensor array. (c) *Left*: CAD design of the flexible sensor array. *Right*: Fabricated flexible sensor array. (d) System block diagram of the custom multiplexing sensor system. 76

Figure 3.2. Characterization of the fabricated flexible sensor array with a benchtop potentiostat. Working electrode area: 0.0071 cm². (a-d) Chronoamperometric responses of the glucose (a,b) and lactate (c,d) sensors with increasing glucose (0 to 1000 μM) and lactate (0 to 40 mM) concentration in 1X PBS solution (n = 3). Bias: -0.1 V, pH 7.4, a 21°C. (e-f) Open circuit potential response of the pH sensor for increasing pH levels (n = 3). (g-h) Resistance response of the temperature sensor to temperature changes (22-45°C). The plots on the second column shows the corresponding calibration plots of the glucose, lactate, pH, and temperature sensors in the physiological relevant ranges. 80

Figure 3.3. System validation of the custom multiplexing system. (a, b) Benchtop potentiostat cyclic voltammetry and peak current vs. square root of scan rate graphs in 5 mM K₃Fe(CN)₆ and 1 M KCl in 1X PBS. R² is 0.99 for both anodic

and cathodic peaks. (c, d) Chronoamperometry measurements with a benchtop potentiostat in an aqueous solution of GO_x ($10 \text{ mg}\cdot\text{mL}^{-1}$) and $\text{K}_3\text{Fe}(\text{CN})_6$ ($10 \text{ mg}\cdot\text{mL}^{-1}$) in 1X PBS solution ($n = 3$). Bias: -0.1 V , pH 7.4. (e, f) Custom system cyclic voltammetry and peak current vs. square root of scan rate graphs in an aqueous solution of $5 \text{ mM K}_3\text{Fe}(\text{CN})_6$ and 1 M KCl in 1X PBS. R^2 is 0.98 and 0.97 for anodic and cathodic peaks, respectively. (g, h) Chronoamperometry measurements with the custom system in an aqueous solution of GO_x ($10 \text{ mg}\cdot\text{mL}^{-1}$) and $\text{K}_3\text{Fe}(\text{CN})_6$ ($10 \text{ mg}\cdot\text{mL}^{-1}$) in 1X PBS ($n = 3$). Bias: -0.1 V , pH 7.4. (i) Intraelectrode crosstalk study within the same channel. “ WE_{1-1} , WE_{1-2} , WE_{1-3} , and WE_{1-4} ”: First, second, third, and fourth working electrodes of the first channel, respectively. (j) Interelectrode crosstalk study among different channels. “ WE_{1-1} , WE_{2-1} , and WE_{3-1} ”: The first working electrode of the first, second, and third channels. Each arrow on the graphs indicates the time when the given electrode is electrically disconnected.

..... 85

Figure 3.4. Characterization of the fabricated flexible sensor array with the custom multiplexing system. (a-d) Chronoamperometric responses of the glucose (a,b) and lactate (c,d) sensors for increasing glucose (0 to $1000 \mu\text{M}$) and lactate (0 to 40 mM) concentrations in 1X PBS ($n = 3$). Bias: -0.1 V , pH 7.4. (c) Open circuit potential response of the pH sensor for increasing pH levels (4 to 8). (d) Voltage response of the temperature sensor to variations in temperature ($23\text{-}42^\circ\text{C}$). (e-g) The corresponding calibration plots of the glucose, lactate, and pH sensors, respectively..... 86

Figure 3.5. Multiplexed reading of glucose, lactate, pH, and temperature with a custom-designed multiplexed system in 1X PBS solution. The plots are replotted from the highlighted regions of the Supplementary Figure S3.13. (a) Multiplexed measurement of glucose, lactate, pH, and temperature after addition of glucose into the test solution (final concentration of glucose in the test solution: $400 \mu\text{M}$). (b) Multiplexed measurement of glucose, lactate, pH, and temperature after addition of lactic acid into the test solution (final concentration of lactic acid in the test solution: 10 mM). Conditions of the chronoamperometric measurements (bias: -0.1 V , pH: 7.4, working electrode area: 0.03 cm^2). The grey highlighted region in (a) and (b) shows the noise generated due to pipetting the analyte solution into the test solution. WE_{1-1} to WE_{1-4} : glucose sensors, WE_{2-1} to WE_{2-4} : blank electrodes, WE_{3-1} to WE_{3-4} : lactate sensors (WE_{x-y} , for $x: 1,2,3$ and $y: 1,2,3,4$, where x and y indicate the channel number and the working electrode number, respectively)..... 89

Figure S3.1. Common amperometric detection schemes from multiple working electrode arrays. Redrawn from (Ramfos et al. 2015). (a) Sequential reading from multiple working electrodes. It uses a single bias/convert unit and one ADC to digitize the results. The main disadvantage of this scheme is that not all working electrodes are biased continuously. (b) Parallel reading from multiple working electrodes. Each working electrode has its own bias/convert and ADC units. This design provides simultaneous and real-time measurement of each

working electrode. (c) One bias/convert for each working electrode and a common ADC. All working electrodes are biased concurrently. This option is area effective compared to the detection scheme in (b). (d) Hybrid multiplexing scheme. Each working electrode is continuously biased. The scheme uses single pole double throw analog switches. This design connects the active working electrode to the bias/convert unit while maintaining all others working electrodes at a constant voltage, thus not disturbing the electrochemical process at each working electrode. This multiplexing scheme was utilized in this study.

..... 99

Figure S3.2. Fabrication process of the flexible sensor array. (a) Cleaning of the polyimide film with acetone and isopropanol. (b) Deposition of Cr/Au using DC sputtering, photolithography, and wet etching of Cr/Au. (c) Spin-coating of the positive photoresist for encapsulation of the conductive traces. (d) Removal of the positive photoresist in the developer to expose electrode areas and connection pads. (e) Optical image of the flexible sensor array. 100

Figure S3.3. Electrodeposition techniques for functionalization of the electrode surfaces. (a) Chronoamperometric deposition of gold nanoparticles at -0.1 V for 15 min in an aqueous solution of 2 mM HAuCl_4 in 2 M H_2SO_4 . (b) Electrodeposition of polyaniline using cyclic voltammetry from -0.2 to 1V at a scan rate of $100 \text{ mV}\cdot\text{s}^{-1}$ in an aqueous solution of 0.1 M aniline in 1 M HCl. (c) Electrodeposition of Prussian blue using cyclic voltammetry from 0 to 0.5 V at a scan rate of $20 \text{ mV}\cdot\text{s}^{-1}$ in an aqueous solution of 100 mM KCl, 2.5 mM FeCl_3 , and 2.5 mM $\text{K}_3\text{Fe}(\text{CN})_6$ in 100 mM HCl. The redox peaks at 0.2 V and 0.18 V are associated with interconversion between Prussian blue and Prussian white (Karyakin 2001). (d) Repeatability of pH sensors in varying pH solutions (pH4 \rightarrow 8 and pH8 \rightarrow 4). 5 min wait time between successive measurements. 101

Figure S3.4. Benchtop chronoamperometric analysis of glucose (a) and lactate (b) sensors with varying exfoliated graphite concentrations (0, 2, and 5 $\text{mg}\cdot\text{mL}^{-1}$) in 1X PBS ($n = 3$). Bias: -0.1 V, pH 7.4. 101

Figure S3.5. Sensitivities of glucose (a) and lactate (b) sensors after 10 days storage at 4°C ($n = 4$). Bias: -0.1 V, pH 7.4. 102

Figure S3.6. (a) Full system block diagram of the custom multiplexing system. The system includes four potentiostats (LMP91000). The three potentiostats are connected to the 12 working electrodes through three single-pole, single-throw switches (SPST), which control which electrode is connected to the potentiostats for each channel. The last potentiostat provides a virtual ground for the working electrodes when they are not active. The temperature and pH sensors use a voltage divider and a pH sensor IC (LMP91200), respectively. The system uses two 16 bits ADCs and a Bluetooth low energy microcontroller (BLE113). (b) Make-before-break switch operation from WE1 to WE2. Each working electrode is connected to two switches in the multiplexer: one is connecting the active working electrode to the potentiostat and another switch is connecting

the working electrode to the virtual ground (1 V) when the electrode is not in use. As the working electrode is alternating between readout and standby mode, a make-before-break multiplexing scheme is utilized to prevent instant peaks during the transitions when the current flow is briefly cut off. 103

Figure S3.7. (a) Digital output vs. input current for varying gain (14 k Ω , 35 k Ω , 120 k Ω , 350 k Ω , 510 k Ω , 1 M Ω , 2 M Ω , and 3.92 M Ω) of the transimpedance amplifier (TIA) in LMP91000 potentiostat. Applied potential: -0.1 V. External resistor values: 100 k Ω , 220 k Ω , 560 k Ω , and 1 M Ω . For a given gain of the TIA and an applied bias (-0.1 V) in the potentiostat, the value of the external resistor was changed to find the value of ADC digital output that corresponded to the magnitude of the current that flowed through the resistor. These four digital output values were extrapolated to find the maximum current that can be read with the custom designed system for a given amplifier gain setting (dotted lines). (b) A replot of the left figure for a narrow range of input currents. These plots help to adjust the gain of the amplifier without saturating the ADC output based on the maximum reduction currents obtained from glucose or lactate sensors in the benchtop measurements. 105

Figure S3.8. Circuit diagrams of the wearable multiplexing system. The schematic shows a system-on-chip, power management units (a battery management unit and switching regulators), an analog-to-digital converter, board-to-board connectors, and a pushbutton connector. 106

Figure S3.9. Circuit diagrams of the wearable multiplexing system. The schematic shows three potentiostats, three multiplexers, a potentiostat for virtual ground and three virtual ground isolation units, a pH sensing unit, an analog-to-digital converter, level shifters, a temperature sensing unit, board-to-board connectors, and a sensor header. 107

Figure S3.10. Optical and SEM images of bare gold electrode and gold nanoparticle deposited electrodes. Images from left to right indicate increasing gold nanoparticle deposition times (0, 5, 10, 15, 30, 45, and 90 min). (a-g) Optical microscopy images of the bare gold electrode and AuNPs deposited gold electrodes. The amount of electrodeposited AuNPs increase with the increased deposition time. (h-n) SEM images of the bare gold electrode and AuNPs deposited gold electrodes. The nucleation of the gold nanoparticle growth starts from the edges of the bare gold electrodes. (o-u) SEM images taken from the center of the electrodes. 110

Figure S3.11. Electrochemical impedance spectroscopy and cyclic voltammetry characterization of the bare gold electrode and gold nanoparticle deposited electrodes in an aqueous solution of 5 mM K₃Fe(CN)₆ in 1xPBS and 10 mM K₃Fe(CN)₆ in 1xPBS, respectively. (a) Bode plots of the bare gold electrode and AuNPs deposited gold electrodes with varying electrodeposition time (5, 10, and 15min). Deposition of AuNPs on the bare gold electrode surface significantly decreases its DC impedance. (b) Cyclic voltammetry plots of the

bare gold electrode and AuNPs deposited gold electrodes with varying electrodeposition time (5, 10, 15, 30, 45, and 90 min). Scan rate: $500 \text{ mV}\cdot\text{s}^{-1}$. Increase of the electrochemically active surface area of the bare gold electrodes results in high current levels. (c) Square root of the scan rate vs. peak current of the bare and AuNPs deposited gold electrodes with varying electrodeposition times. 111

Figure S3.12. Chronoamperometric response of glucose oxidase ($10 \text{ mg}\cdot\text{mL}^{-1}$) + $\text{K}_3\text{Fe}(\text{CN})_6$ ($10 \text{ mg}\cdot\text{mL}^{-1}$) and lactate oxidase ($10 \text{ mg}\cdot\text{mL}^{-1}$) + $\text{K}_3\text{Fe}(\text{CN})_6$ ($10 \text{ mg}\cdot\text{mL}^{-1}$) in 1X PBS to increasing glucose (1 to $600 \mu\text{M}$) and lactate (1 to 40 mM) concentrations, respectively ($n = 1$). The enzymes are dispersed in 1X PBS solution along with the mediator to assist with electron transfer from the active side of the enzyme to the electrode surface. Bias: -0.1 V , pH 7.4. (a-d) Measurement of GO_x current response using (a,b) a benchtop potentiostat and (c,d) the custom multiplexing system. (e-h) Measurement of LO_x current response measurement using (e,f) a benchtop potentiostat and (g,h) the custom multiplexed system. 114

Figure S3.13. Multiplexed reading of glucose, lactate, pH, and temperature with a custom multiplexed sensing system in 1xPBS solution. Glucose was added at 5, 10, and 15 min, yielding 200, 400, and $600 \mu\text{M}$ of glucose in the test solution. Lactic acid was added at 20, 25, and 30 min, giving 5, 10, and 15 mM in the test solution. Conditions of the chronoamperometric measurements (bias: -0.1 V , pH: 7.4, working electrode area: 0.03 cm^2). The grey highlighted regions in the figure shows $400 \mu\text{M}$ glucose and 10 mM lactic acid, respectively. The highlighted regions were shown in Figure 3.5a and Figure 3.5b of the main article in detail. WE_{1-1} to WE_{1-4} : glucose sensors, WE_{2-1} to WE_{2-4} : blank electrodes, WE_{3-1} to WE_{3-4} : lactate sensors (WE_{x-y} , for $x: 1,2,3$ and $y: 1,2,3,4$, where x and y indicate the channel number and the working electrode number, respectively). 115

Figure S3.14. Multiplexed reading of glucose, lactate, pH, and temperature with a custom multiplexed sensing system in 1xPBS solution. Glucose was added at 5, 10, and 15 min, yielding 200, 400, and $600 \mu\text{M}$ of glucose in the test solution. Lactic acid was added at 20, 25, and 30 min, giving 5, 10, and 15 mM in the test solution. Conditions of the chronoamperometric measurements (bias: -0.1 V , pH: 7.4, working electrode area: 0.03 cm^2). The concentration of the glucose and lactate in the solution as well as the pH and temperature of the solution was calculated using the voltage output of the system in Figure S3.13 and the sensitivity of the sensors. The black curve for glucose and lactate sensors represents the average of voltage outputs of four working electrodes. Averaging the responses from four working electrodes smooths the output of sensor and improves the accuracy of analyte detection. The red curves in the plot show further median averaging (100 points) of the black raw data. 116

Figure S3.15. Multiplexed measurement of (a) glucose, (b) lactate, (c) pH, and (d) temperature in the collected sweat sample (pH 7.34) from the Subject 1 using

	the custom multiplexing system. The black line shows the collected sample in all graphs. The red line indicates the collected sweat solution with added glucose or lactate. Addition of glucose or lactate to the collected sweat sample was detected by the custom system (20°C).	118
Figure S3.16.	Multiplexed measurement of (a) glucose, (b) lactate, (c) pH, and (d) temperature in the as-collected sweat sample (pH 6.03) from the Subject 2 using the custom multiplexing system. The black line shows the collected sample in all graphs. The red line indicates the collected sweat solution with added glucose or lactate. Addition of glucose and lactate to the collected sweat sample was detected by the custom system (20°C).	119
Figure S3.17.	Multiplexed measurement of (a) glucose, (b) lactate, (c) pH, and (d) temperature in the artificial sweat solution (pH 4.48) using the custom multiplexing system. The black line shows the artificial sweat sample in all graphs. The red line indicates the artificial sweat solution with added glucose or lactate. Addition of glucose and lactate to the artificial sweat sample was detected by the custom system (20°C). The blue line indicates a “blank sample” (1X PBS).	120
Figure 4.1.	A fully integrated wireless wearable system with electrochemical and optical sensing capabilities. The overall system houses flexible optical and electrochemical sensors that are attached to the custom system via an FFC connector. The optical sensor includes three-wavelength LEDs, a light sensor integrated circuit (IC), and a thermistor, whereas the biochemical sensor incorporates amperometric lactate and potentiometric polyaniline-based pH sensors on a flexible polyimide film. The custom-design system is packaged in silicone and mounted on a nonwoven fabric.	130
Figure 4.2.	(a) Characterization of electrical resistance change of 0402 size 100k thermistor (Murata) with temperature (from 22°C to 45°C). (b) Measurement of the voltage output of a polyaniline pH sensor in varying pH buffer solutions (4 to 8) relative to a printed Ag/AgCl reference electrode.	131
Figure. 4.2.	Continuous photoplethysmogram (PPG) measurement using the developed wireless, wearable system. The PPG signal (black line) was denoised, and its baseline shift was subtracted. LED wavelength: 850 nm. Electrocardiogram (ECG) signal was measured using Zephyr™ Bioharness system.	132
Figure 4.3.	Continuous assessment of tissue oxygenation (HbO ₂ -Hb) and blood volume (HbO ₂ +Hb) on the forearm of a subject via continuous-wave near-infrared spectrometry (CW-NIRS) (LED wavelengths: 625nm and 940nm) A manual inflatable cuff was attached to the upper arm of the subject (sitting), and a brief arterial occlusion (180-200 mmHg) was induced using a manual sphygmomanometer.	132

CHAPTER 1: Introduction

1.1. Objective

Wearable health monitoring systems are body-worn electronic devices for real-time monitoring of physiological parameters of the body to evaluate and understand overall health and wellness as well as disease pathology. These wearable systems decode the physiological information from the body using biophysical and biochemical sensors, process and interpret the physiological data, and eventually inform the user or healthcare provider about the overall health status of the user (Figure 1.1).

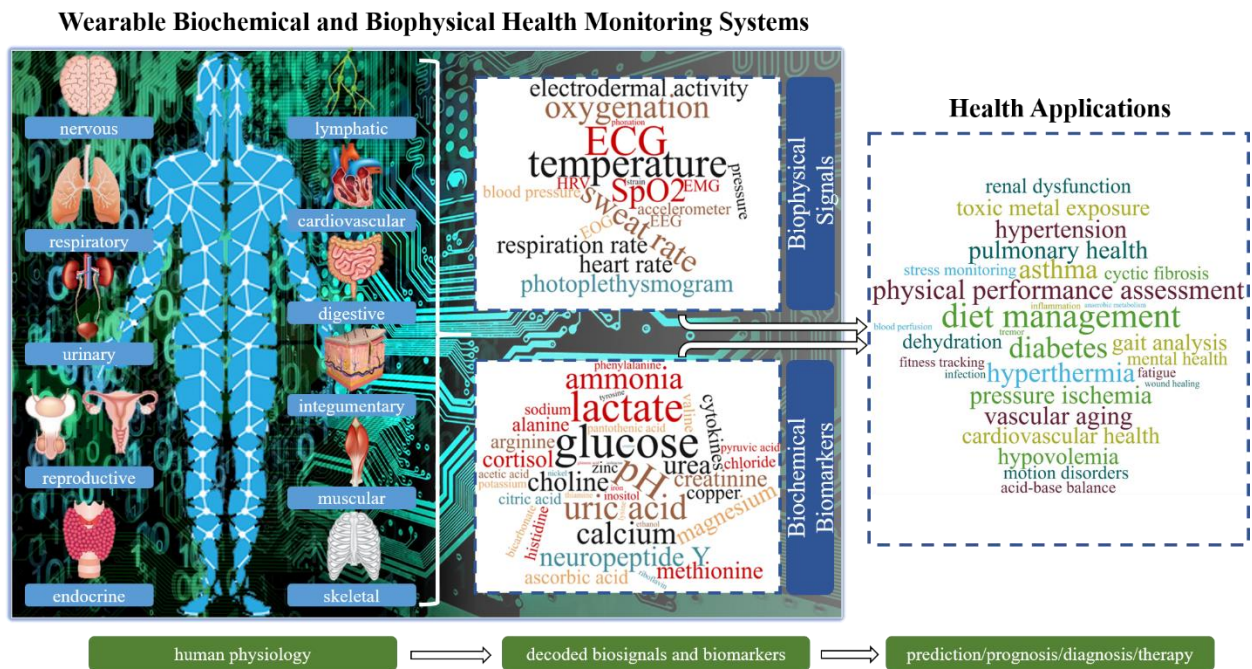


Figure 1.1. Overview of wearable health monitoring systems. Multiplexing biochemical and biophysical sensors opens up new opportunities for health applications toward a comprehensive understanding of overall health and disease states.

Currently available wearables monitor physical parameters like activity, heart rate, respiration rate, burned calories, number of steps, and SpO₂. However, they fail to provide information about human biochemistry at a molecular level, which is critical for the assessment of overall health and disease conditions. The hand-held biochemical monitors, such as glucose or

lactate meters, enable discrete measurement of capillary glucose or lactate levels; however, their invasiveness and inflammation risk limits their ubiquitous use. Besides, they usually miss the sudden drops or peaks of biomarker levels during the day due to the frequency of device use. Therefore, there has been a need for multimodal wearable systems that are unobtrusive and comfortable and can provide the measurement of an increased number of clinically relevant biomarkers. These wearables should (1) provide a continuous and noninvasive assessment of the human biochemistry from biofluids such as sweat and (2) enable multiplexed detection of sweat biomarkers along with other biophysical signals.

Within this context, I developed various wearable health monitoring systems for the assessment of cardiovascular health, dehydration, diet management, and performance monitoring throughout my time in graduate school (**Figure 1.2**). My initial research efforts focused on the development of a wearable “smart ECG garment” for continuous evaluation of cardiovascular health. This work involved the investigation of dry Ag/AgCl printed electrodes and printed stretchable interconnects on textiles to enable the continuous acquisition of distributed biopotentials across the body surface. My subsequent research was on the development of a wearable sweat rate monitoring system for continuous assessment of dehydration. This research involved the fabrication of flexible impedance sensors and paper-based microchannels for real-time sweat loss measurement. Later on, I developed a wearable system toward continuous monitoring of lactate in sweat. This study involved prolonged sensing of lactate in sweat using hydrogels and paper-based microfluidic channels, mainly intended for passive extraction and analysis of sweat for low sweating conditions. My recent efforts was on the development of wearable multiplexed sensing systems for the detection of biomarkers of human metabolism and respiration (glucose, lactate, and oxygen), which constituted the main theme of this dissertation.

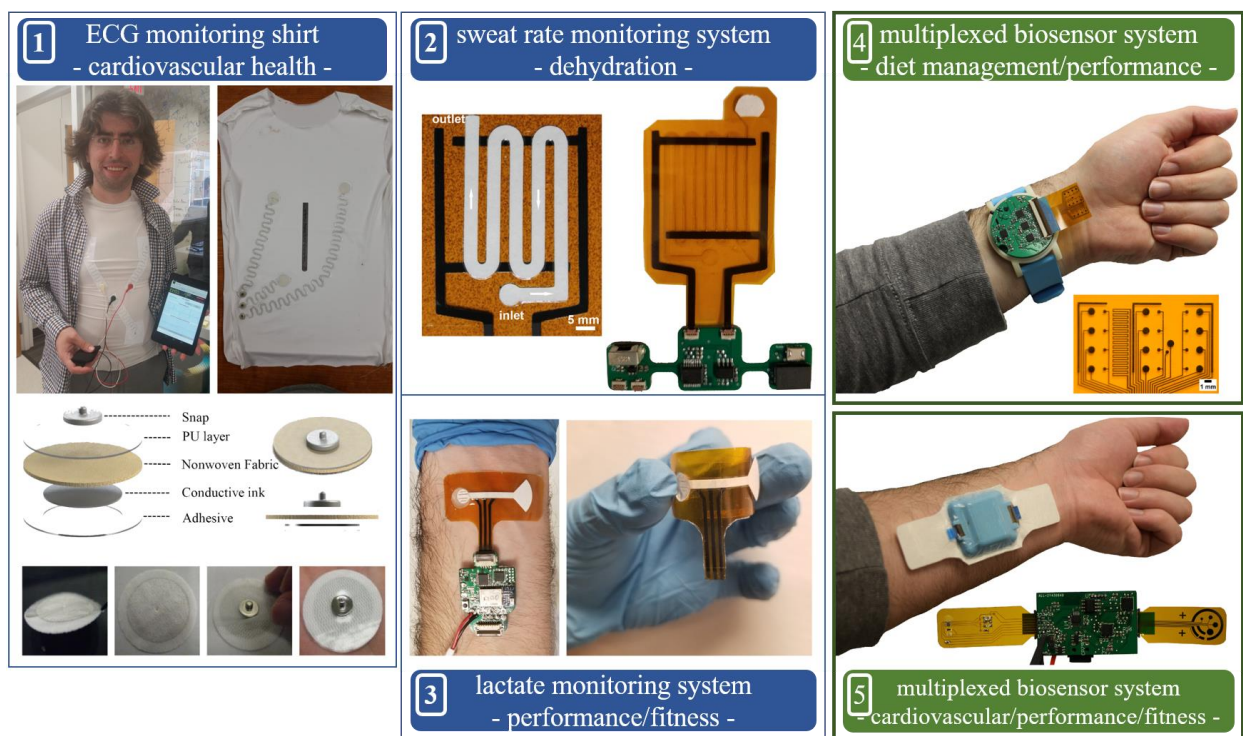


Figure 1.2. Chronological overview of the developed wearable health monitoring systems in this dissertation. The numbers on each figure (1 to 5) indicate the order of the developed systems.

The objective of this dissertation is to develop wearable, wireless systems for continuous and multiplexed detection of biomarkers of human metabolism and respiration. The novelty and contribution of this dissertation is three-fold. (1) It demonstrates examples of non-invasive wearable platforms for the real-time monitoring of vital biomarkers of human respiration and metabolism (i.e., glucose, lactate, and oxygen) via sweat analysis and optical sensing. (2) The developed wearable system includes a multi-array sensing electrode (i.e., redundant electrodes) for increasing the precision and sensitivity of glucose and lactate detection. (3) The wearable system further implements on-site pH and temperature sensors toward accounting for the fluctuation in enzyme activity due to environmental effects on the wearable sensor.

1.2. Dissertation Outline

Chapter 2 introduces the concept of wearable health monitoring from its inception to the present and provides the requirements of such systems. It reviews the methods of sweat extraction and collection, wearable biochemical and biophysical sensors/systems, and highlights examples of wearable multimodal systems with their system specifications. It eventually summarizes the challenges of the current wearable systems and provides my perspectives on multimodal health monitoring systems.

Chapter 3 reports a comprehensive study for the design and characterization of a wearable, wireless system with a flexible sensor array for non-invasive and continuous monitoring of human biochemistry (glucose, lactate, pH, and temperature). The study provides the fabrication and functionalization steps of a multielectrode array for the detection of sweat biomarkers. It explains the design of a custom-designed hardware that can measure chronoamperometric signals from 12 working electrodes along with skin temperature and sweat pH. The study further dives into the characterization of the fabricated sensors with the custom wearable hardware and benchtop equipment. It eventually demonstrates *in-vitro* sensing with an artificial sweat and sampled sweat from human trials.

Chapter 4 summarizes the current work and provides recommendations for future work. It also briefly discusses a custom-designed wearable system for continuous detection of lactate, pH, skin temperature, heart rate, and tissue oxygenation.

Appendix A to F compiles the other two journal articles and four conference papers that I published in chronological order.

Appendix A provides a detailed characterization of printed Ag/AgCl dry electrodes as an alternative to wet electrodes to be used for continuous ECG monitoring. It investigates the skin-

electrode interface, form factor design of electrodes, and on-body placement of the printed dry electrodes. It also compares the signal quality of ECG signals obtained with dry and wet electrodes as a function of body posture and movement toward the development of a smart garment for ambulatory ECG measurement.

Appendix B includes the characterization of stretchability and fatigue life of printed stretchable interconnects on textiles. This research investigates the design and optimization of serpentine-shaped printed conductive lines and demonstrates the integration of electronics on textiles and a continuous ECG sensing garment. The “iron-on” printed electronics approach, which can be easily scaled and integrated into the textile manufacturing chain, enables continuous monitoring of bioelectrical signals while keeping the breathable and stretchable nature of garments.

Appendix C is about the design and COMSOL Multiphysics® simulation of a skin-worn capacitive hydration sensor. This study models the capacitance variation of an interdigitated capacitive sensor as a function of the relative permittivity of the underlying substrate, frequency, and wetness of skin (dry vs. wet skin conditions).

Appendix D is about the development of a wearable, wireless system for perspiration monitoring. The study provides the fabrication steps of a serpentine-shaped interdigitated sensor as an impedance sensor. It further demonstrates the fabrication and characterization of a custom-designed, low-power impedance sensing system on a flexible substrate. The study analyzes the effect of electrolyte concentration, flow rate, and fluid volume on the impedance measured by the wearable system.

Appendix E presents a wearable biosensor patch for biofluid extraction, sampling, and quantitative sensing for low sweating conditions or sedentary subjects. It investigates the use of

hydrogels and paper-based microfluidic channels for combined osmotic and capillary pumping of sweat and continuous lactate sensing with screen-printed electrodes. The study researches the extraction and transportation of lactate from a model skin to the evaporation pad as a function of time and lactate concentration in a model skin. Furthermore, it demonstrates the fabrication, functionalization, and characterization of screen-printed lactate sensors for continuous lactate sensing. The proposed approach minimizes the challenges related to sweat-based sensing systems, such as sweat evaporation, contamination from the skin, and mixing of new sweat with old sweat. It enables continuous and passive sensing of other biomarkers of interest in sweat.

Appendix F provides the benchtop characterization of an impedance-based wearable sensor integrated with a paper-based microfluidic channel for continuous sweat rate monitoring. The study provides the fabrication steps of the integrated system, investigates the spatiotemporal characteristics of fluid flow in the microfluidic channel, and finally demonstrates a continuous impedance-based sweat rate sensing.

Appendix G provides an approved human trial protocol by the Institutional Review Board (IRB) for the evaluation of a wearable, wireless multiplexed system for the measurement of sweat biomarkers and tissue oxygenation.

Finally, Appendix H lists **my contribution to the scientific literature** (as a first author or co-author): 3 full research articles (and 1 article in preparation), 10 conference papers, 1 issued patent, and 2 review articles.

CHAPTER 2: Literature Review

By Murat A. Yokus and Michael A. Daniele

*submitted for publication (under review)

2.1. Introduction

The history of diagnostics dates back to ancient Egypt and Mesopotamia, where the earliest physicians made diagnoses and treatment using their senses ¹. In medieval times, physicians used palpation to understand diseases related to the heart and lungs, and utilized coloration of the skin, smelling, and tasting of wounds, breath, sweat, and urine to describe dysfunctions related to the digestive tract, liver, and spleen. Later on, with the invention of the stethoscope, microscope, endoscope, thermometer, X-rays, electrocardiogram, and other medical devices, significant advancements were made in the study of histology, cytology, and human physiology. The medical diagnostics progressively moved from qualitative and subjective examinations by the physicians to new sensing systems, in which the data could be recorded, analyzed, and compared with the data recorded in the past. With the advent of telemetry, it became common to monitor the physiological condition of patients at a distance from the clinic. The remote home-based monitoring enabled the exchange of discrete medical data (blood pressure cuff, glucose meters, pulse oximeters, or heart monitors) between a patient at home and medical personal at clinics using phone or wireless technology.

Wearable health monitoring systems provide the opportunity to monitor users continuously or on-demand while the users engage in usual daily activities. These wireless systems usually necessitate body-worn systems and are applicable for specific medical conditions where the home-based telemonitoring is not adequate. Some of the best examples of wearable systems are ECG Holter monitor and continuous glucose monitors (CGMs) ²⁻³. Often abnormal heart conditions and

unforeseen changes in blood glucose levels may not be present on routine clinical visits. Ambulatory monitoring with these systems can detect periodic arrhythmias, monitor large fluctuations in blood glucose levels, and provide clinicians with a snapshot of the health condition of patients. Another use of mobile wearable systems is in on-demand and post-intervention monitoring, where the recovery of an athlete or patient from an injury or a medical condition (*e.g.*, heart attack or peripheral artery disease) can be monitored continuously, and efficacy of treatments and planning of subsequent medication can be assessed⁴. The usage of the ambulatory monitoring can be extended to emergency monitoring of first responders, firefighters, and aircraft pilots, and the performance parameters can be remotely monitored by qualified staff with the aim of survival management⁵⁻⁶.

System architecture of a wearable health monitoring system consists of external sensors, a central processing unit, analog-to-digital converter (ADC), a wireless interface, battery, and energy management unit (**Figure 2.1**). The external sensors for mobile applications can include sensors for monitoring heart and lung activity (ECG, respiration, oxygen saturation, and heart rate), biochemical composition (pH, glucose, hormones, and proteins), and body characteristics (temperature and activity). These sensors convert electrical, mechanical, chemical, and radiant energy into an electrical signal that can be recorded by the processing unit. Each biosensor may require specific pre-processing and amplification stages depending on the output type of the sensors (*e.g.*, voltage, current output), dynamic range, and frequency of the biosignals. While typical pre-processing stages are low-noise amplifiers and anti-aliasing filters, additional components may be added depending on the sensor type, such as potentiostats for biochemical sensors and light-emitting diodes, photodetectors, and current drivers for optical sensors. Filtering is performed to reduce the contribution of high-spectral components as well as to remove the

external noises, such as motion artifacts, which is followed by an ADC stage with adequate resolution to acquire biosignals. The processing unit and data storage modules acquire, process (feature extraction and classification), store, and transmit the physiological data. The wireless interface includes wireless communication technologies, such as mid-range RF communications (Bluetooth and Zigbee) and short-range inductively coupled links (RFID and NFC), for the transfer of the physiological data to a nearby device or computer ⁷. The connection of these devices with medical servers over the internet is carried out via GSM/CDMA/LTE/5G cellular networks or Wi-Fi, where physicians and caregivers are connected through a network of health servers and databases. Battery and energy management unit powers the rest of the system and regulates the voltage required for the parts of the system. The design and relevance of the wearable systems usually determine their final use, and in most cases, will be contingent on the requirements of mobile monitoring applications, such as critical importance of physiological biomarker and frequency of device usage.

The integration of wearable health monitoring systems with the body can have different configurations based on the application, source of biosignals, portability, ease of use, and user comfort ⁸. Commercial wearable devices, such as wristwatches, armbands, chest patches, and smart clothing, have been developed by various companies to monitor blood pressure (iHealth), activity and sleep (iHealth, Fitbit, Apple, and Garmin), pulse oximeter (iHealth and Nonin Medical), cardiovascular health (Hexoskin, Zephyr strap, MC10 BioStamp), and glucose (GlucoWatch G2 Biographer and GlucoTrack) ⁹⁻¹⁸. The employment of these systems can range from fitness/wellness monitoring and disease prognosis to anomaly detection and medical diagnosis. Despite the popularity of wearables, user acceptance is limited to specific areas, mostly due to their limited sensing capabilities. This condition restrains their widespread use in health and

clinical applications as most of the clinical conditions cause changes in body biochemistry. As such, wearable systems with multimodal sensing capabilities (physical and biochemical) can provide a wealth of information for a broader understanding of health conditions and disease states.

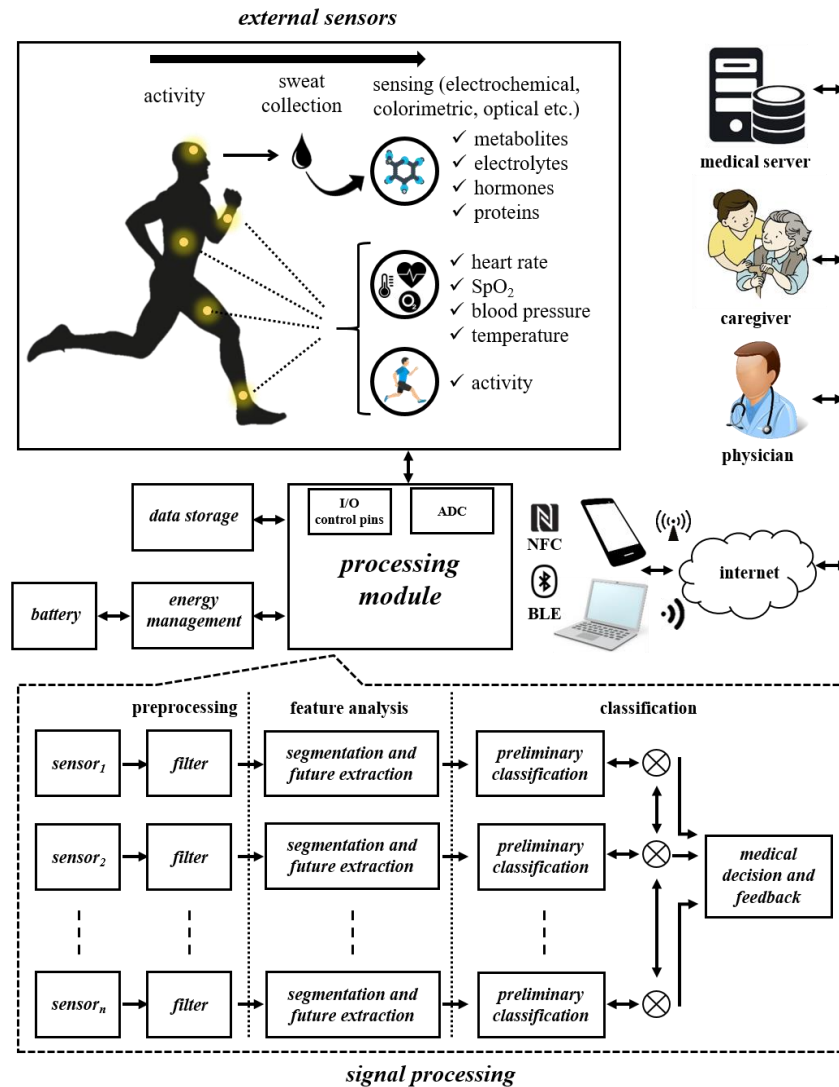


Figure 2.1. A schematic illustration of the architecture of wearable multimodal health monitoring systems. The system consists of external sensors, a central processing unit, analog-to-digital converter (ADC), a wireless interface, battery, and energy management unit. The processing module acquires, processes, and transmits the signals from external biochemical and biophysical sensors. The wearable systems have the capability of sampling and analyzing biofluid of interest (sweat) via biochemical sensors and can wirelessly send the biochemical information with other physical, sensory data to a smartphone or a tablet. The medical data from these devices is sent to the medical servers (i.e., cloud) via cellular networks or Wi-Fi, where physicians and caregivers are connected through a network of health servers and databases to provide feedback, treatment, prognosis, and diagnosis based on the history of the clinically relevant data.

The new class of skin-worn wearable systems can collect and sense biological fluids, such as sweat, in addition to sensing other physiological parameters. Detection of analytes from eccrine sweat glands offers various advantages over other biofluids (blood, tear, and urine) due to its ease of sampling, non-invasiveness, and availability of the eccrine sweat glands across the body. Sweat, specifically, contains electrolytes, metabolites, proteins, and hormones, and offers real-time molecular analysis of the physiological state ¹⁹⁻²¹. The ability to accommodate physical and biochemical sensors on a single wearable platform with on-board processing and wireless connectivity enables new classes of biochemical sensors that can address the needs of clinicians, athletes, and daily users (**Figure 2.1**).

The design of such wireless, skin-worn systems should meet numerous specifications at the sensor, device, and system-levels. The sensor-level requirements include stability (pH, temperature, ionic strength, and humidity), sensitivity, and limit of detection of a sensor for the detection of a biochemical analyte or a physical parameter ²². The device-level requirements embody the design of microfluidics for sweat extraction and collection to minimize analyte degradation, sweat evaporation, and contamination from the skin ²³. In addition to the fluid handling, ease of wear, non-invasiveness, no toxicity, and unobtrusiveness are essential for wearable devices for the mitigation of skin-device mechanical mismatch, skin irritation, and motion artifacts ²⁴. The system-level requirements comprise real-time data acquisition, power consumption and battery lifetime, communication and ubiquitous coverage, fault tolerance (robustness to the common interferences), decision support and user interface, multisensory data management and data mining, data encryption and security, standardization, cost, and scalability ²⁵⁻²⁶. All the design requirements make the design of skin-worn wearable systems a tedious process

to meet the needs of the intended application, such as the selection of optimal sensors, multi-level integration and fabrication, and electronic system design.

This review highlights the research and development in skin-worn, sweat-based wearable sensors and systems in the last five years towards health and performance monitoring. It is aimed to be complementary to the existing reviews in this field^{22, 27-34} by summarizing the current research on biochemical (metabolites, electrolytes, oxygen, and other chemicals) and biophysical (sweat rate and temperature) sensors/systems and featuring examples of wearable multimodal systems with a focus on their system-level operation. With that in mind, sections two to four summarize sweat sampling and collection techniques as well as biochemical and biophysical sensors in current wearable devices. Subsequently, the wearable systems with multimodal biochemical and biochemical sensing capabilities were demonstrated. We eventually discuss and present related challenges and our perspectives on wearable systems in the context of prolonged physiological monitoring.

2.2. Wearable Biochemical Sensors

2.2.1. Sweat Extraction and Sampling Methods in Wearable Sensors

Extraction and continuous collection of sweat is vital for accurate and reliable detection of analytes in real-time sweat sensing applications as the sweat generation varies between individuals and shows regional variation³⁵⁻³⁶. Extraction of sweat from skin can be accomplished by thermal bathing, exercise, or local iontophoresis stimulation. Once an adequate amount of sweat is accumulated on the skin surface, it needs to be further sampled and stored to prevent sweat loss and any potential degradation of analytes. Traditional sweat sampling techniques involve whole body-washdown technique and sweat collection with absorbent patches and Macroduct®³⁷. The whole body-washdown technique is the gold standard for the measurement of total sweat loss and

its composition ³⁸. In this method, subjects exercise on a cycle ergometer in a sealed plastic box. Upon completion of the exercise, subjects, the plastic box, clothes, and equipment are rinsed with deionized water to collect sweat for further analysis. This method involves complex steps and controlled lab settings; therefore, it does not apply to field settings. The absorbent patches are usually applied at specific locations on the body, such as the forearm, upper arm, thigh, and lumbar area, along with a supporting outer membrane ³⁹⁻⁴⁰. The collected sweat is weighed for sweat loss or extracted and analyzed for further analysis. Although this method is simple, its results vary with different sweat regions, and it may overestimate the analyte concentration as compared to the body-washdown technique. The absorbent patches may also block the sweat ducts (hydromeiosis effect) and affect the sweat rate if the sweat pool is formed on the skin surface. Macroduct®, a sweat collecting device for sweat rate and composition analysis, allows continuous collection of sweat in its spiral plastic tubes and minimizes hydromeiosis ⁴¹. The traditional sampling methods require trained personnel, complex procedures, and may suffer from low sweat volumes. They are susceptible to sample evaporation, regional and varying sweating rates, potential sample degradation between collection and analysis steps, making it not suitable for real-time and dynamic sweat monitoring. Therefore, novel approaches and miniaturized sampling devices have been proposed to mitigate some of the challenges of the traditional methods that enable in-situ and continuous sweat collection and analysis on a single sensing device.

Engineering the skin-sensor interface to minimize the contamination from the skin is one of the essential design considerations in sweat sampling. The gap between skin surface and sensor determines the volume of the sampled sweat as well as the time required to thoroughly flush out the old sweat from the skin-sensor interface ⁴². Uneven skin surface, presence of hair, and low sweat rates from the sweat glands increase the time required for replenishment of old sweat;

consequently, it increases the potential of skin contamination from cosmetics or bacteria. Heikenfeld's group proposed a new oil-membrane approach to reduce the sensing sample volumes from μL to nL to minimize the analyte contamination⁴³. A micro-porous polycarbonate membrane is coated with a water-soluble polyvinyl alcohol (PVA) polymer and a cosmetic-grade oil and placed onto the skin (**Figure 2.2a**). Isolating the sweat only to the region above the sweat ducts reduces sweat sampling time to the order of several minutes, and it blocks the low oil solubility contaminants from the skin surface. This method may make the wearable sensor susceptible to biofouling from the lipophilic analytes and the dissolved PVA membrane.

An alternative way of engineering the skin-sensor interface is the placement of sweat-absorbing materials at the skin-sensor interface. The absorbent materials are not only used for absorbing sweat but also for eliminating the direct skin contact, skin irritation, and reducing the motion artifacts in wearable systems. **Figure 2.2b** shows a sponge-like substrate for the collection and analysis of sweat⁴⁴. Its integration with thin and stretchable electronics enabled assessment of sweat volume via a dielectric change and colorimetric analysis of sweat composition, such as pH, copper, and iron concentration. When the pores of the absorbent material were filled with sweat, it caused changes in color and dielectric properties of the absorbent material, which then could be interrogated with a digital camera and near field communication device nearby. Although colorimetric sensing with the absorbent material looks promising, on the system level, the radio frequency characteristics of the sensing device are sensitive to mechanical stretching, salinity, and ionic content of sweat.

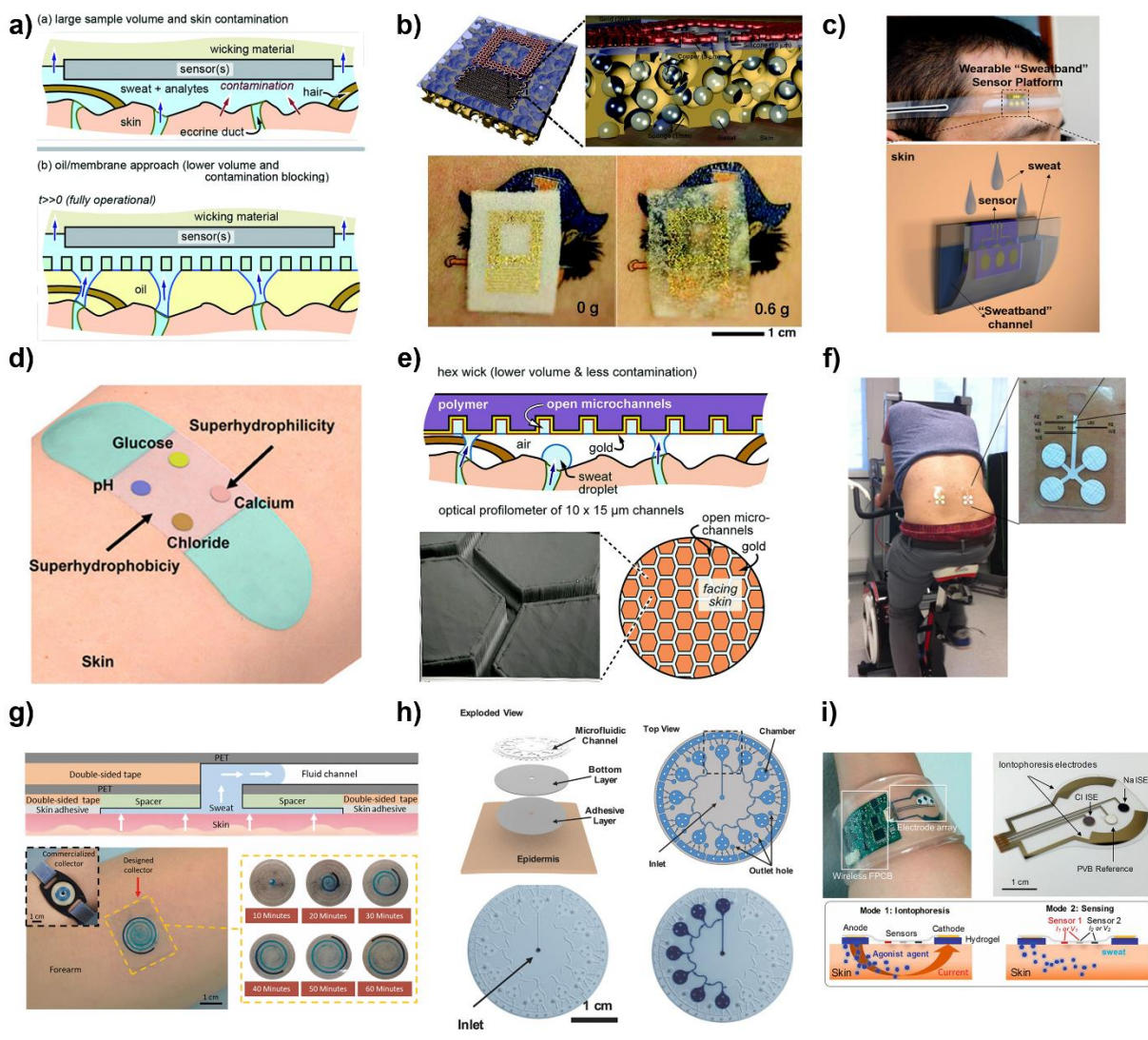


Figure 2.2. Sweat extraction and sampling methods in wearable systems. **a)** An oil-membrane approach for sweat sampling. Reproduced with permission⁴³. Copyright 2016, The Royal Society Chemistry. **b)** An absorbent porous substrate for sweat collection. Reproduced with permission⁴⁴. Copyright 2014, WILEY-VCH Verlag GmbH & Co. **c)** A silicone headband for guiding sweat to the sensing device. Reproduced with permission⁴⁵. Copyright 2017, American Chemical Society. **d)** Superwetable flexible band for sweat sampling. Reproduced with permission⁴⁶. Copyright 2019, American Chemical Society. **e)** A hexagonal network for transport and sampling of low sweat volumes. Reproduced with permission⁴⁷. Copyright 2018, The Royal Society Chemistry. **f)** A paper microfluidic channel for continuous sweat transport and evaporation. Reproduced with permission⁴⁸. Copyright 2017, Elsevier. **g)** 3D microfluidic channels for sweat sampling and measurement of sweat loss. Reproduced with permission⁴⁹. Copyright 2019, The Royal Society Chemistry. **h)** A microfluidic patch with capillary bursting valves for chrono-sampling of sweat. Reproduced with permission⁵⁰. Copyright 2017, WILEY-VCH Verlag GmbH & Co. **i)** A fully integrated platform for iontophoretic sweat stimulation and sensing. Reproduced with permission⁵¹. Copyright 2017, National Academy of Sciences USA.

Directing sweat from the skin surface toward a sensing area is one of the unconventional approaches for analyte sensing. This method is usually achieved either by confining the available

sweat on the skin surface to the well-defined sensing sites or transporting it away from the skin surface to the sensor for chemical analysis. **Figure 2.2c** demonstrates a flexible platform with hydrophobic and hydrophilic regions for multiplexed analyte sensing of pH, chloride, glucose, and calcium ⁴⁵. The hydrophobic areas were achieved by the roll-to-roll coating of nanodendritic silica, which was followed by oxygen plasma to define hydrophilic sensing microwells. The hydrophobic regions limited wetting only to the hydrophilic microwells and enabled colorimetric detection of analytes in the indicator embedded microwells via a nearby camera. This approach offers a facile semi-quantification of sweat, but it fails to achieve real-time monitoring of sweat. Wang et al. designed a sweat collection channel mounted on the forehead for the collection of sweat (**Figure 2.2d**) ⁴⁶. The exercise-induced sweat was transported to the sensor surface and enabled real-time measurement of sodium levels with the wearable system.

With the advancement in materials and fabrication techniques, skin-like and miniaturized microfluidic devices have been developed and integrated with wearable systems with the goal of continuous sensing of analytes ^{29, 52-53}. These epidermal microfluidic devices take advantage of the secretion pressure of sweat glands and capillary pressure of microfluidic channels to guide sweat from the skin surface to the sensing sites ⁵⁴. These novel devices are designed to achieve efficient spatiotemporal sampling of sweat, reduced sweat evaporation, and minimal contamination from the skin surface. Heikenfeld's group designed a hexagonal network of gold-coated microchannel for rapid transport of low sweat volumes to the sensing electrodes (**Figure 2.2e**) ⁴⁷. The gold surface was modified with peptides to have a biocompatible and hydrophilic surface. Engineering the design and surface of the wicking surface endowed the device with increased fluid transport and minimal analyte loss. However, the fluid coupling between the hexagonal network and sensing electrode was made with rayon, which may potentially cause analyte depletion as well as erroneous

readings due to insufficient electrode contact in real-time monitoring. In another study, Anastasova et al. used a paper microfluidic channel to avoid the problems associated with sweat accumulation on the skin surface⁴⁸. As Sweat entered the channel, it was drawn across the length of the paper channel via capillary forces (**Figure 2.2f**). The transported sweat was collected at the end of the channel (reservoirs), where it was continuously evaporated. The continuous fluid sampling, transport, and evaporation enabled the real-time measurement of pH, sodium, and lactate in sweat with a wireless system. Lin et al. devised a simple and inexpensive fabrication method for biofluid sampling, manipulation, and sensing⁴⁹. The method involved laser cutting and vertical alignment of flexible film sheets and double-sided tapes to form 3D and complex microfluidic architectures, such as devices for sweat collection, sample filtration, and biofluids actuation and sensing (**Figure 2.2g**). The high throughput manufacturing technique presented an alternative, low-cost disposable solution to minimize challenges related to contamination from old sweat residues and sensor biofouling. In another study, Choi et al. designed a skin conformable microfluidic patch for chrono-sampling of lactate, sodium, and potassium⁵⁰. The device consisted of a network of microfluidic channels that incorporates capillary bursting valves that allow the fluid passage at different fluid pressures, enabling sequential filling of multiple microreservoirs (**Figure 2.2h**). The microfluidic devices captured and stored fluids about several μL 's and allowed extraction of the collected fluids for ex-situ analysis. Despite its remaining challenges related to low sweat collection volumes and undesired adsorption of some analytes (*i.e.*, hormones and vitamins) on the microfluidic walls, this proposed microfluidic patch enables temporal measurement of some of the physiologically abundant biomarkers in sweat.

The sweat collection methods require prolonged active exercise for the activation of sweat glands and sweat generation, making it inconvenient for elderly and sedentary subjects. For this

purpose, on-demand and continuous monitoring of analytes with wearable sweat extraction and sensing platforms are needed for in situ sweat analysis. Emaminejad et al. developed a wireless system with an electronic iontophoresis interface and sensing electrodes for real-time chloride, sodium, and glucose monitoring⁵¹. The iontophoretic stimulation was carried out with a pair of sweat induction electrodes that interfaced the skin with a sweat gland secretory stimulating agonists, such as acetylcholine or pilocarpine (**Figure 2.2i**). The induced sweat was sensed using sensing electrodes covered with a water-absorbent rayon pad to maintain a reliable sensor reading. Long-term iontophoretic sweat generation may have the potential of electrode corrosion and local skin irritation. Nevertheless, the unique capability of on-demand iontophoretic sweat induction with varying excretion rates and intervals as well as subsequent sweat collection and sensing enabled in situ and wireless measurement of relevant analytes with an integrated wearable system.

Unconventional sweat sampling methods included novel approaches for engineering the device-skin interface, iontophoresis, and transporting the sweat away from the skin with a paper or polymeric microchannel with the goal of sweat sampling with reduced skin contamination, minimal sweat evaporation, and prolonged or on-demand sensing. Continuous delivery of sweat to the sensing sites via these methods enabled the continuous detection of analytes via colorimetric, fluorometric, or electrochemical methods⁵⁵⁻⁵⁷. Unlike colorimetric methods, the wireless sensing with electrochemical methods require the integration of sensing and contact electrodes with microchannels for real-time sensing and data acquisition.

2.2.2. Biochemical Sensing in Current Wearable Devices

2.2.2.1. Metabolites

Metabolites are small molecules produced in biochemical pathways of human metabolism and involved in a myriad of functions, from energy production to signaling. Metabolites in sweat,

such as glucose, lactate, urea, and ethanol, are promising candidates for noninvasive monitoring of human physiology. Glucose, for instance, is the primary source of energy production of the human body and associated with diabetes, Alzheimer's disease, cognitive impairment, and renal complications⁵⁸. Lactate is a primary biomarker of anaerobic metabolism and clinically associated with lactic acidosis. It is the indicator of poor tissue oxygenation (myocardial infarction, sepsis, and hypovolemia), common diseases (diabetes, liver and renal disease, and leukemia), and drugs and toxins⁵⁹. Therefore, glucose and lactate are regarded as a critical health indicators and have received significant attention for the development of noninvasive wearable systems.

Real-time monitoring of glucose and lactate has been accomplished by integrating electrochemical sensing elements in wearable devices⁶⁰. Jia et al. demonstrated one of the first examples of noninvasive and epidermal lactate sensors⁶¹. The lactate sensor was realized by casting a mixture of carbon nanotube (CNT), tetrathiafulvalene, and chitosan on screen-printed carbon electrode. The generation of electric current was based on enzymatic reactions of lactate oxidase (LO_x) with lactate in sweat (**Figure 2.3a**)⁶². The tattoo-like electrochemical sensor conformed to the skin surface and was robust against repeated bending and stretching cycles. In another study, a tattoo-based electrochemical sensor with reverse iontophoretic biofluid extraction was demonstrated⁶³. The Prussian blue (PB) printed epidermal sensor was modified with glucose oxidase (GO_x) and chitosan for enzymatic sensing of glucose. A constant current was applied between a pair of electrodes for the extraction of interstitial fluid, and glucose sensing was performed on the cathodic electrode (**Figure 2.3b**). The developed platform is an alternative to invasive and minimally invasive sensing techniques and holds a potential for continuous diabetes management. Similarly, a Prussian blue-based glucose or lactate sensor with a microfluidic reservoir was developed by the same research group to minimize direct skin contact and sample

evaporation⁶⁴. The microfluidic channels provided short sampling times and efficient transport of glucose or lactate on the sensing electrodes, where the generated current was detected and then wirelessly transmitted to a computer by a wearable system (**Figure 2.3c**). Imani et al. and Sempionotto et al. integrated lactate sensors with electrocardiogram and potassium sensors, respectively⁶⁵⁻⁶⁶. **Figure 2.3d** shows an epidermal patch with a printed three-electrode electrochemical sensor and two ECG electrodes for wireless lactate and electrocardiogram monitoring. The sensing electrode of the lactate sensor was functionalized with PB mediator and LO_x enzyme. It was separated from Ag/AgCl electrocardiogram electrodes via a printed hydrophobic layer to minimize the electrical crosstalk in the presence of perspiration. During a high-intensity workout, the epidermal patch simultaneously measured the sweat lactate and cardiac signals, hence provided simultaneous measurements with both sensors to gain insights regarding cardiac health, human performance, and exertion levels. **Figure 2.3e** shows a multi-analyte eyeglass for amperometric and potentiometric detection of lactate and potassium, respectively⁶⁶. The printed sensors were integrated on the nose pads of the glasses and connected to the printed circuit boards on the different arms of the eyeglasses. This wireless lab-on-a-glass biosensor system demonstrated continuous and crosstalk-free measurement of metabolite and electrolyte levels.

Self-powered lactate and glucose sensing from perspiration eliminates the need for external power sources, amplification, and filtering, making it advantageous for the applications that require continuous recharging or *in vivo* operation. **Figure 2.3f** shows an example of stretchable biofuel cells (BFCs) on a body-worn sock⁶⁷. The BFC comprises a printed anode functionalized with LO_x and a redox material, and a cathode with a silver (I) oxide/silver redox couple. The self-powered biosensor increases its short circuit current with the increase in lactate concentration in

sweat without a need for an applied bias, demonstrating a promising method for epidermal self-powered and energy harvesting applications. Similarly, Lu et al. demonstrated a self-powered and continuous glucose, Na⁺, and K⁺ sensing system based on NiCo₂O₄ micro-supercapacitors (MSCs)⁶⁸. The MSC was used as power units to drive the nonenzymatic NiCo₂O₄/chitosan-based glucose and ion-selective Na⁺ and K⁺ sensors during a strenuous exercise (**Figure 2.3g**).

Apart from glucose and lactate, there are other clinically relevant analytes in sweat, such as ethanol, uric acid, and urea. Overconsumption of alcohol contributes to the emergence of various health complications such as cardiovascular diseases, stroke, and liver cirrhosis⁶⁹. Similarly, uric acid and urea are linked with hypertension, diabetes, cerebral infarction, renal insufficiency, and nervous system infection⁷⁰⁻⁷¹. Therefore, monitoring of these indicators is crucial in clinical settings from therapeutics to diagnostics. Real-time measurement of ethanol has been introduced by Hauke et al. using a skin-worn integrated device (**Figure 2.3h**)⁷². The device comprises an iontophoretic sweat stimulation, fluid handling, and ethanol sensing parts. The ethanol sensor was fabricated by drop-casting alcohol oxidase (AO_x), BSA, and chitosan on the sensing electrode. The reaction between ethanol and AO_x generated hydrogen peroxide as a byproduct, which was transduced by the platinum electrode. The authors demonstrated a significant correlation between blood and sweat ethanol concentration and reported a blood-to-sweat lag time due to the complex pharmacokinetics of ethanol in the body. Lastly, Han et al. developed a self-powered electronic skin for uric acid, urea, lactate, and glucose⁷³. The self-powering and sensing mechanism is based on the coupling between enzymatic reactions of uricase, urease, GO_x, and LO_x, and piezoelectric effect zinc oxide nanowires (**Figure 2.3i**). The study demonstrated real-time self-powered operation of the electronic skin during a running exercise, enabling simultaneous energy harvesting and sensing on flexible substrates.

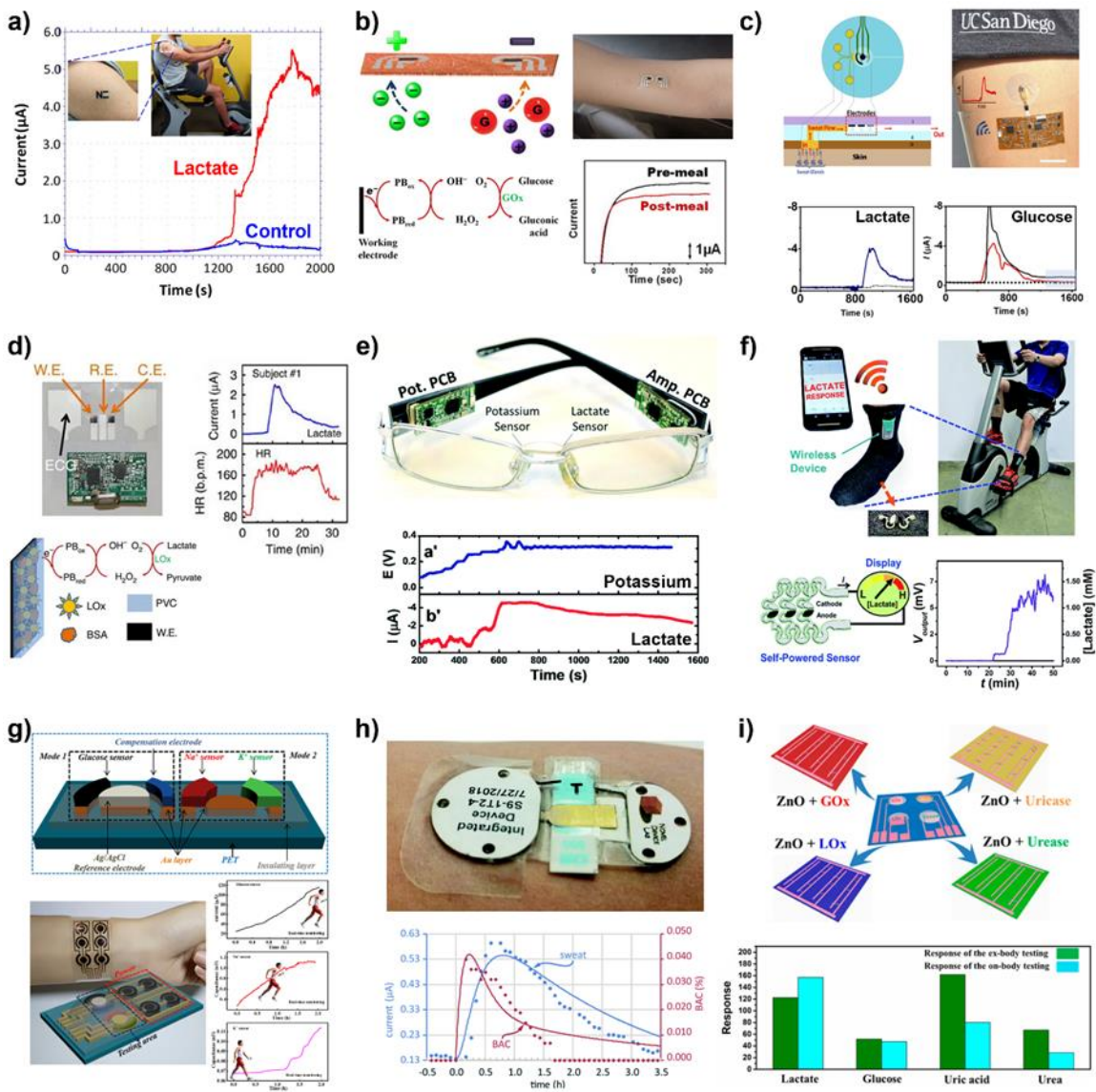


Figure 2.3. Examples of electrochemical wearable metabolite sensors. **a)** A printed electrochemical temporary tattoo sensor for lactate sensing. Reproduced with permission⁶¹. Copyright 2013, American Chemical Society. **b)** A printed tattoo sensor with reverse iontophoresis option for glucose sensing. Reproduced with permission⁶³. Copyright 2015, American Chemical Society. **c)** An epidermal microfluidic platform with sweat collection and glucose or lactate sensing capabilities. Reproduced with permission⁶⁴. Copyright 2017, American Chemical Society. **d)** An epidermal sensor for lactate and electrocardiogram sensing. Reproduced with permission⁶⁵. Copyright 2016, Creative Commons Attribution 4.0 International License. **e)** Eyeglasses with integrated electrochemical lactate and potassium sensors. Reproduced with permission⁶⁶. Copyright 2017, The Royal Society of Chemistry. **f)** Self-powered lactate sensing with biofuel cells. Reproduced with permission⁶⁷. Copyright 2016, The Royal Society of Chemistry. **g)** A self-powered and continuous glucose, Na^+ , and K^+ sensing system based on NiCo_2O_4 micro-supercapacitors. Reproduced with permission⁶⁸. Copyright 2019, Elsevier. **h)** A sweat biosensing device with integrated sweat stimulation for ethanol sensing. Reproduced with permission⁷². Copyright 2018, The Royal Society of Chemistry. **i)** A self-powered electronic skin for measurement of uric acid, urea, glucose, and lactate with piezoelectric-enzymatic-reaction coupling. Reproduced with permission⁷³. Copyright 2017, American Chemical Society.

The overall system architecture of the electrochemical wearable systems consists of an analog front-end circuit (AFE), a microprocessor (MCU) for data collection, processing, and transmission, and an energy management circuit. Amperometric sensors with two or three electrodes require a more complex AFEs for biasing the electrodes and reading current output ⁷⁴. Commercial potentiostat AFEs consist of a differential input amplifier and a programmable gain trans-impedance amplifier for biasing the electrodes at a constant voltage. Potentiostats enable current reading on the orders of pA to mA and have the capability of carrying out various electrochemical techniques, such as chronoamperometry and cyclic voltammetry. For instance, the wearable system in **Figure 2.3d** used an LMP91000 potentiostat, which was controlled by a CC2541 BLE system-on-chip for data processing and communication ⁶⁵. The data was transmitted to a PC via BLE 4.0. The system used a button cell battery (3V, 220 mAh) and a boost converter for energy management. The total current draw of the wearable system was 5 mA and consumed 15 mW in active mode. The system in **Figure 2.3e** used a similar microcontroller (MCU) and AFE and reported 1.6 mA current draw with 100 mAh lithium-ion rechargeable battery during continuous operation ⁶⁶. In another study, Xu et al. demonstrated an NFC powered wearable glucose sensing system ⁷⁵. The system included an NFC chip (NT3H2111, NXP Semiconductor) for power delivery and data transmission with a cellphone. The NFC chip was used to power the MCU (MSP430FR5959, TI) and potentiostat (LMP91002, TI). The MCU included a 12 bits ADC for digitization of output of the potentiostat, which was stored in the EEPROM of the NFC chip. The data was then wirelessly transmitted to a smartphone using a coiled antenna at 13.56 MHz and displayed on an Android app.

When the developments in the past few years are considered, the wearable systems for metabolite sensing have moved from just tattoo-based flexible sensors without signal conditioning

circuitries to more complex wireless systems. The integrated, wireless systems included fluid handling channels for continuous analyte sensing ⁶⁴ as well as biofuel- and solar-powered autonomous monitoring ^{67, 76}.

2.2.2.2. pH and Electrolytes

Regulation of pH in the human body has a crucial role in maintaining physiological homeostasis as the activity of most enzymatic reactions are dependent on pH. Body pH is determined by the dissociation of organic acids into H⁺ ions in living cells. Any fluctuations in acid-base balance in the body may contribute to the development of fatigue and other metabolic diseases ⁷⁷. Continuous monitoring of acid-base levels of the body may provide insights on ongoing disorders, such as metabolic and respiratory acidosis/alkalosis. Therefore, pH sensing has been an extensively researched field of wearable sensors. **Figure 2.4a** demonstrates a roll-to-roll printed wearable electrochemical sensor for detecting pH, K⁺, and Na⁺ ⁷⁸. The pH sensing was achieved by the functionalization of the sensing electrodes with ion-sensitive polymeric layers. The flexible pH sensor was interfaced with a custom PCB for measurement of the potential change on the sensing electrode with respect to the reference electrode. In another study, Pal et al. designed a wearable bandage for the measurement of pH changes using impedimetric analysis (**Figure 2.4b**) ⁷⁹. The bandage included an omniphobic paper, comprising a screen-printed electrode pairs with a polyaniline emeraldine salt (PANI-ES)-silver microflakes. Based on the concentration of H⁺ in the surrounding environment, PANI underwent a reversible chemical reaction between its oxidized and reduced states, leading to an impedance change between the electrode pairs. Integration of the sensor with a miniaturized impedance analyzer atop enabled real-time wireless assessment of pH. In a different study, Kassal et al. demonstrated an optical approach for the quantification of pH within a narrow range (pH 6 to 9) **Figure 2.4c** ⁸⁰. The skin-worn bandage included a polyurethane-

based hydrogel containing a pH-sensitive indicator. The pH indicator dye changed its absorbance at 534 nm as the pH of the buffer solution varied. The sensor was coupled with a LED (527 nm) and a photodiode for the measurement of the reflected light. The intensity of the reflected light decreased as the indicator dye changed its degree of deprotonation. The wearable system used an RFID reader for powering and data transmission as well as a current source and a transimpedance amplifier for driving the LED and measuring the photodiode current. Curto et al. demonstrated a wearable barcode-like microfluidic patch integrated with pH-sensitive ionic liquid polymer gels⁸¹. Incorporation of pH-sensitive dyes with varying pKa values into the ionogels enabled real-time analysis of sweat (**Figure 2.4d**). pH measurement was made by capturing pictures of the barcode at different time intervals with a camera and outputting a single pH value by equally weighing the contribution of each pH-sensitive dye. The addition of reference colors onto the microfluidic patch eliminated the effect of ambient light variations.

The pH monitoring wearable systems employed different AFEs based on their pH transduction techniques (*i.e.*, potentiometric, impedimetric, optical, or colorimetric). The potentiometric sensors included an instrumentation amplifier and filtering stages (1 Hz) to minimize the common-mode interferences and high-frequency noise⁸². The impedimetric sensor included an impedance analyzer (AD5933, Analog Devices Inc.) for pH analysis at 100 Hz⁷⁹. In contrast to electrochemical methods, the optical and colorimetric sensors measured pH by evaluating the change in light intensity and color of the sensor using a photodetector and image analysis, respectively.



Figure 2.4. Examples of electrochemical, optical, and colorimetric wearable sensors for electrolyte sensing. **a)** A roll-to-roll printed electrode arrays for pH, K^+ , and Na^+ sensing. Reproduced with permission⁷⁸. Copyright 2018, American Chemical Society. **b)** An omniphobic paper-based smart bandage for pH sensing. Reproduced with permission⁷⁹. Copyright 2018, Elsevier. **c)** A smart bandage for optical monitoring of pH. Reproduced with permission⁸⁰. Copyright 2017, Elsevier. **d)** A wearable chemical barcode microfluidic platform for pH sensing. Reproduced with permission⁸¹. Copyright 2012, Elsevier. **e)** An RFID patch for Na^+ sensing. Reproduced with permission⁸³. Copyright 2015, IEEE. **f)** SWEATCH wearable Na^+ sensing device. Reproduced with permission⁸⁴. Copyright 2016, John Wiley and Sons. **g)** A wearable patch for monitoring of Na^+ and K^+ . Reproduced with permission⁸⁵. Copyright 2018, The Royal Society of Chemistry. **h)** A thin elastomeric patch with open cellular designs for pH, K^+ , Ca^{2+} sensing. Reproduced with permission⁸⁶. Copyright 2017, WILEY-VCH Verlag GmbH & Co. **i)** A microfluidic patch with superabsorbent valves for time-sequenced colorimetric monitoring of Cl^- . Reproduced with permission⁸⁷. Copyright 2018, WILEY-VCH Verlag GmbH & Co.

Apart from H⁺ sensing, wearable systems for real-time analysis of other ions have been developed. **Figure 2.4e** demonstrates an RFID sensor patch for monitoring of sweat Na⁺ levels⁸³. The flexible patch used ion-selective electrodes (ISEs) with paper microfluidics for potentiometric measurement of electrolyte levels. The patch included a coiled antenna for the inductive powering of an RFID transponder chip. The chip measured the potential difference between two ion-selective electrodes. The transfer of the pH data to the aggregator was done via NFC. The patch operated up to seven days and enabled battery-free detection of other ionic solutes in sweat. In contrast to the battery-free operation, **Figure 2.4f-g** shows battery-powered, wireless wearable devices for real-time Na⁺ or K⁺ measurement⁸⁴⁻⁸⁵. The wearable systems included an absorbent pad for extended sweat collection, pH-sensitive ISEs as well as a miniaturized ShimmerTM board for the differential voltage measurement and wireless transmission. The sweat patch in **Figure 2.4g** used magnetic connectors between the sensor and the electronic module to minimize the motion artifact noise in potentiometric measurements during the human trials, which was necessary for signals with high fidelity. Lee et al. demonstrated a chemical sensing patch with an open cellular design comprising a multiplexed array of sensing electrodes for H⁺, K⁺, and Ca²⁺ monitoring⁸⁶. The thin patch enabled an intimate contact with the skin surface without mechanical irritation and provided a spatiotemporal mapping of the target electrolytes on the skin surface (**Figure 2.4h**). Finally, Kim et al. developed a microfluidic device for colorimetric detection of chloride (Cl⁻) ions⁸⁷. The flexible and skin conformable device comprised microchannels, isolated reservoirs, and super-absorbent polymer valves for time-sequenced discrete sampling as well as measurement of Cl⁻ in sweat (**Figure 2.4i**). The chloride assay relied on competitive chelation between mercury (II), ferrous (II) with a chelating agent, 2,4,6-tris(2-pyridyl)-s-triazine, yielding

blue assay color with increased chloride concentration. The quantitative analysis of the Cl^- was done using digital images of the microfluidic patch.

The wearable systems for pH and electrolyte monitoring included much broader signal transduction alternatives (electrochemical, optical, and colorimetric) compared to the metabolite sensing. While the colorimetric systems are simple to fabricate, they may not be the first choice for the applications that require continuous electrolyte monitoring due to its infrequent sampling and lower sensor resolution. The pre-conditioning circuitry and signal processing for electrochemical electrolyte sensing are more straightforward than that of the optical systems. Therefore, they have been widely used in various applications, ranging from exercise physiology in sports medicine to cystic fibrosis detection in clinical medicine.

2.2.2.3. Oxygen

Oxygen has critical roles in the human body, such as in metabolism (energy production via oxidative phosphorylation), biochemistry (reactive oxygen species and gene transcription), and pathology (determining the condition and function of tissue structure). Its excess leads to inflammation and tissue damage, while its shortage induces severe tissue damage in the heart and brain⁸⁸. Due to its critical importance, various optical methods (photoplethysmography and pulse oximetry) have been developed to quantify its concentration in the body.

Photoplethysmography (PPG) is an optical method that relies on a light source and a detector for the measurement of changes in blood volume⁸⁹. Continuous beating of the heart causes fluctuations in the blood volume of arteries and changes the light attenuation through blood and tissue. The PPG sensors measure the change in the light attenuation using light-emitting diodes (LEDs) or photodiodes (PDs). Similarly, pulse oximeter relies on light absorption differences of oxygenated (HbO_2) and deoxygenated hemoglobin (Hb) and provides an estimation of the arterial

oxygen saturation (SpO_2) using two PPG signals from specific regions of the light spectrum (green-red or red-infrared) ⁹⁰. PPG and pulse oximetry give critical information about cardiovascular health by measuring heart rate, blood pressure, blood oxygenation, and heart rate variability ⁹¹.

In this regard, organic optoelectronic devices have been reported for the development of flexible and stretchable wearable optoelectronic systems. **Figure 2.5a** shows an ultra-flexible organic photonic skin for measurement and a digital display of pulse oximeter information ⁹². The flexible photonic skin was made up of organic LEDs (red and green) and a PD. Due to the soft nature of polymers and prestraining of the underlying substrate, the optical devices maintained their optoelectronic characteristics under repeated stretching cycles and yielded low noise PPG signals due to its excellent adhesion with skin. Khan et al. designed a reflectance oximeter array for the measurement of SpO_2 and spatial 2D oxygenation ⁹³. The flexible patch utilized screen-printing and blade coating for the fabrication of 2×2 pixels of organic LEDs (612 nm and 725 nm) and 8 pixels of organic PD devices on flexible substrates (**Figure 2.5b**). The study showed single-point PPG, heart rate, SpO_2 measurement. Real-time 2D tissue oxygenation during an ischemic event was also demonstrated. This function enabled the measurement of localized tissue oxygenation when the pulsatile arterial blood signal of PPG was low. In another study, Han et al. designed an organic ambient light oximeter (ALO) for the measurement of PPG and SpO_2 from the index finger (**Figure 2.5c**) ⁹⁴. The optoelectronic device used only PDs, eliminating the need for any light source and LED drivers. Since the absorbance spectrum of organic polymers is broad, the ALO used flexible filters on top of PDs for selective detection of green (525 nm), red (610), and near-infrared lights (740 nm) with negligible spectral overlap. Overall, organic optoelectronic devices are skin-conformable and can be fabricated to cover large areas on the skin surface.

However, due to the air stability of organic devices, the operation of the wearable systems in ambient conditions is limited to orders of a few days.

Inorganic optoelectronic devices are air-stable and reliable; therefore, they have been widely used in wearable sensors for oxygen monitoring. **Figure 2.5d** shows a skin-worn optoelectronic system for optical interrogation of the skin ⁹⁵. The wearable device is skin conformable and uses magnetic inductive coupling and near-field communication for powering the LED (950 nm) and transmission of the PPG signal. In another study, Chung et al. designed wireless chest and limb patches for the physiological monitoring of neonatal and pediatric patients (**Figure 2.5e**) ⁹⁶. Both patches employed flexible PCBs with stretchable interconnects and batteries, which were entirely encapsulated in a flexible silicone material. The chest patch provided sensory data such as the electrocardiogram (ECG), respiratory rate, and seismocardiogram (SCG), whereas the limb patch measured PPG, SpO₂, and temperature. The time-synchronized operation of two patches enabled the extraction of pulse arrival time, pulse transit time, and systolic blood pressure from ECG, SCG, and PPG signals, which may not be easily obtainable from a single device. Similarly, Zhang et al. demonstrated an optical system for extended measurement of tissue oxygen saturation levels (rStO₂) using microscale inorganic light-emitting diodes (μ -LEDs) and photodetector (μ -IPD) ⁹⁷. The system included an injectable sensing filament with integrated μ -LEDs (540 nm and 625 nm) and μ -IPD, as shown in **Figure 2.5f**. Similar to other oximeters, the μ -LEDs operated in a time-multiplexed fashion, and the μ -IPD measured the backscattered light by the surrounding tissue and vasculature. Even though the fabrication of the optical sensor included complicated fabrication steps, the use of μ -LEDs and μ -IPD along with a miniaturized wearable system enabled localized tissue oxygenation measurements in deep tissues, which would not be easily achieved by commercial inorganic LEDs and PDs.

The instrumentation for wearable optical systems includes a microcontroller, a wireless transmission module as well as LED drivers, amplifiers, and filters for sequential driving of LEDs, amplification of photodiode current, and elimination of low and high-frequency noise ⁹⁸. For mobile applications, fully integrated AFEs that house an LED driver and a low-noise receiver channel with an integrated ADC have commonly used. For instance, the reflective oximeter array and ambient light oximeter in **Figure 2.5b and 2.5c** used an integrated AFE (AFE4490, TI) with external analog switches for the sequential drive of an array of OLEDs and read out from the OPDs. The optical AFE was controlled by an Arduino Uno microcontroller (500 Hz sampling), and the data was collected using a USB interface. In another study in **Figure 2.5d**, the wireless optoelectronic system used a bare die NFC chip (SL13A, ams AG) to measure PPG signals and heart rate using an LED and a photodetector. The photodetector current was amplified by a transimpedance amplifier and sampled by 10-bit ADC at 25 Hz, which was satisfactory for the detection of systolic and diastolic peaks in the PPG signal. An NFC-enabled smartphone was used for powering the system and data transmission (13.56 MHz, ISO 15693) from the NFC chip. The power management unit of the NFC chip provided the external biasing for the LED and photodetector. The wireless system in **Figure 2.5e** consisted of a time-synchronized operation of the wearable chest and limb units for health monitoring in pediatric and neonatal intensive-care units. The limb unit included an integrated pulse oximeter AFE (MAX30101, Maxim Integrated) for the measurement of dual-wavelength PPG using on-chip LEDs (660 nm and 880 nm) and a photodiode. A BLE SoC (nRF52832, Nordic Semiconductor) was used for sampling the PPG signals (100 Hz), processing, and data logging to a computer. The post-processing of the collected PPG data included band-pass filtering (0.8-8 Hz), onset and beat detection algorithms, as well as FFT, red/IR ratio density estimation and SpO₂ calculation. Battery-powered and wireless-

powering operation of the system was demonstrated for alternative health monitoring options in intensive-care units.

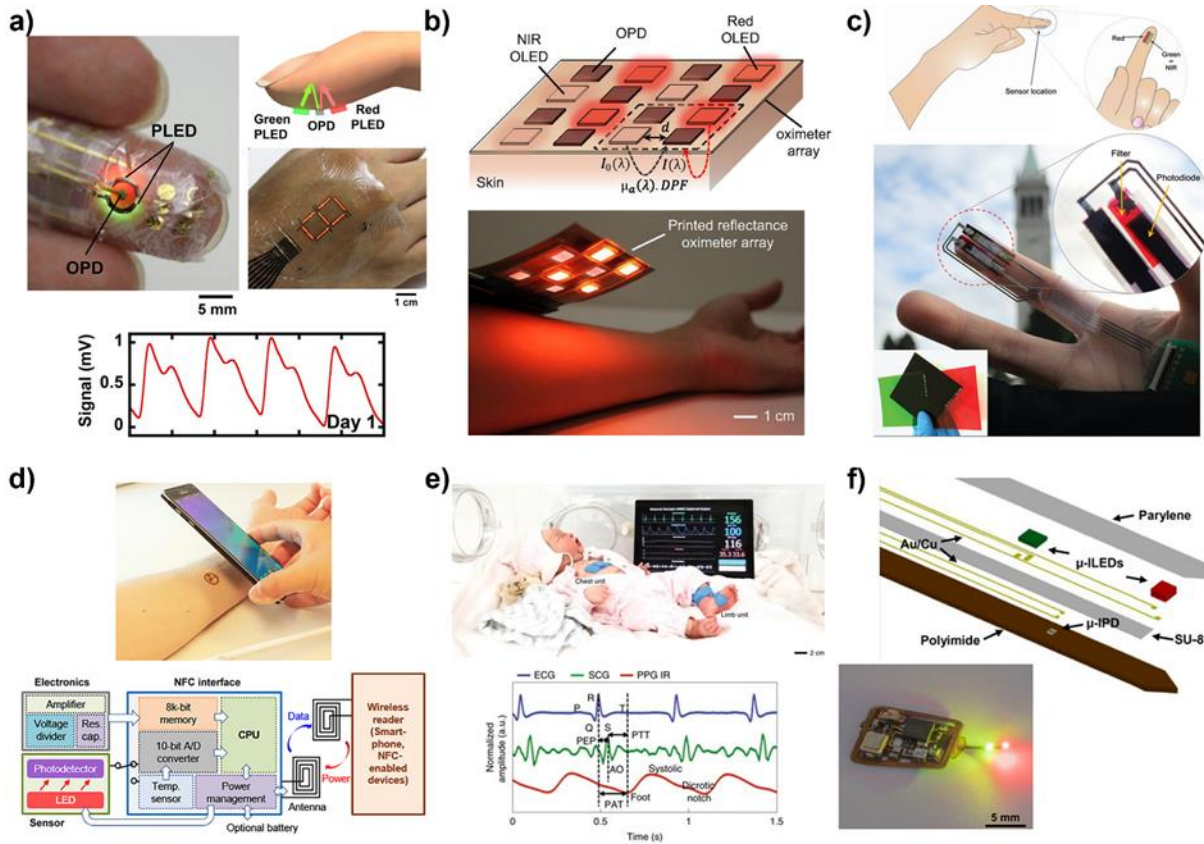


Figure 2.5. Examples of wearable optical sensors for the detection of oxygen. **a)** Smart e-skin system comprising ultra-flexible polymer light-emitting diodes (PLEDs) and an organic photodetector (OPD). Reproduced with permission⁹². Copyright 2016, Creative Commons Attribution 4.0 International License. **b)** A reflective oximeter with an array of red and NIR LEDs and OPDs. Reproduced with permission⁹³. Copyright 2018, Creative Commons Attribution 4.0 International License. **c)** An ambient light oximeter (ALO) with printed OPDs. Reproduced with permission⁹⁴. Copyright 2020, WILEY-VCH Verlag GmbH & Co. **d)** A battery-free, wireless, epidermal optoelectronic system. Reproduced with permission⁹⁵. Copyright 2016, Creative Commons Attribution 4.0 International License. **e)** A soft, wireless chest and limb units for physiological monitoring of neonatal and pediatric patients. Reproduced with permission⁹⁶. Copyright 2020, Springer Nature. **f)** A miniaturized, wireless oximeter with microscale LEDs (μ -LEDs) and a microscale inorganic photodetector (μ -IPD). Reproduced with permission⁹⁷. Copyright 2019, Creative Commons Attribution 4.0 International License.

When NFC and BLE-operated wireless optoelectronic systems are compared, the wireless-powering eliminates the need for battery use; however, the maximum power that can be delivered to the system is limited by the orientation and distance of the NFC device relative to the wireless coil. In wearable optical systems, on-board signal processing and optimization of the critical

parameters of wireless transmission and LEDs, such as duty cycling, LED-detector distance, sampling frequency, clock frequency, and transmission of physiological data in pockets, determine the total power consumption of wearable optical systems in the presence of motion artifacts⁹⁹⁻¹⁰¹.

2.2.2.4. Other Chemical Biomarkers

In addition to metabolites and electrolytes, other biomarkers and chemical substances, such as hormones, and vitamins, heavy metals, and drugs, emerge in sweat that can be used towards stress assessment, doping control, and health and disease monitoring¹⁰²⁻¹⁰⁵. **Figure 2.6a** shows a flexible multiplexed array for heavy metal detection in sweat. The multiplexed array comprises a bismuth (Bi) and a gold (Au) working microelectrode¹⁰⁴. The study used electrochemical square wave anodic stripping voltammetry (SWASV) for the detection of cadmium (Cd), lead (Pb), and zinc (Zn) on the Bi microelectrode. The Au microelectrode was used for the detection of lead, copper (Cu), and mercury (Hg). On-body trials of the flexible array with sweat demonstrated the use of the wearable sensor for gaining insightful information on heavy metal exposure. In another study by Javey's group, a wireless system was developed for real-time monitoring of caffeine in sweat upon a caffeine intake¹⁰⁶. The flexible sensor was modified with carbon nanotube/Nafion solution, and the electrochemical detection of caffeine was made via differential pulse voltammetry (DPV). The DPV parameters were controlled with a microcontroller by adjusting the voltages on the reference and working electrodes using an external digital-to-analog converter. The current on the working electrode was converted into voltage using a transimpedance amplifier, digitized by an external ADC through SPI protocol, and sent to the data aggregator via Bluetooth (**Figure 2.6b**). The wearable device measured the presence of caffeine in iontophoresis and exercise-induced sweat and revealed the potential of using this platform towards clinical pharmacology and precision medicine.

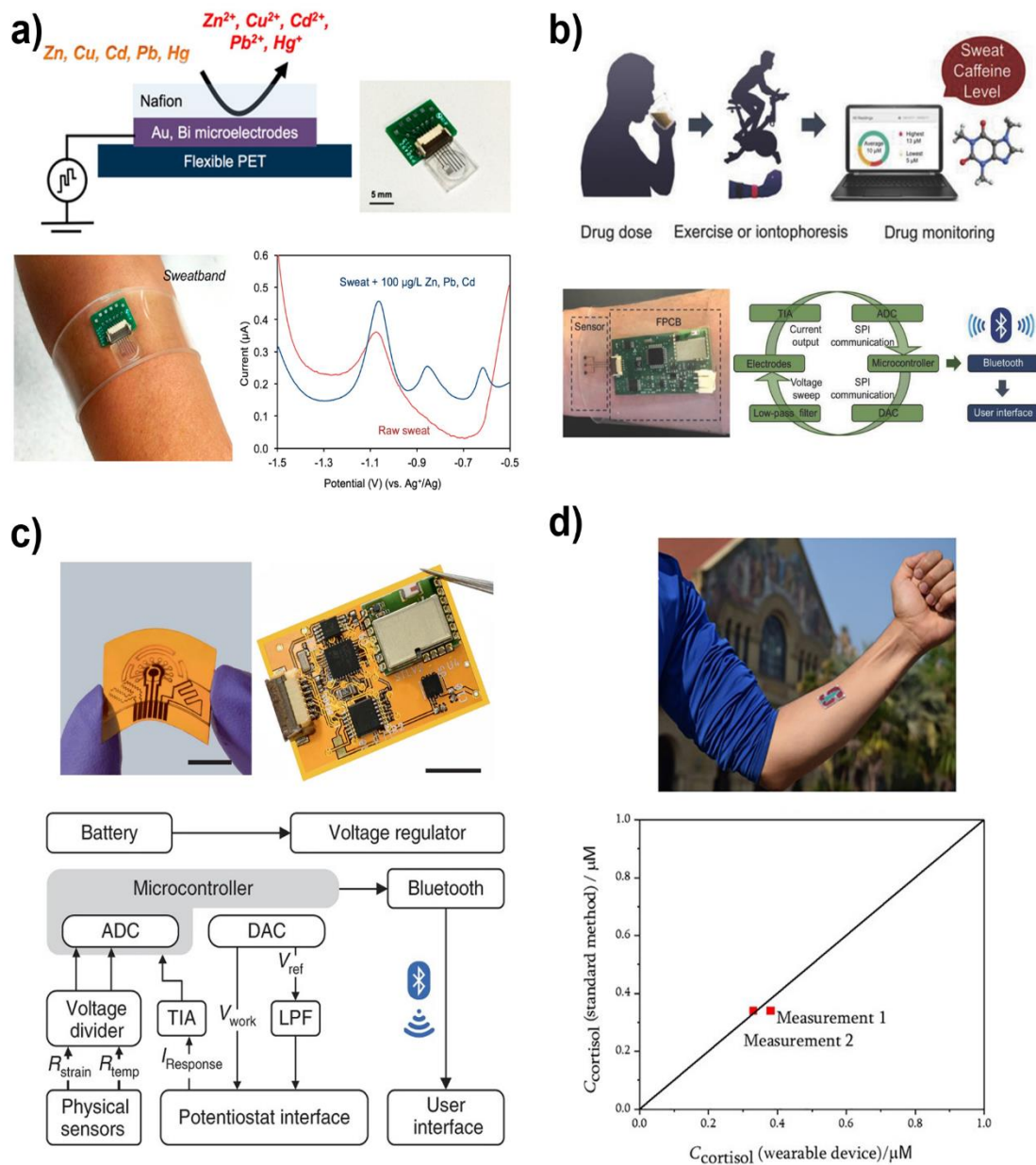


Figure 2.6. Examples of wearable sensors for the detection of other analytes in sweat. **a)** A flexible multiplexed array for detection of Zn, Cd, Pb, Cu, and Hg. Reproduced with permission¹⁰⁴. Copyright 2016, American Chemical Society. **b)** A flexible sweatband for caffeine monitoring. Reproduced with permission¹⁰⁶. Copyright 2018, WILEY-VCH Verlag GmbH & Co. **c)** A laser-engraved graphene-based sensor for uric acid, tyrosine, temperature, and respiration rate monitoring. Reproduced with permission¹⁰⁷. Copyright 2020, Springer Nature. **d)** An organic electrochemical transistor modified with molecularly imprinted polymer for cortisol sensing. Reproduced with permission¹⁰³ Copyright 2018, Creative Commons Attribution Noncommercial License 4.0.

In another study, Yang et al. demonstrated a laser-engraved wearable sensor for uric acid (UA) and tyrosine (TYR) detection in sweat for gout and fitness analysis (**Figure 2.6c**)¹⁰⁷. The chemical sensing of UA and TYR was done using laser-engraved graphene due to its high surface

area and electrochemical activity. A similar AFE design reported in **Figure 2.6b** was used for the measurement of UA and TYR in sweat via the DPV method. On-body sweat and serum measurements revealed the correlation of uric acid in healthy subjects and patients with gout. In another study, Parlak et al. fabricated an organic electrochemical transistor (OECT) for cortisol sensing towards stress evaluation (**Figure 2.6d**)¹⁰³. Detection of cortisol was done by covering the semiconducting channel of the OECT with a cortisol-selective molecularly imprinted polymer. In the presence of the analyte, the ion exchange between the sensing medium and the transistor channel was prevented, leading to a reduced source-drain current of the OECT. The authors demonstrated real-time and selective measurement of cortisol in sweat with the wearable OECT during an exercise.

The detection of heavy metals and drugs in sweat required complex electrochemical methods, such as SWASV or DPV. System-level implementation of these methods were similar to the other electrochemical methods (*i.e.*, chronoamperometry), only differed in the regulation of reference and working electrode voltages using an external DAC to set electrochemical parameters (*i.e.*, frequency, potential, and pulse parameters).

2.3. Wearable Biophysical Sensors

2.3.1. Sweat Rate

Sweat rate is an important physical parameter for the diagnosis and evaluation of excessive sweating and monitoring of dehydration status¹⁰⁸⁻¹⁰⁹. Dehydration causes physical, mental, physiological loss in performance and is commonly associated with heat-induced cramps, fatigue, dizziness, or strokes¹¹⁰⁻¹¹². Therefore, sweat rate sensors have been included in the development of wearable sensors. For example, **Figure 2.7a** shows a simple approach for the detection of sweat volume. The wearable device employed a soft PDMS channel and a Teflon tube for collection and

guiding of sweat into the microchannel. Sweat volume was measured by determining the distance traveled by the fluid in the channel over the duration of the testing. The sweat rate was then calculated by taking the time derivative of the sweat volume ¹¹³. In a different study, a microfluidic channel with a pair of electrodes was constructed for measurement of sweat rate over a wide dynamic range of flow rates (**Figure 2.7b**) ¹¹⁴. Once sweat was captured through an opening, it formed a droplet in the hydrophobic channel, which electrically shorted the bottom electrode (gold electrode) and top electrode (Nickel conductive wicking material) and resulted in a current spike under a constant DC bias. The continuous sweat rate sensing was ensured by a mesh-like conductive top electrode, which removed the collected sweat away from the sensing area and enabled the formation of a new droplet between electrodes. The sweat rate was estimated by dividing the droplet volume by the time between two consecutive current spikes. However, the deposition of salt at the inlet of the device distorted the acquired signal and limited the lifetime of the sensor.

Similarly, Javey's group demonstrated impedance-based, wearable sweat rate sensing systems with integrated microfluidic channels, as shown in **Figure 2.7c and 2.7d**. Both studies incorporated microfluidic channels for extended sweat collection and sweat rate measurement. For instance, the wireless system in **Figure 2.7c** comprises a Na⁺ sensor and a spiral impedance sensor with a microfluidic channel for real-time sweat rate measurement ¹¹⁵. An impedance analyzer (AD5933, Analog Devices) was used for the measurement of impedance at 100 Hz. As the sweat filled out the microfluidic channel, the admittance of the sensor increased because of an increased sweat volume and total ion concentration. Na⁺ concentration in the microfluidic channel contributed to the admittance change; therefore, a Na⁺ sensor was included at the entrance of the microfluidic channel for continuous measurement of Na⁺ levels. Real-time estimation of the sweat

rate was performed using both the admittance and Na^+ concentration. In this study, the output of this sensor was influenced by both sweat ion composition and sweat volume; therefore, an improved impedimetric sweat rate sensor was proposed by the same group¹¹⁶. The sensor consisted of an interdigitated electrode and a serpentine-shaped microfluidic layer. Each time the collected sweat in the microfluidic channel encountered a new electrode finger, the admittance between electrodes gave a sharp jump. The sweat rate was calculated by dividing the total fluid volume between electrodes by the time between admittance jumps. In another study by Rogers's group, a fully integrated battery-free, reusable, NFC integrated sweat rate system was reported (**Figure 2.7e**)¹¹⁷. The wearable system included a microfluidic channel with integrated electrodes for impedimetric sweat rate sensing, and an NFC electronic module for powering, energy harvesting, and data communication. An NFC compatible device (*i.e.*, smartphone) wirelessly powered the NFC module. On power-up, the system applied a 5 kHz waveform to the electrodes in the microfluidic channel, causing a current to flow. Sweat flow in the microchannel changed the resistance between electrodes and attenuated the magnitude of the applied waveform. The waveform was rectified and processed by a microcontroller and sent back to the smartphone over the NFC link. Utilization of a fully integrated fabrication approach along with a re-attachable NFC electronic system via small magnets facilitated real-time monitoring of sweat loss in various exercise conditions. Overall, the integration of electrical impedance sensing with sophisticated fabrication techniques, unique microchannel designs, fluid wicking materials, and miniaturized electronics enabled accurate and real-time detection of sweat rate information.

Alternative wearable sweat rate sensing approaches have also been reported. **Figure 2.7f** shows a skin-like waterproof microfluidic sensor laminated on the skin for sweat capture and colorimetric assessment of sweat loss in aquatic environments¹¹⁸. The inlet of the microfluidic

channel houses a colorimetric reagent for visual assessment of the extent of sweat filling in the microfluidic channel (total volume ~60 μ L). The study reported a good correlation between the sweat collected by the microfluidic device and other sweat loss evaluation techniques such as absorbent patch and whole-body weight loss measurements during swimming and biking exercises. In another study, a skin-worn device with swellable hydrogels were designed for monitoring sweat rate¹¹⁹. Hexagon-shaped hydrogels increased their surface area with the absorption of sweat (**Figure 2.7g**). The increase in the geometry, thus the sweat volume, was measured by taking an image of the hexagon or by measuring the optical reflectance of a local area (white-colored wicking fabric) as the blue-colored hydrogel slowly covered it upon sweat absorption.

Other wearable sweat rate sensors based on the diffusion of the water vapor from the skin surface (**Figure 2.7h**) and chemiresistors (**Figure 2.7i**) were explored. The first wearable system relied on differential measurements from humidity and temperature sensors to calculate the weight of evaporated vapor in a sealed chamber close to the skin surface and enabled real-time sweat rate and sweat loss monitoring¹²⁰. The latter study used single-walled carbon nanotube (SWCNTs) based ink on paper substrates for real-time measurement of the sweat loss¹²¹. Upon sweat absorption, the cellulose fibers swelled and increased the distance between the SWCNTs, thus the resistance. The integration of the chemiresistors with a wireless system provided an inexpensive and disposable sweat sensing approach for real-time dehydration monitoring.

Wearable systems employed various approaches for the estimation of sweat rate, such as impedance- and water vapor-based assessment, visual evaluation of microchannels as well as volumetric expansion of hydrogels upon sweat absorption. The impedance-based approaches were commonly integrated with microfluidic channels and their associated electronics for real-time

assessment of sweat loss. The sweat rate calculation based on sweat vapor is robust to variation in sweat composition and can provide accurate sweat rate measurement. In contrast to the previous approaches, the techniques that relied on visual assessment may require user intervention for discrete and temporal assessment of local sweat rates.

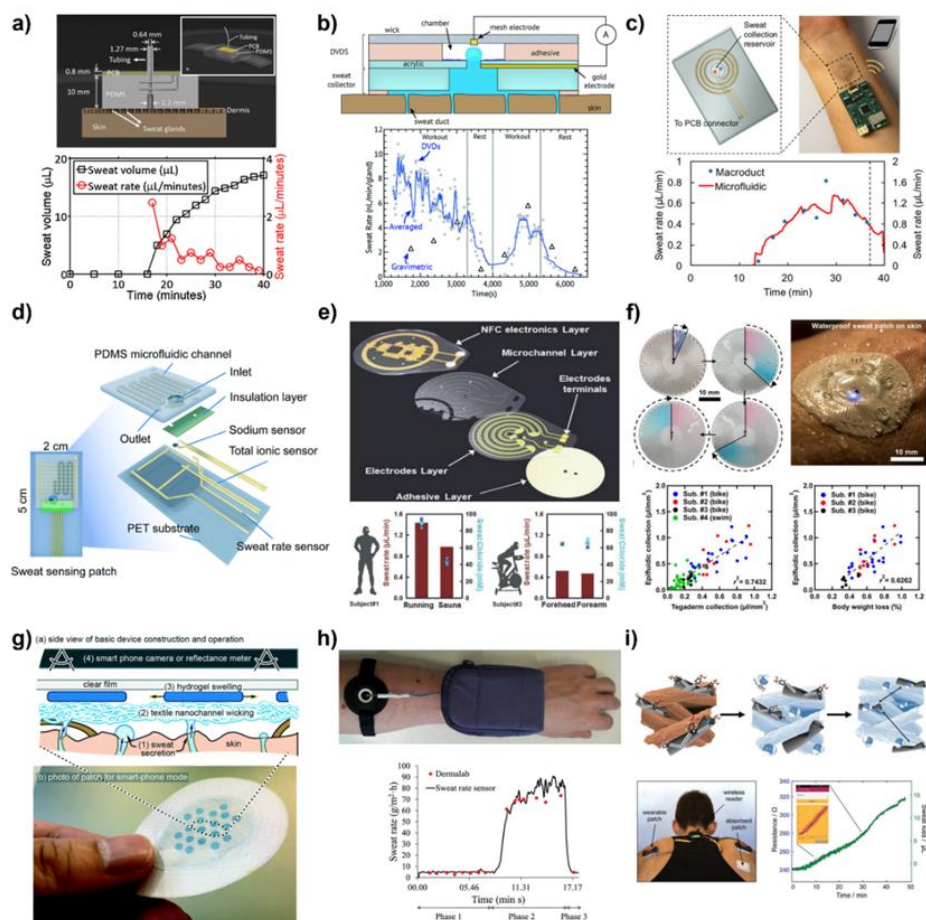


Figure 2.7. Examples of wearable sweat rate sensors. **a)** A wireless sweat volume and conductivity sensor. Reproduced with permission ¹¹³. Copyright 2016, Elsevier. **b)** A digital volume dispensing system for sweat rate measurement. Reproduced with permission ¹¹⁴. Copyright 2019, The Royal Society Chemistry. **c)** A wearable wireless sweat patch for Na⁺ and sweat rate sensing. Reproduced with permission ¹¹⁵. Copyright 2018, American Chemical Society. **d)** A multi-model sweat sensing patch for measurement of Na⁺, sweat rate, and total ionic concentration. Reproduced with permission ¹¹⁶. Copyright 2019, The Royal Society Chemistry. **e)** A battery-free, wireless microfluidic system for sweat rate and loss monitoring. Reproduced with permission ¹¹⁷. Copyright 2018, WILEY-VCH Verlag GmbH & Co. **f)** A waterproof, epidermal microfluidic sweat patch for virtual assessment of sweat loss in an aquatic environment. Reproduced with permission ¹¹⁸. Copyright 2019, Creative Commons Attribution 4.0 International License. **g)** A sweat volume monitoring patch with swellable hydrogels. Reproduced with permission ¹¹⁹. Copyright 2020, The Royal Society Chemistry. **h)** A wearable sweat rate sensor based on the diffusion of the water vapor evaporated from the skin. Reproduced with permission ¹²⁰. Copyright 2018, Elsevier. **i)** A wearable and wireless sweat rate monitoring system based on chemiresistors. Reproduced with permission ¹²¹. Copyright 2019, WILEY-VCH Verlag GmbH & Co.

2.3.2. Temperature

Core body temperature is a significant health indicator in addition to heart rate, blood pressure, and oxygenation. It varies due to endogenous (measurement site, circadian and menstrual rhythms, fitness, and aging) and exogenous factors (environment, diet, and lifestyle) ¹²²⁻¹²³. Variation from the homeostatic body temperature ($\approx 37^{\circ}\text{C}$) gives insights about metabolism, thermoregulation, viral/bacterial infections, inflammation, and pathological conditions, which makes the body temperature as an essential diagnostic indicator ¹²⁴⁻¹²⁵.

Current wearable temperature sensing systems employed resistive and colorimetric methods with varying levels of integration of electronics towards health and wellness monitoring. **Figure 2.8a** and **2.8b** show examples of flexible resistive temperature sensors for skin temperature monitoring ¹²⁶⁻¹²⁷. The sensors were made by screen-printing a mixture of carbon nanotube and poly(3,4-ethylenedioxythiophene)polystyrene sulfonate (PEDOT:PSS) solution. However, the sensors exhibited sensitivity to humidity changes due to the hydrophilic nature of PSS ¹²⁸. **Figure 2.8c** shows a fully flexible, wireless temperature sensing system based on PEDOT:PSS ¹²⁹. The humidity variation of the temperature sensor was minimized by encapsulating the sensors with a fluorinated polymer. The flexible circuitry was realized by ink-jet printing silver ink on a PEN substrate. The system was able to perform on-site temperature reading, conditioning, and wireless transmission of the on-body temperature reading to a smartphone. In another study by Khan et al., a wearable sensor patch with continuous ECG and temperature sensing was demonstrated (**Figure 2.8d**) ¹³⁰. The study used a thermistor composed of nickel oxide nanoparticles mixed in polystyrene-butadiene binder. The resistance of the thermistor was sensed with a voltage divider network. After digitization of the temperature data, the information was sent to a host computer via Bluetooth for further processing.

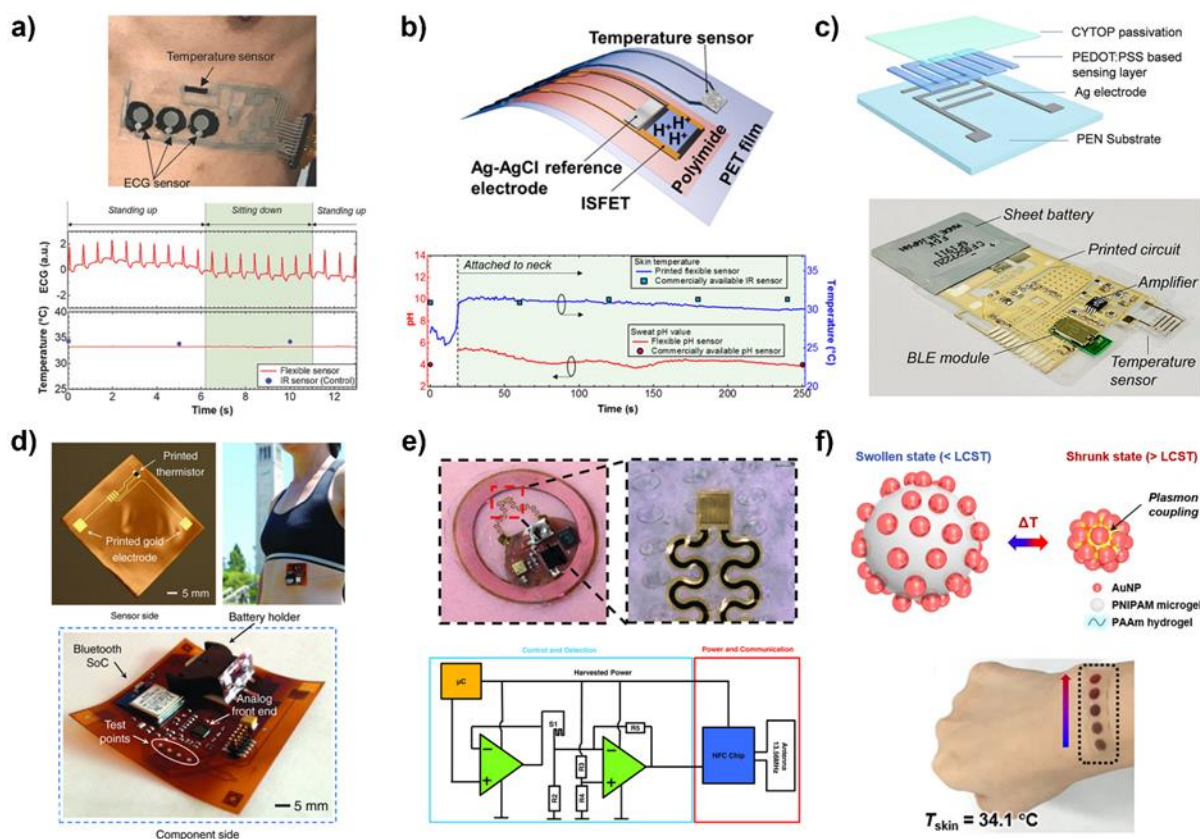


Figure 2.8. Examples of wearable temperature sensors. **a)** A flexible healthcare patch with temperature and ECG sensing capabilities. Reproduced with permission ¹²⁶. Copyright 2017, WILEY-VCH Verlag GmbH & Co. **b)** A wearable, flexible sensor with pH and temperature sensors. Reproduced with permission ¹²⁷. Copyright 2017, American Chemical Society. **c)** A flexible wireless temperature-sensing platform with a printed temperature sensor. Reproduced with permission ¹²⁹. Copyright 2020, Creative Commons Attribution 4.0 International License. **d)** A wireless wearable sensor patch for ECG and temperature sensing. Reproduced with permission ¹³⁰. Copyright 2016, WILEY-VCH Verlag GmbH & Co. **e)** An epidermal wireless thermal sensor (eWTS) with a thin and soft thermal sensing/actuating component. Reproduced with permission ¹³¹. Copyright 2018, WILEY-VCH Verlag GmbH & Co. **f)** A thermoresponsive colorimetric temperature sensor with plasmonic gold nanoparticles in PNIPAM hydrogels. Reproduced with permission ¹³². Copyright 2018, Creative Commons Attribution 4.0 International License.

Different from other wireless systems, Krishnan et al. reported a battery-free and NFC operated flexible system for thermal characterization of the skin ¹³¹. The system measured the blood perfusion, hydration, and trauma on the skin by measuring the thermal conductivity change of the skin with the Cr/Au temperature sensor. The overall system consisted of an inductive coil, a microcontroller, and its associated passive components for RF energy harvesting and data transmission (**Figure 2.8e**). In a different study, Choe et al. demonstrated a cost-effective colorimetric temperature sensor for skin temperature monitoring. The colorimetric sensors were

created by combining plasmonic gold nanoparticles with thermoresponsive poly(N-isopropyl acrylamide) (PNIPAM) hydrogels¹³² (**Figure 2.8f**). The volumetric change of PNIPAM hydrogels upon heating changes the plasmonic coupling between the nanoparticles, resulting in a red shift in its extinction spectra and a change in the RGB color values of the image of the sensor. By tuning the lower critical solution temperatures of the hydrogels, the authors created a colorimetric patch for spatial skin temperature mapping with a satisfactory temperature resolution (0.2°C) and dynamic range.

In comparison to the resistive temperature sensors and thermistors, the colorimetric temperature sensing does not provide sufficient temperature resolution and accuracy for long-term monitoring. Benefits of flexible resistive temperature sensors and thermistors (miniaturization, simplicity of circuit design, and ease of integration with the skin) extended their uses to other exciting applications, such as estimation of the core body temperature¹³³, calibration of the response of temperature-dependent biosensors⁸², and mitigating the risks of the formation of skin ulcers¹³⁴.

2.4. Wearable Systems with Multimodal Sensing

Skin-interfaced wearable biochemical systems provide insights on molecular-level changes in human performance and physiology. A comprehensive understanding of human physiology necessitates continuous monitoring of biochemical data in addition to biophysical and environmental information¹³⁵. The integration of biochemical sensors with other physical sensors, such as heart rate, SpO₂, sweat rate, and temperature, provides a wealth of information that may not be easily obtained from a single type of sensor (**Table 2.1**). These systems not only provide an overall assessment of health and performance by synthesizing and correlating the multisensory data but also enables other features, such as improving the accuracy of the diagnostic decision

based on multiple sensor outputs and calibration of enzymatic sensors with pH and temperature sensors^{65, 75, 82, 127, 136-137}.

Table 2.1. List of biochemical and biophysical sensors with their health applications.

Analyte or Signal	Health Application	References
glucose	diabetes, diet management	138
lactate	physical performance, anaerobic metabolism, Frey's syndrome, pressure ischemia	139
urea, uric acid, creatinine, ammonia	renal dysfunction	140
pH, sodium, chloride	acid-base balance, cystic fibrosis, dehydration, wound healing	141-144
cortisol	stress monitoring	145
ethanol	assessment of intoxication	146
zinc, copper, cadmium, lead, mercury	assessment of toxic metal exposure	104
electrocardiogram, heart rate, heart rate variability	cardiovascular and pulmonary diseases	147-148
photoplethysmogram, SpO ₂	hypertension, vascular aging, blood perfusion, hypovolemia, oxygenation	149-151
sweat rate	dehydration	152
temperature	hyperthermia, infection, inflammation, physical exertion	153
accelerometer	motion disorders, fitness tracking	154

Recent studies have demonstrated the concept of multimodal sensing by integrating multiple sensing modalities into unified wireless platforms. **Figure 2.9a** shows a wearable and wireless multiplexed biosensor system for continuous measurement of glucose, lactate, pH, and temperature using a flexible sensor array¹⁵⁵. The auxiliary physical sensors could measure pH and temperature in physiological range and provide a real-time supplementary data that can be used for compensation of enzymatic loss of the biosensors. The flexible sensing array incorporated twelve working electrodes for simultaneous and multiplexed detection of glucose and lactate. Utilization of three multiplexers and potentiostats enabled parallel readout from glucose or lactate

sensors. As biosensors are sensitive to biofouling and wear and tear due to their prolonged use, continuous sensing with multielectrodes increases the precision of the biochemical sensors by averaging the biosensor responses from electrode arrays. In a similar manner, Hong et al. demonstrated a fully integrated wireless system for the estimation of post-exercise blood glucose levels from sweat glucose levels (**Figure 2.9b**)¹⁵⁶. The wrist-worn wearable system included a disposable patch with glucose and temperature sensors as well as an optical interface and an accelerometer for heart rate, SpO₂, and calculation of burned calories. The glucose sensors utilized three working electrodes that were operated sequentially via a multiplexer and a potentiostat for the detection of sweat glucose. The optical AFE utilized an integrated IC with three LEDs and a photodiode for heart rate and SpO₂ calculation from PPG signals. The accelerometer data (*i.e.*, burned calories), pre-exercise glucose levels, and sweat-to-blood correlation factors of each subject were used in the calculation of post-exercise glucose levels. Continuous measurement with the biochemical and physical sensors provided a stream of physiological data under dynamic and static exercise conditions, enabled correlation between human activity and blood glucose levels, and helped to estimate post-exercise blood glucose levels.

Fully integrated wearable systems with novel integration schemes and self-powered operation have also recently reported to minimize motion-induced noises and to enable battery-free operation¹⁵⁷⁻¹⁵⁸. **Figure 2.9c** demonstrates a wearable freestanding system for continuous measurement of glucose, lactate, choline, and acceleration¹⁵⁷. The system comprises an optional iontophoresis module, a multilayer stack for fluid management, analyte sensing and transduction modules, and data acquisition and transmission with a total power consumption about 100 mW. Due to its unique out-of-plane design, the wearable system minimized strain accumulation on the signal pathway and revealed noise-free detection of amperometric signals under exercise

conditions. The study tested the robustness of the system to motion-induced noises by simultaneously recording biosensor and acceleration data while the subjects were engaging in various motions, such as punching, arm swinging, and forearm twisting. In a similar manner, Gao's research group created a biofuel-powered wearable multiplexed system for continuous monitoring of urea, ammonia, glucose, pH, and skin temperature ¹⁵⁸. The wearable system consisted of a biofuel cell (BFC), a boost converter, a biosensor array, signal conditioning circuitries, a system on chip with an integrated microcontroller, a BLE module, and a temperature sensor with an overall power consumption of 9.35 mW. The BFC relied on the presence of lactate in sweat and generated power as high as 3.6 mW cm⁻². The boost converter drew current from the BFCs, which was used for powering the rest of the circuitry. The study demonstrated self-powered operation and detection of urea and NH₄⁺ or glucose and pH in sweat during an active exercise protocol.

Multimodal systems with different functionalities have been developed towards increasing the precision and robustness of the wearable systems to external factors (*e.g.*, sensor failure and motion-induced interferences), multisensory data correlation, self-powered operation, and prediction of post-exercise biomarker levels. Yet, there are still significant tradeoffs that need to be made when developing such wearable, wireless systems for continuous monitoring, such as power availability from self-powered devices and optimization of power consumption of the multisensory systems with iontophoretic sweat stimulation and wireless transmission.

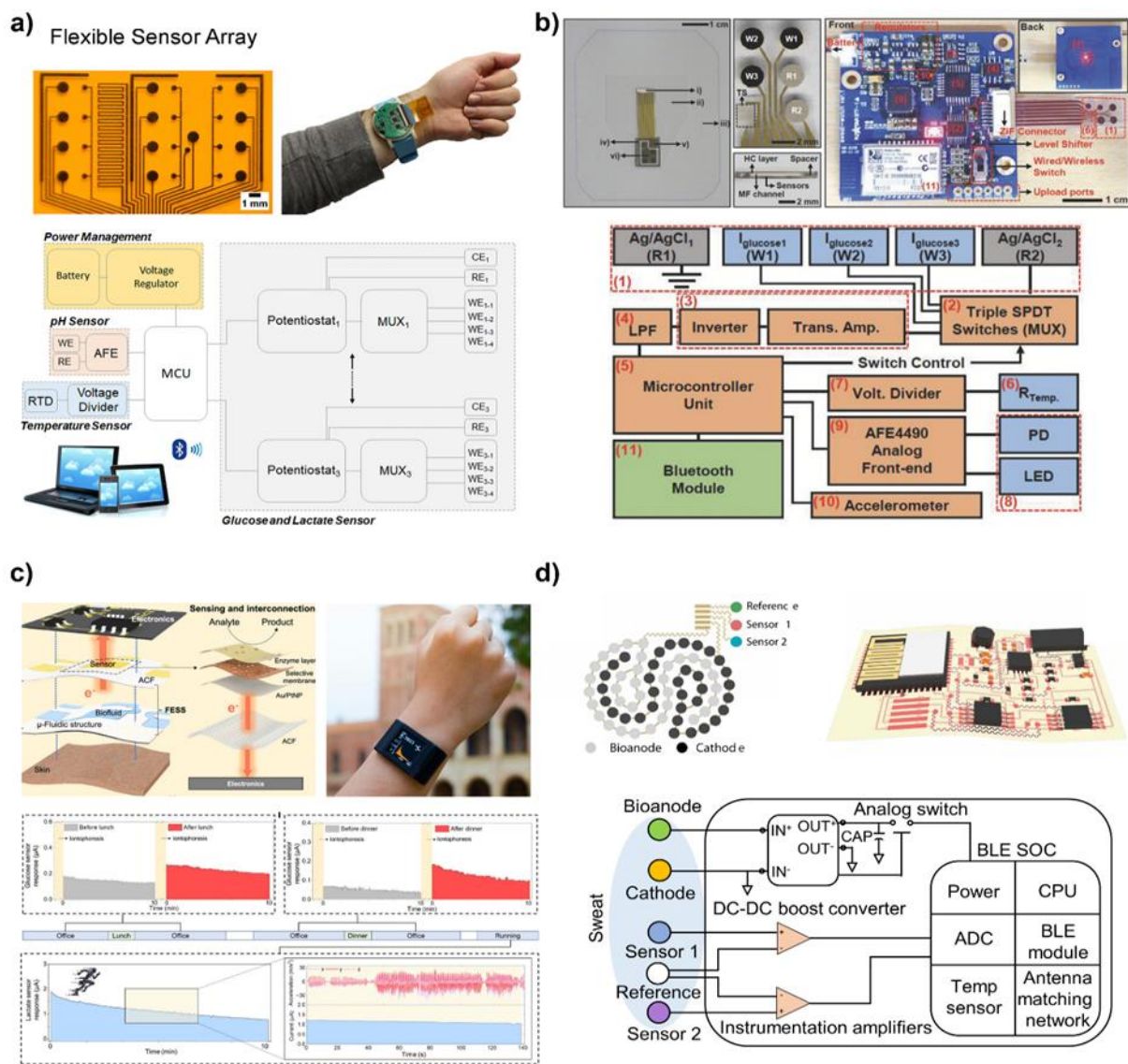


Figure 2.9. Examples of wearable and wireless systems illustrating the integration of biochemical and biophysical sensors on a single platform. **a)** A wearable multiplexed biosensor system with a flexible sensing array for glucose, lactate, pH, and skin temperature measurement. Reproduced with permission ¹⁵⁵. Copyright 2020, Elsevier. **b)** A disposable strip with a wrist-worn system for measurement of glucose, temperature, heart rate, SpO₂, and activity. Reproduced with permission ¹⁵⁶. Copyright 2018, WILEY-VCH Verlag GmbH & Co. **c)** A freestanding electrochemical system with an out-of-plane signal interconnection design for strain isolation in the signal pathway. Reproduced with permission ¹⁵⁷. Copyright 2020, Creative Commons Attribution 4.0 International License. **d)** A perspiration-powered soft electronic skin for urea, NH₄⁺, glucose, pH, and temperature measurement. Reproduced with permission ¹⁵⁸. Copyright 2020, The American Association for the Advancement of Science.

2.5. Summary and Outlook

Wearable biochemical sensing from sweat offers new alternatives for noninvasive and real-time monitoring, and it holds significant potential for wellness and performance monitoring as

well as disease diagnostics and prognosis in healthcare. In this review, we outlined sweat sampling and collection methods that are important for achieving continuous biochemical sensing. We highlighted skin-interfaced wearable sensors and systems for monitoring key sweat analytes and biophysical parameters, such as metabolites, pH, electrolytes, heart rate, arterial oxygenation, sweat rate, and skin temperature, with an emphasis on their sensing techniques, system-level specifications, and multimodal sensing functionalities. Nevertheless, there are still outstanding challenges that restrict the broader acceptance, implementation, and market adoption of such systems. System-level implementation and user/clinical acceptance of wearable multimodal systems will require optimization of multiple factors to meet the requirements of their intended use. To realize such functional platforms, multidisciplinary efforts are needed to create disruptive technologies in wearable and personalized healthcare. Our perspectives on these challenges and potential research areas are briefly outlined below.

- *Continuous sweat analysis for sedentary subjects and intra-or interpersonal sweat volume variance.* Current biochemical sensors rely on exercise/thermal or iontophoretically induced sweat for sweat analysis, limiting its use only to ambulatory subjects and leaving out the sedentary and elderly population. Novel passive sweat extraction, storage, and sensing techniques need to be explored for passive and power-free extraction of sweat to overcome challenges related to sweat generation or skin irritation due to the application of iontophoretic current to the skin¹⁵⁹⁻¹⁶¹. Additionally, as sweating and its composition differ across different regions of the body and vary across different individuals, understanding the secretion mechanism of analytes and integration of sweat rate sensors with the sensing platforms would be helpful for improving the measurement accuracy of sweat analytes by compensating the effect of analyte dilution^{116, 162}.

- *Sensitive and stable sensor operation in the presence of common interferences.* Current biochemical and biophysical sensors have been demonstrated to exhibit excellent performance in *in-vitro* tests or stationary human trials. Extended and repetitive human trials need to be carried out in the presence of external interferences, such as motion artifacts, external pressure, ambient light, humidity, and temperature, to assess their operational stability for long-term daily use. The clinical impact of biochemical and biophysical wearable systems should be evaluated by comparing them with gold-standard measurements/devices, such as sweat-blood correlation for the biochemical sensors and performance evaluation of biophysical sensors with clinically approved devices. In addition to the clinical validation, highly sensitive biochemical sensors with a high signal-to-noise ratio should be developed for the measurement of low levels of analytes in sweat with custom miniaturized electronic systems.
- *Powering of wearable systems, low-power operation, and wireless communication.* The increase in the number of sensing modalities in wearable systems warrant alternative power sources, wireless communication technologies, and efficient system-level operation for extended operation. Most of the current wearable systems use lithium-based batteries, but they are rigid and difficult to miniaturize due to their energy density limitations. Alternative energy storage devices with high energy density, capacitance retention, leakage, and cycling performance and energy harvesting techniques (photovoltaic, thermoelectric, piezoelectric, triboelectric, and biofuel cells) should be employed to enable autonomous self-powering of wearable systems ^{76, 163-164}. Besides energy harvesting alternatives, the power consumption of the systems can be minimized by implementing system-level optimizations, such as selection of low-power nano-enabled sensors, low power radios,

duty cycling, as well as the use of energy-efficient adaptive sampling and context-aware dynamic sensor selection techniques without sacrificing the accuracy of the physiological sensors^{135, 165-166}.

- *Multimodal sensing and data mining.* Fusion of biochemical and biophysical data in a wearable system for providing clinical diagnosis and treatment requires multimodal data fusion techniques with the objective of improving the signal quality and reliability, as well as reducing the uncertainty in data-based clinical decisions. Different pre-processing (data synchronization, filtering, feature extraction, normalization), data correlation, multiple hypothesis tests, and machine learning algorithms can be incorporated into the signal, feature, or decision-level data fusion for discovering the disease patterns, establishing the causes of potential pathologies, and administering a viable treatment¹⁶⁷⁻¹⁶⁸.
- *Wearability, user acceptance, and scalability.* As the wearable systems get more complicated with the addition of various sensing modalities, significant attention should be placed on biocompatibility, breathability, miniaturization, and overall mechanical reliability of the wearable devices to achieve aesthetically pleasing options that are robust against motion artifacts and device failures. Besides, cost-effective and scalable fabrication methods should be implemented for large area coverage and commercial adoption of the new technologies.

2.6. References

1. Berger, D., A brief history of medical diagnosis and the birth of the clinical laboratory. Part 1--Ancient times through the 19th century. *MLO: medical laboratory observer* **1999**, 31 (7), 28-30, 32, 34-40.
2. Galli, A.; Ambrosini, F.; Lombardi, F., Holter Monitoring and Loop Recorders: From Research to Clinical Practice. *Arrhythmia Electrophysiol. Rev.* **2016**, 5 (2), 136-143.
3. Hovorka, R., Continuous glucose monitoring and closed-loop systems. *Diabetic Med* **2006**, 23 (1), 1-12.
4. Haveman, M. E.; Kleiss, S. F.; Ma, K. F.; Vos, C. G.; Unlu, C.; Schuurmann, R. C. L.; Bokkers, R. P. H.; Hermens, H. J.; De Vries, J. P. P. M., Telemedicine in patients with peripheral arterial disease: is it worth the effort? *Expert Rev. Med. Devices* **2019**.
5. Lorincz, K.; Malan, D. J.; Fulford-Jones, T. R. F.; Nawoj, A.; Clavel, A.; Shnayder, V.; Mainland, G.; Welsh, M.; Moulton, S., Sensor networks for emergency response: Challenges and opportunities. *IEEE Pervasive Comput.* **2004**, 3 (4), 16-23.
6. Michahelles, F.; Matter, P.; Schmidt, A.; Schiele, B., Applying wearable sensors to avalanche rescue. *Comput Graph-Uk* **2003**, 27 (6), 839-847.
7. Yuce, M. R., Implementation of wireless body area networks for healthcare systems. *Sensor Actuat a-Phys* **2010**, 162 (1), 116-129.
8. Guk, K.; Han, G.; Lim, J.; Jeong, K.; Kang, T.; Lim, E. K.; Jung, J., Evolution of Wearable Devices with Real-Time Disease Monitoring for Personalized Healthcare. *Nanomaterials-Basel* **2019**, 9 (6).
9. iHealth Wireless wrist blood pressure monitor. <https://ihealthlabs.com/blood-pressure-monitors/wireless-blood-pressure-wrist-monitor-view-bp7s/> (accessed June 17).
10. iHealth Wireless activity and sleep tracker. <https://ihealthlabs.com/fitness-devices/wireless-activity-and-sleep-tracker/>.
11. Fitbit <https://www.fitbit.com/us/home> (accessed June 17).
12. Apple Activity trackers. <https://www.apple.com/watch/> (accessed June 17).
13. Samsung Activity trackers. <https://www.samsung.com/us/mobile/wearables/> (accessed June 17).
14. Nonin Medical Pulse oximeters. <https://www.nonin.com/> (accessed June 17).
15. Hexoskin Heart rate and respiratory rate monitoring. <https://www.hexoskin.com/> (accessed June 17).
16. Vashist, S. K., Non-invasive glucose monitoring technology in diabetes management: A review. *Anal. Chim. Acta* **2012**, 750, 16-27.
17. GlucoTrack Noninvasive glucose monitoring. <http://www.glucotrack.com/> (accessed June 17).
18. Zephyr <https://www.zephyranywhere.com/> (accessed June 17).
19. Baker, L. B., Physiology of sweat gland function: The roles of sweating and sweat composition in human health. *Temperature (Austin, Tex.)* **2019**, 6 (3), 211-259.
20. Robinson, S.; Robinson, A. H., Chemical Composition of Sweat. *Physiol. Rev.* **1954**, 34 (2), 202-220.
21. Kumar, L. S. S.; Wang, X.; Hagen, J.; Naik, R.; Papautsky, I.; Heikenfeld, J., Label free nano-aptasensor for interleukin-6 in protein-dilute bio fluids such as sweat. *Anal. Methods* **2016**, 8 (17), 3440-3444.

22. Bandodkar, A. J.; Jeerapan, I.; Wang, J., Wearable Chemical Sensors: Present Challenges and Future Prospects. *ACS Sensors* **2016**, *1* (5), 464-482.
23. Heikenfeld, J., Non-invasive Analyte Access and Sensing through Eccrine Sweat: Challenges and Outlook circa 2016. *Electroanal* **2016**, *28* (6), 1242-1249.
24. Gemperle, F.; Kasabach, C.; Stivoric, J.; Bauer, M.; Martin, R., Design for wearability. *Second International Symposium on Wearable Computers - Digest of Papers* **1998**, 116-122.
25. Kulkarni, P.; Öztürk, Y., Requirements and design spaces of mobile medical care. *Mobile Computing and Communications Review* **2007**, *11*, 12-30.
26. Pantelopoulos, A.; Bourbakis, N., A survey on wearable biosensor systems for health monitoring. *Conf Proc IEEE Eng Med Biol Soc* **2008**, *2008*, 4887-90.
27. Heikenfeld, J.; Jajack, A.; Rogers, J.; Gutruf, P.; Tian, L.; Pan, T.; Li, R.; Khine, M.; Kim, J.; Wang, J.; Kim, J., Wearable sensors: modalities, challenges, and prospects. *Lab Chip* **2017**.
28. Bariya, M.; Nyein, H. Y. Y.; Javey, A., Wearable sweat sensors. *Nat Electron* **2018**, *1* (3), 160-171.
29. Bandodkar, A. J.; Jeang, W. J.; Ghaffari, R.; Rogers, J. A., Wearable Sensors for Biochemical Sweat Analysis. *Annu Rev Anal Chem* **2019**, *12*, 1-22.
30. Kim, J.; Campbell, A. S.; de Avila, B. E. F.; Wang, J., Wearable biosensors for healthcare monitoring. *Nat. Biotechnol.* **2019**, *37* (4), 389-406.
31. Legner, C.; Kalwa, U.; Patel, V.; Chesmore, A.; Pandey, S., Sweat sensing in the smart wearables era: Towards integrative, multifunctional and body-compliant perspiration analysis. *Sensor Actuat a-Phys* **2019**, *296*, 200-221.
32. Ray, T. R.; Choi, J.; Bandodkar, A. J.; Krishnan, S.; Gutruf, P.; Tian, L. M.; Ghaffari, R.; Rogers, J. A., Bio-Integrated Wearable Systems: A Comprehensive Review. *Chem. Rev.* **2019**, *119* (8), 5461-5533.
33. Sempionatto, J. R.; Jeerapan, I.; Krishnan, S.; Wang, J., Wearable Chemical Sensors: Emerging Systems for On-Body Analytical Chemistry. *Anal. Chem.* **2020**, *92* (1), 378-396.
34. Takei, K.; Gao, W.; Wang, C.; Javey, A., Physical and Chemical Sensing With Electronic Skin. *Proc. IEEE* **2019**, *107* (10), 2155-2167.
35. Sato, K.; Sato, F., Individual Variations in Structure and Function of Human Eccrine Sweat Gland. *Am. J. Physiol.* **1983**, *245* (2), R203-R208.
36. Patterson, M. J.; Galloway, S. D. R.; Nimmo, M. A., Variations in regional sweat composition in normal human males. *Exp Physiol* **2000**, *85* (6), 869-875.
37. Liu, C. H.; Xu, T. L.; Wang, D. D.; Zhang, X. J., The role of sampling in wearable sweat sensors. *Talanta* **2020**, *212*.
38. Baker, L. B.; Stofan, J. R.; Hamilton, A. A.; Horswill, C. A., Comparison of regional patch collection vs. whole body washdown for measuring sweat sodium and potassium loss during exercise. *J. Appl. Physiol.* **2009**, *107* (3), 887-895.
39. Kintz, P.; Tracqui, A.; Mangin, P.; Edel, Y., Sweat testing in opioid users with a sweat patch. *J. Anal. Toxicol.* **1996**, *20* (6), 393-397.
40. Baker, L. B.; Barnes, K. A.; Anderson, M. L.; Passe, D. H.; Stofan, J. R., Normative data for regional sweat sodium concentration and whole-body sweating rate in athletes. *J Sport Sci* **2016**, *34* (4), 358-368.

41. Matzeu, G.; Fay, C.; Vaillant, A.; Coyle, S.; Diamond, D., A Wearable Device for Monitoring Sweat Rates via Image Analysis. *IEEE Trans. Biomed. Eng.* **2016**, *63* (8), 1672-1680.
42. Sonner, Z.; Wilder, E.; Heikenfeld, J.; Kasting, G.; Beyette, F.; Swaile, D.; Sherman, F.; Joyce, J.; Hagen, J.; Kelley-Loughnane, N.; Naik, R., The microfluidics of the eccrine sweat gland, including biomarker partitioning, transport, and biosensing implications. *Biomicrofluidics* **2015**, *9* (3), 031301.
43. Peng, R.; Sonner, Z.; Hauke, A.; Wilder, E.; Kasting, J.; Gaillard, T.; Swaile, D.; Sherman, F.; Mao, X.; Hagen, J.; Murdock, R.; Heikenfeld, J., A new oil/membrane approach for integrated sweat sampling and sensing: sample volumes reduced from μ L's to nL's and reduction of analyte contamination from skin. *Lab Chip* **2016**, *16* (22), 4415-4423.
44. Huang, X.; Liu, Y. H.; Chen, K. L.; Shin, W. J.; Lu, C. J.; Kong, G. W.; Patnaik, D.; Lee, S. H.; Cortes, J. F.; Rogers, J. A., Stretchable, Wireless Sensors and Functional Substrates for Epidermal Characterization of Sweat. *Small* **2014**, *10* (15), 3083-3090.
45. Wang, S. Q.; Wu, Y. J.; Gu, Y.; Li, T.; Luo, H.; Li, L. H.; Bai, Y. Y.; Li, L. L.; Liu, L.; Cao, Y. D.; Ding, H. Y.; Zhang, T., Wearable Sweatband Sensor Platform Based on Gold Nanodendrite Array as Efficient Solid Contact of Ion-Selective Electrode. *Anal. Chem.* **2017**, *89* (19), 10224-10231.
46. He, X. C.; Xu, T. L.; Gu, Z.; Gao, W.; Xu, L. P.; Pan, T. R.; Zhang, X. J., Flexible and Superwetable Bands as a Platform toward Sweat Sampling and Sensing. *Anal. Chem.* **2019**, *91* (7), 4296-4300.
47. Twine, N. B.; Norton, R. M.; Brothers, M. C.; Hauke, A.; Gomez, E. F.; Heikenfeld, J., Open nanofluidic films with rapid transport and no analyte exchange for ultra-low sample volumes. *Lab Chip* **2018**, *18* (18), 2816-2825.
48. Anastasova, S.; Crewther, B.; Bemnowicz, P.; Curto, V.; Ip, H. M. D.; Rosa, B.; Yang, G.-Z., A wearable multisensing patch for continuous sweat monitoring. *Biosens. Bioelectron.* **2017**, *93*, 139-145.
49. Lin, H. S.; Zhao, Y. C.; Lin, S. Y.; Wang, B.; Yeung, C.; Cheng, X. B.; Wang, Z. Q.; Cai, T. Y.; Yu, W. Z.; King, K.; Tan, J. W.; Salahi, K.; Hojaiji, H.; Emaminejad, S., A rapid and low-cost fabrication and integration scheme to render 3D microfluidic architectures for wearable biofluid sampling, manipulation, and sensing. *Lab Chip* **2019**, *19* (17), 2844-2853.
50. Choi, J.; Kang, D.; Han, S.; Kim, S. B.; Rogers, J. A., Thin, Soft, Skin-Mounted Microfluidic Networks with Capillary Bursting Valves for Chrono-Sampling of Sweat. *Adv. Healthcare Mater.* **2017**, *6* (5).
51. Emaminejad, S.; Gao, W.; Wu, E.; Davies, Z. A.; Nyein, H. Y. Y.; Challa, S.; Ryan, S. P.; Fahad, H. M.; Chen, K.; Shahpar, Z.; Talebi, S.; Milla, C.; Javey, A.; Davis, R. W., Autonomous sweat extraction and analysis applied to cystic fibrosis and glucose monitoring using a fully integrated wearable platform. *PNAS* **2017**, *114* (18), 4625-4630.
52. Koh, A.; Kang, D.; Xue, Y.; Lee, S.; Pielak, R. M.; Kim, J.; Hwang, T.; Min, S.; Banks, A.; Bastien, P.; Manco, M. C.; Wang, L.; Ammann, K. R.; Jang, K. I.; Won, P.; Han, S.; Ghaffari, R.; Paik, U.; Slepian, M. J.; Balooch, G.; Huang, Y. G.; Rogers, J. A., A soft, wearable microfluidic device for the capture, storage, and colorimetric sensing of sweat. *Sci. Transl. Med.* **2016**, *8* (366).
53. Bandodkar, A. J.; Choi, J.; Lee, S. P.; Jeang, W. J.; Agyare, P.; Gutruf, P.; Wang, S. Q.; Sponenburg, R. A.; Reeder, J. T.; Schon, S.; Ray, T. R.; Chen, S. L.; Mehta, S.; Ruiz, S.;

- Rogers, J. A., Soft, Skin-Interfaced Microfluidic Systems with Passive Galvanic Stopwatches for Precise Chronometric Sampling of Sweat. *Adv. Mater.* **2019**, *31* (32).
54. Choi, J.; Xue, Y. G.; Xia, W.; Ray, T. R.; Reeder, J. T.; Bandodkar, A. J.; Kang, D.; Xu, S.; Huang, Y. G.; Rogers, J. A., Soft, skin-mounted microfluidic systems for measuring secretory fluidic pressures generated at the surface of the skin by eccrine sweat glands. *Lab Chip* **2017**, *17* (15), 2572-2580.
 55. Choi, J.; Bandodkar, A. J.; Reeder, J. T.; Ray, T. R.; Turnquist, A.; Kim, S. B.; Nyberg, N.; Hourlier-Fargette, A.; Model, J. B.; Aranyosi, A. J.; Xu, S.; Ghaffari, R.; Rogers, J. A., Soft, Skin-Integrated Multifunctional Microfluidic Systems for Accurate Colorimetric Analysis of Sweat Biomarkers and Temperature. *ACS Sensors* **2019**, *4* (2), 379-388.
 56. Sekine, Y.; Kim, S. B.; Zhang, Y.; Bandodkar, A. J.; Xu, S.; Choi, J.; Irie, M.; Ray, T. R.; Kohli, P.; Kozai, N.; Sugita, T.; Wu, Y. X.; Lee, K.; Lee, K. T.; Ghaffari, R.; Rogers, J. A., A fluorometric skin-interfaced microfluidic device and smartphone imaging module for in situ quantitative analysis of sweat chemistry. *Lab Chip* **2018**, *18* (15), 2178-2186.
 57. Zhang, Y.; Guo, H. X.; Kim, S. B.; Wu, Y. X.; Ostojich, D.; Park, S. H.; Wang, X. J.; Weng, Z. Y.; Li, R.; Bandodkar, A. J.; Sekine, Y.; Choi, J.; Xu, S.; Quaggin, S.; Ghaffari, R.; Rogers, J. A., Passive sweat collection and colorimetric analysis of biomarkers relevant to kidney disorders using a soft microfluidic system. *Lab Chip* **2019**, *19* (9), 1545-1555.
 58. Mergenthaler, P.; Lindauer, U.; Dienel, G. A.; Meisel, A., Sugar for the brain: the role of glucose in physiological and pathological brain function. *Trends Neurosci.* **2013**, *36* (10), 587-597.
 59. Kreisberg, R. A., Pathogenesis and Management of Lactic-Acidosis. *Annu Rev Med* **1984**, *35*, 181-193.
 60. Wang, J., Electrochemical Glucose Biosensors. *Chem. Rev.* **2008**, *108* (2), 814-825.
 61. Jia, W.; Bandodkar, A. J.; Valdés-Ramírez, G.; Windmiller, J. R.; Yang, Z.; Ramírez, J.; Chan, G.; Wang, J., Electrochemical Tattoo Biosensors for Real-Time Noninvasive Lactate Monitoring in Human Perspiration. *Anal. Chem.* **2013**, *85* (14), 6553-6560.
 62. Rathee, K.; Dhull, V.; Dhull, R.; Singh, S., Biosensors based on electrochemical lactate detection: A comprehensive review. *Biochemistry and Biophysics Reports* **2016**, *5*, 35-54.
 63. Bandodkar, A. J.; Jia, W. Z.; Yardimci, C.; Wang, X.; Ramirez, J.; Wang, J., Tattoo-Based Noninvasive Glucose Monitoring: A Proof-of-Concept Study. *Anal. Chem.* **2015**, *87* (1), 394-398.
 64. Martin, A.; Kim, J.; Kurniawan, J. F.; Sempionatto, J. R.; Moreto, J. R.; Tang, G. D.; Campbell, A. S.; Shin, A.; Lee, M. Y.; Liu, X. F.; Wang, J., Epidermal Microfluidic Electrochemical Detection System: Enhanced Sweat Sampling and Metabolite Detection. *ACS Sensors* **2017**, *2* (12), 1860-1868.
 65. Imani, S.; Bandodkar, A. J.; Mohan, A. M. V.; Kumar, R.; Yu, S. F.; Wang, J.; Mercier, P. P., A wearable chemical-electrophysiological hybrid biosensing system for real-time health and fitness monitoring. *Nat. Commun.* **2016**, *7*.
 66. Sempionatto, J. R.; Nakagawa, T.; Pavinatto, A.; Mensah, S. T.; Imani, S.; Mercier, P.; Wang, J., Eyeglasses based wireless electrolyte and metabolite sensor platform. *Lab Chip* **2017**, *17* (10), 1834-1842.
 67. Jeerapan, I.; Sempionatto, J. R.; Pavinatto, A.; You, J. M.; Wang, J., Stretchable biofuel cells as wearable textile-based self-powered sensors. *J. Mater. Chem. A* **2016**, *4* (47), 18342-18353.

68. Lu, Y.; Jiang, K.; Chen, D.; Shen, G. Z., Wearable sweat monitoring system with integrated micro-supercapacitors. *Nano Energy* **2019**, *58*, 624-632.
69. Campbell, A. S.; Kim, J.; Wang, J., Wearable electrochemical alcohol biosensors. *Curr. Opin. Electrochem.* **2018**, *10*, 126-135.
70. Singh, M.; Verma, N.; Garg, A. K.; Redhu, N., Urea biosensors. *Sensor Actuat B-Chem* **2008**, *134* (1), 345-351.
71. Zhu, H. C.; Cao, R. L., The relationship between serum levels of uric acid and prognosis of infection in critically ill patients. *World J Emerg Med* **2012**, *3* (3), 186-190.
72. Hauke, A.; Simmers, P.; Ojha, Y. R.; Cameron, B. D.; Ballweg, R.; Zhang, T.; Twine, N.; Brothers, M.; Gomez, E.; Heikenfeld, J., Complete validation of a continuous and blood-correlated sweat biosensing device with integrated sweat stimulation. *Lab Chip* **2018**, *18* (24).
73. Han, W.; He, H.; Zhang, L.; Dong, C.; Zeng, H.; Dai, Y.; Xing, L.; Zhang, Y.; Xue, X., A Self-Powered Wearable Noninvasive Electronic-Skin for Perspiration Analysis Based on Piezo-Biosensing Unit Matrix of Enzyme/ZnO Nanoarrays. *ACS Appl. Mater. Interfaces* **2017**, *9* (35), 29526-29537.
74. Imani, S.; Mercier, P. P.; Bhandodkar, A. J.; Kim, J.; Wang, J., Wearable Chemical Sensors: Opportunities and Challenges. *Ieee Int Symp Circ S* **2016**, 1122-1125.
75. Xu, G.; Cheng, C.; Liu, Z.; Yuan, W.; Wu, X.; Lu, Y.; Low, S. S.; Liu, J.; Zhu, L.; Ji, D.; Li, S.; Chen, Z.; Wang, L.; Yang, Q.; Cui, Z.; Liu, Q., Battery-Free and Wireless Epidermal Electrochemical System with All-Printed Stretchable Electrode Array for Multiplexed In Situ Sweat Analysis. *Advanced Materials Technologies* **2019**, *4* (7), 1800658.
76. Zhao, J. Q.; Lin, Y. J.; Wu, J. B.; Nyein, H. Y. Y.; Bariya, M.; Tai, L. C.; Chao, M. H.; Ji, W. B.; Zhang, G.; Fan, Z. Y.; Javey, A., A Fully Integrated and Self-Powered Smartwatch for Continuous Sweat Glucose Monitoring. *ACS Sensors* **2019**, *4* (7), 1925-1933.
77. Aoi, W.; Marunaka, Y., Importance of pH Homeostasis in Metabolic Health and Diseases: Crucial Role of Membrane Proton Transport. *Biomed Res. Int.* **2014**.
78. Bariya, M.; Shahpar, Z.; Park, H.; Sun, J. F.; Jung, Y.; Gao, W.; Nyein, H. Y. Y.; Liaw, T. S.; Tai, L. C.; Ngo, Q. P.; Chao, M. H.; Zhao, Y. B.; Hettick, M.; Cho, G.; Javey, A., Roll-to-Roll Gravure Printed Electrochemical Sensors for Wearable and Medical Devices. *ACS Nano* **2018**, *12* (7), 6978-6987.
79. Pal, A.; Goswami, D.; Cuellar, H. E.; Castro, B.; Kuang, S. H.; Martinez, R. V., Early detection and monitoring of chronic wounds using low-cost, omniphobic paper-based smart bandages. *Biosens Bioelectron* **2018**, *117*, 696-705.
80. Kassal, P.; Zubak, M.; Scheipl, G.; Mohr, G. J.; Steinberg, M. D.; Steinberg, I. M., Smart bandage with wireless connectivity for optical monitoring of pH. *Sensor Actuat B-Chem* **2017**, *246*, 455-460.
81. Curto, V. F.; Fay, C.; Coyle, S.; Byrne, R.; O'Toole, C.; Barry, C.; Hughes, S.; Moyna, N.; Diamond, D.; Benito-Lopez, F., Real-time sweat pH monitoring based on a wearable chemical barcode micro-fluidic platform incorporating ionic liquids. *Sensor Actuat B-Chem* **2012**, *171*, 1327-1334.
82. Gao, W.; Emaminejad, S.; Nyein, H. Y. Y.; Challa, S.; Chen, K.; Peck, A.; Fahad, H. M.; Ota, H.; Shiraki, H.; Kiriya, D.; Lien, D.-H.; Brooks, G. A.; Davis, R. W.; Javey, A., Fully integrated wearable sensor arrays for multiplexed in situ perspiration analysis. *Nature* **2016**, *529* (7587), 509-514.

83. Rose, D. P.; Ratterman, M. E.; Griffin, D. K.; Hou, L.; Kelley-Loughnane, N.; Naik, R. R.; Hagen, J. A.; Papautsky, I.; Heikenfeld, J. C., Adhesive RFID Sensor Patch for Monitoring of Sweat Electrolytes. *IEEE Trans. Biomed. Eng.* **2015**, *62* (6), 1457-1465.
84. Glennon, T.; O'Quigley, C.; McCaul, M.; Matzeu, G.; Beirne, S.; Wallace, G. G.; Stroiescu, F.; O'Mahoney, N.; White, P.; Diamond, D., "SWEATCH': A Wearable Platform for Harvesting and Analysing Sweat Sodium Content. *Electroanal* **2016**, *28* (6), 1283-1289.
85. Alizadeh, A.; Burns, A.; Lenigk, R.; Gettings, R.; Ashe, J.; Porter, A.; McCaul, M.; Barrett, R.; Diamond, D.; White, P.; Skeath, P.; Tomczak, M., A wearable patch for continuous monitoring of sweat electrolytes during exertion. *Lab Chip* **2018**, *18* (17), 2632-2641.
86. Lee, Y. K.; Jang, K. I.; Ma, Y. J.; Koh, A.; Chen, H.; Jung, H. N.; Kim, Y.; Kwak, J. W.; Wang, L.; Xue, Y. G.; Yang, Y. Y.; Tian, W. L.; Jiang, Y.; Zhang, Y. H.; Feng, X.; Huang, Y. G.; Rogers, J. A., Chemical Sensing Systems that Utilize Soft Electronics on Thin Elastomeric Substrates with Open Cellular Designs. *Adv. Funct. Mater.* **2017**, *27* (9).
87. Kim, S. B.; Zhang, Y.; Won, S. M.; Bandodkar, A. J.; Sekine, Y.; Xue, Y. G.; Koo, J.; Harshman, S. W.; Martin, J. A.; Park, J. M.; Ray, T. R.; Crawford, K. E.; Lee, K. T.; Choi, J.; Pitsch, R. L.; Grigsby, C. C.; Strang, A. J.; Chen, Y. Y.; Xu, S.; Kim, J.; Koh, A.; Ha, J. S.; Huang, Y. G.; Kim, S. W.; Rogers, J. A., Super-Absorbent Polymer Valves and Colorimetric Chemistries for Time-Sequenced Discrete Sampling and Chloride Analysis of Sweat via Skin-Mounted Soft Microfluidics. *Small* **2018**, *14* (12).
88. Wagner, P. D., The biology of oxygen. *Eur Respir J* **2008**, *31* (4), 887-890.
89. Kamal, A. A. R.; Harness, J. B.; Irving, G.; Mearns, A. J., Skin Photoplethysmography - a Review. *Comput. Methods Programs Biomed.* **1989**, *28* (4), 257-269.
90. Bowes, W. A.; Corke, B. C.; Hulka, J., Pulse Oximetry - a Review of the Theory, Accuracy, and Clinical-Applications. *Obstet Gynecol* **1989**, *74* (3), 541-546.
91. Allen, J., Photoplethysmography and its application in clinical physiological measurement. *Physiol. Meas.* **2007**, *28* (3), R1-R39.
92. Yokota, T.; Zalar, P.; Kaltenbrunner, M.; Jinno, H.; Matsuhisa, N.; Kitanosako, H.; Tachibana, Y.; Yukita, W.; Koizumi, M.; Someya, T., Ultraflexible organic photonic skin. *Sci. Adv.* **2016**, *2* (4).
93. Khan, Y.; Han, D.; Pierre, A.; Ting, J.; Wang, X. C.; Lochner, C. M.; Bovo, G.; Yaacobi-Gross, N.; Newsome, C.; Wilson, R.; Arias, A. C., A flexible organic reflectance oximeter array. *PNAS* **2018**, *115* (47), E11015-E11024.
94. Han, D.; Khan, Y.; Ting, J.; Zhu, J.; Combe, C.; Wadsworth, A.; McCulloch, I.; Arias, A. C., Pulse Oximetry Using Organic Optoelectronics under Ambient Light. *Advanced Materials Technologies* **2020**, *5* (5), 1901122.
95. Kim, J.; Salvatore, G. A.; Araki, H.; Chiarelli, A. M.; Xie, Z.; Banks, A.; Sheng, X.; Liu, Y.; Lee, J. W.; Jang, K.-I.; Heo, S. Y.; Cho, K.; Luo, H.; Zimmerman, B.; Kim, J.; Yan, L.; Feng, X.; Xu, S.; Fabiani, M.; Gratton, G.; Huang, Y.; Paik, U.; Rogers, J. A., Battery-free, stretchable optoelectronic systems for wireless optical characterization of the skin. *Sci. Adv.* **2016**, *2* (8).
96. Chung, H. U.; Rwei, A. Y.; Hourlier-Fargette, A.; Xu, S.; Lee, K.; Dunne, E. C.; Xie, Z.; Liu, C.; Carlini, A.; Kim, D. H.; Ryu, D.; Kulikova, E.; Cao, J.; Odland, I. C.; Fields, K. B.; Hopkins, B.; Banks, A.; Ogle, C.; Grande, D.; Park, J. B.; Kim, J.; Irie, M.; Jang, H.; Lee, J.; Park, Y.; Kim, J.; Jo, H. H.; Hahm, H.; Avila, R.; Xu, Y.; Namkoong, M.; Kwak, J. W.; Suen, E.; Paulus, M. A.; Kim, R. J.; Parsons, B. V.; Human, K. A.; Kim, S. S.; Patel, M.; Reuther, W.; Kim, H. S.; Lee, S. H.; Leedle, J. D.; Yun, Y.; Rigali, S.; Son, T.; Jung,

- I.; Arafa, H.; Soundararajan, V. R.; Ollech, A.; Shukla, A.; Bradley, A.; Schau, M.; Rand, C. M.; Marsillio, L. E.; Harris, Z. L.; Huang, Y.; Hamvas, A.; Paller, A. S.; Weese-Mayer, D. E.; Lee, J. Y.; Rogers, J. A., Skin-interfaced biosensors for advanced wireless physiological monitoring in neonatal and pediatric intensive-care units. *Nat. Med.* **2020**, *26* (3), 418-429.
97. Zhang, H.; Gutruf, P.; Meacham, K.; Montana, M. C.; Zhao, X.; Chiarelli, A. M.; Vázquez-Guardado, A.; Norris, A.; Lu, L.; Guo, Q.; Xu, C.; Wu, Y.; Zhao, H.; Ning, X.; Bai, W.; Kandela, I.; Haney, C. R.; Chanda, D.; Gereau, R. W.; Rogers, J. A., Wireless, battery-free optoelectronic systems as subdermal implants for local tissue oximetry. *Sci. Adv.* **2019**, *5* (3), eaaw0873.
98. Webster, J. G., *Design of Pulse Oximeters*. CRC Press 1997.
99. Rhee, S.; Yang, B. H.; Asada, H. H., Artifact-resistant power-efficient design of finger-ring plethysmographic sensors. *IEEE Trans. Biomed. Eng.* **2001**, *48* (7), 795-805.
100. Pelaez, E. A.; Villegas, E. R., LED power reduction trade-offs for ambulatory pulse oximetry. *2007 Annual International Conference of the Ieee Engineering in Medicine and Biology Society, Vols 1-16* **2007**, 2296-2299.
101. Tamura, T., Current progress of photoplethysmography and SPO2 for health monitoring. *Biomed. Eng. Lett.* **2019**, *9* (1), 21-36.
102. Sempionatto, J. R.; Khorshed, A. A.; Ahmed, A.; De Loyola e Silva, A. N.; Barfidokht, A.; Yin, L.; Goud, K. Y.; Mohamed, M. A.; Bailey, E.; May, J.; Aebischer, C.; Chatelle, C.; Wang, J., Epidermal Enzymatic Biosensors for Sweat Vitamin C: Toward Personalized Nutrition. *ACS Sensors* **2020**, *5* (6), 1804-1813.
103. Parlak, O.; Keene, S. T.; Marais, A.; Curto, V. F.; Salleo, A., Molecularly selective nanoporous membrane-based wearable organic electrochemical device for noninvasive cortisol sensing. *Sci. Adv.* **2018**, *4* (7).
104. Gao, W.; Nyein, H. Y. Y.; Shahpar, Z.; Fahad, H. M.; Chen, K.; Emaminejad, S.; Gao, Y. J.; Tai, L. C.; Ota, H.; Wu, E.; Bullock, J.; Zeng, Y. P.; Lien, D. H.; Javey, A., Wearable Microsensor Array for Multiplexed Heavy Metal Monitoring of Body Fluids. *ACS Sensors* **2016**, *1* (7), 866-874.
105. Tai, L.-C.; Ahn, C. H.; Nyein, H. Y. Y.; Ji, W.; Bariya, M.; Lin, Y.; Li, L.; Javey, A., Nicotine Monitoring with a Wearable Sweat Band. *ACS Sensors* **2020**, *5* (6), 1831-1837.
106. Tai, L. C.; Gao, W.; Chao, M. H.; Bariya, M.; Ngo, Q. P.; Shahpar, Z.; Nyein, H. Y. Y.; Park, H.; Sun, J.; Jung, Y.; Wu, E.; Fahad, H. M.; Lien, D. H.; Ota, H.; Cho, G.; Javey, A., Methylxanthine Drug Monitoring with Wearable Sweat Sensors. *Adv. Mater.* **2018**, *30* (23).
107. Yang, Y. R.; Song, Y.; Bo, X. J.; Min, J. H.; Pak, O. S.; Zhu, L. L.; Wang, M. Q.; Tu, J. B.; Kogan, A.; Zhang, H. X.; Hsiai, T. K.; Li, Z. P.; Gao, W., A laser-engraved wearable sensor for sensitive detection of uric acid and tyrosine in sweat. *Nat. Biotechnol.* **2020**, *38* (2), 217-224.
108. Atkins, J. L.; Butler, P. E. M., Hyperhidrosis: A review of current management. *Plastic and Reconstructive Surgery* **2002**, *110* (1), 222-228.
109. Brake, D. J.; Bates, G. P., Fluid losses and hydration status of industrial workers under thermal stress working extended shifts. *Occup. Environ. Med.* **2003**, *60* (2), 90-96.
110. Leithead, C.; Lind, Ar, Heat-Stress and Heat Disorders *Roy Soc Health J* **1964**, *84* (4), 213-213.

111. Gopinathan, P. M.; Pichan, G.; Sharma, V. M., Role of Dehydration in Heat Stress-Induced Variations in Mental Performance. *Arch Environ Health* **1988**, *43* (1), 15-17.
112. Casa, D. J.; Armstrong, L. E.; Hillman, S. K.; Montain, S. J.; Reiff, R. V.; Rich, B. S. E.; Roberts, W. O.; Stone, J. A., National Athletic Trainers' Association position statement: Fluid replacement for athletes. *J Athl Training* **2000**, *35* (2), 212-224.
113. Liu, G.; Hob, C.; Slappey, N.; Zhou, Z.; Snelgrove, S. E.; Brown, M.; Grabinski, A.; Guo, X.; Chen, D. Y.; Miller, K.; Edwards, J.; Kaya, T., A wearable conductivity sensor for wireless real-time sweat monitoring. *Sensor Actuat B-Chem* **2016**, *227*, 35-42.
114. Francis, J.; Stamper, I.; Heikenfeld, J.; Gomez, E. F., Digital nanoliter to milliliter flow rate sensor with in vivo demonstration for continuous sweat rate measurement. *Lab Chip* **2019**, *19* (1), 178-185.
115. Nyein, H. Y. Y.; Tai, L. C.; Ngo, Q. P.; Chao, M. H.; Zhang, G. B.; Gao, W.; Bariya, M.; Bullock, J.; Kim, H.; Fahad, H. M.; Javey, A., A Wearable Microfluidic Sensing Patch for Dynamic Sweat Secretion Analysis. *ACS Sensors* **2018**, *3* (5), 944-952.
116. Yuan, Z.; Hou, L.; Bariya, M.; Nyein, H. Y. Y.; Tai, L. C.; Ji, W. B.; Liabc, L.; Javey, A., A multi-modal sweat sensing patch for cross-verification of sweat rate, total ionic charge, and Na⁺ concentration. *Lab Chip* **2019**, *19* (19), 3179-3189.
117. Kim, S. B.; Lee, K.; Raj, M. S.; Lee, B.; Reeder, J. T.; Koo, J.; Hourlier-Fargette, A.; Bandodkar, A. J.; Won, S. M.; Sekine, Y.; Choi, J.; Zhang, Y.; Yoon, J.; Kim, B. H.; Yun, Y.; Lee, S.; Shin, J.; Kim, J.; Ghaffari, R.; Rogers, J. A., Soft, Skin-Interfaced Microfluidic Systems with Wireless, Battery-Free Electronics for Digital, Real-Time Tracking of Sweat Loss and Electrolyte Composition. *Small* **2018**, *14* (45).
118. Reeder, J. T.; Choi, J.; Xue, Y. G.; Gutruf, P.; Hanson, J.; Liu, M.; Ray, T.; Bandodkar, A. J.; Avila, R.; Xia, W.; Krishnan, S.; Xu, S.; Barnes, K.; Pahnke, M.; Ghaffari, R.; Huang, Y.; Rogers, J. A., Waterproof, electronics-enabled, epidermal microfluidic devices for sweat collection, biomarker analysis, and thermography in aquatic settings. *Sci. Adv.* **2019**, *5* (1).
119. Zhao, F. J.; Bonmarin, M.; Chen, Z. C.; Larson, M.; Fay, D.; Runnoe, D.; Heikenfeld, J., Ultra-simple wearable local sweat volume monitoring patch based on swellable hydrogels. *Lab Chip* **2020**, *20* (1), 168-174.
120. Salvo, P.; Pingitore, A.; Barbini, A.; Di Francesco, F., A wearable sweat rate sensor to monitor the athletes' performance during training. *Sci. Sports* **2018**, *33* (2), e51-e58.
121. Parrilla, M.; Guinovart, T.; Ferre, J.; Blondeau, P.; Andrade, F. J., A Wearable Paper-Based Sweat Sensor for Human Perspiration Monitoring. *Adv. Healthcare Mater.* **2019**.
122. Kelly, G., Body temperature variability (Part 1): A review of the history of body temperature and its variability due to site selection, biological rhythms, fitness, and aging. *Altern Med Rev* **2006**, *11* (4), 278-293.
123. Kelly, G. S., Body temperature variability (part 2): Masking influences of body temperature variability and a review of body temperature variability in disease. *Altern Med Rev* **2007**, *12* (1), 49-62.
124. Clark, R. P., Human Skin Temperature and Its Relevance in Physiology and Clinical Assessment. In *Recent Advances in Medical Thermology*, Ring, E. F. J.; Phillips, B., Eds. Springer New York: Boston, MA, 1984; pp 5-15.
125. Kelechi, T. J.; Michel, Y., A descriptive study of skin temperature, tissue perfusion, and tissue oxygen in patients with chronic venous disease. *Biol Res Nurs* **2007**, *9* (1), 70-80.

126. Yamamoto, Y.; Yamamoto, D.; Takada, M.; Naito, H.; Arie, T.; Akita, S.; Takei, K., Efficient Skin Temperature Sensor and Stable Gel-Less Sticky ECG Sensor for a Wearable Flexible Healthcare Patch. *Adv. Healthcare Mater.* **2017**, *6* (17).
127. Nakata, S.; Arie, T.; Akita, S.; Takei, K., Wearable, Flexible, and Multifunctional Healthcare Device with an ISFET Chemical Sensor for Simultaneous Sweat pH and Skin Temperature Monitoring. *ACS Sensors* **2017**, *2* (3), 443-448.
128. Benchirouf, A.; Palaniyappan, S.; Ramalingame, R.; Raghunandan, P.; Jagemann, T.; Muller, C.; Hietschold, M.; Kanoun, O., Electrical properties of multi-walled carbon nanotubes/PEDOT:PSS nanocomposites thin films under temperature and humidity effects. *Sensor Actuat B-Chem* **2016**, *224*, 344-350.
129. Wang, Y. F.; Sekine, T.; Takeda, Y.; Yokosawa, K.; Matsui, H.; Kumaki, D.; Shiba, T.; Nishikawa, T.; Tokito, S., Fully Printed PEDOT:PSS-based Temperature Sensor with High Humidity Stability for Wireless Healthcare Monitoring. *Sci Rep* **2020**, *10* (1), 2467.
130. Khan, Y.; Garg, M.; Gui, Q.; Schadt, M.; Gaikwad, A.; Han, D. G.; Yamamoto, N. A. D.; Hart, P.; Welte, R.; Wilson, W.; Czarnecki, S.; Poliks, M.; Jin, Z. P.; Ghose, K.; Egitto, F.; Turner, J.; Arias, A. C., Flexible Hybrid Electronics: Direct Interfacing of Soft and Hard Electronics for Wearable Health Monitoring. *Adv. Funct. Mater.* **2016**, *26* (47), 8764-8775.
131. Krishnan, S. R.; Su, C. J.; Xie, Z. Q.; Patel, M.; Madhvapathy, S. R.; Xu, Y. S.; Freudman, J.; Ng, B.; Heo, S. Y.; Wang, H. L.; Ray, T. R.; Leshock, J.; Stankiewicz, I.; Feng, X.; Huang, Y. G.; Gutruf, P.; Rogers, J. A., Wireless, Battery-Free Epidermal Electronics for Continuous, Quantitative, Multimodal Thermal Characterization of Skin. *Small* **2018**, *14* (47).
132. Choe, A.; Yeom, J.; Shanker, R.; Kim, M. P.; Kang, S.; Ko, H., Stretchable and wearable colorimetric patches based on thermoresponsive plasmonic microgels embedded in a hydrogel film. *NPG Asia Mater.* **2018**, *10*, 912-922.
133. Zhang, Y. H.; Webb, R. C.; Luo, H. Y.; Xue, Y. G.; Kurniawan, J.; Cho, N. H.; Krishnan, S.; Li, Y. H.; Huang, Y. G.; Rogers, J. A., Theoretical and Experimental Studies of Epidermal Heat Flux Sensors for Measurements of Core Body Temperature. *Adv. Healthcare Mater.* **2016**, *5* (1), 119-127.
134. Han, S.; Kim, J.; Won, S. M.; Ma, Y. J.; Kang, D.; Xie, Z. Q.; Lee, K. T.; Chung, H. U.; Banks, A.; Min, S.; Heo, S. Y.; Davies, C. R.; Lee, J. W.; Lee, C. H.; Kim, B. H.; Li, K.; Zhou, Y. D.; Wei, C.; Feng, X.; Huang, Y. G.; Rogers, J. A., Battery-free, wireless sensors for full-body pressure and temperature mapping. *Sci. Transl. Med.* **2018**, *10* (435).
135. Misra, V.; Bozkurt, A.; Calhoun, B. H.; Datta, S.; Dickey, M.; Kiani, M.; Lach, J.; Lee, B.; Jur, J.; Oralkan, O.; Ozturk, M.; Rajagopalan, R.; Roundy, S.; Strohmaier, J.; Trolier-McKinstry, S.; Vashae, D.; Wentzloff, D.; Werner, D., Optimizing the energy balance to achieve autonomous self-powering for vigilant health and IoT applications. *J. Phys. Conf. Ser.* **2019**, *1407*, 012001.
136. Lee, H.; Song, C.; Hong, Y. S.; Kim, M. S.; Cho, H. R.; Kang, T.; Shin, K.; Choi, S. H.; Hyeon, T.; Kim, D. H., Wearable/disposable sweat-based glucose monitoring device with multistage transdermal drug delivery module. *Sci. Adv.* **2017**, *3* (3).
137. Wiorek, A.; Parrilla, M.; Cuartero, M.; Crespo, G. A., Epidermal Patch with Glucose Biosensor: pH and Temperature Correction toward More Accurate Sweat Analysis during Sport Practice. *Anal. Chem.* **2020**.

138. Moyer, J.; Wilson, D.; Finkelshtein, I.; Wong, B.; Potts, R., Correlation Between Sweat Glucose and Blood Glucose in Subjects with Diabetes. *Diabetes Technol. Ther.* **2012**, *14* (5), 398-402.
139. Derbyshire, P. J.; Barr, H.; Davis, F.; Higson, S. P. J., Lactate in human sweat: a critical review of research to the present day. *J Physiol Sci* **2012**, *62* (6), 429-440.
140. Tricoli, A.; Neri, G., Miniaturized Bio-and Chemical-Sensors for Point-of-Care Monitoring of Chronic Kidney Diseases. *Sensors-Basel* **2018**, *18* (4).
141. Chevront, S. N.; Kenefick, R. W., Dehydration: Physiology, Assessment, and Performance Effects. *Compr Physiol* **2014**, *4* (1), 257-285.
142. Gibson, L. E.; Cooke, R. E., A Test for Concentration of Electrolytes in Sweat in Cystic Fibrosis of the Pancreas Utilizing Pilocarpine by Iontophoresis. *Pediatrics* **1959**, *23* (3), 545-549.
143. Dill, D.; Hall, F.; Edwards, H., Changes in composition of sweat during acclimatization to heat. *American Journal of Physiology-Legacy Content* **1938**, *123* (2), 412-419.
144. Percival, S. L.; McCarty, S.; Hunt, J. A.; Woods, E. J., The effects of pH on wound healing, biofilms, and antimicrobial efficacy. *Wound Repair Regen.* **2014**, *22* (2), 174-186.
145. Torrente-Rodriguez, R. M.; Tu, J. B.; Yang, Y. R.; Min, J. H.; Wang, M. Q.; Song, Y.; Yu, Y.; Xu, C. H.; Ye, C.; IsHak, W. W.; Gao, W., Investigation of Cortisol Dynamics in Human Sweat Using a Graphene-Based Wireless mHealth System. *Matter* **2020**, *2* (4), 921-937.
146. Buono, M. J., Sweat ethanol concentrations are highly correlated with co-existing blood values in humans. *Exp Physiol* **1999**, *84* (2), 401-404.
147. Sessa, F.; Anna, V.; Messina, G.; Cibelli, G.; Monda, V.; Marsala, G.; Ruberto, M.; Biondi, A.; Cascio, O.; Bertozzi, G.; Pisanelli, D.; Maglietta, F.; Messina, A.; Mollica, M. P.; Salerno, M., Heart rate variability as predictive factor for sudden cardiac death. *Aging-Ur* **2018**, *10* (2), 166-177.
148. Agarwal, R. L.; Kumar, D.; Gurpreet; Agarwal, D. K.; Chabra, G. S., Diagnostic Values of Electrocardiogram in Chronic Obstructive Pulmonary Disease (COPD). *Lung India* **2008**, *25* (2), 78-81.
149. Elgendi, M.; Fletcher, R.; Liang, Y. B.; Howard, N.; Lovell, N. H.; Abbott, D.; Lim, K.; Ward, R., The use of photoplethysmography for assessing hypertension. *Npj Digit Med* **2019**, *2*.
150. Yousef, Q.; Reaz, M. B. I.; Ali, M. A. M., The Analysis of PPG Morphology: Investigating the Effects of Aging on Arterial Compliance. *Meas Sci Rev* **2012**, *12* (6), 266-271.
151. Roederer, A.; Weimer, J.; DiMartino, J.; Gutsche, J.; Lee, I., Robust Monitoring of Hypovolemia in Intensive Care Patients using Photoplethysmogram Signals. *2015 37th Annual International Conference of the IEEE Engineering in Medicine and Biology Society (EMBC)* **2015**, 1504-1507.
152. Maughan, R. J.; Shirreffs, S. M., Dehydration and rehydration in competitive sport. *Scand J Med Sci Spor* **2010**, *20*, 40-47.
153. Lim, C. L.; Byrne, C.; Lee, J. K. W., Human thermoregulation and measurement of body temperature in exercise and clinical settings. *Ann Acad Med Singap* **2008**, *37* (4), 347-353.
154. Lorenzi, P.; Rao, R.; Romano, G.; Kita, A.; Irrera, F., Mobile Devices for the Real-Time Detection of Specific Human Motion Disorders. *IEEE Sens. J.* **2016**, *16* (23), 8220-8227.

155. Yokus, M. A.; Songkakul, T.; Pozdin, V. A.; Bozkurt, A.; Daniele, M. A., Wearable multiplexed biosensor system toward continuous monitoring of metabolites. *Biosens. Bioelectron.* **2020**, *153*, 112038.
156. Hong, Y. J.; Lee, H.; Kim, J.; Lee, M.; Choi, H. J.; Hyeon, T.; Kim, D. H., Multifunctional Wearable System that Integrates Sweat-Based Sensing and Vital-Sign Monitoring to Estimate Pre-/Post-Exercise Glucose Levels. *Adv. Funct. Mater.* **2018**, *28* (47).
157. Zhao, Y. C.; Wang, B.; Hojaiji, H.; Wang, Z. Q.; Lin, S. Y.; Yeung, C.; Lin, H. S.; Nguyen, P.; Chiu, K. L.; Salahi, K.; Cheng, X. B.; Tan, J. W.; Cerrillos, B. A.; Emaminejad, S., A wearable freestanding electrochemical sensing system. *Sci. Adv.* **2020**, *6* (12).
158. Yu, Y.; Nassar, J.; Xu, C.; Min, J.; Yang, Y.; Dai, A.; Doshi, R.; Huang, A.; Song, Y.; Gehlhar, R.; Ames, A. D.; Gao, W., Biofuel-powered soft electronic skin with multiplexed and wireless sensing for human-machine interfaces. *Sci. Rob.* **2020**, *5* (41), eaaz7946.
159. Lin, S. Y.; Wang, B.; Zhao, Y. C.; Shih, R.; Cheng, X. B.; Yu, W. Z.; Hojaiji, H.; Lin, H. S.; Hoffman, C.; Ly, D.; Tan, J. W.; Chen, Y.; Di Carlo, D.; Milla, C.; Emaminejad, S., Natural Perspiration Sampling and in Situ Electrochemical Analysis with Hydrogel Micropatches for User-Identifiable and Wireless Chemo/Biosensing. *ACS Sensors* **2020**, *5* (1), 93-102.
160. Shay, T.; Saha, T.; Dickey, M. D.; Velev, O. D., Principles of long-term fluids handling in paper-based wearables with capillary–evaporative transport. *Biomicrofluidics* **2020**, *14* (3), 034112.
161. Yokus, M. A.; Saha, T.; Fang, J.; Dickey, M. D.; Velev, O. D.; Daniele, M. A. In *Towards Wearable Electrochemical Lactate Sensing using Osmotic-Capillary Microfluidic Pumping*, 2019 IEEE SENSORS, 27-30 Oct. 2019; 2019; pp 1-4.
162. Yokus, M. A.; Hass, C.; Agcayazi, T.; Bozkurt, A.; Daniele, M. A., Towards a Wearable Perspiration Sensor. *2017 Ieee Sensors* **2017**, 1260-1262.
163. Jung, S.; Hong, S.; Kim, J.; Lee, S.; Hyeon, T.; Lee, M.; Kim, D. H., Wearable Fall Detector using Integrated Sensors and Energy Devices. *Sci. Rep.* **2015**, *5*.
164. Ostfeld, A. E.; Gaikwad, A. M.; Khan, Y.; Arias, A. C., High-performance flexible energy storage and harvesting system for wearable electronics. *Sci. Rep.* **2016**, *6*.
165. Starliper, N.; Mohammadzadeh, F.; Songkakul, T.; Hernandez, M.; Bozkurt, A.; Lobaton, E., Activity-Aware Wearable System for Power-Efficient Prediction of Physiological Responses. *Sensors-Basel* **2019**, *19* (3).
166. Dieffenderfer, J.; Goodell, H.; Mills, S.; McKnight, M.; Yao, S. S.; Lin, F. Y.; Beppler, E.; Bent, B.; Lee, B.; Misra, V.; Zhu, Y.; Oralkan, O.; Strohmaier, J.; Muth, J.; Peden, D.; Bozkurt, A., Low-Power Wearable Systems for Continuous Monitoring of Environment and Health for Chronic Respiratory Disease. *IEEE J. Biomed. Health. Inf.* **2016**, *20* (5).
167. King, R. C.; Villeneuve, E.; White, R. J.; Sherratt, R. S.; Holderbaum, W.; Harwin, W. S., Application of data fusion techniques and technologies for wearable health monitoring. *Med. Eng. Phys.* **2017**, *42*, 1-12.
168. Lee, H.; Choi, T. K.; Lee, Y. B.; Cho, H. R.; Ghaffari, R.; Wang, L.; Choi, H. J.; Chung, T. D.; Lu, N.; Hyeon, T.; Choi, S. H.; Kim, D.-H., A graphene-based electrochemical device with thermoresponsive microneedles for diabetes monitoring and therapy. *Nat Nano* **2016**, *11* (6), 566-572.

CHAPTER 3: Wearable Multiplexed Biosensor System Toward Continuous Monitoring of Metabolites

By Murat A. Yokus, Tanner Songkakul, Vladimir A. Pozdin, Alper Bozkurt, and Michael A. Daniele

*As published in *Biosensors and Bioelectronics*, 153, 112038 (2020)

Authorship contribution statement

Murat A. Yokus: Investigation, Methodology, Formal analysis, Visualization, Writing - original draft. **Tanner Songkakul:** Investigation, Software, Writing - review & editing. **Vladimir A. Pozdin:** Investigation, Writing - review & editing. **Alper Bozkurt:** Conceptualization, Writing - review & editing, Supervision, Funding acquisition. **Michael A. Daniele:** Conceptualization, Methodology, Writing - original draft, Supervision, Project administration, Funding acquisition.

3.1. Abstract

Comprehensive metabolic panels are the most reliable and common methods for monitoring general physiology in clinical healthcare. Translation of this clinical practice to personal health and wellness tracking requires reliable, non-invasive, miniaturized, ambulatory, and inexpensive systems for continuous measurement of biochemical analytes. We report the design and characterization of a wearable system with a flexible sensor array for non-invasive and continuous monitoring of human biochemistry. The system includes signal conditioning, processing, and transmission parts for continuous measurement of glucose, lactate, pH, and temperature. The system can operate three discrete electrochemical cells. The system draws 15 mA under continuous operation when powered by a 3.7 V 150 mAh battery. The analog front-end of the electrochemical cells has four potentiostats and three multiplexers for multiplexed and parallel readout from twelve working electrodes. Utilization of redundant working electrodes improves the measurement accuracy of sensors by averaging chronoamperometric responses

across the array. The operation of the system is demonstrated in vitro by simultaneous measurement of glucose and lactate, pH, and skin temperature. In benchtop measurements, the sensors are shown to have sensitivities of $26.31 \mu\text{A}\cdot\text{mM}^{-1}\cdot\text{cm}^{-2}$ for glucose, $1.49 \mu\text{A}\cdot\text{mM}^{-1}\cdot\text{cm}^{-2}$ for lactate, $54 \text{mV}\cdot\text{pH}^{-1}$ for pH, and $0.002 \text{ }^\circ\text{C}^{-1}$ for temperature. With the custom wearable system, these values were $0.84 \pm 0.03 \text{mV}\cdot\mu\text{M}^{-1}\cdot\text{cm}^{-2}$ for glucose, $31.87 \pm 9.03 \text{mV}\cdot\text{mM}^{-1}\cdot\text{cm}^{-2}$ for lactate, $57.18 \pm 1.43 \text{mV}\cdot\text{pH}^{-1}$ for pH, and $63.4 \mu\text{V}\cdot^\circ\text{C}^{-1}$ for temperature. This miniaturized wearable system enables future evaluation of temporal changes of the sweat biomarkers.

3.2. Introduction

Wearable health and wellness monitoring systems (wearables) are promising solutions to alleviate the burden of chronic diseases on the healthcare system by eliminating patient's dependence on bulky and expensive lab equipment for point-of-care testing and diagnosis. Chronic diseases, such as cardiovascular disorders, cancer, obesity, and diabetes, are projected to account for almost 75% of all deaths worldwide ¹. The development and progression of chronic diseases are dependent on dietary, activity, and metabolic patterns ². Integrating wearables into health and wellness regimens can aid in early diagnosis or management of these diseases. To this end, wearables may improve patient health by providing continuous streams of physiological data to healthcare providers to track biomarkers and quickly identify anomalous or pathological patterns.

Long-term monitoring of metabolic biomarkers is one way of benchmarking general patient wellness. Glucose, oxygen, pH, and lactate are some of the metabolic biomarkers. When monitored continuously, these biomarkers can give insights regarding abrupt or chronic changes of physiology ³. For example, during intense exercise, metabolic production of energy switches from aerobic to anaerobic processes, resulting in lactate accumulation in the blood ⁴. Insufficient supply of glucose or impaired clearance of lactate may jeopardize the viability of many organs and

result in emergence of various symptoms that may affect the daily life such as exhaustion, cramps, rapid heart rate, shortness of breath, and rapid decrease in blood pH levels ⁵. Therefore, continuous monitoring of these biomarkers may provide longitudinal assessment of the patient's health or real-time actionable information for the healthcare provider.

Although continuous monitoring of metabolic biomarkers can provide new medical insights, clinical characterization of biomarkers traditionally requires expensive equipment, skilled technicians, and long turnaround time (hours or days) with very poor temporal resolution ⁶; however, with the advent of point-of-care (PoC) devices (*e.g.*, i-STAT®, Abbott), blood metabolite levels can be measured within a few minutes with a single blood draw volume of about 65-95 μL ⁷ or even less today (<5 μL). PoC devices enable discrete sampling of biomarker levels; however, they cannot measure abrupt or unforeseen fluctuations between discrete measurement times. Current continuous glucose monitoring devices overcome this issue by monitoring the analyte levels from a few weeks (Dexcom G6® and Abbott FreeStyle Libre®) up to three months (Senseonics Eversense®), but they are invasive systems requiring the insertion of a subcutaneous needle or surgical implant ⁸⁻⁹.

In the recent decade, a shift toward non-invasive metabolite and electrolyte sensors, based on sweat analysis, has been reported because conventional blood tests for analyzing glucose and lactate levels are invasive and painful ¹⁰⁻¹². Sweat offers non-invasive and pain-free assessment of biomarkers of human metabolism. Sweat contains biologically relevant ions (*e.g.*, Na^+ , Cl^- , K^+ , and NH_4^+), small molecules (*e.g.*, ethanol, glucose, lactate, and urea), and small proteins ¹³⁻¹⁶. Sweat based sensors have been developed for detection of ethanol ¹⁷, glucose ¹⁸, pH and calcium ¹⁹, and lactate ¹⁴. For example, lactate in sweat was studied for the characterization of physiological performance, pressure ischemia, cystic fibrosis, and panic disorder ²⁰⁻²¹. Despite the ongoing

debate regarding the exact correlation between sweat and blood metabolites ²²⁻²³, there have been recent reports illustrating the correlation between sweat and blood glucose concentrations ^{18, 24-26}. Therefore, sweat may present an alternative way of continuous monitoring of overall physiological condition.

Wearable system integration and redundancy are major technical hurdles. First, most reports demonstrate sensors for single analyte detection, which may be insufficient to evaluate the overall health condition. These sensors use a single working electrode, which results in poor reliability due to fundamental sensor failure, sensor delamination from skin surface, or cessation of sweating where the sensor is in contact with the skin. Second, the best performing sensors are demonstrated with benchtop hardware, but they are rarely demonstrated as wearable system-level solutions. To date, there are a few emerging examples of fully-integrated wearables for sweat analysis ^{25, 27-31}. These systems monitor levels of sweat metabolites and electrolytes along with additional sensors, such as sweat rate, blood oxygenation, or ECG. The systems use either electrochemical or colorimetric detection techniques for quantification of biomarkers. Selected studies are summarized in **Supplementary Table S3.1**. A common feature of these systems, with one exception ²⁵, is that they have a single sensing electrode per analyte. This lack of redundancy may yield imprecise or inaccurate results due to sensor-to-sensor variation and operating conditions, which is very common in enzymatic electrochemical sensors used in wearables.

To build on the groundbreaking work by the Heikenfeld, Javey, Lee, and Gao research teams, developing a system with an electrode array for multiple analyte detection and redundancy may mitigate signal reliability issues. First, electrode arrays can be functionalized with various recognition elements so that multiple concurrent tests can be performed. Second, the precision of sensor output can be improved by running simultaneous measurements across multiple electrodes

or by including functionalized and non-functionalized electrodes (*i.e.*, positive and negative controls) to subtract the effect of common interferences. Last, multi-biasing can be applied to detect analytes with different redox potentials. However, to provide these benefits, the operation of electrode arrays requires a next-generation of miniaturized and multiplexed electronic hardware.

Accordingly, the use of electrode arrays for the detection of multiple analytes requires a system with signal conditioning modules (biasing, filtering, and amplification) and multiplexing capabilities for each type of sensor. Many single analyte (single electrode) detection systems have been reported, they include custom-designed potentiostats for electrochemical detection of metabolites, heavy metals, drugs, and DNA molecules for applications, such as cellular microphysiometry, wearable sensing, and point-of-care sensing (**Supplementary Table S3.2**)³²⁻³⁴. These systems were able to perform electrochemical techniques, such as chronoamperometry, cyclic voltammetry, and square wave voltammetry. Fewer reports have designed systems for multiplexed analyte detection. These designs used either a separate readout unit for each working electrodes³⁵⁻³⁷ or multiplexing between an array of working electrodes³⁸⁻³⁹ (**Supplementary Figure S3.1**). A separate readout unit for each working electrodes offers rapid measurement because of simultaneous measurement functionality but requires a large circuit area. The latter approach uses multiplexing scheme to read from each individual electrode results in an area efficient design, but with a compromise of reduced sampling rate as it scans through an entire array of electrodes. To overcome some of these challenges, a hybrid multiplexing topology was proposed⁴⁰⁻⁴¹ (**Supplementary Figure S3.1d**), providing multiplexing and parallelization that results in both reduced circuit area and improved real-time performance. Consequently, a miniaturized and inexpensive hybrid-multiplexing system would enable simultaneous detection of multiple analytes as well as multiplexed reading from redundant electrodes.

Herein, we report an array-based flexible sensor platform integrated with a low-cost multiplexing system for simultaneous detection of glucose, lactate, pH, and temperature. The array of electrodes was fabricated on a flexible thin polymeric film and functionalized via selective electrodeposition. The wearable hardware is a miniaturized and inexpensive stand-alone system, which is fabricated with commercially available discrete components. The custom system consists of analog front-end designs for pH and temperature sensors. It also includes potentiostats along with multiplexers to record from twelve working electrodes designed for glucose and/or lactate sensing. The multiplexing system along with the flexible sensing array presents another step toward an on-body solution for continuous monitoring of metabolic biomarkers.

3.3. Materials and Methods

3.3.1. Fabrication of Flexible Electrode Array

A more detailed fabrication procedure is provided in the supplementary text. Briefly, polydimethylsiloxane (10:1 ratio; Sylgard 184, Dow Corning) was spin-coated on a 100 mm glass wafer as a sacrificial layer. The PDMS film was cured at 70°C for 1.5 h in a vacuum oven. A 50 μm thick polyimide (PI) film was temporarily adhered to the PDMS coated wafer. The wafer was cleaned with acetone and isopropyl alcohol. A Cr/Au thin film (20 nm/300 nm) was deposited on the PI film by DC sputtering. The Cr/Au thin film was patterned by photolithography and wet etching. The conductive traces were encapsulated by spin coating of a positive photoresist (Microposit® S1813). The electrode areas and the pads were exposed by developing the photoresist layer. Additional details are provided in **Supplementary Text 3.6.1.3** and **Supplementary Figure S3.2**.

3.3.2. Functionalization of the Flexible Electrode Array

(i) *Electrodeposition of gold nanoparticles.* The surface of planar gold electrodes was cleaned in 50 mM H₂SO₄ solution (product #258105, Sigma-Aldrich) using cyclic voltammetry method from -0.4 to 1 V at a scan rate of 100 mV·s⁻¹ for 10 cycles. An aqueous solution of 2 mM HAuCl₄ (product #254169, Sigma-Aldrich) in 2 M H₂SO₄ (product #258105, Sigma-Aldrich) was prepared. The electrode was dipped in the prepared solution. Gold nanoparticles (AuNPs) were electrodeposited on bare gold electrode surface using chronoamperometric method. The deposition was performed for 15 min at -0.1 V with an external Pt counter electrode and an Ag/AgCl reference electrode (**Supplementary Figure S3.3a**). AuNPs deposited electrodes were used for glucose and lactate sensors.

(ii) *Electrodeposition of Prussian blue.* An aqueous solution of 100 mM KCl (product #746436, Sigma-Aldrich), 2.5 mM FeCl₃ (product #97064-656, VWR), and 2.5 mM K₃Fe(CN)₆ (product #97062-260, VWR) in 100 mM HCl (product #AAAL13091, VWR) was prepared. The AuNPs deposited gold electrode was dipped into the solution. Prussian blue was electrodeposited by cyclic voltammetry method from 0 to 0.5 V at a scan rate of 20 mV·s⁻¹ with an external Pt counter electrode and an Ag/AgCl reference electrode (**Supplementary Figure S3.3c**).

(iii) *GOx immobilization.* 5 mg·mL⁻¹ exfoliated graphite (product #282863, Sigma-Aldrich) solution was prepared in 1X phosphate-buffered saline (PBS) (product #BP2944, Fisher Scientific). The exfoliation process was completed using an ultrasonic bath (product #15337410, Fisher Scientific) for 1.5 h. The exfoliated graphite solution was mixed with GOx (50 mg·mL⁻¹, product#G7141, Sigma-Aldrich) and bovine serum albumin (BSA) (10 mg·mL⁻¹, product #0332, VWR). GOx/BSA/exfoliated graphite (0.5 μL) was drop-cast on the Prussian blue coated (4 cycles) electrode. The electrodes were kept in ambient temperature for 30 min for drying.

Glutaraldehyde solution (0.5 μL of 2 wt. %; product #TC0067, VWR) was drop-cast on the electrode and kept in the fridge (4°C) for drying. Afterwards, 0.8 μL of 0.5 wt. % Nafion® (product #70160, Sigma-Aldrich) was drop-cast on the electrode and dried at room temperature.

(iv) *LOx immobilization.* A solution of LOx (50 $\text{mg}\cdot\text{mL}^{-1}$, product#E2030703P1, Gwent Group) and BSA (10 $\text{mg}\cdot\text{mL}^{-1}$) was prepared in 1X PBS. LOx and BSA solution (0.4 μL) were drop casted on the Prussian blue coated (20 cycles) planar gold electrode. The electrodes were dried at room temperature for 30 min. Glutaraldehyde solution (0.4 μL of 2 wt. %) was drop-cast on the electrode and kept at 4°C until it was tested. Nafion® (0.8 μL of 0.5 wt. %) was drop-cast on the electrode and dried at room temperature. The exfoliated graphite was not used in fabrication of the lactate sensor because its incorporation did not improve the sensitivity of the sensor according to benchtop analysis (**Supplementary Figure S3.4b**).

(v) *Electrodeposition of polyaniline.* An aqueous solution of 0.1 M aniline (product#242284, Sigma-Aldrich) in 1 M HCl was prepared. Polyaniline (PANI) was deposited on the planar gold electrode by cyclic voltammetry method by sweeping the potential from -0.2 to 1 V at a scan rate of 100 $\text{mV}\cdot\text{s}^{-1}$ for 30 cycles with an external Pt counter electrode and an Ag/AgCl reference electrode (**Supplementary Figure S3.3b**).

(vi) *Encapsulation of temperature sensor.* The surface of the temperature sensor was exposed by patterning in the fabrication process. Its surface can be coated with polymeric films to control its thermal properties. In our case, the encapsulation of the temperature sensor was made using liquid bandage spray (Walgreen's).

(vii) *Fabrication of reference electrode.* The reference electrodes of glucose, lactate, pH sensors were fabricated by drop casting an Ag/AgCl ink (product #C2130809D5, Gwent Group) on the planar gold electrodes. The electrodes were subsequently cured at 80°C for 15 min.

(viii) *Selective functionalization of the electrodes.* Electrodeposition is a technique for selective deposition of various materials on a single platform with minimal cross-contamination. We used electrodeposition of AuNPs and Prussian blue (PB) for fabrication of glucose and lactate sensors. Similarly, polyaniline (PANI) electrodeposition was carried out for fabrication of pH sensors. The selective functionalization of the flexible array started with the electrodeposition PANI on the working electrode of the pH sensor. Then, the sample was cured at 80°C for 5 min. PANI was chosen due to its surface sensitivity to protonation in different pH solutions. This step was followed with the electrodeposition of AuNPs on the planar gold electrode surface (*i.e.*, working electrodes of glucose and lactate sensors). Afterwards, PB was electrodeposited on the AuNPs electrodes, and the sample was cured at 80°C for 45 min. PB is selected due to its high catalytic activity towards hydrogen peroxide, which is a byproduct of the reaction between glucose oxidase-glucose or lactate oxidase-lactate. Afterwards, an Ag/AgCl ink was drop casted on the reference electrodes of the pH, glucose, and lactate sensors. The sample was cured at 80°C for 15 min. Later on, the working electrode surfaces of glucose and lactate sensors were functionalized with GO_x and LO_x enzyme mixtures, respectively. Chemical crosslinking of the enzymes to bovine serum albumin (BSA) was performed with 2% glutaraldehyde solution. Finally, a 0.5% Nafion® film was drop-casted on top of the working electrodes as encapsulation layer. The samples were stored at 4°C when not in use.

3.3.3. Characterization of the Flexible Sensor Array

(i) *Characterization of electrodeposited gold nanoparticles.* The characterization of electrodeposited porous gold electrodes was performed by electrochemical impedance spectroscopy (EIS) with a Gamry 600+ benchtop potentiostat. The electrodes were dipped into an aqueous solution of 5 mM K₃Fe(CN)₆ in 1X PBS. EIS measurement was performed with an

external Pt counter electrode and an Ag/AgCl reference electrode from 1 Hz to 5 MHz ($V_{AC}=10$ mV and $V_{DC}=0$ V). Cyclic voltammetry measurements were carried out in an aqueous solution of 10 mM $K_3Fe(CN)_6$ in 1X PBS from -0.3 to 0.9 V with a scan rate of $100\text{ mV}\cdot\text{s}^{-1}$ with an external Pt counter electrode and an Ag/AgCl electrode. Scanning electron micrographs were obtained with an FEI Verios 460L.

(ii) *Characterization of glucose and lactate sensors.* Chronoamperometric characterization of glucose and lactate sensors were performed with a Gamry 600+ benchtop potentiostat at -0.1 V in 1X PBS solution. A conditioning step was performed at -0.1 V. A steady state current was obtained after 10 min. Measurements of glucose or lactate were made at 5 min intervals to ensure a homogenous solution. Chronoamperometric measurement were made at -0.1 V for 100 s.

(iii) *Characterization of pH and temperature sensors.* Open circuit potential measurements (OCP) in buffer solutions (pH = 4.0–8.0, Fisher Scientific) were performed with a benchtop Gamry 600+ potentiostat. The PANI deposited electrodes were dipped into the buffer solutions and OCP readings were carried out for 5 min. The characterization of the temperature sensor was performed on a hot plate. Resistance measurements were performed to calibrate the temperature sensor as the hot plate temperature was changed from 22°C to 45°C at a rate of $1^\circ\text{C}\cdot\text{min}^{-1}$. The temperature sensor was brought in contact with the surface of the hot plate. A K-type surface thermocouple with adhesive backing was adhered next to the sensor to measure the surface temperature of the hot plate. The temperature sensor was connected to source measure unit (B2902a, Keysight) for resistance measurement. A custom-designed LabVIEW script was used to measure the surface thermocouple temperature and the resistance change of the temperature sensor.

(iv) *Intraelectrode and interelectrode crosstalk study.* Intraelectrode crosstalk test was performed in aqueous solution of 5 mM $K_3Fe(CN)_6$ and 1 M KCl in 1X PBS. Four carbon-working

electrodes (product# RRPE1001C, PINE Research) were electrically connected to WE₁₋₁, WE₁₋₂, WE₁₋₃, and WE₁₋₄ of the first channel (WE_{x-y}, for x : 1,2,3 and y : 1,2,3,4, where x and y indicate the channel number and the working electrode number, respectively). The counter and reference electrode inputs of the potentiostat were connected to an external Pt counter electrode and an Ag/AgCl reference electrode. The carbon electrodes were conditioned in the same aqueous solution at -0.1 V. A steady state current was obtained after 30 min. A PANI coated carbon electrode and an Ag/AgCl reference electrode (PINE Research) were used as pH sensors. Afterwards, the intraelectrode crosstalk test was started. The reference and working electrode of the pH sensor were disconnected after 10 min. Similarly, WE₁₋₄, WE₁₋₃, and WE₁₋₂ were disconnected at 15, 20, and 25 minutes, respectively. The overall test was completed in 30 min.

For interelectrode crosstalk, new carbon electrodes were electrically connected to the WE₁₋₁, WE₂₋₁, and WE₃₋₁ of the first, second, and the third channels of the multiplexing system. The electrodes were then dipped into a similar aqueous solution and preconditioning step was completed at the same conditions as the intraelectrode crosstalk study. The interelectrode crosstalk study was performed by disconnecting the reference and working electrode of the pH sensor after 10 min. Similarly, WE₃₋₁ and WE₂₋₁ were disconnected at 15 and 20 minutes, respectively. The overall test was completed in 25 min. The temperature sensor was not involved in the crosstalk test since its surface is encapsulated and thus insulated from crosstalk.

(v) *Off-body measurement of sampled sweat.* The off-body evaluation of the custom multiplexing system was performed in compliance with the protocol that was approved by the institutional review board at University of North Carolina, Chapel Hill (#18-0984). Three healthy subjects (1 female and 2 males), aged 18-35, were recruited from the North Carolina State University campus through word of mouth. All subjects gave written and informed consent before

participation in the study. The study was conducted at a constant workload on a cycle ergometer (Life Sciences ® 95Ri recumbent exercise bike). The power output was monitored through the cycle ergometer. For the constant workload exercise, the subjects exercised at 50 W for 5 min. The workload was increased to 150 W and the exercise was maintained at this workload for 20 min. Then, it was followed by cool-down at 50 W for 5 min. The cycling was kept at 60 rpm for all exercise levels. Sweat was collected in the 20 min intense exercise period by dragging a 1.5 mL microcentrifuge vial across the forehead of the subjects. Off-body measurement of the collected sweat samples were performed by the custom-designed multiplexing system. The system was also tested with a stabilized artificial sweat solution (product#1700-0020, Pickering Laboratories) as a reference. The artificial sweat solution includes 19 different amino acids, 4 metabolites (uric acid, urea, lactic acid, and ammonia), and 8 different minerals. For our measurements, 200 μ M glucose was added to the artificial sweat solution since it did not contain glucose. The concentration of glucose and lactate in the collected and artificial sweat was measured using colorimetric glucose (Amplex™ Red Glucose Assay Kit, product#A22189, ThermoFisher Scientific) and lactate (Amplite™ L-Lactate Assay Kit, product#13815, AAT Bioquest) assay kits. Black non-binding (product# 07000634, Fisher Scientific) and white medium binding (product# 07000097, Fisher Scientific) 96 well plates were used for glucose and lactate assays, respectively.

3.4. Results and Discussion

3.4.1. Design of Flexible Sensor Array and Custom Multiplexing System

The design of the flexible sensor array (length: 28 mm, width: 22 mm) is shown in **Figure 3.1**. The sensor was fabricated on a polyimide film to form a flexible sensor. The sensor is comprised of a layered structure (**Figure 3.1a**): polyimide (bottom), metallization (intermediate), and encapsulation (top) layers. The metallization layer allows the various sensors along with their

corresponding electrical contact pads to be easily inserted into a surface mount connector on the custom-built printed circuit board (PCB) (**Figure 3.1b**). The flexible sensor array consists of a total of twelve (12) working electrodes along with three reference and counter electrodes for glucose, lactate, and background current (**Supplementary Figure S3.6a**). The array also has a serpentine resistive temperature sensor and a pair of electrodes for pH sensing (**Figure 3.1c**). Each channel has a three-electrode electrochemical cell configuration with an array of four working electrodes (WE_{1-1} to WE_{1-4} , WE_{2-1} to WE_{2-4} , and WE_{3-1} to WE_{3-4}), a reference and a counter electrode. The working electrodes in each individual channel have been either functionalized for amperometric detection of glucose and lactate or left blank for background current detection. The four working electrodes in each channel are connected to a potentiostat through a multiplexer in the custom-designed system (**Figure 3.1d** and **Supplementary Figure S3.6a**).

A four-layer PCB was designed to interface with the flexible sensor (**Figure 3.1b**). The system consists of six different units: system-on-chip (a microcontroller with wireless transceiver), three multiplexing units for glucose and lactate sensors, four potentiostats, a pH-sensing unit, a temperature-sensing unit, and a power management unit (**Figure 3.1d**). The system-on-chip (SoC) is a Bluegiga BLE113 Bluetooth® Smart Module and provides the processing and communication capability. The SoC coordinates proper switching between working electrodes, data processing, and wirelessly transmits to a data aggregator, such as a smartphone or tablet via Bluetooth Low Energy (BLE). The multiplexers are connected to three potentiostats (LMP91000, Texas Instruments). To measure different analyte concentrations, the three potentiostats are configured as three-lead electrochemical cells, one potentiostat for each of the analyte channels. Each analyte channel contains four working electrodes, one reference and one counter electrode (**Supplementary Figure S3.6a**). The fourth potentiostat is used for generating 1 V virtual ground.

The four working electrodes of each potentiostat are connected to an 8-channel single-pole, single-throw (SPST) switch (MAX14662, Maxim Integrated) to multiplex between the four working electrodes. In total, twelve I²C controlled single pull single throw (SPST) switches can be toggled to connect each of the four electrodes on each analyte channel to the potentiostat individually. Twelve additional SPST switches connect each of the electrodes to a virtual ground, which matches the virtual ground internal to the potentiostat. This creates a software-controlled make-before-break single-pull double-throw (SPDT) switch for each working electrode wherein each working electrode is connected to the virtual ground when not in use (**Supplementary Figure S3.1d** and **Figure S3.6b**). This is necessary because multiplexing with break-before-make SPDT switches or simply using SPST switches between the working electrodes and the potentiostat creates intermittent biasing, which disrupts the electrochemical processes of the cell ⁴². The LMP91000 also contains a transimpedance amplifier with adjustable gain, which allows for measurement of very high and very low analyte concentrations without saturation or inadequate precision (**Supplementary Table S3.3** and **Supplementary Figure S3.7a-b**). The pH-sensing unit (LMP91200, Texas Instruments) performs the pH measurement between a reference electrode and pH indicator electrode. The temperature-sensing unit measures temperature via a voltage divider (10 k Ω). The potentiostat outputs, pH, and temperature measurements are all read by the microcontroller via 16-bit analog-to-digital converters (ADS1115, Texas Instruments). The power management circuit of the system starts with a 3.7 V, 150mAh lithium-polymer battery to power the device. This battery can be charged by a 5 V external power supply (USB) through a battery management and a fuel gauge integrated circuit (MCP73831, Microchip). To increase power efficiency, switching regulators are utilized for the voltage rails of the device. The battery voltage is regulated to 3.3 V by a step down converter (TPS62162, Texas Instruments) in order to power

the microcontroller and peripherals. The 3.3 V rail is boosted up to 5 V by a boost converter (TPS61222, Texas Instruments). The 5 V rail serves as a reference for the potentiostat and increases range of voltage sweeps. A pushbutton controller (MAX16054, Maxim Integrated) allows the user to power the device on and off.

Overall, the system can perform concurrent cyclic voltammetry (CV) sweeps on all 12 channels between -1.2 V and 1.2 V at sweep rates between 10 $\text{mV}\cdot\text{s}^{-1}$ and 1000 $\text{mV}\cdot\text{s}^{-1}$ with a 0.1 V step size, while simultaneously measuring pH and temperature. Alternatively, the system can carry out concurrent chronoamperometric measurement of all 12 channels at a sampling rate of 10 Hz, again while measuring pH and temperature. The system is powered by a 3.7 V 150 mAh battery and consumes around 15 mA when actively measuring analyte concentrations and transmitting data, giving a battery life of 9.9 hours for continuous measurement and wireless data transmission. The system consumes 60 μA when in idle mode, allowing for a drastic reduction in average power consumption for applications in which intermittent sampling is appropriate. For example, reducing the sampling rate by sampling for 30 seconds and then entering idle mode for 10 minutes decreases the average current consumption to 0.25 $\text{mA}\cdot\text{s}^{-1}$ and extends battery lifetime to 600 hours. The final system has a diameter of 40 mm and a thickness of 9 mm. The custom multiplexing potentiostat system costs $\$92$ each at prototype quantities, with significant cost reduction possible at higher production quantities. The summary of specifications of the custom-designed potentiostat, the specifications of the components used in the custom system is provided in **Supplementary Table S3.3-S3.5** and **Supplementary Figure S3.8, S3.9**.

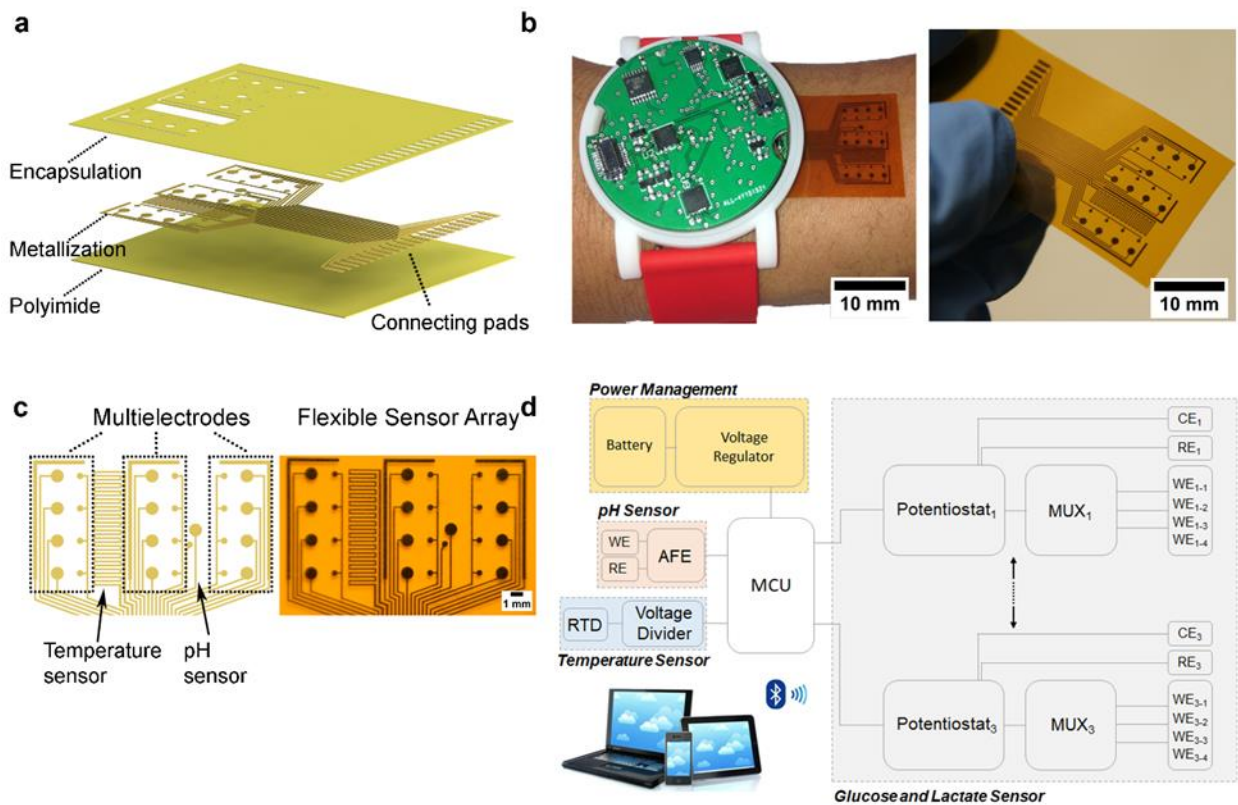


Figure 3.1. Images and system block diagram of the custom multiplexing system along with a flexible sensor array. **(a)** Exploded view of the flexible sensor array showing the polyimide (bottom), metallization (intermediate), and encapsulation (top) layers. **(b) Left:** Picture of wrist-worn, wearable multiplexing system in a 3D printed watch enclosure for demonstration purposes only. **Right:** Picture of the flexible sensor array. **(c) Left:** CAD design of the flexible sensor array. **Right:** Fabricated flexible sensor array. **(d)** System block diagram of the custom multiplexing sensor system.

3.4.2. In-vitro Characterization of Glucose, Lactate, pH, and Temperature Sensors

The concentration of glucose and lactate in sweat depends on various factors such as sampling site, sampling techniques, participant's age, diet, degree of acclimation, gender, race, and activity levels⁴³. Sweat concentrations are different from blood concentrations and have been reported to be 5.6 μM to 2.2 mM for glucose and 3.7 mM to 50 mM for lactate^{16, 44-45}. Median concentrations for glucose and lactate are reported to be 170 μM and 14 mM, respectively⁴⁵. A wide working range, fast response, and interference-free operation is required for continuous monitoring of sweat metabolites.

The fabrication of glucose and lactate sensors started with the electrodeposition of gold nanoparticles on the planar gold electrodes (**Supplementary Text 3.6.1.4, Supplementary Figure S3.3a and Figure S3.10**). 15 min gold deposition time was used because the deposition time was sufficient to cover the surface of the bare gold electrodes. After 15 min of the porous gold deposition, the electrochemically active surface area increased by 1.38 times (**Supplementary Table S3.6**), which decreased the DC electrode impedance by two orders of magnitude (**Supplementary Figure S3.11a**) and resulted in 1.36 times increased current (**Supplementary Figure S3.11b-c**).

We first characterized the sensors using a benchtop potentiostat. The chronoamperometric response of glucose and lactate sensors is shown in **Figure 3.2a** and **Figure 3.2c**, respectively. The response of glucose and lactate sensors were separately recorded using a benchtop potentiostat at a constant potential of -0.1 V vs. an Ag/AgCl reference electrode for 100 s in 1X PBS solution. The operation potential was selected based on electro-oxidation of glucose and lactate by the fabricated flexible sensor during cyclic voltammetry tests. When the sensor is exposed to glucose or lactate in the solution, GOx or LOx enzymes catalyze the oxidation of metabolites and generates gluconic acid and pyruvate, respectively⁴⁶. Both reactions generate hydrogen peroxide (H_2O_2) that is reduced by the Prussian blue mediator, leading to a change in the cathodic current⁴⁷. The cathodic detection of H_2O_2 at low potentials eliminates interferences from other oxidizable metabolites in sweat (*e.g.*, uric acid and ascorbic acid)^{43, 48-49}. The chronoamperometric response of the glucose and lactate sensors to increasing glucose and lactate concentrations are shown in **Figure 3.2a-b** and **Figure 3.2c-d**. The linear range of the sensors were $60\ \mu\text{M}$ to $1000\ \mu\text{M}$ and $5\ \text{mM}$ to $20\ \text{mM}$ for glucose and lactate sensors, respectively. While the linear range of the lactate sensors covers both blood and interstitial fluid levels, the linear region of the lactate sensor could

be further extended to cover sweat levels by decreasing the diffusion coefficient of the lactate through the encapsulation layer (*i.e.*, selection of proper encapsulation layer material with a different substrate permeability), selecting a different electron-transfer system, or increasing the thickness of the encapsulation layer⁵⁰⁻⁵⁴. Such improvements may come at the cost of reduced signal magnitude.

The sensitivity of the glucose and lactate sensors were $26.31 \pm 0.63 \mu\text{A}\cdot\text{mM}^{-1}\cdot\text{cm}^{-2}$ (or $0.186 \pm 0.004 \mu\text{A}\cdot\text{mM}^{-1}$) and $1.49 \pm 0.20 \mu\text{A}\cdot\text{mM}^{-1}\cdot\text{cm}^{-2}$ (or $0.011 \pm 0.002 \mu\text{A}\cdot\text{mM}^{-1}$), respectively. The specifications of the sensors fabricated in this study fall within specifications of the previously reported glucose and lactate sensors that are characterized by a benchtop potentiostat (**Supplementary Table S3.7 and S3.8**). The differences in fabrication methods (*e.g.*, drop-casting, layer-by-layer deposition, or electrodeposition), materials (*e.g.*, electrode, nanoparticles, and encapsulating film), test conditions (*e.g.*, applied potential, pH of test solution, stirring effect) results in sensors with varying specifications. The storage stability of the sensors was tested by keeping the fabricated sensors in a sealed petri dish at 4 °C in a fridge. The sensitivity of the glucose and lactate sensors decreased to $8.96 \pm 0.65 \mu\text{A}\cdot\text{mM}^{-1}\cdot\text{cm}^{-2}$ (or $0.064 \pm 0.005 \mu\text{A}\cdot\text{mM}^{-1}$) and $0.23 \pm 0.08 \mu\text{A}\cdot\text{mM}^{-1}\cdot\text{cm}^{-2}$ (or $0.002 \pm 0.001 \mu\text{A}\cdot\text{mM}^{-1}$) after 10 days storage, respectively (**Supplementary Figure S3.5**).

Sweat pH varies between 4.0 to 8.0 during an intense exercise⁵⁵⁻⁵⁶. In our flexible sensor array, we electrodeposited electrically conductive polyaniline polymer as a pH sensor (**Supplementary Figure S3.3b**), whose protonation strongly depends on the oxidation state of the polymer and the pH of the aqueous solution⁵⁷. The pH sensor was calibrated with standard buffer solutions (**Figure 3.2e**). The open-circuit potential of the sensor vs. printed Ag/AgCl reference electrode decreased in high pH buffer solutions due to the deprotonation of the polyaniline. The

sensitivity of the pH sensor was $54 \pm 3.61 \text{ mV} \cdot \text{pH}^{-1}$ (**Figure 3.2f**). The sensitivity of the PANI pH sensor falls between the sensitivity range of other polymer or oxide-based pH sensors (40 to 61 $\text{mV} \cdot \text{pH}^{-1}$)⁵⁸⁻⁶⁰. The sensors showed good repeatability in successive measurements of pH in buffer solutions (**Supplementary Fig. S3.3d**).

Human skin temperature is dependent on body core temperature, ambient conditions, and exercise intensity, and it varies between roughly 25 to 40°C⁶¹⁻⁶². A skin conformable temperature sensor should be sensitive to the variations in skin temperature. The serpentine-shaped temperature sensor on the flexible sensor array (**Figure 3.1c**) is made of a thin chromium/gold layer, whose resistance varies with temperature (**Figure 3.2g,h**). As the temperature increases, the thermal vibrations of the atoms in the solid lattice increases (*i.e.*, phonons). The likelihood of electrons and phonons collision increases, resulting in a resistance increase. The temperature coefficient of resistance (α) of the sensor was calculated as $0.002 \text{ }^\circ\text{C}^{-1}$. The temperature coefficient values were similar to other thin-film-based (*e.g.*, platinum or gold) temperature sensors⁶³⁻⁶⁴.

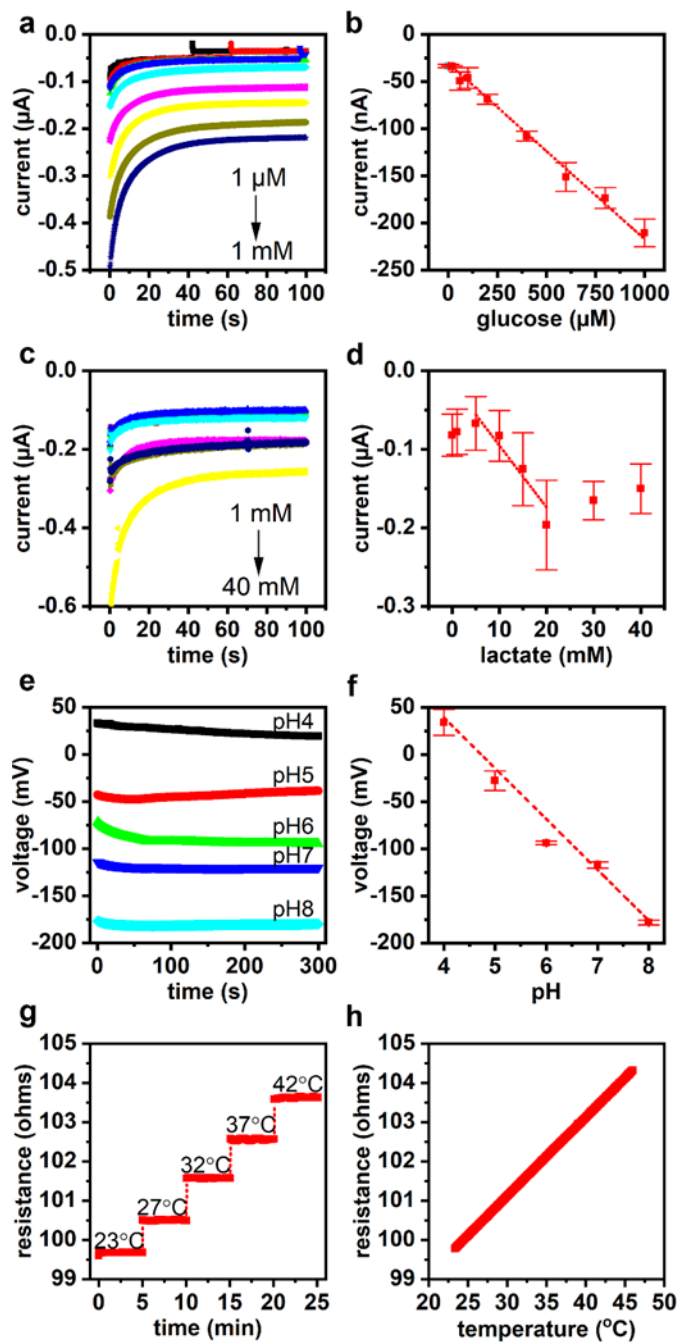


Figure 3.2. Characterization of the fabricated flexible sensor array with a benchtop potentiostat. Working electrode area: 0.0071 cm^2 . (a-d) Chronoamperometric responses of the glucose (a,b) and lactate (c,d) sensors with increasing glucose (0 to $1000 \text{ } \mu\text{M}$) and lactate (0 to 40 mM) concentration in 1X PBS solution ($n = 3$). Bias: -0.1 V , pH 7.4, a 21°C . (e-f) Open circuit potential response of the pH sensor for increasing pH levels ($n = 3$). (g-h) Resistance response of the temperature sensor to temperature changes ($22\text{-}45^\circ\text{C}$). The plots on the second column shows the corresponding calibration plots of the glucose, lactate, pH, and temperature sensors in the physiological relevant ranges.

3.4.3. System Validation of the Custom Multiplexing System

The custom system was validated using commercial electrodes as controls. First, cyclic voltammetry measurements of the ferricyanide/ferrocyanide redox reaction were performed to demonstrate the operation of the custom hardware. A carbon working electrode, an Ag/AgCl reference electrode, and a Pt counter electrode were used for all tests. The electrodes were submerged in an aqueous solution of 5 mM $\text{K}_3\text{Fe}(\text{CN})_6$ and 1 M KCl (**Figure 3.3e,f**). Similar cyclic voltammetry tests were also repeated with a benchtop potentiostat. The ferricyanide/ferrocyanide redox potentials and peak amplitudes obtained with the custom system and the benchtop potentiostat were identical (**Figure 3.3a,e**). In cyclic voltammetry experiments, the resolution of the applied bias in our system was set as a percentage of the reference voltage in the potentiostat. The resolution of the applied bias in the custom-designed potentiostat is 0.1 V, which is less than the resolution of the commercial benchtop potentiostat (0.2 mV) (**Supplementary Table S3.3**). The resolution of the applied bias could be further increased by decreasing the reference voltage of the potentiostat. The peak current of oxidation and reduction was proportional to the square root of the scan rate, indicating that the surface reaction on the electrode is reversible and diffusion-controlled (**Figure 3.3b,f**). Similarly, we verified the chronoamperometric response of our custom system by performing standard enzymatic glucose and lactate assays. The enzymatic oxidation of glucose (1 μM to 600 μM) and lactate (1 mM to 40 mM) were measured in corresponding enzyme and mediator solutions (*i.e.*, $\text{GO}_x + \text{K}_3\text{Fe}(\text{CN})_6$ in 1X PBS or $\text{LO}_x + \text{K}_3\text{Fe}(\text{CN})_6$ in 1X PBS) (**Figure 3.3g,h** and **Supplementary Figure S3.12c,d** and **Figure S3.12g,h**). The same experiments were also repeated with the benchtop potentiostat (**Figure 3.3c,d** and **Supplementary Figure S3.12a,b** and **Figure S3.12e,f**). Our custom-designed system was able to differentiate the addition of glucose or lactate into the cell, similar to the benchtop potentiostat. It is important to note that the

magnitude of the cathodic current decreased as we increased the concentration of glucose or lactate in the test solution, which was different from the response when the enzyme was functionalized on the electrode surface (**Figure 3.2a and 3.2b**). This different trend may be attributed to the electron transport differences between the enzyme and electrode surface when they are either immobilized on an electrode surface or dispersed in an aqueous solution. Since glucose does not dissociate into ions in water, increasing the glucose concentration in the test solution and conformational changes of the protein make it even more difficult to transfer the electrons from the redox site of the enzyme to the electrode surface.

It is crucial to have a crosstalk-free operation of glucose, lactate, pH, and temperature sensors fabricated as a part of the flexible sensor array. The intraelectrode crosstalk is defined as the interference between the four working electrodes for a given channel. Similarly, the interelectrode crosstalk is defined as the interference between the working electrodes of the three separate channels. Thus, we performed intraelectrode and interelectrode crosstalk tests in an aqueous solution to investigate potential interference from surrounding electrodes. For the intraelectrode crosstalk test, four working electrodes (*i.e.*, commercial carbon electrodes) with shared common and reference electrodes of one potentiostat and pH electrodes were submerged into the test solution (explained in detail in Materials and Methods section). In case of the interelectrode crosstalk test, only the first working electrode of each channel, separate counter and reference electrodes, and the pH electrodes were submerged into the test solution. Only the first electrode of each channel is used because one working electrode is electrically connected to a potentiostat per channel for a given time. After the signal acquisition was started, the electrodes were disconnected sequentially to observe if there would be any shift in baseline current. Any shift in the baseline current would indicate a possible crosstalk. It was demonstrated that disconnecting

each working electrode sequentially in the inraelectrode test did not cause any intermittent noise in the chronoamperometric readings of the surrounding electrodes since the working electrodes were connected to the virtual ground when they were not in use (**Figure 3.3i** and **Supplementary Figure S3.6a-b**). In the typical operation, such as inraelectrode switching, the SPDT multiplexer connects only one working electrode to the potentiostat with a working electrode bias of 1 V and all the others to the virtual ground of 1 V. Similarly, there was no interelectrode crosstalk observed (**Figure 3.3j**).

With the sensors characterized with the benchtop potentiostat in the Section 3.2, we proceeded to measure our sensors with the custom multiplexing system. The chronoamperometric responses of the glucose and lactate sensors were tested separately in the range of 0 to 1000 μM and 0 to 40 mM in 1X PBS, respectively (**Figure 3.4a and 3.4c**). The cathodic current increased with addition of glucose or lactic acid into the test solution. In the wearable system, the output of sensors were plotted in volts, which can be further converted to current using the **Supplementary Table S3.3**. The glucose sensor showed a linear response up to 1000 μM , while the lactate sensor showed a linear response up to 15 mM. The small variation of the linear region of the lactate sensor may be attributed to the process variability of the drop-casting method. The sensitivity of glucose and lactate sensors with the custom PCB was $0.84 \pm 0.03 \text{ mV} \cdot \mu\text{M}^{-1} \cdot \text{cm}^{-2}$ and $31.87 \pm 9.03 \text{ mV} \cdot \text{mM}^{-1} \cdot \text{cm}^{-2}$, respectively. The amperometric signal measured with the custom PCB system was noisier than the signal acquired by the benchtop potentiostat due to an advanced filtering in the benchtop potentiostat. Therefore, a moving average with a window size of 11 was applied to smooth the chronoamperometric data. To minimize the effect of sample-to-sample variation during the sensor fabrication caused by the electrodeposition, drop-casting, and the contribution of the other electrical interferences, the calibration graphs of the glucose and lactate sensor with the

custom system were plotted as voltage difference ($\Delta V = V_{0 \text{ mM}} - V_{\text{final concentration}}$) vs. concentration in **Figure 3.4b and 3.4d**. Similarly, **Figure 3.4e and 3.4f** show the voltage output of the pH sensor in the buffer solutions from pH 4 to 8. The pH response of the sensors decreased as the test solution became more basic, similarly to the benchtop system measurements ($\Delta V = V_{\text{final pH}} - V_{\text{pH4}}$). The sensitivity of the sensor with the custom system was calculated as $57.18 \pm 1.43 \text{ mV} \cdot \text{pH}^{-1}$. **Figure 3.4g and 3.4h** shows the response of the temperature sensor when the temperature was varied from 23 to 42°C. The sensitivity of the sensor with the custom system was calculated to be $63.4 \mu\text{V} \cdot \text{°C}^{-1}$ ($\Delta V = V_{23\text{°C}} - V_{\text{final temperature}}$).

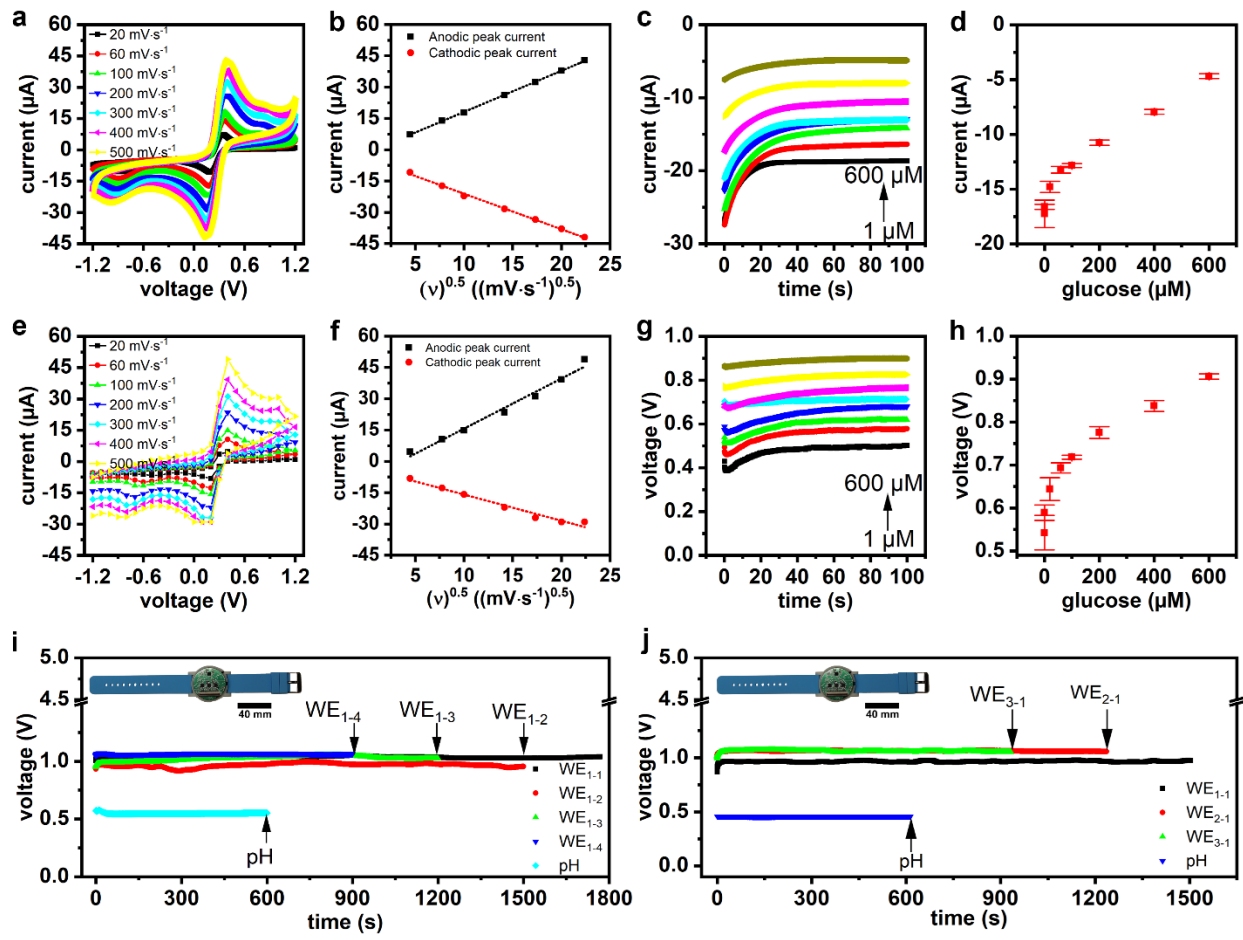


Figure 3.3. System validation of the custom multiplexing system. **(a, b)** Benchtop potentiostat cyclic voltammetry and peak current vs. square root of scan rate graphs in 5 mM $K_3Fe(CN)_6$ and 1 M KCl in 1X PBS. R^2 is 0.99 for both anodic and cathodic peaks. **(c, d)** Chronoamperometry measurements with a benchtop potentiostat in an aqueous solution of GO_x ($10 \text{ mg}\cdot\text{mL}^{-1}$) and $K_3Fe(CN)_6$ ($10 \text{ mg}\cdot\text{mL}^{-1}$) in 1X PBS solution ($n = 3$). Bias: -0.1 V , pH 7.4. **(e, f)** Custom system cyclic voltammetry and peak current vs. square root of scan rate graphs in an aqueous solution of 5 mM $K_3Fe(CN)_6$ and 1 M KCl in 1X PBS. R^2 is 0.98 and 0.97 for anodic and cathodic peaks, respectively. **(g, h)** Chronoamperometry measurements with the custom system in an aqueous solution of GO_x ($10 \text{ mg}\cdot\text{mL}^{-1}$) and $K_3Fe(CN)_6$ ($10 \text{ mg}\cdot\text{mL}^{-1}$) in 1X PBS ($n = 3$). Bias: -0.1 V , pH 7.4. **(i)** Intraelectrode crosstalk study within the same channel. “ WE_{1-1} , WE_{1-2} , WE_{1-3} , and WE_{1-4} ”: First, second, third, and fourth working electrodes of the first channel, respectively. **(j)** Interelectrode crosstalk study among different channels. “ WE_{1-1} , WE_{2-1} , and WE_{3-1} ”: The first working electrode of the first, second, and third channels. Each arrow on the graphs indicates the time when the given electrode is electrically disconnected.

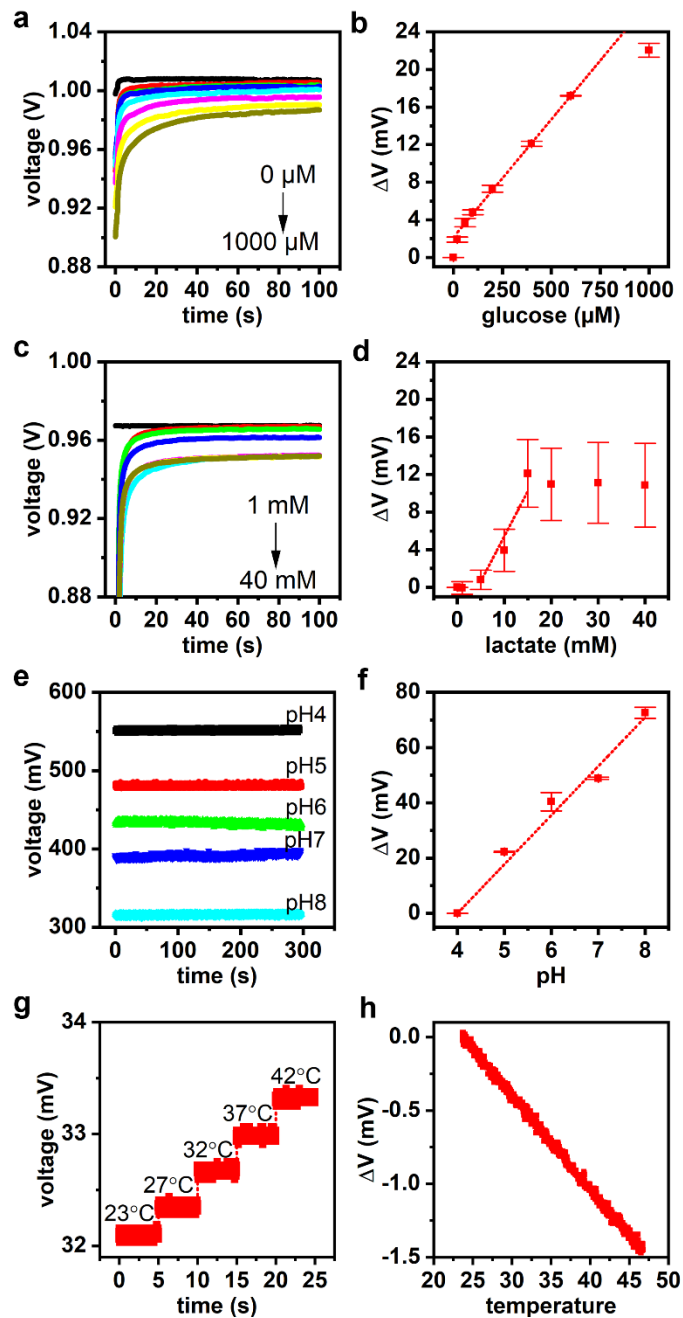


Figure 3.4. Characterization of the fabricated flexible sensor array with the custom multiplexing system. **(a-d)** Chronoamperometric responses of the glucose **(a,b)** and lactate **(c,d)** sensors for increasing glucose (0 to 1000 μM) and lactate (0 to 40 mM) concentrations in 1X PBS ($n = 3$). Bias: -0.1 V , pH 7.4. **(e)** Open circuit potential response of the pH sensor for increasing pH levels (4 to 8). **(d)** Voltage response of the temperature sensor to variations in temperature (23–42°C). **(e-g)** The corresponding calibration plots of the glucose, lactate, and pH sensors, respectively.

3.4.4. Simultaneous Measurement of Glucose, Lactate, pH, and Temperature

The multiplexing system with the flexible sensor array was evaluated by sequential addition of glucose and lactic acid into the test solution (sampling frequency=10 Hz). The full data was provided in **Supplementary Figure S3.13** and **Figure S3.14** for successive additions of 200, 400, and 600 μM of glucose and 5, 10, and 15 mM of lactic acid into the test solution with 5 min intervals. The unfiltered response of sensors to 400 μM glucose and 10 mM lactic acid additions is shown in **Figure 3.5a and 3.5b**, respectively.

The addition of glucose into the test solution resulted in a drop in the cathodic current in all working electrodes that were functionalized for glucose sensing (WE₁₋₁ to WE₁₋₄). The output of the four glucose sensors were slightly different due to the variations in their fabrication processes. It was reported that use of multiple (redundant) electrodes for sensing of a specific analyte improved the accuracy, consistency, and reliability of measurement in amperometric measurements⁶⁵⁻⁶⁷. These improvements were achieved by either combining the mean or median of multiple WEs outputs or applying intelligent algorithms with time-varying weight factors. In our case, the effect of sensor-to-sensor variation on the determination of the concentration of glucose in the solution was minimized by averaging the responses of the four glucose sensors. The concentration of the glucose in the solution was calculated using the voltage output of the system and the sensitivity of the glucose sensor. The baseline current did not change for the blank electrodes (WE₂₋₁ to WE₂₋₄), lactate sensors, and pH sensors after the glucose addition. During testing, the addition of the test solution created noise because of the disruption of the electrode-electrolyte interface (grey regions in **Figure 3.5a and 3.5b**). The responses of all sensors to 10 mM lactic acid solution are shown in **Figure 3.5b**. The lactate sensors (WE₃₋₁ to WE₃₋₄) responded to the lactic acid addition with a decrease in cathodic current. The concentration of the lactic acid

in the solution was calculated using the average output of the lactate sensors. The calculated lactate concentration showed an increase in lactic acid levels. Furthermore, the addition the lactic acid into the solution lowered the overall pH of the solution, which was detected with a sharp peak in the output of the pH sensor. This caused the calculated pH values to be close to zero upon the initial addition of lactic acid, but a steady-state level was reached (pH 4.8) as the lactic acid diffused through the solution. This sudden change may be due to the voltage change across the reference electrode with the lactic acid addition, which could be minimized by encapsulating the reference electrode with NaCl loaded polymeric membranes ⁶⁸. Similar pH sensor trend was observed for 5 and 15 mM lactic acid additions as well (**Supplementary Figure S3.13** and **Fig. S3.14**). The output of the glucose sensors and blank working electrodes slightly changed by the lactic acid addition. The change in the response of the glucose sensor may be attributed to variation in electrochemical activity of the Prussian blue mediator and glucose oxidase in acidic solutions. The lactic acid addition created significant noise in WE₁₋₄ (glucose sensor). However, the effect of the lactic acid addition on the calculation of glucose concentration in the solution was minimized by averaging the responses of four glucose sensors (WE₁₋₁ to WE₁₋₄). The output of the temperature sensor did not change throughout the testing. The grey highlighted regions in **Figure 3.5** shows generated noise due to motion artifacts. The motion artifacts were introduced due to the variations of the speed and the volume of the pipetting as well as the sensor movement throughout the duration of the measurement. In wearable sweat sensing applications, the fluid management for the wearable sensor is not going to include pipetting volumes of analytes; therefore, this type of noise generation may not be experienced.

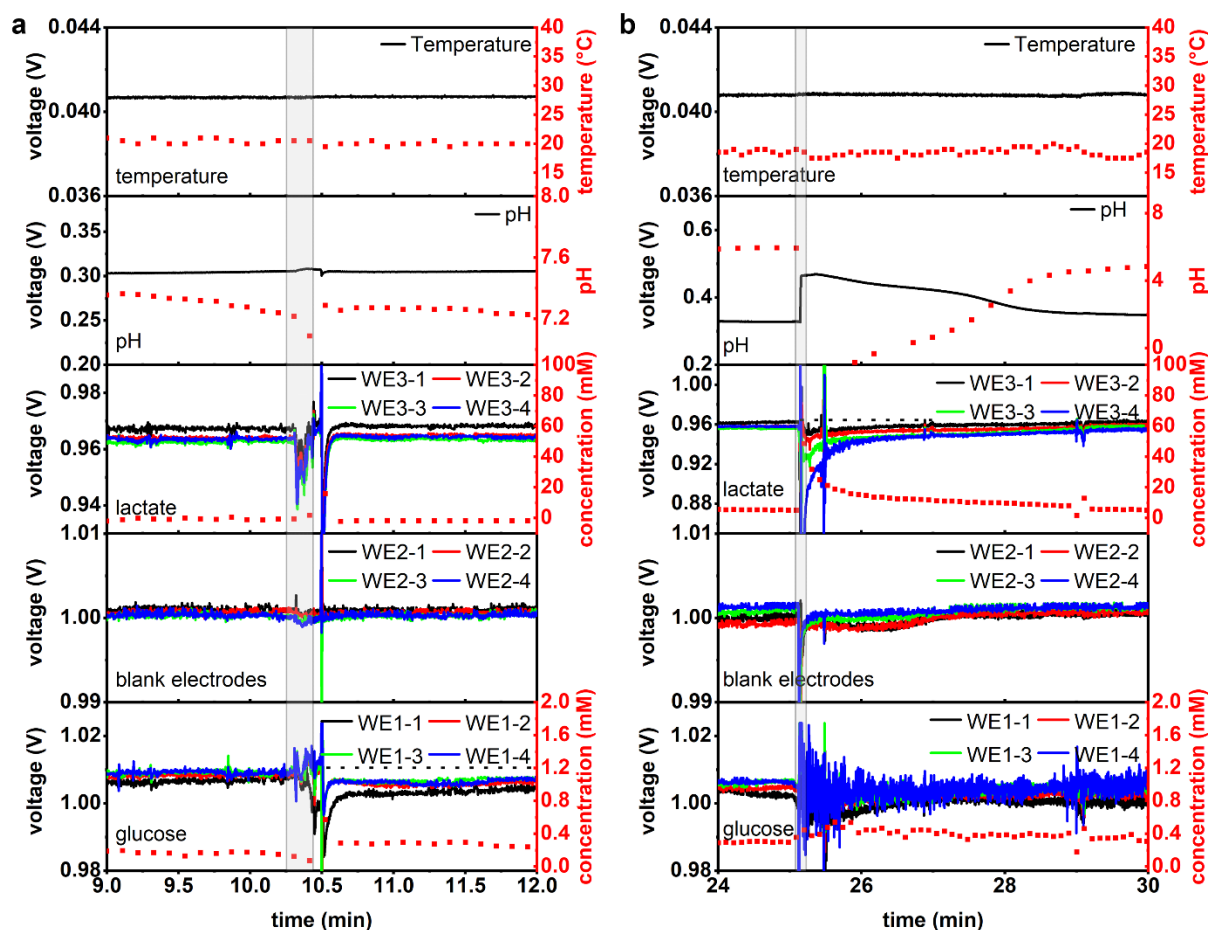


Figure 3.5. Multiplexed reading of glucose, lactate, pH, and temperature with a custom-designed multiplexed system in 1X PBS solution. The plots are replotted from the highlighted regions of the **Supplementary Figure S3.13**. **(a)** Multiplexed measurement of glucose, lactate, pH, and temperature after addition of glucose into the test solution (final concentration of glucose in the test solution: 400 μ M). **(b)** Multiplexed measurement of glucose, lactate, pH, and temperature after addition of lactic acid into the test solution (final concentration of lactic acid in the test solution: 10 mM). Conditions of the chronoamperometric measurements (bias: -0.1 V, pH: 7.4, working electrode area: 0.03 cm²). The grey highlighted region in **(a)** and **(b)** shows the noise generated due to pipetting the analyte solution into the test solution. WE₁₋₁ to WE₁₋₄: glucose sensors, WE₂₋₁ to WE₂₋₄: blank electrodes, WE₃₋₁ to WE₃₋₄: lactate sensors (WE_{x-y}, for x: 1,2,3 and y: 1,2,3,4, where x and y indicate the channel number and the working electrode number, respectively).

Off-body analysis of the collected sweat samples from all participants was performed with the multiplexed sensing system. Approximately 1.2 mL of sweat was collected from subject 1 and 2. The amount of sweat collected from the last subject was less than 200 μ L; therefore, it was not included in the testing. The concentration of glucose and lactate in the collected sweat samples were quantified with the colorimetric assays (Supplementary Table S9). The concentration of glucose and lactate was 24.25 μ L and 40.36 mM and 40.17 μ L and 39.35 mM for subject 1 and 2,

respectively. 150 μ L of the collected sweat samples was drop-casted on the flexible sensor, and its multiplexed analysis was performed with the custom system. The results were shown for both subjects in Supplementary Fig. S15 and Fig. S16. To be able to increase the concentration of the glucose and lactate in the collected sweat sample (i.e., to detect the increased enzymatic current), some amount of 1 mM glucose solution and 1 M lactic acid solution were sequentially added to the drop-casted volume. For both subjects, the addition of glucose and lactic acid to the sweat sample resulted in a decrease in the sensor's output (i.e., increased enzymatic current generation). The output of the pH sensor increased (i.e., became more acidic), and the output of the temperature sensor remained unchanged. Similar tests that were repeated with the artificial sweat solution showed similar trends in the sensor outputs (**Supplementary Figure S3.17**). It is important to note that the sensors in our study were calibrated in 1X PBS solution in Fig. 4. The output of the enzymatic sensors (**Supplementary Figure S3.17a-b**) were different when they were tested with a real or artificial sweat sample. For instance, the current generation of lactate sensor in 1X PBS was higher than the current generation of the artificial sweat with added lactic acid. This shift in the sensor output or direct utilization of the calibration curves of the enzymatic sensors for the real sweat solutions may lead to miscalculation of the correct concentration of the metabolites in the sweat sample. To minimize this error, future calibration of the sensors will need to be performed in an artificial sweat solution that has a similar composition and conductivity as the real sweat.

3.5. Conclusion

In this study, we have demonstrated a custom-designed multiplexing system with a flexible sensor array for a multiplexed detection of glucose, lactate, pH, and temperature. The flexible sensor array is disposable and can be easily mounted on the custom-designed board for multiplexed, wireless, simultaneous, and continuous readout from all sensors. The utilization of

the custom multiplexing system enables fast and simultaneous readout from multiple working electrodes. The custom multiplexing system consumes 15 mA during active measurement and data transmission, costs \$92 per unit, and has a wearable form factor ($40 \times 40 \times 9$ mm). The system demonstrates comparable performance to benchtop hardware for conventional cyclic voltammetry and chronoamperometry. In vitro tests demonstrated that the system could quantify and discriminate between two metabolic biomarkers present in sweat—glucose and lactate. These measurements are made in parallel with the characterization of pH and temperature in typical physiological ranges. The utilization of the redundant electrodes along with the custom multiplexing system enables accurate calculation of the analyte levels in the test solution. Future work will focus on further optimization of the system at different pH and temperatures for compensating any potential enzymatic activity loss of the glucose and lactate sensors. This wearable system is a promising demonstration of the necessary measurement tools for non-invasive, wireless, and continuous electrochemical measurement of biomarkers in sweat.

3.6. Supplementary Material

3.6.1. Supplementary Text

3.6.1.1. *Comparison of wearable multimodal systems*

A comparison of wearable multimodal systems with multiple analyte sensing capability is given in **Supplementary Table S3.1**. The table summarizes the type of analytes and electrochemical techniques along with their unique features.

3.6.1.2. *Comparison of custom-built potentiostats*

The comparison of custom-designed potentiostats is given in **Supplementary Table S3.2**. This table categorizes the previous potentiostat designs according to their multichannel/multiplexed operation, capability of interfacing with multiple electrode arrays, type of analytical techniques they can perform, analyte of interest, communication scheme, and their application field.

3.6.1.3. *Fabrication of the flexible sensor array*

The fabrication of the flexible sensor array starts with cleaning 100 mm glass wafers in Nanostrip® solution for 15 min to remove any organic materials from the wafer surface. Then, a thin layer of polydimethylsiloxane (PDMS) was spin-coated on the wafers at 1000 rpm for 3 min and cured at 70 °C for 1.5 h in a vacuum oven to form a sacrificial layer. A 50 μm thick polyimide layer was then temporarily laminated on the PDMS surface and cleaned with acetone and IPA to remove any residual dust. Chromium (20 nm) and gold (300 nm) were deposited at rates of 50 Å·s⁻¹ and 66 Å·s⁻¹ on the polyimide film via DC sputtering at 4×10⁻⁶ Torr. A positive photoresist (Microposit® S1813) was spin-coated on the metallization layer at 4000 rpm for 40 s and exposed to UV light for 10 s. The exposed resist was developed in Microposit® MF-319 for 1 min (20°C), rinsed in DI water, and dried with nitrogen gas. Chromium and gold layers were removed in their

corresponding wet etchants (CR-7 Chromium Etchant (etch time: 10 s, 20°C) and Transene TFA gold etchant (etch time: 110 s, 20°C)). The wafers were rinsed in DI water and dried with nitrogen gas. Afterward, the resist was stripped off in N-Methyl-2-pyrrolidone (NMP, 20°C) for 5 min. The conductive traces were encapsulated with the same positive photoresist at similar spin settings. The photoresist layer on the electrode areas and pads was removed through photolithography and MF-319 developer to prepare the gold surface for further functionalization and to make an electrical connection to the measurement instrument. Finally, the flexible sensor was peeled off from the sacrificial PDMS layer for further use. The fabrication process is summarized in **Supplementary Figure S3.2**.

3.6.1.4. Electrode functionalization and characterization

Electrodeposition of gold nanoparticles (AuNPs) on the planar gold electrodes were performed at -0.1 V using a commercial Pt counter electrode (BASI®) and an Ag/AgCl reference electrode (PINE Research) with varying electrodeposition times (5, 10, 15, 30, 45, and 90 min) in an aqueous solution of 2 mM HAuCl_4 and 2 M H_2SO_4 . Optical and scanning electron microscope images of the electrodeposited AuNPs were taken with a stereoscope and a Field Emission Scanning Electrode Microscope (FEI Verios 460L), respectively (**Supplementary Figure S3.10**). The electrochemical measurements (cyclic voltammetry and AC impedance measurements) were carried out in an aqueous solution of 10 mM $\text{K}_3\text{Fe}(\text{CN})_6$ in 1xPBS and 5 mM $\text{K}_3\text{Fe}(\text{CN})_6$ in 1X PBS, respectively (with respect to a commercial Pt counter electrode and an Ag/AgCl reference electrode). The electrochemical characterization results of the planar gold and AuNPs deposited electrodes were given in **Supplementary Figure S3.11** and **Supplementary Table S3.6**.

Electrodeposition of AuNPs starts from the edges of the circular planar gold electrodes (*i.e.* at the interface of the gold electrode with the encapsulation layer) due to the increased current

density on the edges (Rubinstein et al. 1987) (**Supplementary Figure S3.10**). As the AuNPs electrodeposition time increases, the amount of deposited AuNPs increases and the deposited gold nanoparticles start to appear at the center of the planar gold electrode. The size of the AuNPs ranges from approx. 40 nm (circular nanoparticles) to 630 nm (rod-like nanoparticles) for the electrodeposition time of 15 min. The deposition of AuNPs on the planar electrodes increases their electrochemically active surface area. The electrochemically active surface area of the AuNPs deposited electrodes were estimated using the Randles-Sevcik equation for a reversible electrochemical process (Ferrari et al. 2018) with the diffusion coefficient of ferri- and ferrocyanide ions in aqueous media (Hrapovic et al. 2004).

The cycle voltammetry measurements were undertaken with eight different scan rates (10, 20, 60, 100, 200, 300, 400, and 500 mV·s⁻¹). The results of the estimated effective electrochemically active surface area are shown in **Supplementary Table S3.6**. The normalized surface area was calculated by dividing the effective electrochemically active surface area by the geometrical surface area of the bare gold electrodes (0.0071 cm²), according to the equation below. To be able to match the geometrical surface area of the bare electrodes with the electrochemically active surface area, the normalization equation was multiplied with a constant of 1.47. The minimum and maximum increase in the normalized area via electrodeposition of AuNPs on the bare gold electrodes was 1.15 and 2.96, corresponding to 5 min and 90 min electrodeposition times.

$$\text{Normalized surface area} = \frac{\text{Effective electrochemically active surface area}}{\text{Geometrical surface area}} * 1.47$$

The effect of AuNPs deposition on the surface area of the bare electrodes was tested using cyclic voltammetry and AC impedance measurements. The magnitude of the electrode impedance decreased with increasing the effective electrochemical surface area (**Supplementary Figure**

S3.11a). Similarly, the peak amplitudes in cycle voltammetry measurements increased with the increase in electrochemically active surface area (**Supplementary Figure S3.11b,c**).

3.6.1.5. Selective functionalization of the electrodes

Electrodeposition is a technique for selective deposition of various materials on a single platform with minimal cross-contamination. We used the electrodeposition of AuNPs and Prussian blue (PB) for the fabrication of glucose and lactate sensors. Similarly, polyaniline (PANI) electrodeposition was carried out for the fabrication of pH sensors. The selective functionalization of the flexible array started with the electrodeposition PANI on the working electrode of the pH sensor. Then, the sample was cured at 80°C for 5 min. PANI was chosen due to its surface sensitivity to protonation in different pH solutions. This step was followed by the electrodeposition of AuNPs on the planar gold electrode surface (*i.e.*, working electrodes of glucose and lactate sensors). Afterward, PB was electrodeposited on the AuNPs electrodes, and the sample was cured at 80°C for 45 min. PB is selected due to its high catalytic activity towards hydrogen peroxide, which is a byproduct of the reaction between glucose oxidase-glucose or lactate oxidase-lactate. Afterward, an Ag/AgCl ink was drop casted on the reference electrodes of the pH, glucose, and lactate sensors. The sample was cured at 80°C for 15 min. Later on, the working electrode surfaces of glucose and lactate sensors were functionalized with GO_x and LO_x enzyme mixtures, respectively. Chemical crosslinking of the enzymes to bovine serum albumin (BSA) was performed with 2% glutaraldehyde solution. Finally, a 0.5% Nafion® film was drop-casted on top of the working electrodes as an encapsulation layer. The samples were stored at 4°C when not in use.

3.6.1.6. Comparison of the glucose and lactate sensors with previous studies

The performances of our glucose and lactate sensors were compared with the previous studies in the literature. Sensitivity, linear range, limit of detection, and operation conditions (*e.g.*, operation potential, pH, and stirring) are summarized in **Supplementary Table S3.7 and S3.8** for glucose and lactate sensors, respectively.

3.6.2. Supplementary Tables and Figures

Supplementary Table S3.1. Selected wearable sweat sensors

Multimodal sensors	Technique	Feature	Reference
K ⁺ and lactate	Potentiometry and chronoamperometry	Integrated on eyeglasses	69
Lactate and ECG	Chronoamperometry and electrophysiology	Hybrid sensor patch	30
Ethanol	Chronoamperometry	Sweat extraction via iontophoresis	17
Humidity, pH, temperature, glucose	Potentiometry, chronoamperometry, impedimetry	pH/temperature compensation and drug delivery	25, 70
Na ⁺ , Cl ⁻ , and glucose	Potentiometry and chronoamperometry	Sweat extraction via iontophoresis	19
Na ⁺ , K ⁺ , lactate, glucose, and temperature	Potentiometry, chronoamperometry, impedimetry	Temperature compensation	29
Ca ²⁺ , pH, and temperature	Potentiometry and impedimetry	Armband	59
Na ⁺ , K ⁺ , and lactate	Colorimetry	Chrono-sampling of sweat	71
Cl ⁻ , pH, glucose, creatinine, and lactate	Colorimetry	NFC integration	72
Sweat rate, pH, temperature, Cl ⁻ , glucose, and lactate	Colorimetry	Microfluidic sweat collection and chrono-sampling of sweat	28
Sweat rate, Na ⁺ , K ⁺ , and glucose	Chronoamperometry	Microfluidic sweat collection	73
Lactate, glucose, urea, and uric acid	Piezoelectric-enzymatic reaction	Self-powered sensing	74
Glucose, Na ⁺ , and K ⁺	Chronoamperometry and capacitive ion sensors	Self-powered sensing	75
Glucose, heart rate, blood oxygen saturation, temperature, and activity	Chronoamperometry	Estimation of post-exercise blood glucose level	24
Glucose, pH, Na ⁺ , and K ⁺	Chronoamperometry	NFC integration	76

Supplementary Table S3.2. Comparison of state-of-the-art custom-designed potentiostats

Multichannel / Multiplexer	Electrode Array	Technique	Analyte	Communication	Use	Reference
No/No	No	CA	Glucose, ethanol, cholesterol	USB	POC	77
No/No	No	CV	Lysozyme	USB	POC	78
No/No	No	CA, CV, DPV, SWV, POT	Glucose, Lead, Na ⁺ , malarial antigen	Audio cable	POC	32
No/No	No	CV	Cortisol	SSH	POC	79
No/No	No	CA, CV, POT, SWV, DPV	Ferrocene, 4-aminophenol, H ⁺	USB	Open-source potentiostat/POC	80
No/No	No	CV, LSV, SWV, ASV	Ascorbic acid, Ferricyanide, acetaminophen, arsenic, DNA	USB	Open-source potentiostat/POC	33
No/No	No	CA, CV, POT, SWV	Ferricyanide	BLE	Open-source potentiostat/POC	81
No/No	No	POT	H ⁺	NFC	IOT	82
No/No	No	CA	Glucose	NFC	Wearable sensing	34
No/No	No	CA, POT	Lactate, H ⁺ , Na ⁺	BLE	Wearable sensing	83
No/No	No	CA, POT	Lactate, H ₂ O ₂ , H ⁺ , Na ⁺	BLE	Wearable sensing	84
Yes/No	Yes	CA, CV	Glucose, lactate, K ⁺ , Na ⁺	BLE	Wearable sensing	29
Yes/No	Yes	CA, CV, POT, EIS	Glucose, Lactoferrin, H ⁺ , Neutroavidin	Serial	Wearable sensing	85
Yes/No	Yes	CA, POT	Glucose, lactate, oxygen, H ⁺	USB	Cellular microphysiometry	37
Yes/No	Yes	CA, CV	Ferrocene	Serial	General purpose potentiostat	35
No/Yes	Yes	CA	Glucose, lactate, uric acid	USB	POC	86
No/Yes	Yes	CA	Glucose	-	POC	87
Yes/Yes	Yes	CA	H ₂ O ₂	USB	LoC	40
Yes/Yes	Yes	CA	-	Serial	LoC	41
Yes/Yes	Yes	CA, CV	Glucose, lactate, pH	BLE	Wearable sensing	This work

CA: Chronoamperometry; CV: Cyclic voltammetry; POT: Potentiometry; SWV: Square wave voltammetry; DPV: Differential pulse voltammetry; LSV: Linear sweep voltammetry; ASV: Anodic strip voltammetry; EIS: Electrical impedance spectroscopy; NFC: Near field communication; BLE: Bluetooth; H₂O₂: Hydrogen peroxide; POC: Point of care; LoC: Lab on a chip; SSH: Secure Shell; IOT: Internet of things.

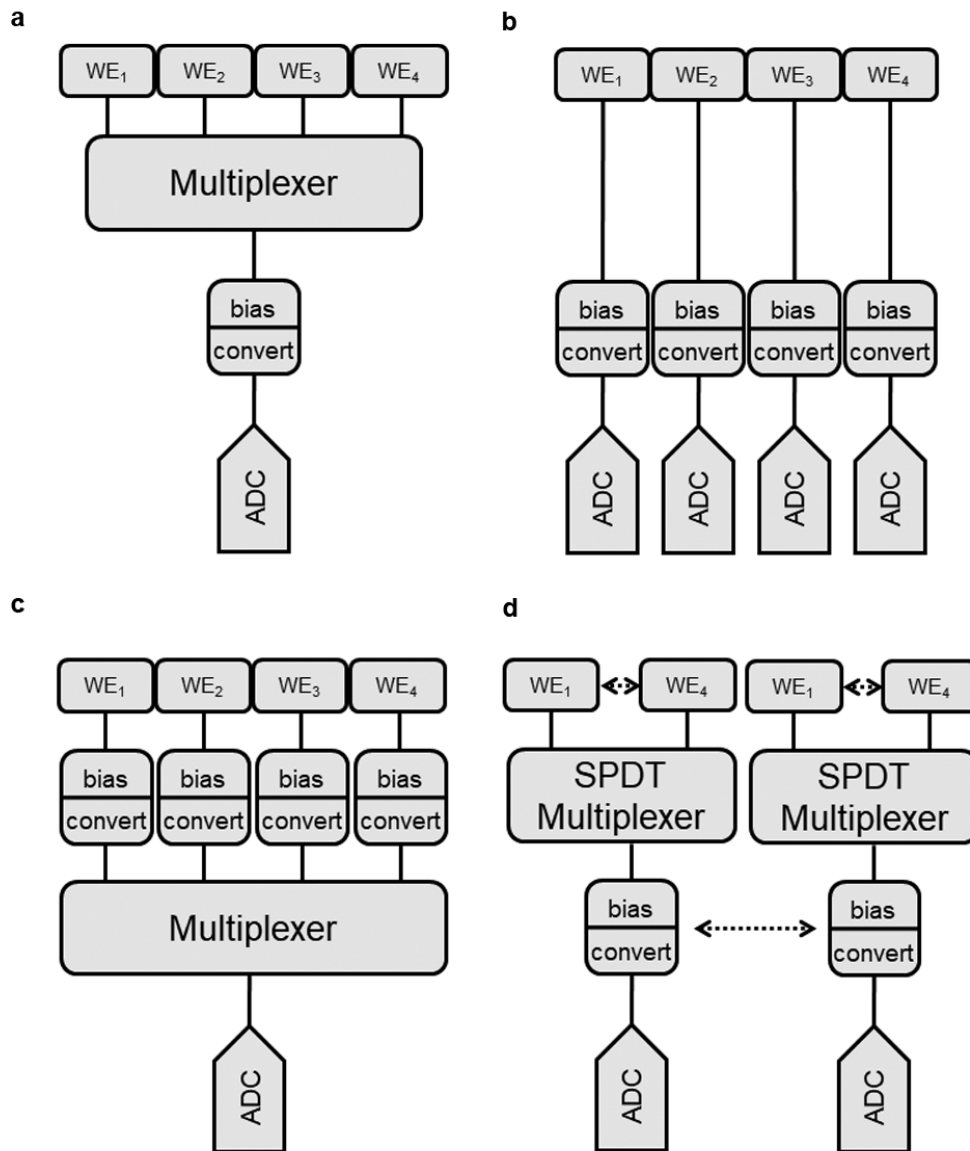


Figure S3.1. Common amperometric detection schemes from multiple working electrode arrays. Redrawn from (Ramfos et al. 2015). **(a)** Sequential reading from multiple working electrodes. It uses a single bias/convert unit and one ADC to digitize the results. The main disadvantage of this scheme is that not all working electrodes are biased continuously. **(b)** Parallel reading from multiple working electrodes. Each working electrode has its own bias/convert and ADC units. This design provides simultaneous and real-time measurement of each working electrode. **(c)** One bias/convert for each working electrode and a common ADC. All working electrodes are biased concurrently. This option is area effective compared to the detection scheme in (b). **(d)** Hybrid multiplexing scheme. Each working electrode is continuously biased. The scheme uses single pole double throw analog switches. This design connects the active working electrode to the bias/convert unit while maintaining all others working electrodes at a constant voltage, thus not disturbing the electrochemical process at each working electrode. This multiplexing scheme was utilized in this study.

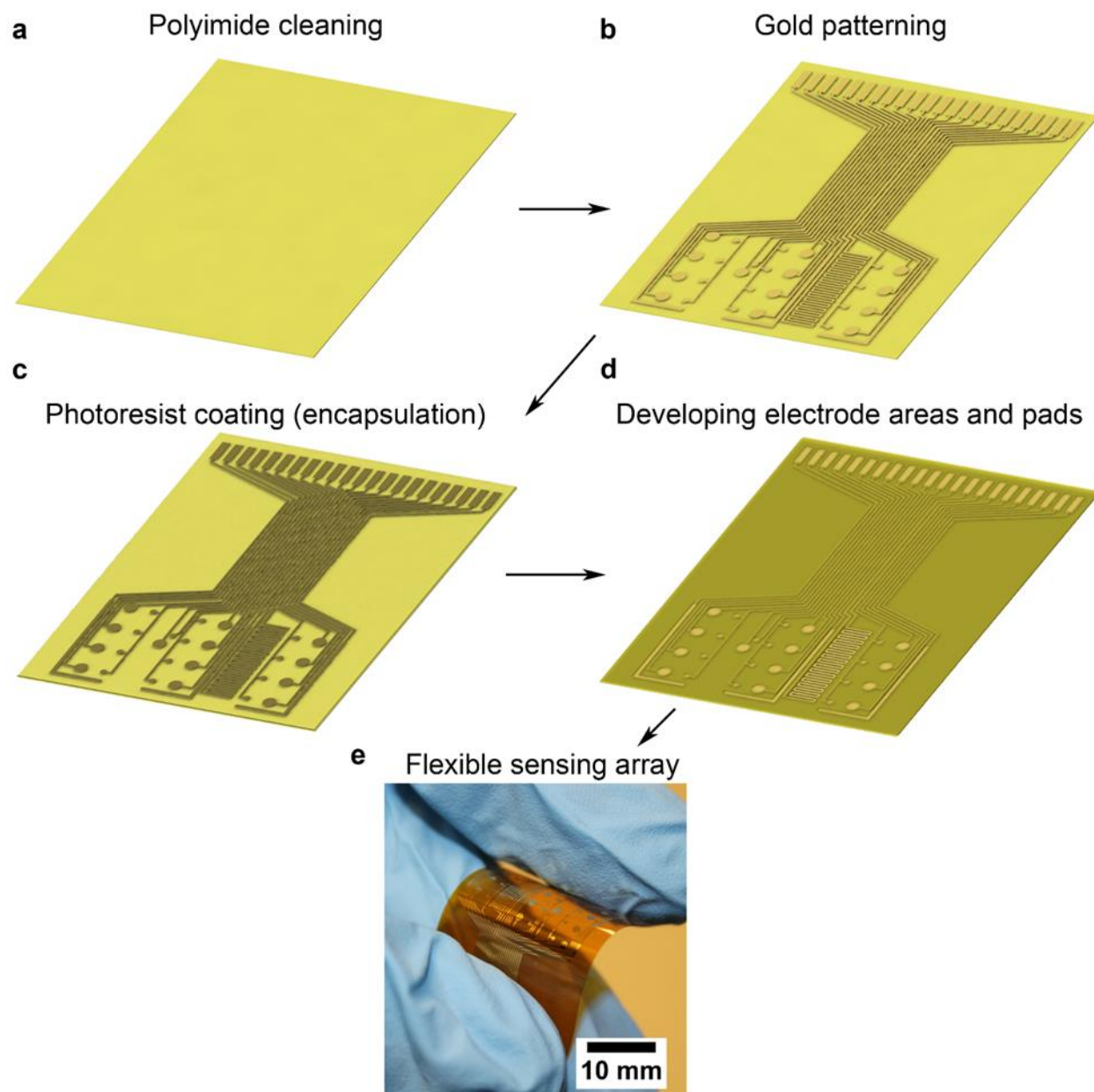


Figure S3.2. Fabrication process of the flexible sensor array. **(a)** Cleaning of the polyimide film with acetone and isopropanol. **(b)** Deposition of Cr/Au using DC sputtering, photolithography, and wet etching of Cr/Au. **(c)** Spin-coating of the positive photoresist for encapsulation of the conductive traces. **(d)** Removal of the positive photoresist in the developer to expose electrode areas and connection pads. **(e)** Optical image of the flexible sensor array.

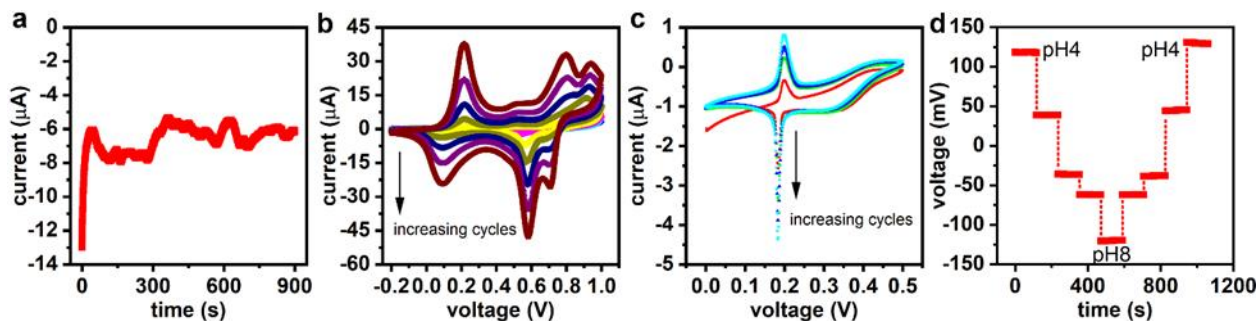


Figure S3.3. Electrodeposition techniques for functionalization of the electrode surfaces. (a) Chronoamperometric deposition of gold nanoparticles at -0.1 V for 15 min in an aqueous solution of 2 mM HAuCl_4 in 2 M H_2SO_4 . (b) Electrodeposition of polyaniline using cyclic voltammetry from -0.2 to 1V at a scan rate of $100 \text{ mV}\cdot\text{s}^{-1}$ in an aqueous solution of 0.1 M aniline in 1 M HCl. (c) Electrodeposition of Prussian blue using cyclic voltammetry from 0 to 0.5 V at a scan rate of $20 \text{ mV}\cdot\text{s}^{-1}$ in an aqueous solution of 100 mM KCl, 2.5 mM FeCl_3 , and 2.5 mM $\text{K}_3\text{Fe}(\text{CN})_6$ in 100 mM HCl. The redox peaks at 0.2 V and 0.18 V are associated with interconversion between Prussian blue and Prussian white (Karyakin 2001). (d) Repeatability of pH sensors in varying pH solutions (pH4 \rightarrow 8 and pH8 \rightarrow 4). 5 min wait time between successive measurements.

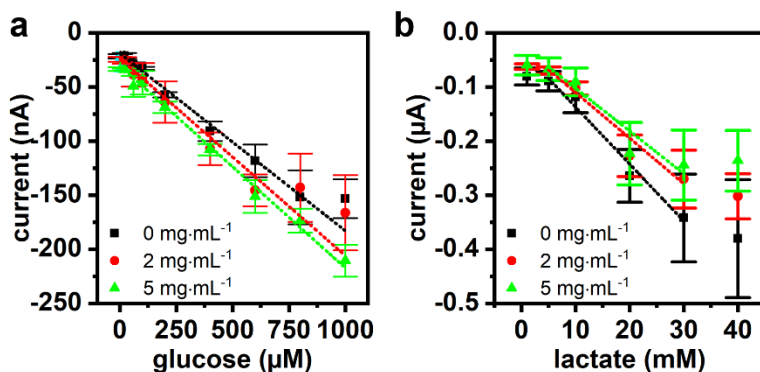


Figure S3.4. Benchtop chronoamperometric analysis of glucose (a) and lactate (b) sensors with varying exfoliated graphite concentrations (0, 2, and 5 $\text{mg}\cdot\text{mL}^{-1}$) in 1X PBS ($n = 3$). Bias: -0.1 V, pH 7.4.

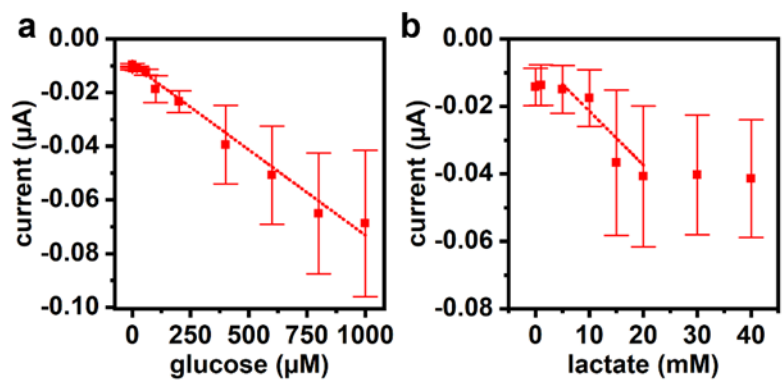


Figure S3.5. Sensitivities of glucose (a) and lactate (b) sensors after 10 days storage at 4 °C (n = 4). Bias: -0.1 V, pH 7.4.

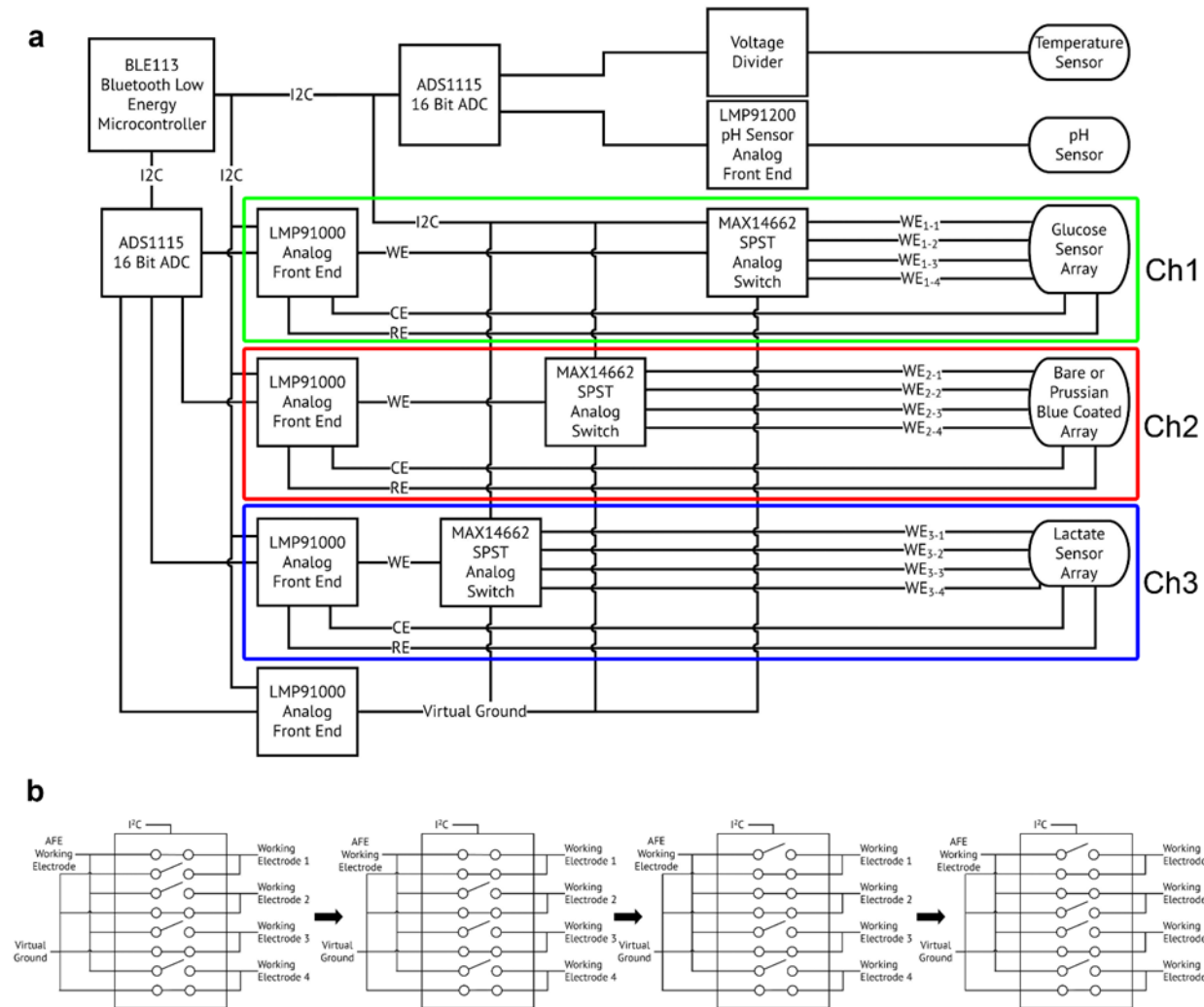


Figure S3.6. (a) Full system block diagram of the custom multiplexing system. The system includes four potentiostats (LMP91000). The three potentiostats are connected to the 12 working electrodes through three single-pole, single-throw switches (SPST), which control which electrode is connected to the potentiostats for each channel. The last potentiostat provides a virtual ground for the working electrodes when they are not active. The temperature and pH sensors use a voltage divider and a pH sensor IC (LMP91200), respectively. The system uses two 16 bits ADCs and a Bluetooth low energy microcontroller (BLE113). **(b)** Make-before-break switch operation from WE1 to WE2. Each working electrode is connected to two switches in the multiplexer: one is connecting the active working electrode to the potentiostat, and another switch is connecting the working electrode to the virtual ground (1 V) when the electrode is not in use. As the working electrode is alternating between readout and standby mode, a make-before-break multiplexing scheme is utilized to prevent instant peaks during the transitions when the current flow is briefly cut off.

Supplementary Table S3.3. Specifications of the custom-designed potentiostat.

Potentiostat (Chronoamperometry)		
Range of applied potential	$5 \text{ V} * \pm 0.24 = \pm 1.2 \text{ V}$	
Resolution of applied potential	$5 \text{ V} * 0.02 = 0.1 \text{ V}$	
For 560 kOhm resistor at -0.1 V, current resolution (i.e., conversion factor):		
	<u>Gain</u>	
	<u>Resolution</u>	
Current resolution	14 k	2.22 nA/digit
	35 k	0.90 nA/digit
	120 k	0.28 nA/digit
	350 k	0.11 nA/digit
	510 k	61.35 pA/digit
	1 M	1.36 pA/digit
	2 M	5.83 pA/digit
	3.92 M	7.98 pA/digit
For 560 kOhm resistor at -0.1 V:		
	<u>Gain</u>	<u>Current range</u>
Current range	14 k	$-71.00 \mu\text{A}$ to $0 \mu\text{A}$
	35 k	$-28.92 \mu\text{A}$ to $0 \mu\text{A}$
	120 k	$-8.96 \mu\text{A}$ to $0 \mu\text{A}$
	350 k	$-3.53 \mu\text{A}$ to $0 \mu\text{A}$
	510 k	$-1.95 \mu\text{A}$ to $0 \mu\text{A}$
	1 M	$-1.00 \mu\text{A}$ to $0 \mu\text{A}$
	2 M	$-0.51 \mu\text{A}$ to $0 \mu\text{A}$
	3.92 M	$-0.26 \mu\text{A}$ to $0 \mu\text{A}$
For 560 kOhm resistor at -0.1 V:		
	<u>Gain</u>	<u>Noise</u>
Peak-to-peak noise	14 k	62.13 nA
	35 k	21.57 nA
	120 k	8.02 nA
	350 k	5.57 nA
	510 k	10.55 nA
	1 M	11.60 nA
	2 M	10.86 nA
	3.92 M	11.81 nA
Max. sampling rate	10 Hz	

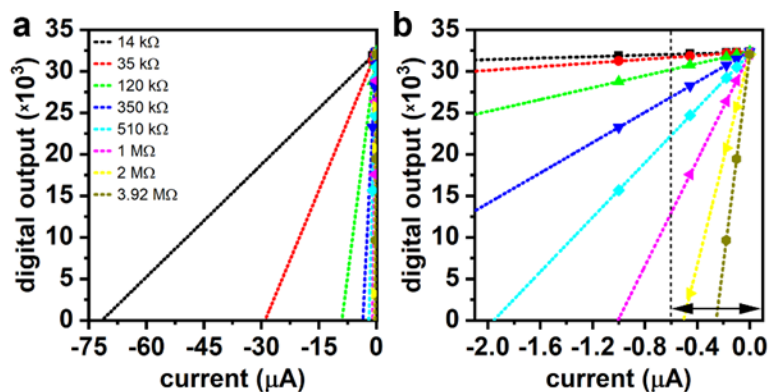


Figure S3.7. (a) Digital output vs. input current for varying gain (14 k Ω , 35 k Ω , 120 k Ω , 350 k Ω , 510 k Ω , 1 M Ω , 2 M Ω , and 3.92 M Ω) of the transimpedance amplifier (TIA) in LMP91000 potentiostat. Applied potential: -0.1 V. External resistor values: 100 k Ω , 220 k Ω , 560 k Ω , and 1 M Ω . For a given gain of the TIA and an applied bias (-0.1 V) in the potentiostat, the value of the external resistor was changed to find the value of ADC digital output that corresponded to the magnitude of the current that flowed through the resistor. These four digital output values were extrapolated to find the maximum current that can be read with the custom designed system for a given amplifier gain setting (dotted lines). (b) A replot of the left figure for a narrow range of input currents. These plots help to adjust the gain of the amplifier without saturating the ADC output based on the maximum reduction currents obtained from glucose or lactate sensors in the benchtop measurements.

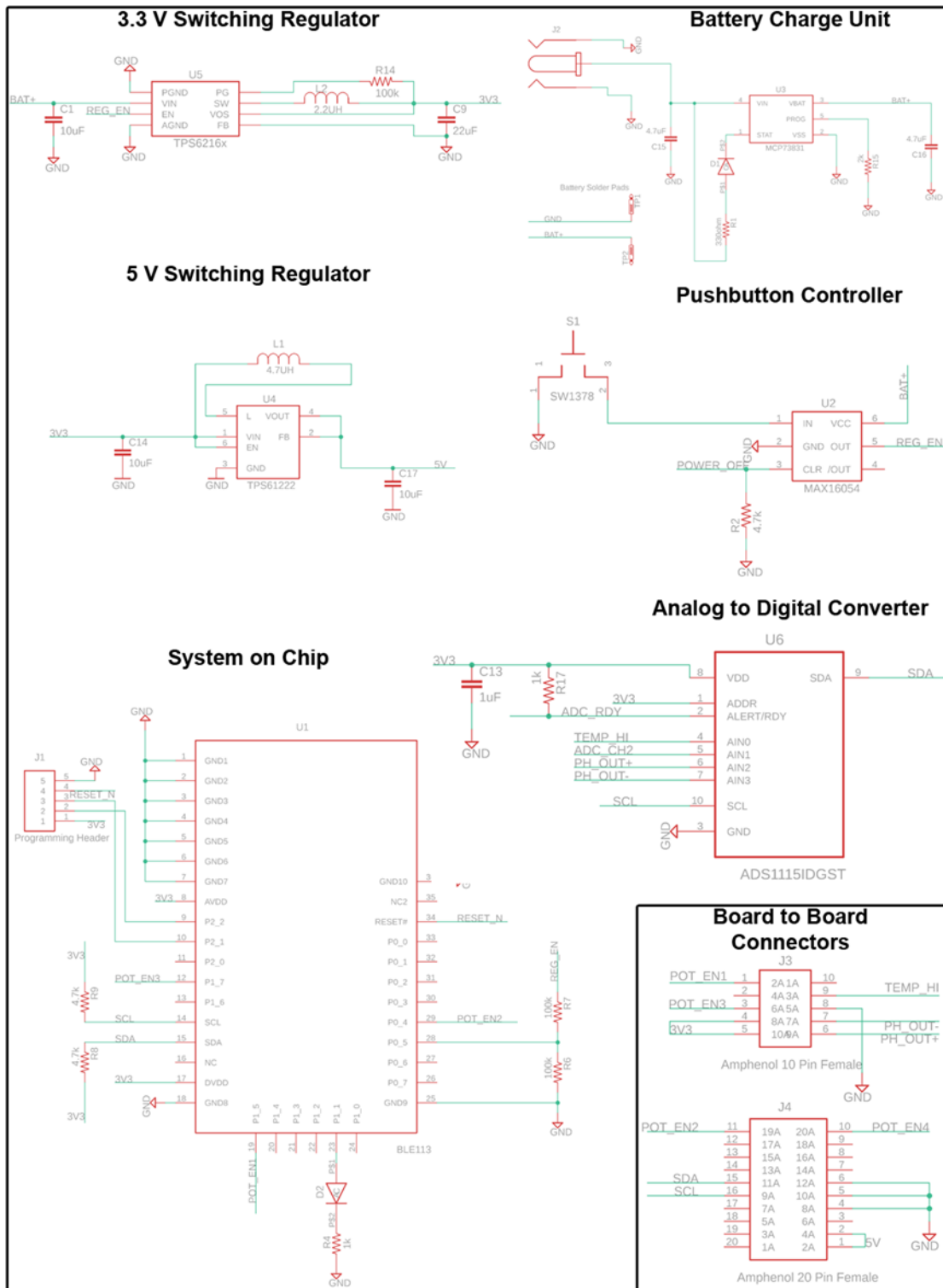


Figure S3.8. Circuit diagrams of the wearable multiplexing system. The schematic shows a system-on-chip, power management units (a battery management unit and switching regulators), an analog-to-digital converter, board-to-board connectors, and a pushbutton connector.

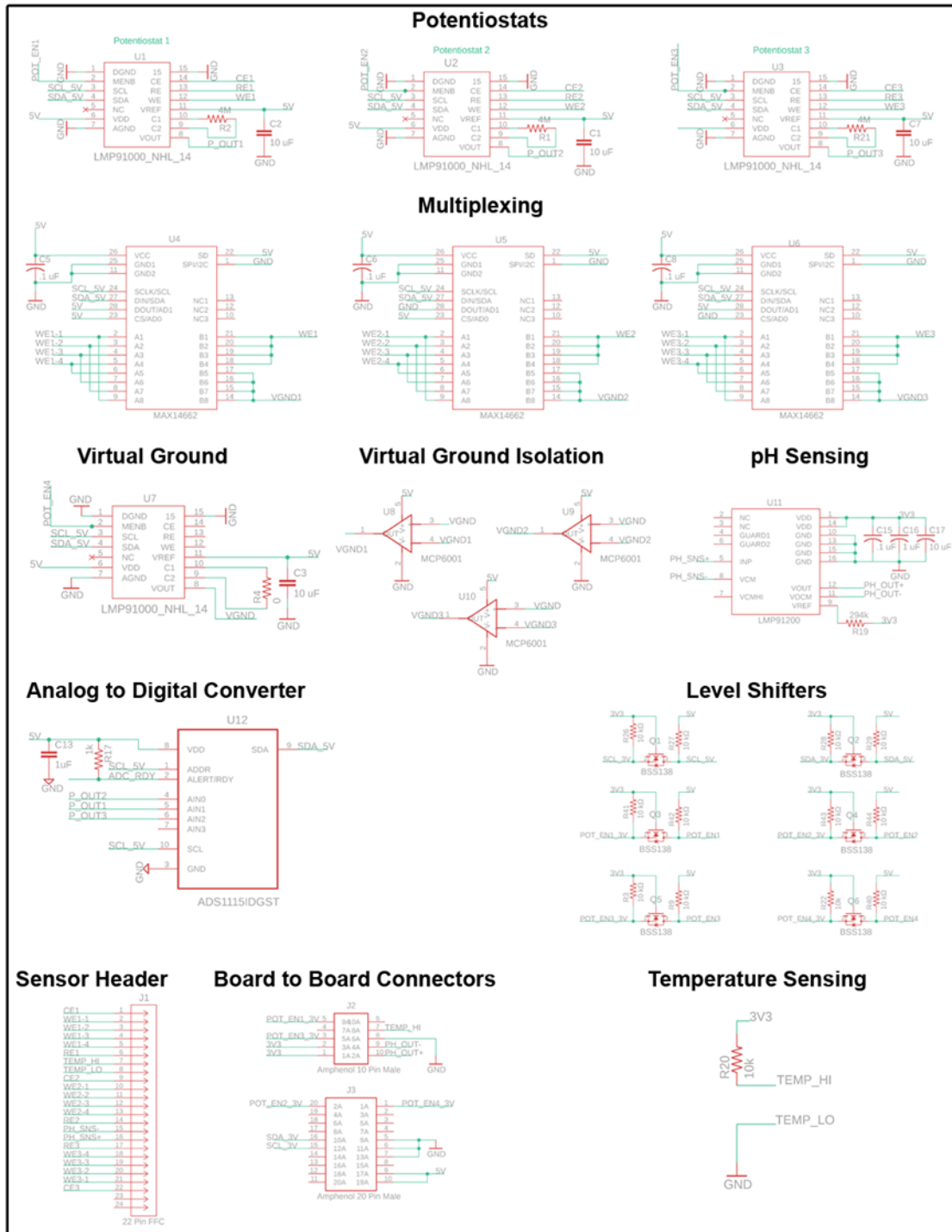


Figure S3.9. Circuit diagrams of the wearable multiplexing system. The schematic shows three potentiostats, three multiplexers, a potentiostat for virtual ground and three virtual ground isolation units, a pH sensing unit, an analog-to-digital converter, level shifters, a temperature sensing unit, board-to-board connectors, and a sensor header.

Supplementary Table S3.4. Bill of materials of the schematic in **Figure S3.8**.

Component	Description	Value	Part Number	Quantity	Price (\$)
C1, C14, C17	Capacitor	10 μ F	CC0603MRX5R5BB106	3	0.75
C13	Capacitor	1 μ F	CC0402KRX5R5BB105	1	0.10
C15, C16	Capacitor	4.7 μ F	CC0402KRX5R5BB475	2	0.68
C2	Capacitor	0.1 μ F	CC0402KRX5R7BB104	1	0.10
C9	Capacitor	22 μ F	CC0805MKX5R5BB226	1	0.55
D1	Battery Charging Indicator LED	Green	APT1608SGC	1	0.37
D2	Blue Notification LED	Blue	APT1608QBC/D	1	0.46
J1	5 Pin Programming Header	-	851-87-005-10-001101	1	0.80
J2	DC Power Jack	-	PJ-040	1	1.10
J3	10 Position Female Connector	-	10132797-015100LF	1	0.70
J4	20 Position Female Connector	-	10132797-025100LF	1	1.35
L1	Inductor	4.7 μ H	VLS3015ET-4R7M-CA	1	0.61
L2	Inductor	2.2 μ H	VLF3012ST-2R2M1R4	1	0.61
R1	Resistor	330	ERJ-2RKF3300X	1	0.10
R15	Resistor	2 k	ERJ-2RKF2001X	1	0.10
R2, R8, R9	Resistor	4.7 k	ERJ-2GEJ472X	3	0.30
R4, R17	Resistor	1 k	ERJ-2RKF1001X	2	0.20
R6, R7, R14	Resistor	100 k	ERJ-PA2J104X	3	0.48
S1	Pushbutton	-	A9PS16-0012	1	9.02
U1	Bluetooth System-On-Chip	-	BLE113	1	12.67
U2	On/Off Controller	-	MAX16054	1	2.59
U3	Battery Charge Management	-	MCP73831	1	0.58
U4	5V Boost Switching Regulator	-	TPS61222	1	1.14
U5	3.3V Step-Down Converter	-	TPS6216X	1	1.79
U6	Quad Analog-to-Digital Converter	-	ADS1115IDGST	1	6.35
				Total	\$43.5

Supplementary Table S3.5. Bill of materials of the schematic in **Figure S3.9**.

Component	Description	Value	Part Number	Quantity	Price (\$)
C1, C2, C3, C7	Capacitor	10 μ F	CC0402MRX5R5BB106	4	1.80
C13, C16	Capacitor	1 μ F	CC0402KRX5R5BB105	2	0.20
C17	Capacitor	10 μ F	CC0603MRX5R5BB106	1	0.25
C5, C6, C8, C15	Capacitor	0.1 μ F	CC0402KRX5R7BB104	4	0.40
J1	22 Pin FFC Sensor Connector	-	CON22_1X22_DRBF_HST	1	1.66
J2	10 Pin Male Connector	-	10132798-015100LF	1	0.57
J3	20 Pin Male Connector	-	10132798-025100LF	1	0.84
Q1, Q2, Q3, Q4, Q5, Q6	N-Channel MOSFET	-	BSS138	6	1.62
R1, R2, R21	Resistor	1 M	ERJ-2RKF1004X	3	0.30
R17	Resistor	1 k	ERJ-2RKF1001X	1	0.10
R19	Resistor	294 k	ERJ-2RKF2943X	1	0.10
R3, R9, R20, R22, R26, R27, R28, R29, R40, R41, R42, R43, R44	Resistor	10 k	ERJ-2GEJ103X	13	0.31
R4	Resistor	0	ERJ-2GE0R00X	1	0.10
U1, U2, U3, U7	Potentiostat AFE	-	LMP91000	4	17.36
U11	Configurable AFE for pH Measurement	-	LMP91200	1	6.28
U12	Quad Analog-to-Digital Converter	-	ADS1115IDGST	1	6.35
U4, U5, U6	Multiplexer	-	MAX14662	3	9.39
U8, U9, U10	Op Amp	-	MCP6001	3	0.75
				Total	\$48.38

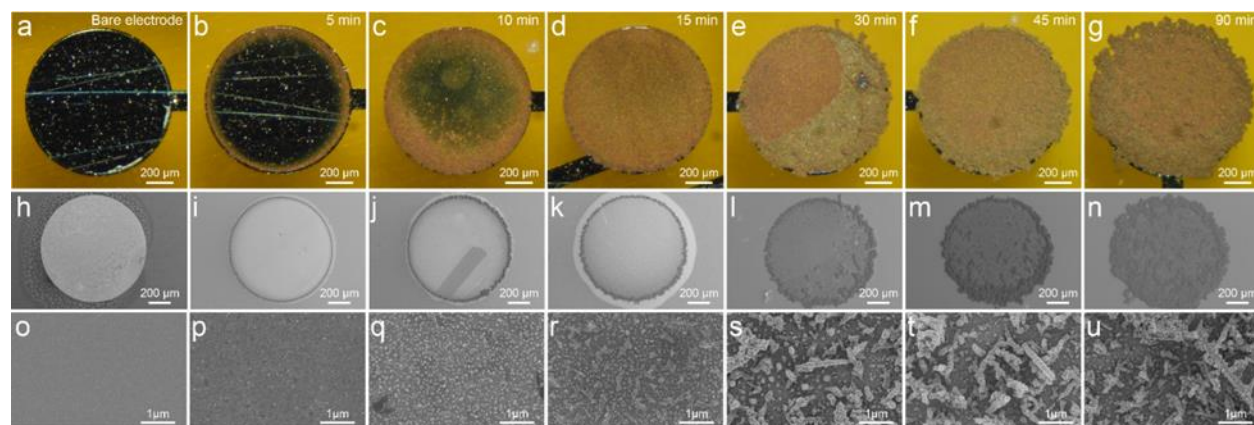


Figure S3.10. Optical and SEM images of the bare gold electrode and gold nanoparticle deposited electrodes. Images from left to right indicate increasing gold nanoparticle deposition times (0, 5, 10, 15, 30, 45, and 90 min). **(a-g)** Optical microscopy images of the bare gold electrode and AuNPs deposited gold electrodes. The amount of electrodeposited AuNPs increase with the increased deposition time. **(h-n)** SEM images of the bare gold electrode and AuNPs deposited gold electrodes. The nucleation of the gold nanoparticle growth starts from the edges of the bare gold electrodes. **(o-u)** SEM images were taken from the center of the electrodes.

Supplementary Table S3.6. Effective electrochemically active surface area of gold nanoparticle deposited electrodes.

Effective Electrochemically Active Surface Area (cm²)

<i>Bare planar electrode</i>	<i>5min</i>	<i>10min</i>	<i>15min</i>	<i>30min</i>	<i>45min</i>	<i>90min</i>
0.0048	0.0055	0.0061	0.0066	0.0079	0.0101	0.0143
Normalized Surface Area						
1.0000	1.1464	1.2620	1.3758	1.6450	2.0916	2.9662

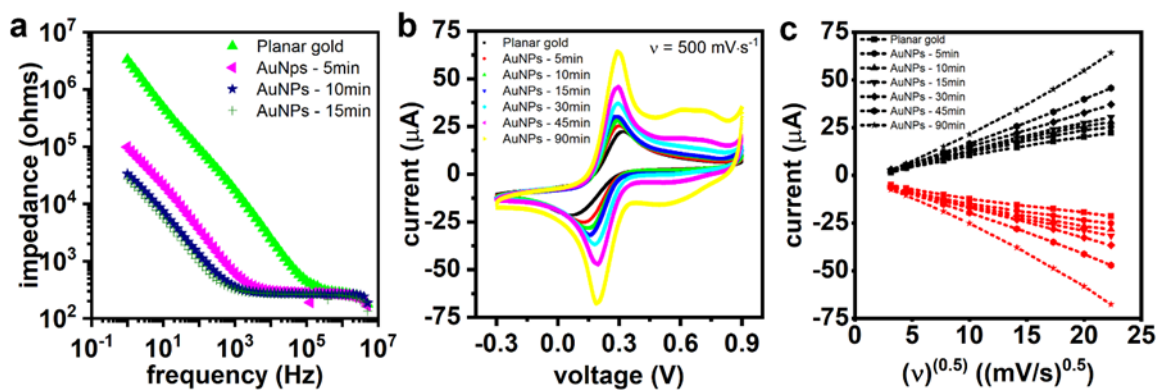


Figure S3.11. Electrochemical impedance spectroscopy and cyclic voltammetry characterization of the bare gold electrode and gold nanoparticle deposited electrodes in an aqueous solution of 5 mM $\text{K}_3\text{Fe}(\text{CN})_6$ in 1xPBS and 10 mM $\text{K}_3\text{Fe}(\text{CN})_6$ in 1xPBS, respectively. **(a)** Bode plots of the bare gold electrode and AuNPs deposited gold electrodes with varying electrodeposition time (5, 10, and 15min). Deposition of AuNPs on the bare gold electrode surface significantly decreases its DC impedance. **(b)** Cyclic voltammetry plots of the bare gold electrode and AuNPs deposited gold electrodes with varying electrodeposition time (5, 10, 15, 30, 45, and 90 min). Scan rate: $500 \text{ mV}\cdot\text{s}^{-1}$. Increase of the electrochemically active surface area of the bare gold electrodes results in high current levels. **(c)** The square root of the scan rate vs. peak current of the bare and AuNPs deposited gold electrodes with varying electrodeposition times.

Supplementary Table S3.7. Comparison of glucose sensors (benchtop potentiostat results)

Modification/Electrode	Enzyme	Slope ($\mu\text{A}\cdot\text{mM}^{-1}\cdot\text{cm}^{-2}$)	Linear range (μM)	LOD (μM)	Potential/pH	Stirring	Reference
Chi-GO _x -PDA-PtNPs-(PB-Au) _n /GCE	GO _x	114	5 - 790	0.5	-0.05 V/pH 7.0	Yes	88
GO _x -Graphene-PB/Au	GO _x	162	10 - 800	-	-0.05 V/pH 6.5	-	89
PPy-PB-GO _x /Graphite	GO _x	1.0 - 1.9	100 - 20000	-	0.05 V/pH 7.3	Yes	90
GO _x -Chi-IL-PB/Pt	GO _x	37.8	10 - 4200	5	-0.05 V/pH 6.5	-	91
(GO _x -Chi) _n /Au	GO _x	5.17	6 - 1600	3.1	0 V/pH 6.0	Yes	92
GO _x -Chi-AuNPs-PB/GCE	GO _x	69.26	1 - 1600	0.69	-0.05 V/pH 7.0	Yes	93
(GO _x -PB) _n -PSS-PDDA/Au	GO _x	3.6	100 - 11000	10	-0.1 V/pH 7.4	Yes	94
PA-GO _x -PB/Pt	GO _x	3 $\mu\text{A}\cdot\text{cm}^{-2}$	< 12000	-	0 V/pH 7.3	Yes	95
Nafion-GO _x -PB/Graphite	GO _x	-	10 - 3000	2	-0.05 V/pH 6.4	-	96
Nafion-GO _x -Exfoliated Graphite-PB/Au	GO _x	26.31	60 - 1000	-	-0.1 V/pH 7.4	No	This work

GO_x: Glucose oxidase; PDA: Polydopamine; PB: Prussian Blue; GCE: Glassy carbon electrode; PPy: Polypyrrole; PtNPs: Platinum nanoparticles; Chi: Chitosan; IL: Ionic liquid; PA: Polyaniline; Au: Gold; Pt: Platinum; PDDA: Poly(diallyldimethylammonium chloride); PSS: poly(styrenesulfonate); PA: Polyaniline.

Supplementary Table S3.8. Comparison of lactate sensors (benchtop potentiostat results)

Modification/Electrode	Enzyme	Slope ($\mu\text{A}\cdot\text{mM}^{-1}\cdot\text{cm}^{-2}$)	Linear range (mM)	LOD (mM)	Potential/pH	Stirring	Reference
Nafion- LO_x /GCE	LO_x	51.43 ^a	< 0.8	<0.001	-0.05 V/pH 5.5	Yes	⁹⁷
Nafion- LO_x - PB/Graphite	LO_x	-	0.025 - 0.25	0.01	-0.05 V/pH 7.4	No	⁹⁸
Chi- LO_x -PB/Ag	LO_x	0.096 $\mu\text{A}\cdot\text{mM}^{-1}$ ^b	0 - 28	-	-0.1 V/pH 7.0	No	³⁰
PPD- LO_x -PB/Graphite	LO_x	0.553 $\mu\text{A}\cdot\text{mM}^{-1}$ ^b	0.1 - 1	0.05	0.042 V/pH 7.0	No	⁹⁹
LO_x -PtNPs-CNF- PDDA/Carbon	LO_x	36.8	0.025 - 1.5	11	0.5 V/pH 7.0	No	¹⁰⁰
PC- LO_x -PC/Pt	LO_x	0.23 ^a	< 20	0.2	0.65 V/pH 7.4	No	²¹
Chi-CNT-TTF/Carbon	LO_x	10.31	1 - 20	-	0.05 V/pH 7.0	No	¹⁴
Nafion- LO_x -PB/Au	LO_x	1.49	5 - 20	-	-0.1 V/pH 7.4	No	This work

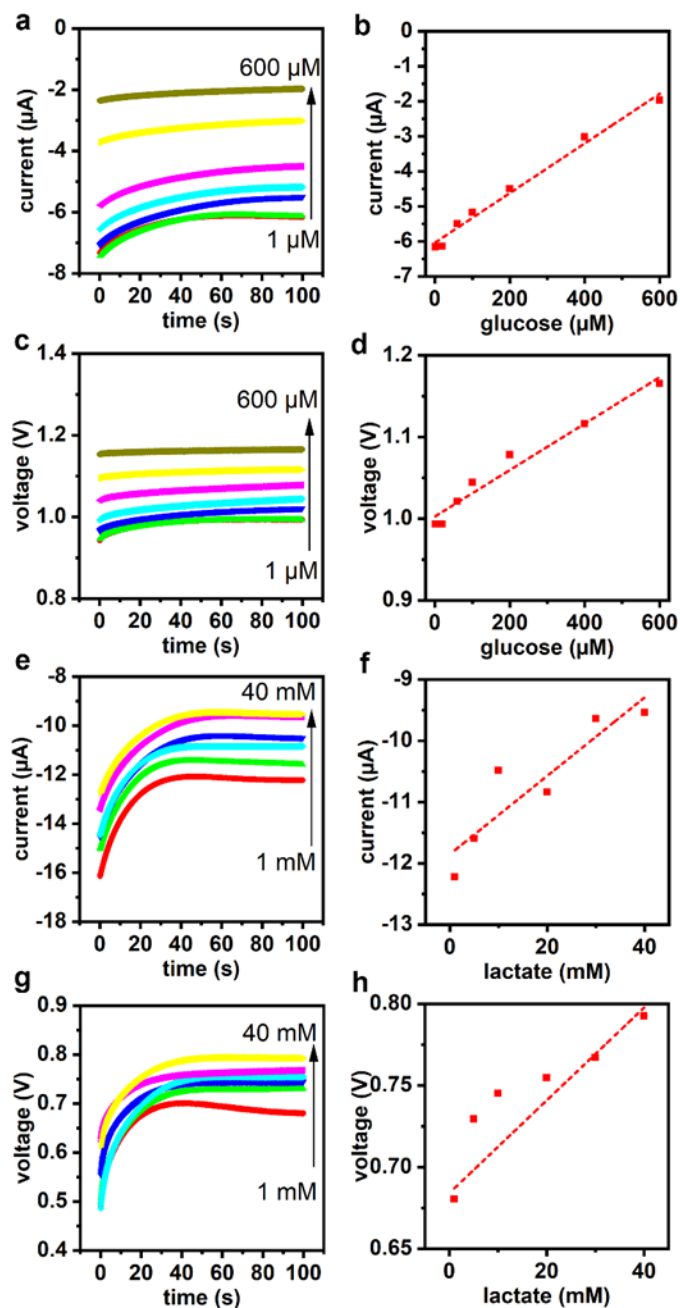


Figure S3.12. Chronoamperometric response of glucose oxidase ($10 \text{ mg}\cdot\text{mL}^{-1}$) + $\text{K}_3\text{Fe}(\text{CN})_6$ ($10 \text{ mg}\cdot\text{mL}^{-1}$) and lactate oxidase ($10 \text{ mg}\cdot\text{mL}^{-1}$) + $\text{K}_3\text{Fe}(\text{CN})_6$ ($10 \text{ mg}\cdot\text{mL}^{-1}$) in 1X PBS to increasing glucose (1 to 600 μM) and lactate (1 to 40 mM) concentrations, respectively ($n = 1$). The enzymes are dispersed in 1X PBS solution along with the mediator to assist with electron transfer from the active side of the enzyme to the electrode surface. Bias: -0.1 V , pH 7.4. **(a-d)** Measurement of GO_x current response using **(a,b)** a benchtop potentiostat and **(c,d)** the custom multiplexing system. **(e-h)** Measurement of LO_x current response measurement using **(e,f)** a benchtop potentiostat and **(g,h)** the custom multiplexed system.

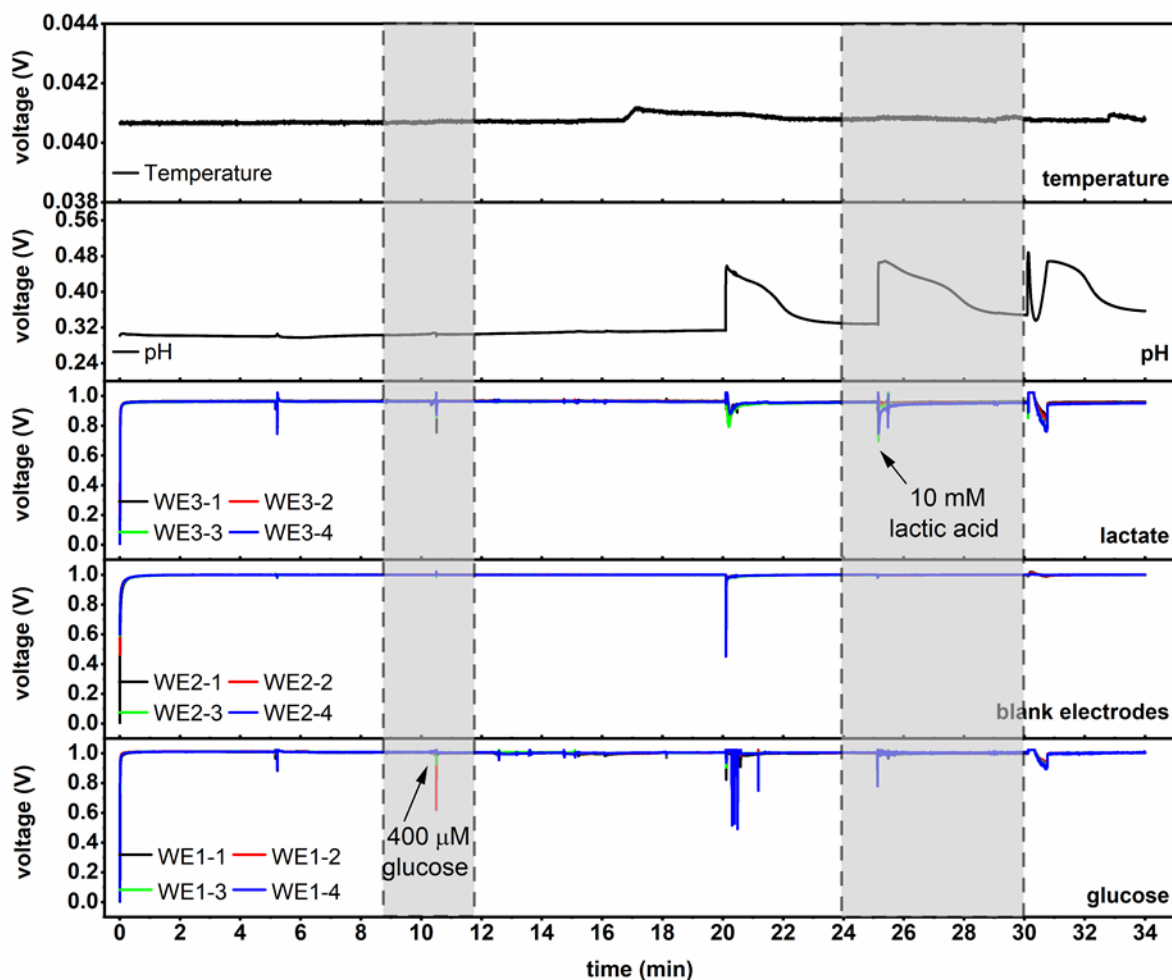


Figure S3.13. Multiplexed reading of glucose, lactate, pH, and temperature with a custom multiplexed sensing system in 1xPBS solution. Glucose was added at 5, 10, and 15 min, yielding 200, 400, and 600 μM of glucose in the test solution. Lactic acid was added at 20, 25, and 30 min, giving 5, 10, and 15 mM in the test solution. Conditions of the chronoamperometric measurements (bias: -0.1 V, pH: 7.4, working electrode area: 0.03 cm^2). The grey highlighted regions in the figure shows 400 μM glucose and 10 mM lactic acid, respectively. The highlighted regions were shown in **Figure 3.5a** and **Figure 3.5b** of the main article in detail. WE₁₋₁ to WE₁₋₄: glucose sensors, WE₂₋₁ to WE₂₋₄: blank electrodes, WE₃₋₁ to WE₃₋₄: lactate sensors (WE_{x-y}, for x: 1,2,3 and y: 1,2,3,4, where x and y indicate the channel number and the working electrode number, respectively).

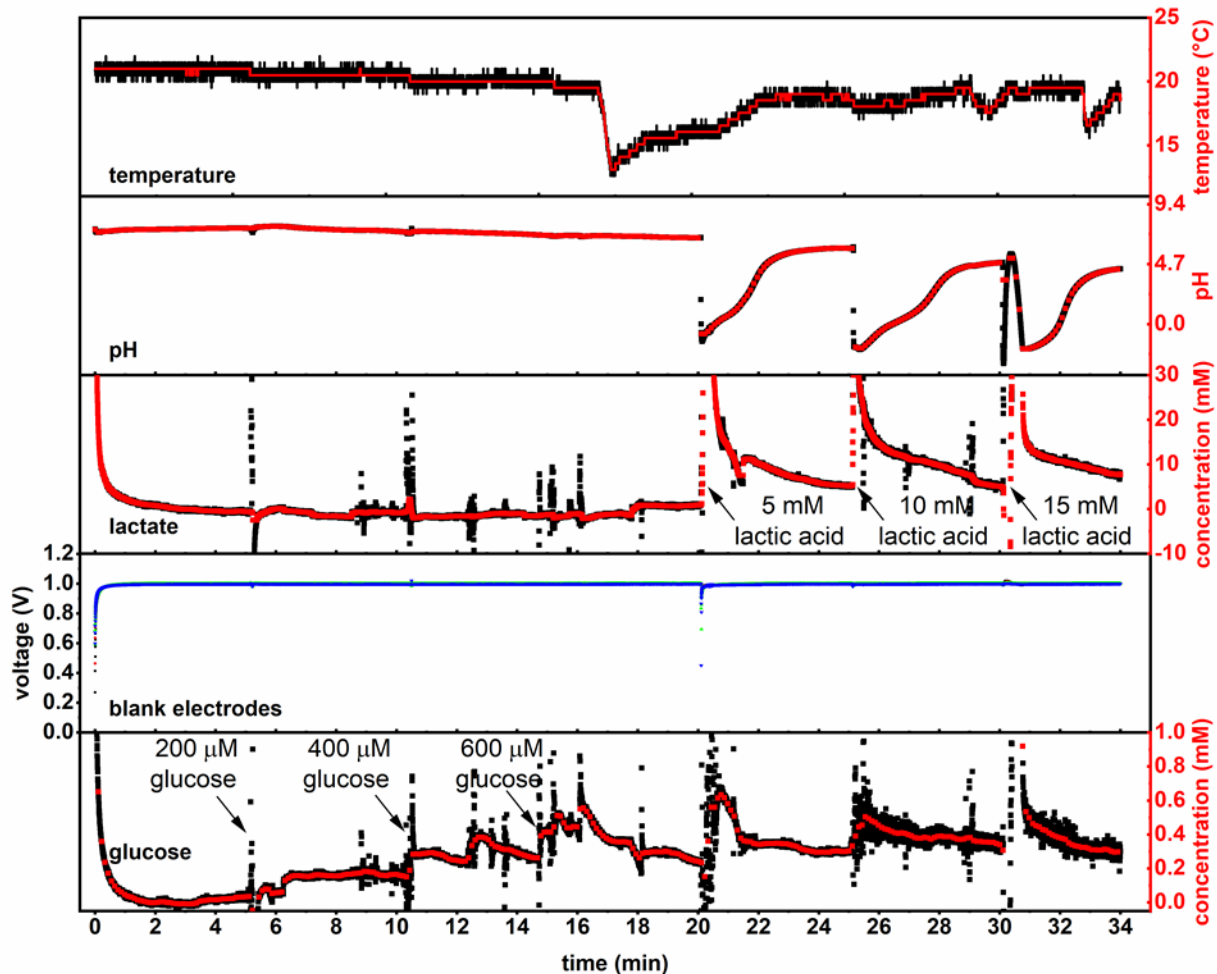


Figure S3.14. Multiplexed reading of glucose, lactate, pH, and temperature with a custom multiplexed sensing system in 1xPBS solution. Glucose was added at 5, 10, and 15 min, yielding 200, 400, and 600 μM of glucose in the test solution. Lactic acid was added at 20, 25, and 30 min, giving 5, 10, and 15 mM in the test solution. Conditions of the chronoamperometric measurements (bias: -0.1 V, pH: 7.4, working electrode area: 0.03 cm^2). The concentration of the glucose and lactate in the solution as well as the pH and temperature of the solution was calculated using the voltage output of the system in **Figure S3.13** and the sensitivity of the sensors. The black curve for glucose and lactate sensors represents the average of voltage outputs of four working electrodes. Averaging the responses from four working electrodes smooths the output of sensor and improves the accuracy of analyte detection. The red curves in the plot show further median averaging (100 points) of the black raw data.

Supplementary Table S3.9. Concentration of glucose and lactate in the collected and artificial sweat samples (n = 3).

	as-collected Glucose (μM)	as-collected Lactate (mM)	after glucose supplement Glucose (μM)	after lactate supplement Lactate (mM)
Subject 1	24.25	40.36	219.40 ^a	43.73 ^a
Subject 2	40.17	39.35	232.14 ^a	43.14 ^a
Artificial sweat	–	6.85	200 ^a	11.93 ^a

^aThese values were calculated based on the addition of stock solutions of glucose (1 mM) and lactate (1 M) to the as-collected or purchased samples. Starting concentrations were taken to be the values measured for the as-collected or purchased samples.

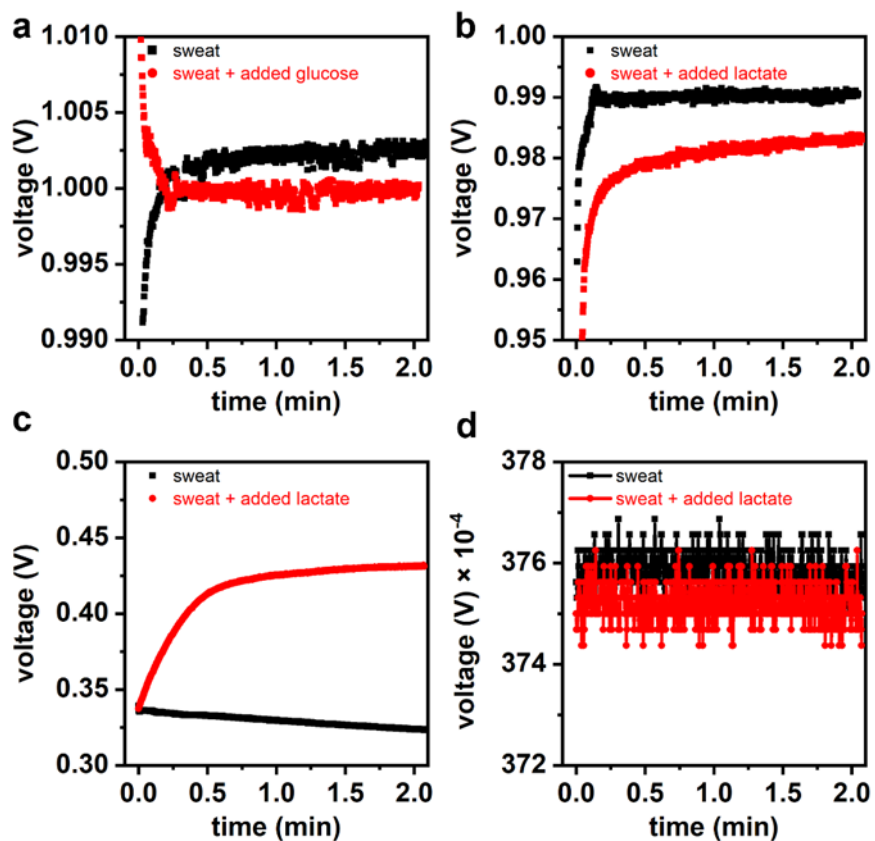


Figure S3.15. Multiplexed measurement of (a) glucose, (b) lactate, (c) pH, and (d) temperature in the collected sweat sample (pH 7.34) from the **Subject 1** using the custom multiplexing system. The black line shows the collected sample in all graphs. The red line indicates the collected sweat solution with added glucose or lactate. Addition of glucose or lactate to the collected sweat sample was detected by the custom system (20°C).

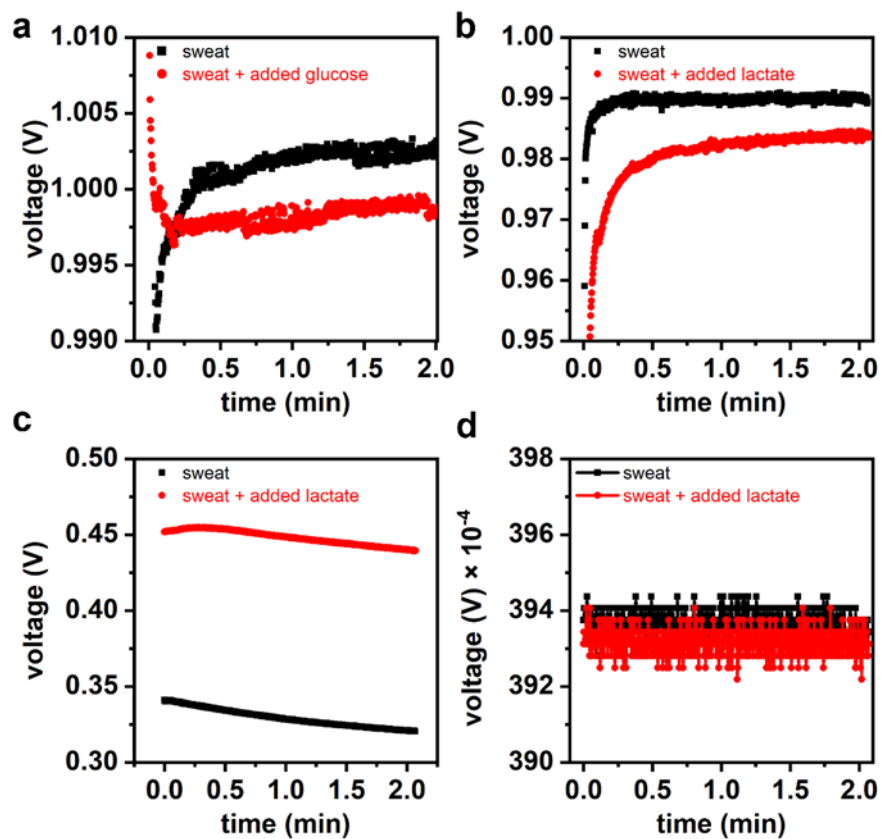


Figure S3.16. Multiplexed measurement of (a) glucose, (b) lactate, (c) pH, and (d) temperature in the as-collected sweat sample (pH 6.03) from the **Subject 2** using the custom multiplexing system. The black line shows the collected sample in all graphs. The red line indicates the collected sweat solution with added glucose or lactate. Addition of glucose and lactate to the collected sweat sample was detected by the custom system (20°C).

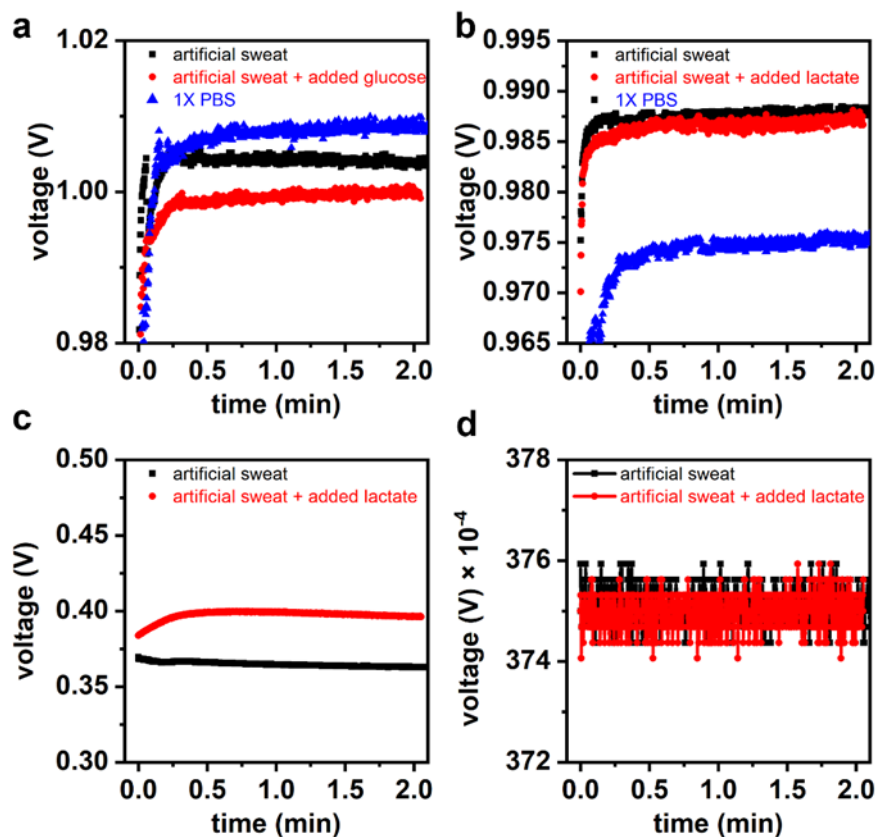


Figure S3.17. Multiplexed measurement of (a) glucose, (b) lactate, (c) pH, and (d) temperature in the artificial sweat solution (pH 4.48) using the custom multiplexing system. The black line shows the artificial sweat sample in all graphs. The red line indicates the artificial sweat solution with added glucose or lactate. Addition of glucose and lactate to the artificial sweat sample was detected by the custom system (20°C). The blue line indicates a “blank sample” (1X PBS).

3.7. References

1. WHO *Diet, nutrition and the prevention of chronic diseases*; Geneva, 2003.
2. Willett, W. C.; Koplan, J. P.; Nugent, R.; Dusenbury, C.; Puska, P.; Gaziano, T. A., Prevention of Chronic Disease by Means of Diet and Lifestyle Changes. *Disease Control Priorities in Developing Countries, 2nd Edition* **2006**, 833-850.
3. Phypers, B.; Pierce, J. T., Lactate physiology in health and disease. *Continuing Education in Anaesthesia, Critical Care & Pain* **2006**, *6* (3), 128-132.
4. Finsterer, J., Biomarkers of peripheral muscle fatigue during exercise. *Bmc Musculoskel Dis* **2012**, *13*.
5. Rassaei, L.; Olthuis, W.; Tsujimura, S.; Sudholter, E. J. R.; van den Berg, A., Lactate biosensors: current status and outlook. *Anal. Bioanal.Chem.* **2014**, *406* (1), 123-137.
6. Tudos, A. J.; Besselink, G. A. J.; Schasfoort, R. B. M., Trends in miniaturized total analysis systems for point-of-care testing in clinical chemistry. *Lab Chip* **2001**, *1* (2), 83-95.
7. Martin, C. L., i-STAT – Combining Chemistry and Haematology in PoCT. *The Clinical Biochemist Reviews* **2010**, *31* (3), 81-84.
8. Deiss, D.; Szadkowska, A.; Gordon, D.; Mallipedhi, A.; Schutz-Fuhrmann, I.; Aguilera, E.; Ringsell, C.; De Block, C.; Irace, C., Clinical Practice Recommendations on the Routine Use of Eversense, the First Long-Term Implantable Continuous Glucose Monitoring System. *Diabetes Technol. Ther.* **2019**, *21* (5), 254-264.
9. Shah, V. N.; Laffel, L. M.; Wadwa, R. P.; Garg, S. K., Performance of a Factory-Calibrated Real-Time Continuous Glucose Monitoring System Utilizing an Automated Sensor Applicator. *Diabetes Technol. Ther.* **2018**, *20* (6), 428-433.
10. Bariya, M.; Nyein, H. Y. Y.; Javey, A., Wearable sweat sensors. *Nat Electron* **2018**, *1* (3), 160-171.
11. Choi, J.; Ghaffari, R.; Baker, L. B.; Rogers, J. A., Skin-interfaced systems for sweat collection and analytics. *Sci. Adv.* **2018**, *4* (2).
12. Heikenfeld, J.; Jajack, A.; Feldman, B.; Granger, S. W.; Gaitonde, S.; Begtrup, G.; Katchman, B. A., Accessing analytes in biofluids for peripheral biochemical monitoring. *Nat. Biotechnol.* **2019**, *37* (4), 407-419.
13. Bandodkar, A. J.; Molinnus, D.; Mirza, O.; Guinovart, T.; Windmiller, J. R.; Valdés-Ramírez, G.; Andrade, F. J.; Schöning, M. J.; Wang, J., Epidermal tattoo potentiometric sodium sensors with wireless signal transduction for continuous non-invasive sweat monitoring. *Biosens. Bioelectron.* **2014**, *54*, 603-609.
14. Jia, W.; Bandodkar, A. J.; Valdés-Ramírez, G.; Windmiller, J. R.; Yang, Z.; Ramírez, J.; Chan, G.; Wang, J., Electrochemical Tattoo Biosensors for Real-Time Noninvasive Lactate Monitoring in Human Perspiration. *Anal. Chem.* **2013**, *85* (14), 6553-6560.
15. Kim, J.; de Araujo, W. R.; Samek, I. A.; Bandodkar, A. J.; Jia, W. Z.; Brunetti, B.; Paixao, T. R. L. C.; Wang, J., Wearable temporary tattoo sensor for real-time trace metal monitoring in human sweat. *Electrochem. Commun.* **2015**, *51*, 41-45.
16. Sonner, Z.; Wilder, E.; Heikenfeld, J.; Kasting, G.; Beyette, F.; Swaile, D.; Sherman, F.; Joyce, J.; Hagen, J.; Kelley-Loughnane, N.; Naik, R., The microfluidics of the eccrine sweat gland, including biomarker partitioning, transport, and biosensing implications. *Biomicrofluidics* **2015**, *9* (3), 031301.

17. Kim, J.; Jeerapan, I.; Imani, S.; Cho, T. N.; Bandodkar, A.; Cinti, S.; Mercier, P. P.; Wang, J., Noninvasive Alcohol Monitoring Using a Wearable Tattoo-Based Iontophoretic-Biosensing System. *ACS Sensors* **2016**, *1* (8), 1011-1019.
18. Bandodkar, A. J.; Jia, W. Z.; Yardimci, C.; Wang, X.; Ramirez, J.; Wang, J., Tattoo-Based Noninvasive Glucose Monitoring: A Proof-of-Concept Study. *Anal. Chem.* **2015**, *87* (1), 394-398.
19. Emaminejad, S.; Gao, W.; Wu, E.; Davies, Z. A.; Nyein, H. Y. Y.; Challa, S.; Ryan, S. P.; Fahad, H. M.; Chen, K.; Shahpar, Z.; Talebi, S.; Milla, C.; Javey, A.; Davis, R. W., Autonomous sweat extraction and analysis applied to cystic fibrosis and glucose monitoring using a fully integrated wearable platform. *PNAS* **2017**, *114* (18), 4625-4630.
20. Derbyshire, P. J.; Barr, H.; Davis, F.; Higson, S. P. J., Lactate in human sweat: a critical review of research to the present day. *J Physiol Sci* **2012**, *62* (6), 429-440.
21. Tur-Garcia, E. L.; Davis, F.; Collyer, S. D.; Holmes, J. L.; Barr, H.; Higson, S. P. J., Novel flexible enzyme laminate-based sensor for analysis of lactate in sweat. *Sensor Actuat B-Chem* **2017**, *242*, 502-510.
22. Heikenfeld, J., Non-invasive Analyte Access and Sensing through Eccrine Sweat: Challenges and Outlook circa 2016. *Electroanal* **2016**, *28* (6), 1242-1249.
23. Wolfe, S.; Cage, G.; Epstein, M.; Tice, L.; Miller, H.; Gordon, R. S., Jr., Metabolic studies of isolated human eccrine sweat glands. *The Journal of Clinical Investigation* **1970**, *49* (10), 1880-1884.
24. Hong, Y. J.; Lee, H.; Kim, J.; Lee, M.; Choi, H. J.; Hyeon, T.; Kim, D. H., Multifunctional Wearable System that Integrates Sweat-Based Sensing and Vital-Sign Monitoring to Estimate Pre-/Post-Exercise Glucose Levels. *Adv. Funct. Mater.* **2018**, *28* (47).
25. Lee, H.; Song, C.; Hong, Y. S.; Kim, M. S.; Cho, H. R.; Kang, T.; Shin, K.; Choi, S. H.; Hyeon, T.; Kim, D. H., Wearable/disposable sweat-based glucose monitoring device with multistage transdermal drug delivery module. *Sci. Adv.* **2017**, *3* (3).
26. Sakharov, D. A.; Shkurnikov, M. U.; Vagin, M. Y.; Yashina, E. I.; Karyakin, A. A.; Tonevitsky, A. G., Relationship between lactate concentrations in active muscle sweat and whole blood. *Bull Exp Biol Med* **2010**, *150* (1), 83-5.
27. Bandodkar, A. J.; Gutruf, P.; Choi, J.; Lee, K.; Sekine, Y.; Reeder, J. T.; Jeang, W. J.; Aranyosi, A. J.; Lee, S. P.; Model, J. B.; Ghaffari, R.; Su, C.-J.; Leshock, J. P.; Ray, T.; Verrillo, A.; Thomas, K.; Krishnamurthi, V.; Han, S.; Kim, J.; Krishnan, S.; Hang, T.; Rogers, J. A., Battery-free, skin-interfaced microfluidic/electronic systems for simultaneous electrochemical, colorimetric, and volumetric analysis of sweat. *Sci. Adv.* **2019**, *5* (1).
28. Choi, J.; Bandodkar, A. J.; Reeder, J. T.; Ray, T. R.; Turnquist, A.; Kim, S. B.; Nyberg, N.; Hourlier-Fargette, A.; Model, J. B.; Aranyosi, A. J.; Xu, S.; Ghaffari, R.; Rogers, J. A., Soft, Skin-Integrated Multifunctional Microfluidic Systems for Accurate Colorimetric Analysis of Sweat Biomarkers and Temperature. *ACS Sensors* **2019**, *4* (2), 379-388.
29. Gao, W.; Emaminejad, S.; Nyein, H. Y. Y.; Challa, S.; Chen, K.; Peck, A.; Fahad, H. M.; Ota, H.; Shiraki, H.; Kiriya, D.; Lien, D.-H.; Brooks, G. A.; Davis, R. W.; Javey, A., Fully integrated wearable sensor arrays for multiplexed in situ perspiration analysis. *Nature* **2016**, *529* (7587), 509-514.
30. Imani, S.; Bandodkar, A. J.; Mohan, A. M. V.; Kumar, R.; Yu, S. F.; Wang, J.; Mercier, P. P., A wearable chemical-electrophysiological hybrid biosensing system for real-time health and fitness monitoring. *Nat. Commun.* **2016**, *7*.

31. Lei, Y.; Zhao, W.; Zhang, Y.; Jiang, Q.; He, J.-H.; Baeumner, A. J.; Wolfbeis, O. S.; Wang, Z. L.; Salama, K. N.; Alshareef, H. N., A MXene-Based Wearable Biosensor System for High-Performance In Vitro Perspiration Analysis. *Small* **2019**, *15* (19), 1901190.
32. Nemiroski, A.; Christodouleas, D. C.; Hennek, J. W.; Kumar, A. A.; Maxwell, E. J.; Fernandez-Abedul, M. T.; Whitesides, G. M., Universal mobile electrochemical detector designed for use in resource-limited applications. *PNAS* **2014**, *111* (33), 11984-11989.
33. Rowe, A. A.; Bonham, A. J.; White, R. J.; Zimmer, M. P.; Yadgar, R. J.; Hobza, T. M.; Honea, J. W.; Ben-Yaacov, I.; Plaxco, K. W., CheapStat: An Open-Source, “Do-It-Yourself” Potentiostat for Analytical and Educational Applications. *PLoS One* **2011**, *6* (9), e23783.
34. Steinberg, M. D.; Kassal, P.; Kerekovic, I.; Steinberg, I. M., A wireless potentiostat for mobile chemical sensing and biosensing. *Talanta* **2015**, *143*, 178-183.
35. Harrington, M. S.; Anderson, L. B.; Robbins, J. A.; Karweik, D. H., Multiple Electrode Potentiostat. *Rev. Sci. Instrum.* **1989**, *60* (10), 3323-3328.
36. Levine, P. M.; Gong, P.; Levicky, R.; Shepard, K. L., Active CMOS sensor array for electrochemical biomolecular detection. *IEEE J. Solid-State Circuits* **2008**, *43* (8), 1859-1871.
37. Lima, E. A.; Snider, R. M.; Reiserer, R. S.; McKenzie, J. R.; Kimmel, D. W.; Eklund, S. E.; Wikswo, J. P.; Cliffel, D. E., Multichamber multipotentiostat system for cellular microphysiometry. *Sensor Actuat B-Chem* **2014**, *204*, 536-543.
38. Ghoreishizadeh, S. S.; Baj-Rossi, C.; Cavallini, A.; Carrara, S.; De Micheli, G., An Integrated Control and Readout Circuit for Implantable Multi-Target Electrochemical Biosensing. *IEEE Trans. Biomed. Circuits Syst.* **2014**, *8* (6), 891-898.
39. Yang, C.; Huang, Y.; Hassler, B. L.; Worden, R. M.; Mason, A. J., Amperometric Electrochemical Microsystem for a Miniaturized Protein Biosensor Array. *IEEE Trans. Biomed. Circuits Syst.* **2009**, *3* (3), 160-168.
40. Hu, Y. X.; Sharma, S.; Weatherwax, J.; Cass, A.; Georgiou, P., A Portable Multi-Channel Potentiostat for Real-Time Amperometric Measurement of Multi-Electrode Sensor Arrays. *Ieee Int Symp Circ S* **2016**, 1306-1309.
41. Ramfos, I.; Blionas, S.; Birbas, A., Architecture of a modular, multichannel readout system for dense electrochemical biosensor microarrays. *Meas. Sci. Technol.* **2015**, *26* (1).
42. Ramfos, I.; Vassiliadis, N.; Blionas, S.; Efstathiou, K.; Fragoso, A.; O'Sullivan, C. K.; Birbas, A., A compact hybrid-multiplexed potentiostat for real-time electrochemical biosensing applications. *Biosens Bioelectron* **2013**, *47*, 482-489.
43. Stefaniak, A. B.; Harvey, C. J., Dissolution of materials in artificial skin surface film liquids. *Toxicol. in Vitro* **2006**, *20* (8), 1265-1283.
44. Boysen, T. C.; Yanagawa, S.; Sato, F.; Sato, K., A modified anaerobic method of sweat collection. *J. Appl. Physiol.* **1984**, *56* (5), 1302-1307.
45. Harvey, C. J.; LeBouf, R. F.; Stefaniak, A. B., Formulation and stability of a novel artificial human sweat under conditions of storage and use. *Toxicol In Vitro* **2010**, *24* (6), 1790-6.
46. Wang, J., Electrochemical Glucose Biosensors. *Chem. Rev.* **2008**, *108* (2), 814-825.
47. Karyakin, A. A., Advances of Prussian blue and its analogues in (bio)sensors. *Curr. Opin. Electrochem.* **2017**, *5* (1), 92-98.
48. Mickelsen, O.; Keys, A., The composition of sweat, with special reference to the vitamins. *J. Biol. Chem.* **1943**, *149* (2), 479-490.

49. O'Halloran, M. P.; Pravda, M.; Guilbault, G. G., Prussian Blue bulk modified screen-printed electrodes for H₂O₂ detection and for biosensors. *Talanta* **2001**, *55* (3), 605-611.
50. Payne, M. E.; Zamarayeva, A.; Pister, V. I.; Yamamoto, N. A. D.; Arias, A. C., Printed, Flexible Lactate Sensors: Design Considerations Before Performing On-Body Measurements. *Sci. Rep.* **2019**, *9*.
51. Rathee, K.; Dhull, V.; Dhull, R.; Singh, S., Biosensors based on electrochemical lactate detection: A comprehensive review. *Biochemistry and Biophysics Reports* **2016**, *5*, 35-54.
52. Han, J. H.; Taylor, J. D.; Kim, D. S.; Kim, Y. S.; Kim, Y. T.; Cha, G. S.; Nam, H., Glucose biosensor with a hydrophilic polyurethane (HPU) blended with polyvinyl alcohol/vinyl butyral copolymer (PVAB) outer membrane. *Sens. Actuators, B* **2007**, *123* (1), 384-390.
53. Lyons, M. E. G., Modelling the transport and kinetics of electroenzymes at the electrode/solution interface. *Sensors-Basel* **2006**, *6* (12), 1765-1790.
54. Stikoniene, O.; Ivanauskas, F.; Laurinavicius, V., The influence of external factors on the operational stability of the biosensor response. *Talanta* **2010**, *81* (4-5), 1245-1249.
55. Patterson, M. J.; Galloway, S. D. R.; Nimmo, M. A., Variations in regional sweat composition in normal human males. *Exp Physiol* **2000**, *85* (6), 869-875.
56. Robergs, R. A.; Ghiasvand, F.; Parker, D., Biochemistry of exercise-induced metabolic acidosis. *Am J Physiol-Reg I* **2004**, *287* (3), R502-R516.
57. Song, E.; Choi, J. W., Conducting Polyaniline Nanowire and Its Applications in Chemiresistive Sensing. *Nanomaterials-Basel* **2013**, *3* (3), 498-523.
58. Chung, H. J.; Sulkin, M. S.; Kim, J. S.; Goudeseune, C.; Chao, H. Y.; Song, J. W.; Yang, S. Y.; Hsu, Y. Y.; Ghaffari, R.; Efimov, I. R.; Rogers, J. A., Stretchable, Multiplexed pH Sensors With Demonstrations on Rabbit and Human Hearts Undergoing Ischemia. *Adv. Healthcare Mater.* **2014**, *3* (1), 59-68.
59. Nyein, H. Y. Y.; Gao, W.; Shahpar, Z.; Emaminejad, S.; Challa, S.; Chen, K.; Fahad, H. M.; Tai, L. C.; Ota, H.; Davis, R. W.; Javey, A., A Wearable Electrochemical Platform for Noninvasive Simultaneous Monitoring of Ca²⁺ and pH. *ACS Nano* **2016**, *10* (7), 7216-7224.
60. Salvo, P.; Calisi, N.; Melai, B.; Cortigiani, B.; Mannini, M.; Caneschi, A.; Lorenzetti, G.; Paoletti, C.; Lomonaco, T.; Paolicchi, A.; Scataglini, I.; Dini, V.; Romanelli, M.; Fuoco, R.; Di Francesco, F., Temperature and pH sensors based on graphenic materials. *Biosens Bioelectron* **2017**, *91*, 870-877.
61. Abe, T.; Mayuzumi, J.; Kikuchi, N.; Arai, S., Seasonal-Variations in Skin Temperature, Skin Ph, Evaporative Water-Loss and Skin Surface Lipid Values on Human-Skin. *Chem Pharm Bull* **1980**, *28* (2), 387-392.
62. Saltin, B.; Stolwijk, J. A.; Bergh, U.; Gagge, A. P., Body Temperatures and Sweating during Exhaustive Exercise. *J. Appl. Physiol.* **1972**, *32* (5), 635-&.
63. Chen, Y.; Lu, B. W.; Chen, Y. H.; Feng, X., Breathable and Stretchable Temperature Sensors Inspired by Skin. *Sci. Rep.* **2015**, *5*.
64. Lacy, F., Using Nanometer Platinum Films as Temperature Sensors (Constraints From Experimental, Mathematical, and Finite-Element Analysis). *IEEE Sens. J.* **2009**, *9* (9), 1111-1117.
65. Schmidtke, D. W.; Pishko, M. V.; Quinn, C. P.; Heller, A., Statistics for Critical Clinical Decision Making Based on Readings of Pairs of Implanted Sensors. *Anal. Chem.* **1996**, *68* (17), 2845-2849.

66. Sharifi, A.; Varsavsky, A.; Ulloa, J.; Horsburgh, J. C.; McAuley, S. A.; Krishnamurthy, B.; Jenkins, A. J.; Colman, P. G.; Ward, G. M.; MacIsaac, R. J.; Shah, R.; O'Neal, D. N., Redundancy in Glucose Sensing: Enhanced Accuracy and Reliability of an Electrochemical Redundant Sensor for Continuous Glucose Monitoring. *J. Diabetes Sci. Technol.* **2016**, *10* (3), 669-678.
67. Ward, W. K.; Casey, H. M.; Quinn, M. J.; Federiuk, I. F.; Wood, M. D., A Fully Implantable Subcutaneous Glucose Sensor Array: Enhanced Accuracy from Multiple Sensing Units and a Median-Based Algorithm. *Diabetes Technol. Ther.* **2003**, *5* (6), 943-952.
68. Guinovart, T.; Crespo, G. A.; Rius, F. X.; Andrade, F. J., A reference electrode based on polyvinyl butyral (PVB) polymer for decentralized chemical measurements. *Anal. Chim. Acta* **2014**, *821*, 72-80.
69. Sempionatto, J. R.; Nakagawa, T.; Pavinatto, A.; Mensah, S. T.; Imani, S.; Mercier, P.; Wang, J., Eyeglasses based wireless electrolyte and metabolite sensor platform. *Lab Chip* **2017**, *17* (10), 1834-1842.
70. Lee, H.; Choi, T. K.; Lee, Y. B.; Cho, H. R.; Ghaffari, R.; Wang, L.; Choi, H. J.; Chung, T. D.; Lu, N.; Hyeon, T.; Choi, S. H.; Kim, D.-H., A graphene-based electrochemical device with thermoresponsive microneedles for diabetes monitoring and therapy. *Nat Nano* **2016**, *11* (6), 566-572.
71. Choi, J.; Kang, D.; Han, S.; Kim, S. B.; Rogers, J. A., Thin, Soft, Skin-Mounted Microfluidic Networks with Capillary Bursting Valves for Chrono-Sampling of Sweat. *Adv. Healthcare Mater.* **2017**, *6* (5).
72. Koh, A.; Kang, D.; Xue, Y.; Lee, S.; Pielak, R. M.; Kim, J.; Hwang, T.; Min, S.; Banks, A.; Bastien, P.; Manco, M. C.; Wang, L.; Ammann, K. R.; Jang, K. I.; Won, P.; Han, S.; Ghaffari, R.; Paik, U.; Slepian, M. J.; Balooch, G.; Huang, Y. G.; Rogers, J. A., A soft, wearable microfluidic device for the capture, storage, and colorimetric sensing of sweat. *Sci. Transl. Med.* **2016**, *8* (366).
73. Nyein, H. Y. Y.; Bariya, M.; Kivimäki, L.; Uusitalo, S.; Liaw, T. S.; Jansson, E.; Ahn, C. H.; Hangasky, J. A.; Zhao, J.; Lin, Y.; Happonen, T.; Chao, M.; Liedert, C.; Zhao, Y.; Tai, L.-C.; Hiltunen, J.; Javey, A., Regional and correlative sweat analysis using high-throughput microfluidic sensing patches toward decoding sweat. *Sci. Adv.* **2019**, *5* (8), eaaw9906.
74. Han, W.; He, H.; Zhang, L.; Dong, C.; Zeng, H.; Dai, Y.; Xing, L.; Zhang, Y.; Xue, X., A Self-Powered Wearable Noninvasive Electronic-Skin for Perspiration Analysis Based on Piezo-Biosensing Unit Matrix of Enzyme/ZnO Nanoarrays. *ACS Appl. Mater. Interfaces* **2017**, *9* (35), 29526-29537.
75. Lu, Y.; Jiang, K.; Chen, D.; Shen, G. Z., Wearable sweat monitoring system with integrated micro-supercapacitors. *Nano Energy* **2019**, *58*, 624-632.
76. Xu, G.; Cheng, C.; Liu, Z.; Yuan, W.; Wu, X.; Lu, Y.; Low, S. S.; Liu, J.; Zhu, L.; Ji, D.; Li, S.; Chen, Z.; Wang, L.; Yang, Q.; Cui, Z.; Liu, Q., Battery-Free and Wireless Epidermal Electrochemical System with All-Printed Stretchable Electrode Array for Multiplexed In Situ Sweat Analysis. *Advanced Materials Technologies* **2019**, *4* (7), 1800658.
77. Blanco, J. R.; Ferrero, F. J.; Campo, J. C.; Anton, J. C.; Pingarron, J. M.; Reviejo, A. J.; Manso, J. In *Design of a Low-Cost Portable Potentiostat for Amperometric Biosensors*, 2006 IEEE Instrumentation and Measurement Technology Conference Proceedings, 24-27 April 2006; 2006; pp 690-694.

78. Loncaric, C.; Tang, Y. T.; Ho, C.; Parameswaran, M. A.; Yu, H. Z., A USB-based electrochemical biosensor prototype for point-of-care diagnosis. *Sensor Actuat B-Chem* **2012**, *161* (1), 908-913.
79. Cruz, A. F. D.; Norena, N.; Kaushik, A.; Bhansali, S., A low-cost miniaturized potentiostat for point-of-care diagnosis. *Biosens Bioelectron* **2014**, *62*, 249-254.
80. Dryden, M. D. M.; Wheeler, A. R., DStat: A Versatile, Open-Source Potentiostat for Electroanalysis and Integration. *PLoS One* **2015**, *10* (10).
81. Ainla, A.; Mousavi, M. P. S.; Tsaloglou, M. N.; Redston, J.; Bell, J. G.; Fernandez-Abedul, M. T.; Whitesides, G. M., Open-Source Potentiostat for Wireless Electrochemical Detection with Smartphones. *Anal. Chem.* **2018**, *90* (10), 6240-6246.
82. Kassal, P.; Steinberg, I. M.; Steinberg, M. D., Wireless smart tag with potentiometric input for ultra low-power chemical sensing. *Sensor Actuat B-Chem* **2013**, *184*, 254-259.
83. Anastasova, S.; Crewther, B.; Bembnowicz, P.; Curto, V.; Ip, H. M. D.; Rosa, B.; Yang, G.-Z., A wearable multisensing patch for continuous sweat monitoring. *Biosens. Bioelectron.* **2017**, *93*, 139-145.
84. Bembnowicz, P.; Yang, G. Z.; Anastasova, S.; Spehar-Deleze, A. M.; Vadgama, P., Wearable Electronic Sensor for Potentiometric and Amperometric Measurements. *2013 Ieee International Conference on Body Sensor Networks (Bsn)* **2013**.
85. Sun, A.; Venkatesh, A. G.; Hall, D. A., A Multi-Technique Reconfigurable Electrochemical Biosensor: Enabling Personal Health Monitoring in Mobile Devices. *IEEE Trans. Biomed. Circuits Syst.* **2016**, *10* (5), 945-954.
86. Zhao, C.; Thuo, M. M.; Liu, X., A microfluidic paper-based electrochemical biosensor array for multiplexed detection of metabolic biomarkers. *Sci. Technol. Adv. Mater.* **2013**, *14* (5), 054402.
87. De Venuto, D.; Torre, M. D.; Boero, C.; Carrara, S.; De Micheli, G., A Novel Multi-Working Electrode Potentiostat for Electrochemical Detection of Metabolites. *2010 Ieee Sensors* **2010**, 1572-1577.
88. Chao, L.; Wang, W.; Dai, M. Z.; Ma, Y. X.; Sun, L. G.; Qin, X. L.; Xie, Q. J., Step-by-step electrodeposition of a high-performance Prussian blue-gold nanocomposite for H₂O₂ sensing and glucose biosensing. *J. Electroanal. Chem.* **2016**, *778*, 66-73.
89. Li, L. L.; Peng, J. M.; Chu, Z. Y.; Jiang, D. F.; Jin, W. Q., Single layer of graphene/Prussian blue nano-grid as the low-potential biosensors with high electrocatalysis. *Electrochim. Acta* **2016**, *217*, 210-217.
90. Ramanavicius, A.; Rekeraitė, A. I.; Valiunas, R.; Valiuniene, A., Single-step procedure for the modification of graphite electrode by composite layer based on polypyrrole, Prussian blue and glucose oxidase. *Sensor Actuat B-Chem* **2017**, *240*, 220-223.
91. Zhang, Y. N.; Liu, Y.; Chu, Z. Y.; Shi, L.; Jin, W. Q., Amperometric glucose biosensor based on direct assembly of Prussian blue film with ionic liquid-chitosan matrix assisted enzyme immobilization. *Sensor Actuat B-Chem* **2013**, *176*, 978-984.
92. Yin, B.; Yuan, R.; Chai, Y.; Chen, S.; Cao, S.; Xu, Y.; Fu, P., Amperometric glucose biosensors based on layer-by-layer assembly of chitosan and glucose oxidase on the Prussian blue-modified gold electrode. *Biotechnol. Lett* **2008**, *30* (2), 317-322.
93. Xue, M. H.; Xu, Q.; Zhou, M.; Zhu, J. J., In situ immobilization of glucose oxidase in chitosan-gold nanoparticle hybrid film on Prussian Blue modified electrode for high-sensitivity glucose detection. *Electrochem. Commun.* **2006**, *8* (9), 1468-1474.

94. Zhao, W.; Xu, J. J.; Shi, C. G.; Chen, H. Y., Multilayer membranes via layer-by-layer deposition of organic polymer protected Prussian blue nanoparticles and glucose oxidase for glucose biosensing. *Langmuir* **2005**, *21* (21), 9630-9634.
95. Garjonyte, R.; Malinauskas, A., Amperometric glucose biosensors based on Prussian Blue- and polyaniline-glucose oxidase modified electrodes. *Biosens Bioelectron* **2000**, *15* (9-10), 445-451.
96. Chi, Q. J.; Dong, S. J., Amperometric Biosensors Based on the Immobilization of Oxidases in a Prussian Blue Film by Electrochemical Codeposition. *Anal. Chim. Acta* **1995**, *310* (3), 429-436.
97. Garjonyte, R.; Yigzaw, Y.; Meskys, R.; Malinauskas, A.; Gorton, L., Prussian Blue- and lactate oxidase-based amperometric biosensor for lactic acid. *Sensor Actuat B-Chem* **2001**, *79* (1), 33-38.
98. Petropoulos, K.; Piermarini, S.; Bernardini, S.; Palleschi, G.; Moscone, D., Development of a disposable biosensor for lactate monitoring in saliva. *Sensor Actuat B-Chem* **2016**, *237*, 8-15.
99. Kim, J.; Valdes-Ramirez, G.; Bandodkar, A. J.; Jia, W. Z.; Martinez, A. G.; Ramirez, J.; Mercier, P.; Wang, J., Non-invasive mouthguard biosensor for continuous salivary monitoring of metabolites. *Analyst* **2014**, *139* (7), 1632-1636.
100. Lamas-Ardisana, P. J.; Loaiza, O. A.; Anorga, L.; Jubete, E.; Borghei, M.; Ruiz, V.; Ochoteco, E.; Cabanero, G.; Grande, H. J., Disposable amperometric biosensor based on lactate oxidase immobilised on platinum nanoparticle-decorated carbon nanofiber and poly(diallyldimethylammonium chloride) films. *Biosens Bioelectron* **2014**, *56*, 345-351.

CHAPTER 4: Conclusion and Future Work

4.1. Summary

The fusion of biochemical sensors with biophysical sensors in a wireless wearable system opens up new opportunities in digital health and personalized medicine, such as overall health and wellness management, disease prediction and therapeutics, and evaluation of the trends in disease progression in large populations. This dissertation contributes to this vision by developing a fully integrated wireless multiplexed systems that can analyze the composition of sweat noninvasively and provide the trends of human biochemistry at a molecular level.

To this end, a wearable system with a flexible multiplexed sensor array is demonstrated in this dissertation to measure metabolites in sweat (glucose and lactate) along with sweat pH and skin temperature. The flexible sensing array can measure the variations of sweat analytes and skin temperature in the physiological ranges of these biomarkers. The developed wearable system integrates commercially available analog-front-ends (*e.g.*, potentiostats) and enables simultaneous and multiplexed reading from the flexible sensor array. The demonstrated system acts as a miniaturized form of three benchtop potentiostats and can perform chronoamperometric measurements from multiple electrodes. With this integrated system, we demonstrated an *in-vitro* analysis of artificial sweat as well as collected sweat from human trials.

There are still remaining challenges that need to be addressed in order to realize a fully functioning wearable system that is commercially viable. Closing this technological gap will require cross-disciplinary efforts in physiology, biochemistry, material science, physics, and electronics. First, sensor stability is one of the main areas that need to be improved to enable long-term use of biochemical sensors in wearables, which will require a dramatic improvement from what is currently available in the literature. Second, the signal to noise ratio of the sensors needs

to be improved to create wearables that are immune to the environmental and motion interferences. Third, long-term human trials with varying exercise intensity and movements need to be carried out to assess the accuracy of the system. Finally, standardized sweat collection methods need to be developed for wearables for varying sweat rate conditions, and the biomarker levels in sweat needs to be correlated with gold-standard measurements (*i.e.*, blood) to demonstrate its clinical relevance. Meeting these steps will create new disruptive technologies that can continuously sense the biomarkers of human physiology that many of us are excited to see in our daily lives.

4.2. Future Work: Multiplexed Electrochemical and Biophotonic Sensing

Another research I explored was about the development of a wearable, wireless system toward the measurement of cardiovascular health and athletic performance (**Figure 4.1**). The motivation of this research originated from the relation of lactate and oxygen in anaerobic respiration, where the rise of blood lactate is accompanied by inadequate tissue perfusion or reduced tissue oxygenation. *The objective of this study is to develop a wearable system for continuous measurement and correlation of sweat lactate and tissue oxygenation via noninvasive electrochemical and optical sensors.* The overview of the designed system is briefly discussed below with its preliminary results. Future work will include a comprehensive benchtop analysis of the wearable system and its performance evaluation in human trials. The approved human trial protocol by the Institutional Review Board (IRB) is provided in Appendix G.

System overview: The wearable system comprises flexible optical and biochemical sensors that can continuously measure sweat lactate and pH, heart rate, skin temperature, and tissue oxygenation. A custom wireless wearable optical and electrochemical sensing system was developed for integration with the optical and electrochemical sensors. The wearable system is controlled by a system-on-chip (BLE113, Texas Instruments), which reads data from the various

analog data sources and transmits the data over Bluetooth Low Energy (BLE) to a data aggregator (PC). A potentiostat analog-front-end (LMP91000, Texas Instruments) is used to interface with the lactate sensor. The potentiostat outputs an analog signal proportional to the current generated by the electrochemical lactate sensor, which is converted to a 16-bit digital value by an analog-to-digital converter (ADS1115, Texas Instruments). The ADC is also interfaced with an analog-front-end (LMP91200, Texas Instruments) for pH measurement. Both the LMP91000 and LMP91200 are connected to the lactate and pH sensors via a 5-Pin flexible flat cable (FFC) ribbon connector.

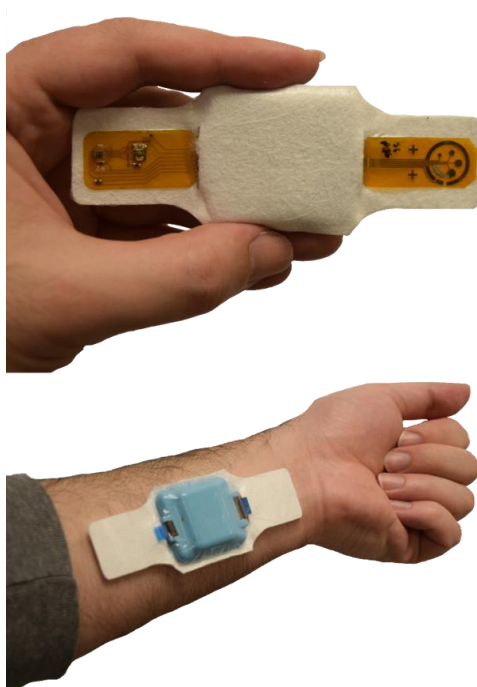


Figure 4.1. A fully integrated wireless wearable system with electrochemical and optical sensing capabilities. The overall system houses flexible optical and electrochemical sensors that are attached to the custom system via an FFC connector. The optical sensor includes three-wavelength LEDs, a light sensor integrated circuit (IC), and a thermistor, whereas the biochemical sensor incorporates amperometric lactate and potentiometric polyaniline-based pH sensors on a flexible polyimide film. The custom-design system is packaged in silicone and mounted on a nonwoven fabric.

The main circuit board also connects via a 5-pin terminal to a secondary board containing an FFC connector and supporting circuitry for the Si1143 Light Sensor IC (Silicon Labs), which contains integrated LED drive control as well as a near-infrared spectrum photodiode. The Si1143 and LEDs are mounted on the custom flexible optical sensor.

The total average power consumption of the wireless wearable optical and electrochemical sensing system during data collection and transmission is 14.6 mA. The device uses a 150 mAh battery, which gives the device a battery life of approximately 10 hours. The system is packaged in silicone and integrated onto a nonwoven fabric to improve device durability and user comfort during its use.

Preliminary Results: The initial benchtop characterization of the optical and biochemical sensors are given in **Figure 4.2 - 4.4**. Characterization of the temperature sensor was performed by placing the temperature sensor on a hot plate and varying its temperature from 22 to 45°C (**Figure 4.2a**). The resistance of the sensor, a negative temperature coefficient (NTC) thermistor, decreased with temperature due to the increase in the number of electrons in the conduction band of the semiconductor. **Figure 4.2b** demonstrates the characterization of electrodeposited polyaniline (PANI) pH sensor in aqueous buffer solutions with different pH values. The pH sensor deprotonates in alkaline solutions, which decreases its output potential relative to an Ag/AgCl reference electrode.

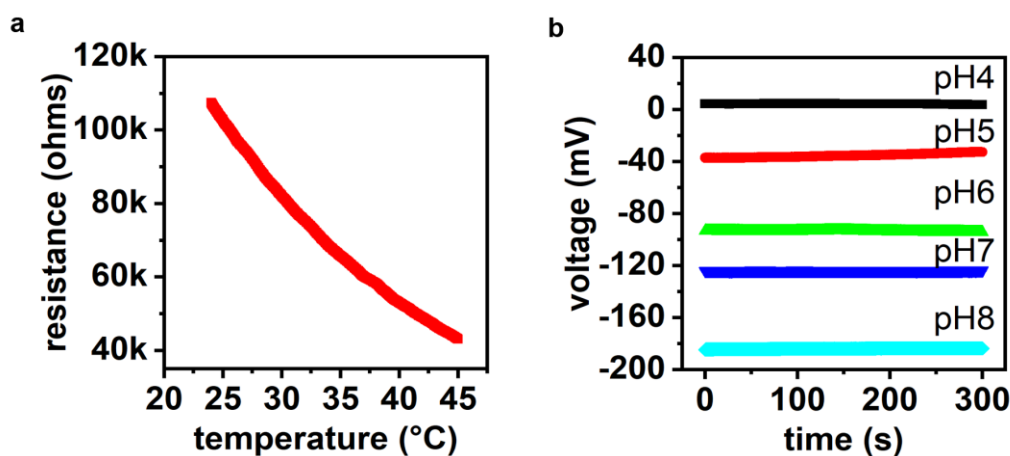


Figure 4.2. (a) Characterization of electrical resistance change of 0402 size 100k thermistor (Murata) with temperature (from 22°C to 45°C). (b) Measurement of the voltage output of a polyaniline pH sensor in varying pH buffer solutions (4 to 8) relative to a printed Ag/AgCl reference electrode.

The optical sensor interfaces the skin and measures the changes in the light attenuation.

Figure 4.2 shows a photoplethysmography (PPG) signal along with an ECG signal. The ECG signal was measured with a chest-worn instrument (Zephyr™ Bioharness) and used as a control for heart rate calculations. The PPG signal (black curve) shows the intensity of light that is modulated by the blood volume changes due to each heartbeat. The systolic peaks were used for measurement of heart rate over time.

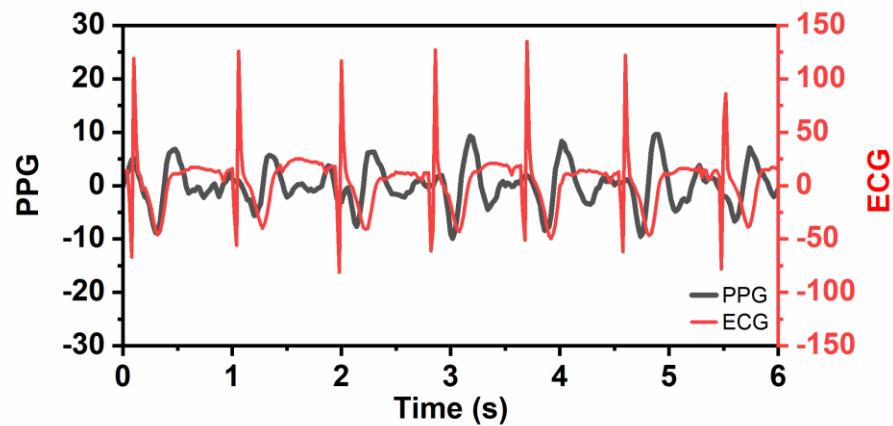


Figure 4.2. Continuous photoplethysmogram (PPG) measurement using the developed wireless, wearable system. The PPG signal (black line) was denoised, and its baseline shift was subtracted. LED wavelength: 850 nm. Electrocardiogram (ECG) signal was measured using Zephyr™ Bioharness system.

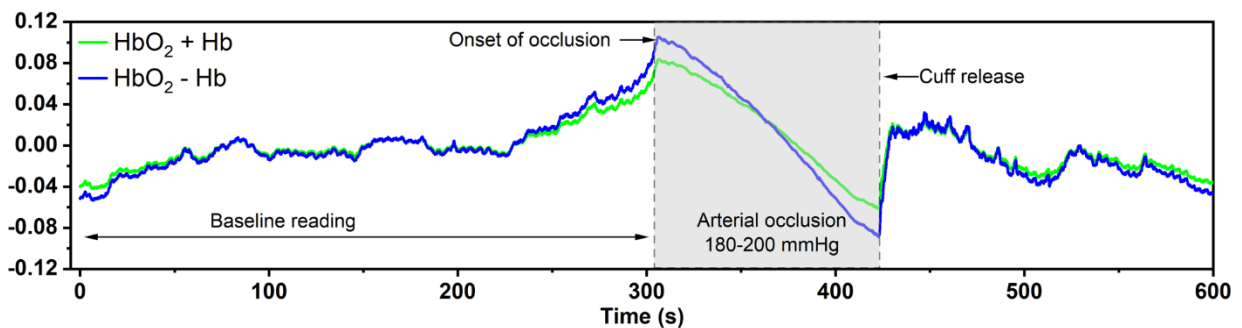


Figure 4.3. Continuous assessment of tissue oxygenation (HbO_2-Hb) and blood volume (HbO_2+Hb) on the forearm of a subject via continuous-wave near-infrared spectrometry (CW-NIRS) (LED wavelengths: 625nm and 940nm). A manual inflatable cuff was attached to the upper arm of the subject (sitting), and a brief arterial occlusion (180-200 mmHg) was induced using a manual sphygmomanometer.

Figure 4.3 shows the blood volume and oxygenation changes over time on the forearm of a subject in a sitting position upon an arterial occlusion on the upper arm with an inflatable cuff. The relative changes in oxygenation and blood volume were measured using continuous-wave near-infrared spectroscopy (CW-NIRS). The NIRS method utilizes absorption coefficient differences of oxygenated (HbO₂) and deoxygenated hemoglobin (Hb) in the blood and provides relative measurements of HbO₂, Hb, oxygenation (HbO₂-Hb), blood volume (HbO₂+Hb) according to the Modified Beer-Lambert Law, as shown in Equations 1 to 5. The attenuation of the light is given by the Eqn. 1. OD_λ is the optical density (attenuation) for wavelength λ. I_{in} and I_{out} are the incident light intensity (*i.e.*, irradiance, W/cm²) and detected light intensity (W/cm²), respectively. A_λ and S_λ are the attenuation due to absorbance and scattering at wavelength λ. The absorbance due to Hb and HbO₂ is given in Eqn. 2, where ε_{i,λ} and C_i are the extinction coefficients of Hb and HbO₂ at wavelength λ and concentration of Hb and HbO₂, respectively. L_λ is the path length of light, which is equal to the multiplication of the light source-detector distance (d) by the differential path length factor (DPF_λ). DPF_λ is a wavelength-dependent constant (Eqn. 3) and required for the correction of the photon path length in the tissue due to scattering. μ_{a,λ} and μ'_{s,λ} are the absorption and reduced scattering coefficients at wavelength λ, respectively. With the assumption of constant DPF_λ, two successive measurements of the OD_λ yields differential optical density (ΔOD_λ), canceling out the effect of scattering and absorption due to other time-invariant chromophores in the tissue (Eqn. 4). When Eqn. 4 is solved for two unknown variables (*i.e.*, ΔC_{Hb} and ΔC_{HbO₂}) at two different wavelengths, Eqn. 5 is obtained.

$$\text{Attenuation} = OD_{\lambda} = -\log_{10} \frac{I_{out}}{I_{in}} = A_{\lambda} + S_{\lambda} \quad (1)$$

$$A_{\lambda} = \sum_{i=Hb, HbO_2} \varepsilon_{i,\lambda} C_i L_{\lambda} = \sum_{i=Hb, HbO_2} \varepsilon_{i,\lambda} C_i d DPF_{\lambda} \quad (2)$$

$$DPF_{\lambda} = \frac{1}{2} \left(\frac{3\mu'_{s,\lambda}}{\mu_{a,\lambda}} \right)^{1/2} \left[1 - \frac{1}{1 + d \cdot (3\mu'_{s,\lambda} \mu_{a,\lambda})^{1/2}} \right] \quad (3)$$

$$\Delta OD_{\lambda} = OD_{\lambda,final} - OD_{\lambda,initial} = \sum_{i=Hb,HbO_2} \varepsilon_{i,\lambda} \Delta C_i d DPF_{\lambda} \quad (4)$$

$$\begin{bmatrix} \Delta C_{HbO_2} \\ \Delta C_{Hb} \end{bmatrix} = \left\{ d \cdot \begin{bmatrix} \varepsilon_{HbO_2(\lambda_1)} & \varepsilon_{HbO_2(\lambda_2)} \\ \varepsilon_{Hb(\lambda_1)} & \varepsilon_{Hb(\lambda_2)} \end{bmatrix} x \begin{bmatrix} DPF_{\lambda_1} & 0 \\ 0 & DPF_{\lambda_2} \end{bmatrix} \right\}^{-1} x \begin{bmatrix} \Delta OD_{\lambda_1} \\ \Delta OD_{\lambda_2} \end{bmatrix} \quad (5)$$

Upon a brief arterial occlusion (180-200 mmHg), the blood flow to the forearm decreased, and subsequently, oxygen utilization in the local tissue and deoxygenated hemoglobin concentration continued to increase. This brief disturbance in tissue hemodynamics is highlighted in **Figure 4.3**. The oxygenation and blood volume dropped until the arm cuff was deflated, and the blood perfusion is restored.

Overall, this study demonstrated continuous measurement of tissue oxygenation and PPG and provided benchtop analyses of temperature and pH sensors. Future work will involve the incorporation of stable lactate sensors, benchtop trials with the developed custom wireless system, and its implementation in human trials. Continuous measurement of sweat biomarkers along with heart rate, blood pressure, and tissue oxygenation will unveil the intricate physiological patterns and benefit real-time assessment of the cardiovascular, pulmonary, and muscular systems.

APPENDICES

Appendix A: Fabric-Based Wearable Dry Electrodes for Body Surface Biopotential

Recording

Murat A. Yokus and Jesse S. Jur

**As published in IEEE Transactions on Biomedical Engineering (2015)*

Abstract

A flexible and conformable dry electrode design on nonwoven fabrics is examined as a sensing platform for biopotential measurements. Due to limitations of commercial wet electrodes (e.g. shelf life, skin irritation), dry electrodes are investigated as potential candidates for long term monitoring of ECG signals. Multi-layered dry electrodes are fabricated by screen-printing of Ag/AgCl conductive inks on flexible nonwoven fabrics. This study focuses on the investigation of the skin-electrode interface, form factor design, electrode body placement of printed dry electrodes for a wearable sensing platform. ECG signals obtained with dry and wet electrodes are comparatively studied as a function of body posture and movement. Experimental results show that skin-electrode impedance is influenced by the printed electrode area, skin-electrode interface material, and applied pressure. The printed electrode yields comparable ECG signals to wet electrodes, and the QRS peak amplitude of the ECG signal is dependent on the printed electrode area and electrode on body spacing. Overall, fabric-based printed dry electrodes present an inexpensive health monitoring platform solution for mobile wearable electronics applications by fulfilling user comfort and wearability.

Introduction

Increase in human life standards with advancements in electronics, telecommunications, complex computing, artificial intelligence and notable growth in chronic cardiovascular diseases (e.g. arrhythmia, hypertension and angina pectoris) have resulted in the evolution of fabric/textile-

based wearable biomedical health monitoring systems such as WEALTHY [1], LifeShirt® [2], LifeGuard [3], which can be worn in everyday situations. This mobile and ubiquitous wearable monitoring provides users an opportunity to track their physical activities (e.g. steps, calorie burned) and monitor their health conditions (e.g. heart rate, ExG, sweat, SpO₂, and body temperature). These wearable systems are also critical in early detection of diseases such as sudden infant death syndrome [4] and follow up examination of patients who experienced a cardiovascular surgery or a pharmacological treatment. These unobtrusive wearable devices not only increase user comfort but also decrease the dependency on large and bulky hospital equipment, especially for those who have chronic diseases and need to be monitored continuously for long periods of time, which eliminates high hospitalization expenses.

Due to the dominance of heart-related issues, electrocardiogram (ECG) is a commonly studied analysis in wearable health monitoring systems to investigate the electrical activity of the heart. The most common ECG electrode type in a hospital environment is the disposable wet electrodes due to their good signal performance in a short period of time. However, short shelf life, skin irritation and dermal inflammation issues as well as conductance variation of wet electrode gels over time (i.e. distorted signals, noise, and artifacts) limit their usage for long term monitoring [5]. Wearable textile-based knitted [6], woven [7], and embroidered [8] dry textile electrodes have been proposed in the literature to enable long term monitoring. The benefit of textile-based electrodes is that conductive yarns or fibers can be knitted or woven into a complete wearable sensing system. Whole garment knitting machines enable a multi-conductive yarn feeding system, which is useful for customized electrodes on desired locations on a garment. However, these electrodes tend to change their electrical properties upon stretching. Additionally, the rough surface texture formed by conductive yarn loops in a garment may create skin irritation during

persistent motion and eventually result in discomfort. Moreover, carbon nanotube-polydimethylsiloxane (CNT-PDMS) polymeric composites and Au deposited on PDMS have also been studied as a potential flexible dry electrodes [9], [10]. CNT loaded polymeric electrodes yields varying conductivity levels depending on percent filler content. Both CNT loaded and Au deposited polymeric substrates have been designed as individual sensing electrodes or as a wearable wristband for long-term monitoring of physiological signals. Invasiveness (i.e., skin penetration) of the electrode structure, complications with regard to filler dispersion in polymeric matrix, polymeric electrode integration on wearables, the necessity of expensive clean lab tools and complex manufacturing steps have the potential to restrain their ubiquitous utilization in current wearable monitoring systems. As an alternative to the aforementioned electrodes, screen-printed dry electrodes have been studied. Screen printing methods offer a low cost means toward functional wearable electronics. Yoo *et al.* fabricated silver ink differential dry electrodes on a t-shirt by screen printing [11]. In another study, Merritt *et al.* fabricated dry screen-printed active electrodes by using silver/silver chloride (Ag/AgCl) paste and improved the performance of dry electrodes [12]. However, direct attachment of active electrode circuitry posed durability issues.

Another type of electrode classification is based upon the change in half-cell potential of the double charge layer when current passes electrode-electrolyte interface [13]. In polarizable electrodes, there is no actual charge traveling across the interface. However, ideal nonpolarizable electrodes have charge transfer across the electrode-electrolyte interface, and half-cell potential does not change when current is applied. Nonpolarizable electrodes are desired for recording small-amplitude biosignals from the body surface. Ag/AgCl electrodes have low half-cell potential and also show similar characteristics to perfectly nonpolarizable electrodes. A comprehensive long-term study of surface electrode materials was performed in 0.9% NaCl solution by Hoffmann

et al. [14]. It was shown that nonpolarizable electrodes (e.g., Ag/AgCl, platinum black) show low impedance values at low frequencies compared to polarizable electrodes (e.g., silver and platinum).

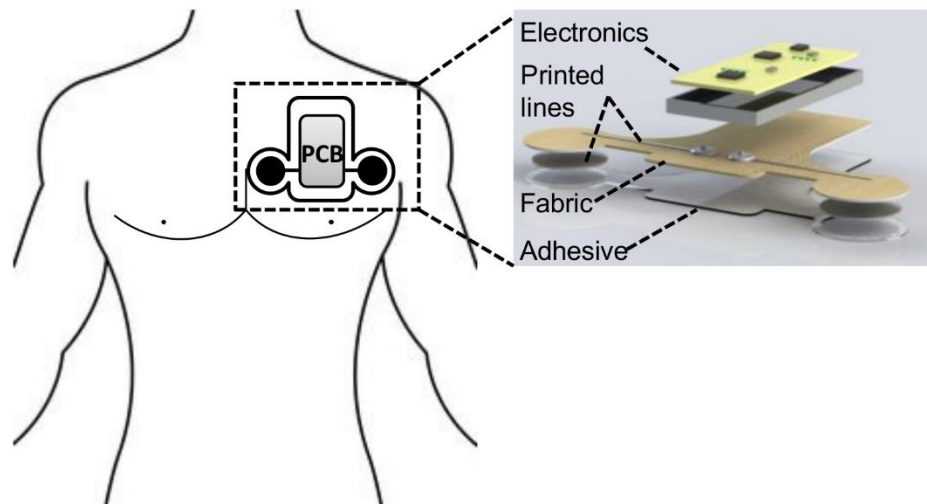


Fig. 1. Wearable health monitoring platform being developed by ASSIST that serves as a modular platform, deconvoluting the design of the electronic architecture from an inexpensive fabric-based biopotential electrode system.

In this study, flexible and conformable dry passive electrodes were fabricated by screen-printing of Ag/AgCl on nonwoven fabrics platforms. This proposed work is designed to constitute the fundamental research that is required to create an inexpensive fabric-based chest-worn wearable health-monitoring platform (Fig. 1) that involves multi-sensors for long-term monitoring of biopotential signals as proposed by the NSF funded Nanosystems Engineering Research Center on Advanced Self-Powered Systems of Integrated Sensors and Technologies (ASSIST). The focus in this effort has been placed on the skin-electrode interface, electrode on body placement, and form factor design of single dry electrodes to represent individual parts of a wearable platform. In addition, ECG signal quality comparison was made by incorporating triaxial accelerometer and gyroscope sensors into our measurements while in stationary and movement conditions. Herein, we aim to investigate the skin-electrode interface of a custom multi-layered fabric-based electrode

design, as well as determine design constraints that influence the performance of ECG data acquisition on such a platform.

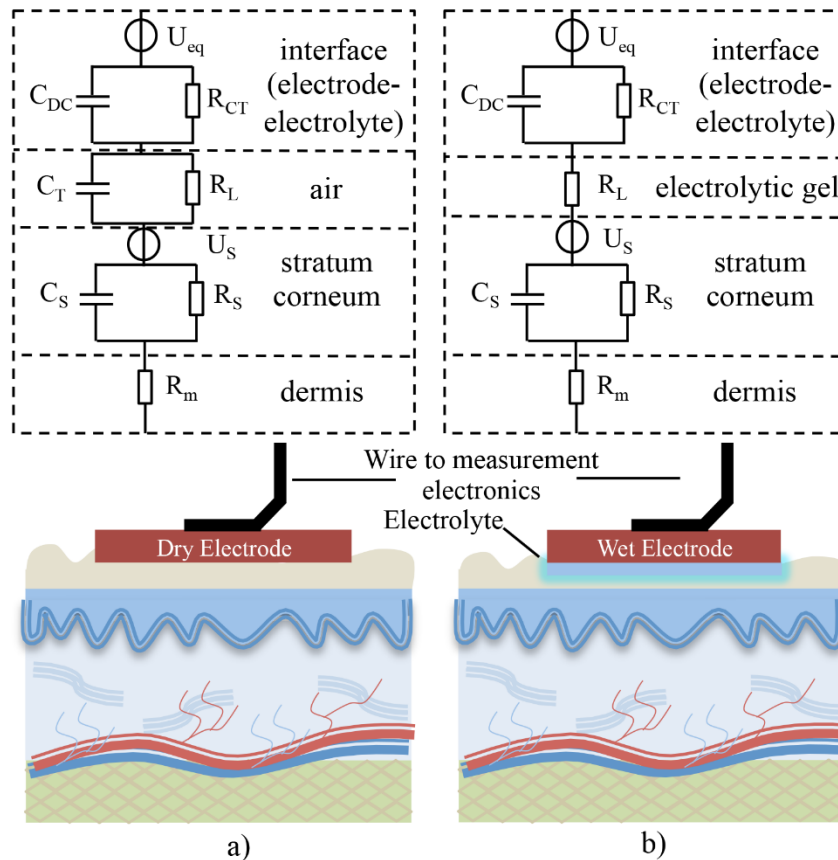


Fig. 2. Equivalent circuitries of (a) dry and (b) wet electrodes skin-electrode interface.

Skin-Electrode Interface

Electrical signals, which are created by heart muscle cells and transported to body surface via ions (i.e., Na^+ , Cl^- , Ca^+), are acquired by the placement of surface electrodes on the body. The electrodes act as a transducer by converting ionic current within the tissue to electrical current in electronic instruments. The skin-electrode interface is represented by the equivalent circuits presented in Fig. 2. When the electrode comes in contact with the skin or electrolyte, a double charged layer is created (C_{DC}). R_{CT} and U_{eq} show the leakage resistance across C_{DC} and electrode potential, respectively. In Fig. 2b, R_L is the resistance of the electrolyte for the wet electrode. On

the other hand, R_L is used for sweat and moisture build-up in dry electrodes in Fig 2a. Since dry electrodes do not utilize an ionic conductive medium, high interface capacitance (C_T) values are present. Skin has a layered architecture viz. stratum corneum (SC), stratum germinativum (SG), dermis, and subcutaneous layers. The layered structure of the skin is modeled by a capacitor, C_S , and a resistor, R_S . U_S shows the electrical potential created due to ion concentration difference within the layered structure of the skin. R_m represents the resistance of the dermis layer [15].

Skin-electrode impedance is important for the acquisition of high fidelity ECG signals. High skin-electrode impedance results in low signal-to-noise (SNR) ratios. Also, high skin-electrode impedance will decrease the amplitude of the signal that is fed to the subsequent amplifier due to a loading effect, which will result in a low SNR ratio. The major causes of noise in ECG are motion artifacts and common mode interference, generated as a result of electrical potential and skin-electrode impedance change at the skin-electrode interface [16].

Dry Electrode Fabrication

A. Screen Printing of Dry Electrodes

In this work, a dry electrode was fabricated on VistamaxxTM propylene-based elastomeric melt-blown nonwoven fabric obtained from Nonwovens Institute at North Carolina State University. To strengthen the fabric mat, an in-line calendaring (patterned heating) was performed, which primarily affects the surface texture on one side of the fabric. The surface on the opposite side of the fabric, in contact with the belt, remains smooth and nearly planar, ideal for reduced penetration of printed inks. After the process, the elastomeric fabric remains highly flexible and stretchable. Creative Materials Ag/AgCl (product number: 124-36) medical grade electrically conductive ink was used for the electrodes printing as it exhibits excellent adhesion to a variety of substrates and has shown adequate resistance to flexing and creasing.

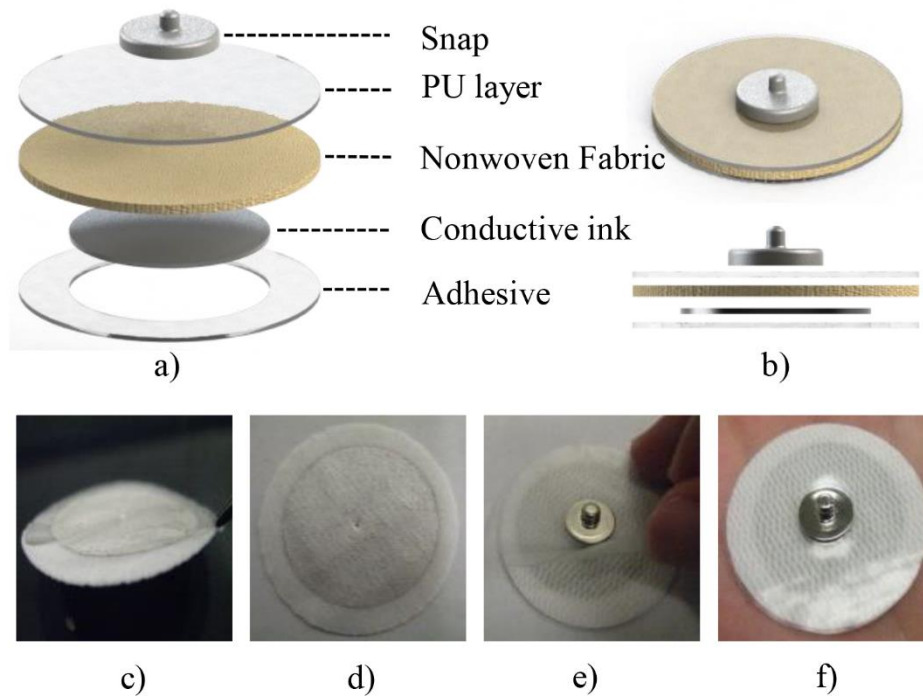


Fig. 3. Multi-layered structure of dry electrode. (a) Expanded view, (b) top and side view of dry electrode models. (c) Adhesive layer, (d) Ag/AgCl conductive ink, (e) PU film layer, (f) final dry electrode.

The printing of conductive ink onto nonwoven fabric was performed by the use of hand-operated lab-scale screen-printing equipment. A CAD designed electrode shape was transferred to an adhesive stencil by a Silhouette Cameo die cutter for rapid prototyping. The adhesive stencil was placed on 100 size screen-printing mesh, and the conductive ink was transferred onto the nonwoven fabric by handheld squeegee with 45° angle at an operator-controlled pressure. By printing on the smooth side of the nonwoven fabric, a continuous conformal coating is achieved.

B. Multi-layered Electrode Design

The multi-layer dry electrode fabricated in this effort is shown in Fig. 3. A biocompatible and reusable pressure-sensitive adhesive (MA-31, 2 mil), obtained from Adhesive Research Inc., PA, USA, lies at the bottom of nonwoven fabric. According to the manufacturer, the pressure-sensitive adhesive passed skin irritation, cytotoxicity, and skin sensitization tests based on the requirements of ISO 10993. However, some skin types can still be sensitive to prolonged use of

adhesive, which might cause skin irritation issues. The adhesive encircles the Ag/AgCl printed ink area at the center. The top layer of dry electrode was encapsulated by an adhesive-backed polyurethane (PU) film (MA-31, 2 mil / 4 mil polyurethane), also acquired from Adhesive Research Inc. An Ag/AgCl snap sandwiches the PU film and allows for a compatible interface to the ECG monitor used later in the experimentation.

Three different electrode sizes were created with diameters of 10 mm, 20 mm, and 30 mm. The fabricated dry electrode with 30 mm diameter is shown in Fig. 3 in various orientations. A facile six-step process for fabrication of the multi-layered dry electrode design is as follows:

- 1) Create 1 mm hole at the center of nonwoven fabric.
- 2) Print conductive ink on the backside of fabric and cure at 70 °C for 15 min.
- 3) Punch 2 mm hole on PU adhesive film and fasten male and female parts of snaps together while keeping the PU film in between.
- 4) Cut 5 mm width circular adhesive sheet and adhere to the periphery of the printed area.
- 5) Mix part A and part B of CircuitWorks 2400 conductive silver epoxy and fill out the 1 mm hole on fabric.
- 6) Combine PU film with fabric and cure at room temperature for 24 h.

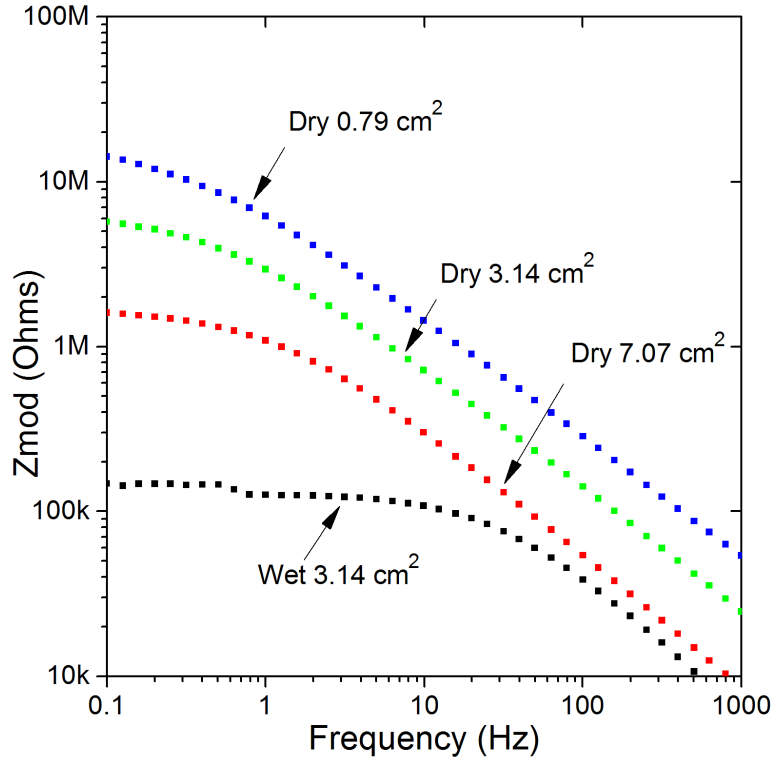


Fig. 4. Skin-electrode impedances of dry electrodes with printed area of 0.79 cm², 3.14 cm² and 7.07 cm². The commercial wet electrode (3M Red Dot)'s conductive area is 3.14 cm².

Results and Discussions

A. Dry Electrode Impedance Measurement

The impedance of the skin-electrode interface was examined by the use of a Gamry Reference 600TM potentiostat. The measurement was conducted on the left arm of a male subject. A three-electrode measurement system was utilized, where the counter and working electrodes carry current, and the working and reference electrodes measure voltage. The distance between the counter electrode and the reference electrode was set to 8 cm. The working electrode and working sense electrodes were clipped together, and the distance between these two electrodes and the reference electrode was set to 4 cm. 3M Red Dot wet electrodes were used as reference and counter electrodes. A screen-printed dry electrode was connected to the working sense electrode for impedance measurement. The signal magnitude (V_{rms}) was set to 10 mV, and the frequency sweep

was performed from 0.1 Hz to 1000 Hz. Impedance measurements were repeated on the printed dry electrodes with 10 mm, 20 mm, and 30 mm diameters. The 3M Red Dot wet electrodes were used as a reference measurement. No washing, degreasing, or abrading was performed upon the skin surface, which is often used to decrease the total impedance by removing poorly conductive lipid substances or top surface of the skin. The measurement was started upon the testing setup completion (~8 min). To minimize skin related variations (number of sweat glands, thickness of stratum corneum, male-female physiological differences) among different subjects and test locations, the skin-electrode measurements were only tested on one subject. Therefore, subject-to-subject variations of skin-electrode impedance is not addressed. The impedance measurement results of dry and wet electrodes are provided in Fig. 4. The dry electrodes had higher impedance values than wet electrodes, attributed to the capacitive dry electrode interface, as shown in Fig. 2. The absence of conductive medium at the interface resulted in high impedance values. As expected, the skin-electrode impedance is observed to be inversely proportional to the printed area; with higher printed areas showing lower impedance. The measured impedance values are in the same range (1M-15M Ω for the electrode diameter of 10mm to 30 mm) as in [5], [6], [9], [10], and [11]. To reduce the impedance, a biocompatible hydrogel (AG 603, obtained from Axelgaard Manufacturing Co., Ltd., CA, USA) was applied at the interface of the skin and electrode. The printed electrodes with an applied hydrogel showed the impedance values that are lower than the 3M Red Dot electrodes impedance values (Fig. 5). The measured impedance values were between 10k Ω -100k Ω for the 10mm, 20mm, and 30mm diameter printed electrodes with hydrogel. This impedance results are similar to the embroidered dry electrodes with hydrogel in [8]. The hydrogel improves and stabilizes the skin-electrode interface because it improves the contact between the skin and printed electrode (i.e., increases the contact area) [17] and also eases the charge transfer

due to presence of ions. However, the hydrogel is still vulnerable to conductance variation as dehydration will decrease conductance over time.

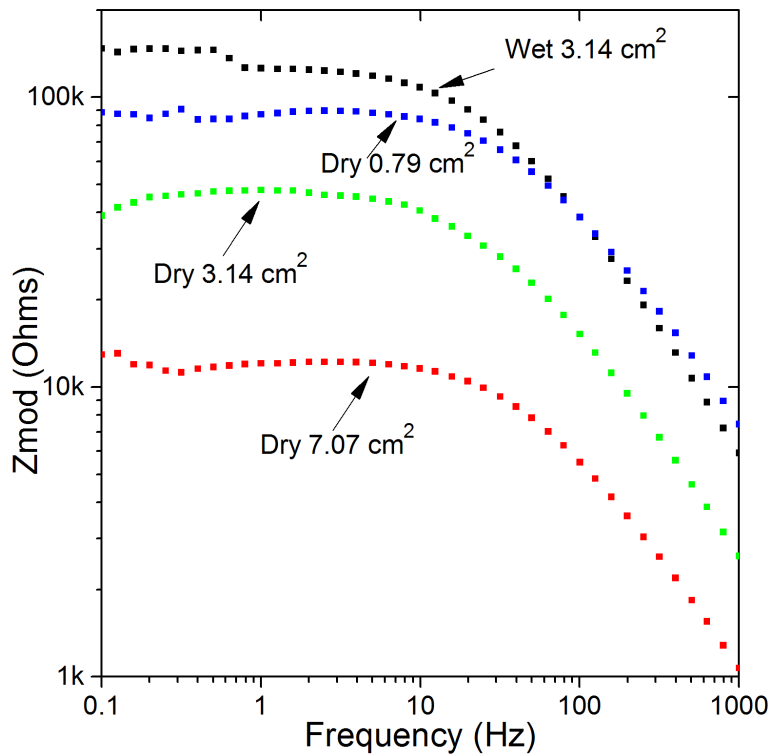


Fig. 5. Skin-electrode impedances of dry electrodes with hydrogel at the skin-electrode interface. A wet electrode (3M Red Dot) is given as a reference.

It is important to note that the skin-electrode impedance measurements are susceptible to applied pressure between the electrode and the skin. To investigate the impedance change with pressure, impedance measurements were performed with and without application of pressure (pressure was applied by the use of an adjustable arm strap) on the dry electrode over a period of 70 minutes. A fabricated electrode with a 30 mm printed area weighs 1.154 g, which applies 8.996 Pa (0.068 mmHg) pressure to the skin surface with the assumption of homogenous pressure distribution. A digital force measurement tool (Chatillon DFS II) was used to evaluate the applied pressure by the strap. The applied pressure was equal to 2 N, which was equal to 12 mmHg for the 30 mm electrode. Pressure >30 mmHg increased the tightness of the strap and caused discomfort.

A similar inverse pressure and impedance relation is observed in [7]. Moreover, it is stated in [11] that mild pressure (~20 mmHg) is necessary for on-body electrode stability and motion artifact minimization. No skin irritation was observed upon completion of the test. The fabricated electrode includes a porous nonwoven fabric, which could enable the air circulation to the skin surface. Gamry Echem Analyst software was applied to extract the equivalent circuit model parameters of skin-electrode interface using a single time constant model that was developed by Swanson and Webster [18]. This model is comprised of a resistor (R_p) in series with a parallel connected a resistor (R_u) and a capacitor (C_f). C_f indicates the electrical charge layer, and R_u represents the resistance across this capacitor. R_p is used to show the resistance of sweat and underlying tissues. Fig. 6 and Fig. 7 display the equivalent circuit model parameters of the skin-electrode interface over time. Error bars indicate the fitting errors for R_u , R_p , and C_f values. The difference in the capacitance vs. time trend in Fig. 6 and Fig. 7 can be explained by the change in electrode distance relative to the body surface. Change in electrode distance to body surface resulted in fluctuation in C_f when there was no pressure on the dry electrode (Fig. 6). Without pressure, the value of C_f decreased over time. An abrupt drop in capacitance was observed as a result of the local electrode movement as the loading from the electrode attachment pulled the printed electrode away from skin and resulted in an increase in skin-printed electrode distance. With pressure application (Fig. 7), C_f decreased exponentially and reached a steady state with time. Due to the smaller electrode-skin distance and higher contact surface area, the magnitude of C_f increased with pressure application compared to C_f magnitude in Fig. 6 (i.e. $C = \epsilon A / d$, where ϵ : permittivity, A : area, d : distance). By applying pressure on electrodes, the contact between the dry electrode and skin improved, as observed by a decrease in resistance values (R_p and R_u). The decrease in magnitude of the resistances (R_p and R_u) may also be attributed to sweat build-up resulting from the pressure.

This is observed further by the increasing resistance vs. time in Fig. 6 and Fig. 7, which can be explained by the closure of sweat ducts over time that lowers the conduction through the skin layers.

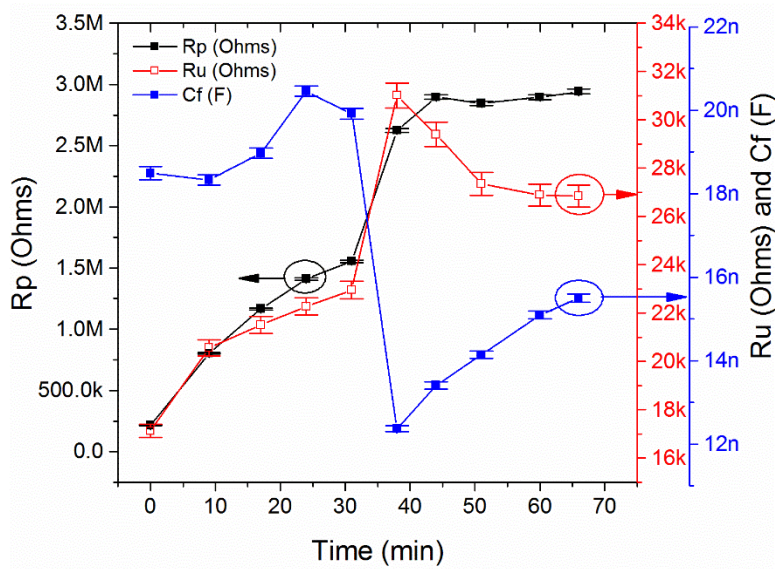


Fig. 6. Equivalent circuit parameters of skin-electrode impedance (without pressure).

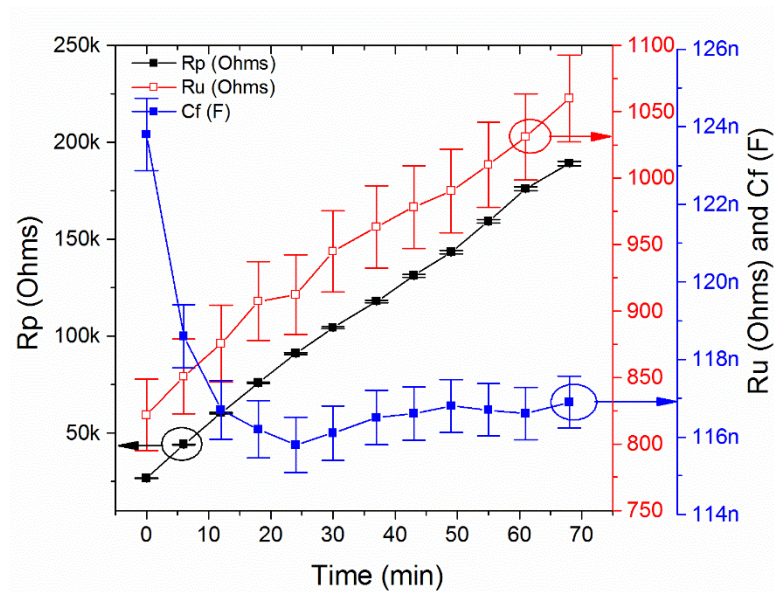


Fig. 7. Equivalent circuit parameters of skin-electrode impedance (with pressure).

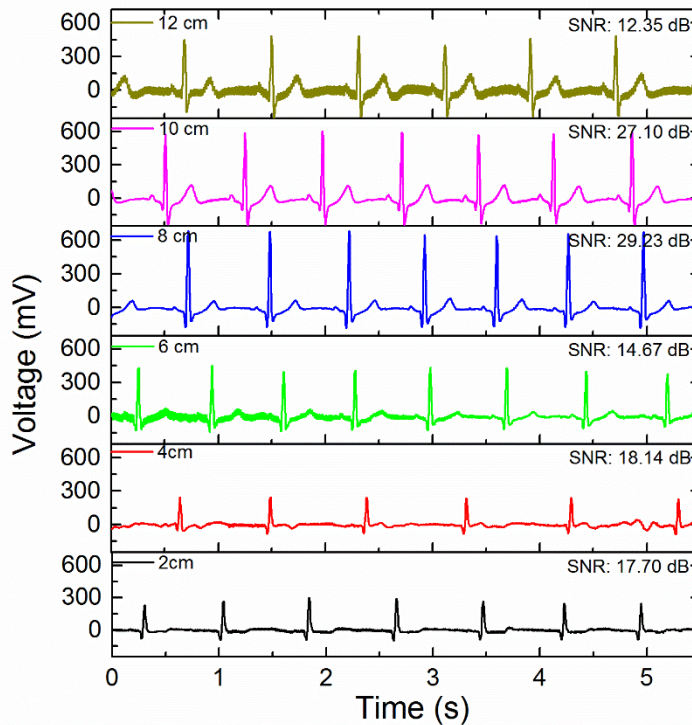


Fig. 8. ECG signal strength variation with respect to electrode distance.

B. Electrode Form Factor and Electrode Placement

The effect of electrode area and electrode on-body placement on the ECG signal was investigated using a standard General Electric bedside monitor (GE Dash 4000, WI USA). It has a gain of $1 \text{ V/mV} \pm 10\%$. Shielded cables were used between the electrodes and the measurement equipment to decrease electromagnetic interference, which is created due to the current that runs through the loop that is formed by the ECG equipment, cables and the measurement subject. This induces a voltage drop in the measurement cables. To mitigate this effect, the measurement cables were also twisted together prior to measurement to decrease the loop area. A healthy (no history on myocardial infarction, ventricular hypertrophy) male subject (age: 25, height: 175 cm, weight: 80 kg) wore the dry electrodes for evaluation. A three-electrode ECG measurement was performed by placing two dry electrodes on the chest and third reference 3M Red Dot electrode on the left leg. The right dry electrode (30 mm diameter) was placed at the center of the chest, while the left

dry electrode (30 mm) was placed to the level of the second rib on the chest, close to the left arm. This region of the chest was selected due to high user compliance and less sensitivity to body movements. Lead L1 of Einthoven's triangle configuration was used to measure the potential difference between two fabric-based dry electrodes. The right electrode was moved towards the left electrode in such a way that the distance between the two dry electrodes was set to 2 cm, 4 cm, 6 cm, 8 cm, 10 cm, and 12 cm while the subject was in standing position. ECG measurement was performed at each location with a sampling rate of 240 Hz. In comparison to the prior analysis, the hydrogel was not used at the interface of the electrode and skin during measurements, and additional pressure was not applied. The comparison of ECG signals at various electrode distances was made upon baseline wander and noise-free ECG signals. Signal processing of the ECG signals was performed in MATLAB software. The baseline wander in raw ECG signal was removed by using the moving average method. Denoising of the ECG signals was performed in the Wavelet Analysis Toolbox. The noise in raw ECG signal was calculated by subtracting the baseline-free denoised signal from baseline-free noisy raw ECG signal. Power spectral densities of the denoised ECG signal and the noise were found by using a fast Fourier transform method. The area under the power spectral density curve is equal to the total power. SNR of the ECG signals was calculated by dividing the total power of the denoised ECG signal by the total power of noise ($SNR = P_{\text{signal}}/P_{\text{noise}}$). Also, the comparison of R peak magnitude in ECG signals was made due to its distinct presence among other P, Q, S, and T waveforms.

Fig. 8 shows the ECG signal strength variation with electrode distance, and a numerical comparison is also provided in Table I. It was found that the R peak magnitude increased (except 4 cm) as electrode pairs were moved away from each other. It was maximized at an electrode distance of 8 cm and then started decreasing again as electrode pairs are moved even further to 12

cm. This is attributed to the difference in body surface potential distribution (i.e. body surface isopotential maps). The isopotential map shows the instant and spatial distribution of potentials on the body surface at each cardiac cycle [19]. Similar surface potential values are shown on the same contour. The body surface potential distribution in resting conditions during ventricular excitation and recovery is reported elsewhere [20]. For the R peak, the magnitude of potential difference (left arm-right arm) on the body surface increases and then decreases as the electrode is moved from the sternum closer to the left arm. This explains the change in R peak magnitude as the left arm dry electrode is moved towards the right arm dry electrode. Close placement of right and left arm dry electrodes to each other (i.e., 2 cm) may correspond to similar or close contour lines on isopotential lines; thus, yields smaller R peak magnitudes on Lead I. Similar electrode distance vs. QRS peak amplitude relation was obtained in precordial electrode placement when the electrode pairs were moved towards each other [21]. Also, the R peak magnitude trend obtained in [11] matched with our results. However, the R peak magnitude in this study was slightly higher due to a larger printed area of 30 mm. Total signal power (i.e., integral of PSD graph) demonstrates a similar trend as the R peak amplitude. However, the total noise power varied due to the difference of noise content in ECG signals. The electrode pair distance of 8 cm yielded the highest SNR value of 29.23 dB among other electrode pair distances.

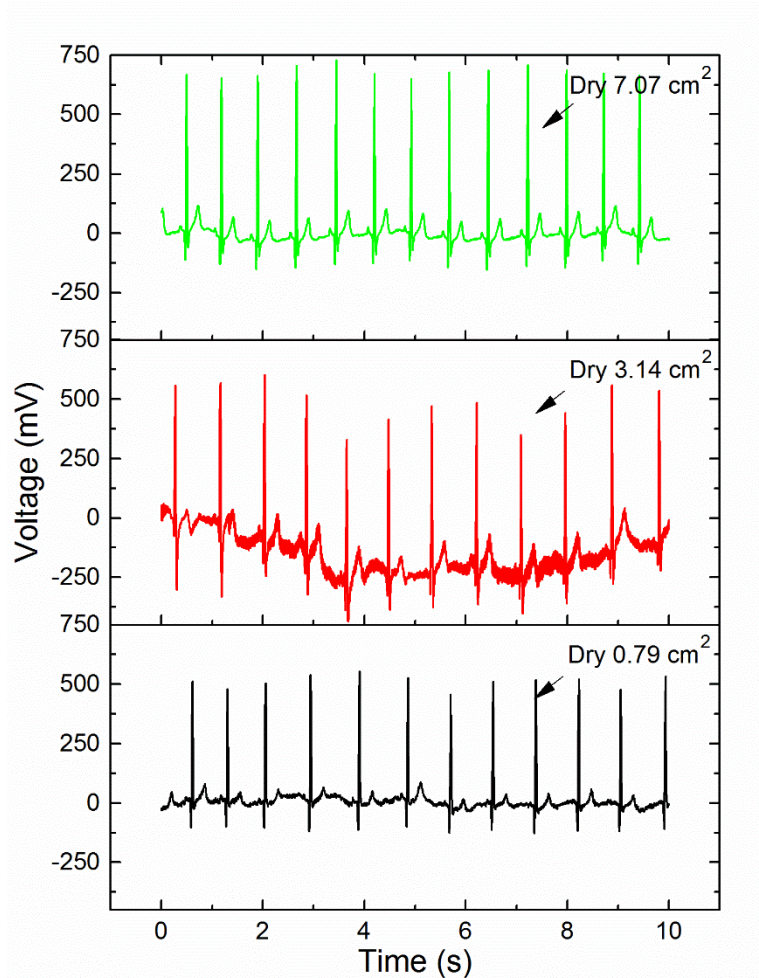


Fig. 9. ECG signal variation with respect to the printed electrode area.

A comparison of the ECG signal quality of dry electrodes with printed diameters of 10 mm, 20 mm and 30 mm, using a constant 8 cm electrode pair distance is presented in Fig. 9. As expected, the larger electrode area, and subsequent skin contact, results in a higher ECG amplitudes. A comparison of the electrodes with different printed areas is provided in Table II. The comparison is based upon denoised and baseline wander free ECG signals of the printed electrodes. The data shows that higher printed areas results in higher R wave peak magnitudes. This can be explained by lower skin-electrode impedance of larger printed areas. A similar increasing trend with increasing printed area was observed when the total area under the power spectral density graph of the denoised ECG signal was calculated. The printed electrode with the

30 mm printed area gave the highest SNR value. Due to high noise content in the ECG signal, the 20 mm printed electrode yielded the lowest SNR value.

Table 1. Comparison of Electrode Pair Distances

Electrode pair distance (cm)	R wave peak amplitude (mV)	Signal power ((mV) ²)	Noise power ((mV) ²)	SNR (dB)
2 cm	247.60 (±25.10)	1538.36	26.10	17.70
4 cm	221.4 (±7.41)	1125.76	17.28	18.14
6 cm	403.32 (±18.30)	4123.55	140.82	14.67
8 cm	646.45 (±18.24)	9926.17	11.85	29.23
10 cm	570.03 (±13.97)	9113.67	17.76	27.10
12 cm	439.38 (±24.19)	5418.01	315.22	12.35

Table 2. Comparison of Printed Electrodes Areas

Electrode diameter (mm)	R wave peak amplitude (mV)	Signal power ((mV) ²)	Noise power ((mV) ²)	SNR (dB)
10 mm	460.47 (±22.5)	4719.80	23.01	23.11
20 mm	591.86 (±34.9)	8655.90	202.56	16.30
30 mm	630 (±28.4)	9473.50	12.71	28.72

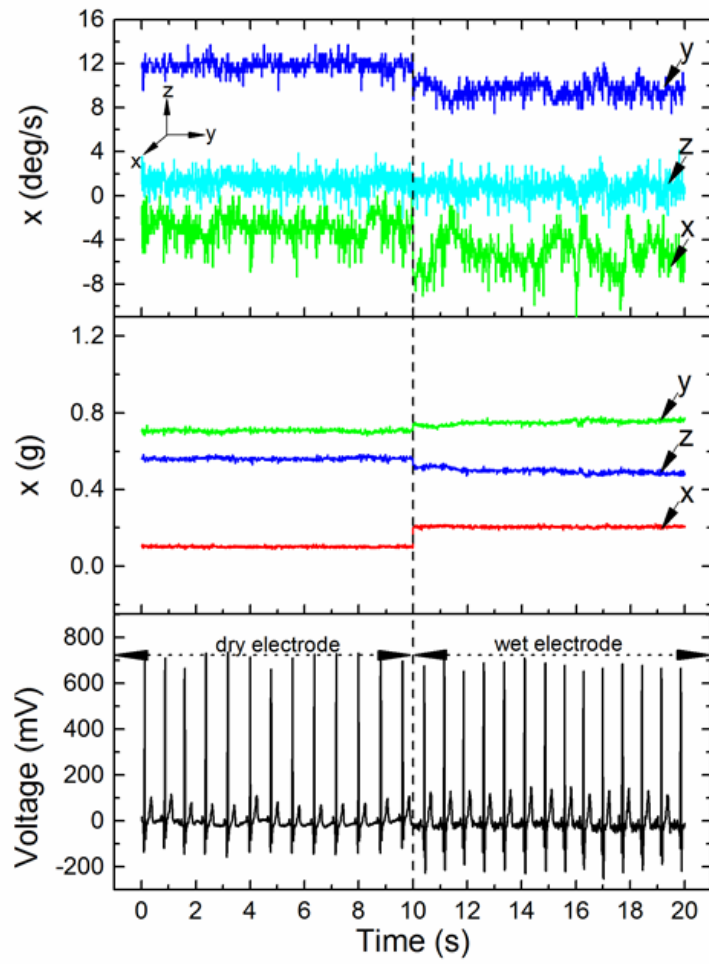


Fig. 10. ECG signals of dry and wet electrodes while sitting.

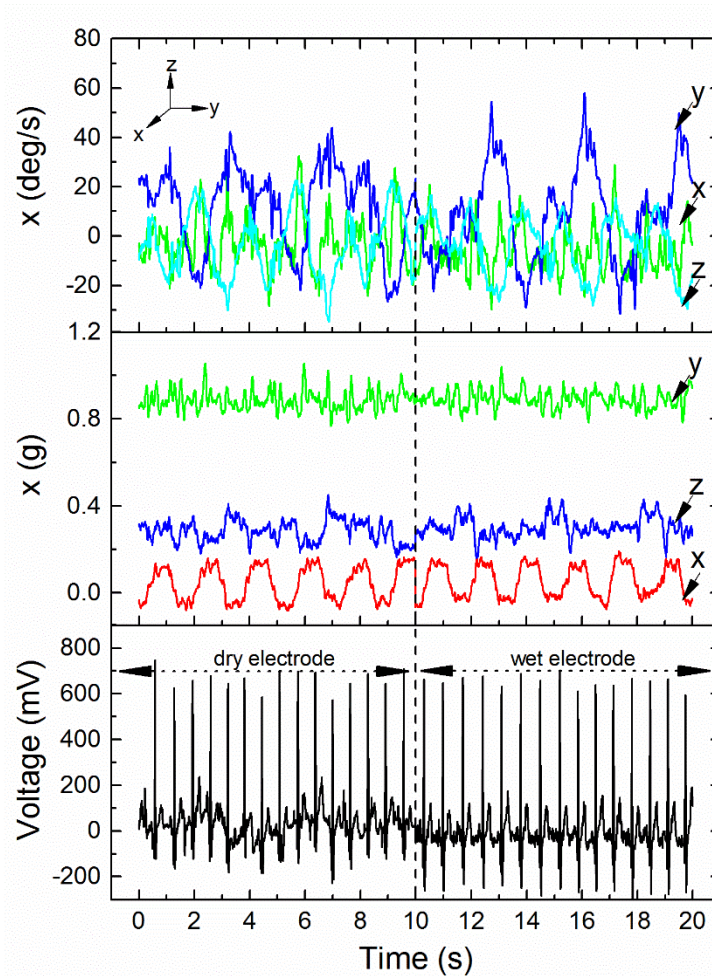


Fig. 11. ECG signals of dry and wet electrodes while moving.

C. Comparison of ECG Signal Quality and Body Movement Correlation

Finally, a comparison of ECG signals acquired by dry and wet electrodes was performed within prescribed motions. ECG signals were recorded for both dry and wet (3M Red Dot) electrodes for 15 min while a healthy male subject (age: 25, height: 175 cm, weight: 80 kg) was sitting on a chair and also remaining in standing position. During the standing position, the subject performed 4 min. front-back movement, 4 min. up-down movement (kneeling down), 3 min. standing still, and 4 min. right-left stepping repeatedly at a constant speed. Due to the acquisition system's short cables, electrode performance during walking and running were not conducted. Also, the dry electrodes did not give any discomfort throughout the measurement. In this analysis,

the 30 mm printed fabric-based electrodes were employed, and an electrode pair distance of 8 cm was maintained for the dry and wet electrodes. In addition to the ECG signal acquisition, a wearable posture detection chest strap, TEMPO (Technology-Enabled Medical Precision Observation) [22], was worn to relate body motion and rotation to provided triaxial acceleration and triaxial gyroscope data with a sampling rate of 128 Hz. ECG signal acquisitions (240 Hz) were made while the subject wore the chest strap and dry and wet electrodes simultaneously during sitting and moving conditions. The dry electrode and commercial wet electrodes were not tested simultaneously on the same location due to the natural limitations of the ECG acquisition system. A successive individual measurement procedure was followed for dry and wet electrodes. Fig. 10 shows the ECG signals of dry and wet electrodes as the subject sat on a chair. Dry electrode and wet electrode ECG signals were relatively similar during resting state, and the QRS complex was still detectable. Fig. 11 displays the ECG signal comparison during movement (front-back movement). Right-left movement and up-down movement yielded qualitatively similar ECG signals compared to front-back movement; therefore, only front-back movement results are discussed. Both dry and wet electrodes yielded comparable QRS peaks during forward-backward move. The introduction of movement introduced noise and baseline shifts. Similar qualitative changes on ECG signals were also observed in other dry electrodes types [6], [9], and [10] with the introduction of movement. SNR values of dry printed and wet electrodes are given in Table III., calculated by using the same approach as outlined in Section B. The dry electrode had slightly higher SNR value during sitting, attributed to the larger area of dry electrode compared to the commercial wet electrode. Higher SNR dry electrodes relative to commercial electrodes were also obtained in CNT/PDMS composite dry electrodes without movement [9]. The SNR values of the electrodes decreased due to noise introduction with the subject is in motion. The dry electrode had

slightly less SNR value than the wet electrode due to a higher noise presence in the ECG signal. However, the adhesive surrounding the printed area reduced the large baseline shift by immobilizing the dry printed electrode on the skin surface, enabling the acquisition of less noised ECG signal. The dry electrode still demonstrates a transient baseline change due to the skin-electrode impedance changes with electrode motion. This is attributed to the voltage divider effect resulting from the amplifier input voltage changing as the skin-electrode impedance changes with respect to the input impedance of the amplifier [23]. Also, the distribution of potentials within skin layers (U_s) and at the skin-electrode interface (U_{eq}) can change with skin stretching, local electrode movement, and body movement, which causes the motion artifacts in ECG signals [24].

Table 3. Comparison of Signal to Noise Ratios

Electrodes	Sitting	Moving
Dry printed electrode	28.68 dB	24.73 dB
Wet electrode	26.70 dB	25.77 dB

Conclusion

Printing of Ag/AgCl conductive ink on the nonwoven fabric was investigated to construct passive dry electrodes by inexpensive and scalable screen-printing methods. The screen-printed transducer layer was then integrated into a flexible multi-layered dry electrode form to realize a complete electrode design. The layered electrode design approach included a multi-stick pressure-sensitive adhesive on the skin side that enabled re-application of the electrode and also minimized significant electrode movements on the body surface.

Analysis of the dry electrode demonstrated high skin-electrode impedance values. However, the impedance of the dry electrodes can be tuned by changing the printed electrode area, skin-electrode interface material, and applied pressure on the electrode. Moreover, it was observed

that the amplitude of the ECG signal changed with the printed electrode area and placement of electrode pairs on the body surface due to location-dependent body surface potential variation.

Dry printed electrodes and wet electrodes yielded similar baseline shift-free ECG signals when the user is not moving. While dry printed electrode had a slight baseline shift when the object is in motion. Yet, low cost printed dry electrodes on fabrics are appealing for the fabrication of long term wearable multi-use platforms due to the non-existence of electrode dehydration and skin related issues. This present study has the utmost importance in designing optimal wearable electronic platforms (wearable patches and straps) for physiological sensing applications.

References

- [1] R. Paradiso et al., "Wealthy-a wearable healthcare system: new frontier on e-textile," *J. Telecommun. Inf. Technol.*, pp. 105–113, 2005.
- [2] K. J. Heilman and S. W. Porges, "Accuracy of the LifeShirt® (Vivometrics) in the detection of cardiac rhythms," *Biol. Psychol.*, vol. 75, no. 3, pp. 300–305, Jul. 2007.
- [3] C. W. Mundt et al., "A multiparameter wearable physiologic monitoring system for space and terrestrial applications," *IEEE Trans. Inf. Technol. Biomed.*, vol. 9, no. 3, pp. 382–391, Sep. 2005.
- [4] J. Coosemans et al., "Integrating wireless ECG monitoring in textiles," *Sens. Actuators Phys.*, vol. 130–131, pp. 48–53, Aug. 2006.
- [5] A. Searle and L. Kirkup, "A direct comparison of wet, dry and insulating bioelectric recording electrodes," *Physiol. Meas.*, vol. 21, no. 2, p. 271, May 2000.
- [6] R. Paradiso et al., "A wearable health care system based on knitted integrated sensors," *IEEE Trans. Inf. Technol. Biomed.*, vol. 9, no. 3, pp. 337–344, Sep. 2005.
- [7] L. Beckmann et al., "Characterization of textile electrodes and conductors using standardized measurement setups," *Physiol. Meas.*, vol. 31, no. 2, p. 233, Feb. 2010.
- [8] M. M. Puurtinen et al., "Measurement of noise and impedance of dry and wet textile electrodes, and textile electrodes with hydrogel," in *28th Annual International Conference of the IEEE Engineering in Medicine and Biology Society, 2006. EMBS '06*, 2006, pp. 6012–6015.
- [9] H.-C. Jung et al., "CNT/PDMS Composite Flexible Dry Electrodes for Long-Term ECG Monitoring," *IEEE Trans. Biomed. Eng.*, vol. 59, no. 5, pp. 1472–1479, May 2012.
- [10] J.-Y. Baek et al., "Flexible polymeric dry electrodes for the long-term monitoring of ECG," *Sens. Actuators Phys.*, vol. 143, no. 2, pp. 423–429, May 2008.
- [11] J. Yoo et al., "A Wearable ECG Acquisition System With Compact Planar-Fashionable Circuit Board-Based Shirt," *IEEE Trans. Inf. Technol. Biomed.*, vol. 13, no. 6, pp. 897–902, Nov. 2009.
- [12] C. R. Merritt et al., "Fabric-Based Active Electrode Design and Fabrication for Health Monitoring Clothing," *IEEE Trans. Inf. Technol. Biomed.*, vol. 13, no. 2, pp. 274–280, Mar. 2009.
- [13] M. R. Neumann, "Biopotential Electrodes," in *Medical Instrumentation Application and Design*, 3rd ed., New York, NY, USA: Wiley, 1988, pp. 189–201.
- [14] K.-P. Hoffmann et al., "Long-term characterization of electrode materials for surface electrodes in biopotential recording," *Conf. Proc. Annu. Int. Conf. IEEE Eng. Med. Biol. Soc. IEEE Eng. Med. Biol. Soc. Annu. Conf.*, vol. 1, pp. 2239–2242, 2006.
- [15] J. G. Webster, *Medical Instrumentation: Application and Design*, 3rd ed. John Wiley & Sons, Inc., 1998.
- [16] M. Catrysse et al., "Towards the integration of textile sensors in a wireless monitoring suit," *Sens. Actuators Phys.*, vol. 114, no. 2–3, pp. 302–311, Sep. 2004.
- [17] E. T. McAdams et al., "Factors affecting electrode-gel-skin interface impedance in electrical impedance tomography," *Med. Biol. Eng. Comput.*, vol. 34, no. 6, pp. 397–408, Nov. 1996.
- [18] D. K. Swanson and J. G. Webster, "A model for skin-electrode impedance," in *Biomedical Electrode Technology - Theory and Practice*, Academic Press, 1974, pp. 117–128.

- [19] B. Taccardi et al., “Useful lessons from body surface mapping,” *J. Cardiovasc. Electrophysiol.*, vol. 9, no. 7, pp. 773–786, Jul. 1998.
- [20] W. T. Miller et al., “Total body surface potential mapping during exercise: QRS-T-wave changes in normal young adults,” *Circulation*, vol. 62, no. 3, pp. 632–645, Sep. 1980.
- [21] S. Nedios et al., “Precordial electrode placement for optimal ECG monitoring: implications or ambulatory monitor devices and event recorders,” *J. Electrocardiol.*, vol. 47, no. 5, pp. 669–676, Oct. 2014.
- [22] A. T. Barth et al., “TEMPO 3.1: A Body Area Sensor Network Platform for Continuous Movement Assessment,” in *Sixth International Workshop on Wearable and Implantable Body Sensor Networks, 2009. BSN 2009*, 2009, pp. 71–76.
- [23] G. M. Friesen et al., “A comparison of the noise sensitivity of nine QRS detection algorithms,” *IEEE Trans. Biomed. Eng.*, vol. 37, no. 1, pp. 85–98, Jan. 1990.
- [24] D. Buxi et al., “Correlation Between Electrode-Tissue Impedance and Motion Artifact in Biopotential Recordings,” *IEEE Sens. J.*, vol. 12, no. 12, pp. 3373–3383, Dec. 2012.

Appendix B: Printed Stretchable Interconnects for Smart Garments: Design, Fabrication and Characterization

Murat A. Yokus, Rachel Foote and Jesse S. Jur

*As published in *IEEE Sensors* (2016)

Abstract

This paper explores the stretchability and fatigue life of inexpensive printed stretchable interconnects for smart garments. Multilayer stretchable interconnects are created on a knit fabric by screen-printing of Ag/AgCl conductive inks on thermoplastic polyurethane film (TPU). Heat lamination of this layer onto a knit fabric and its protective encapsulation with a second TPU layer yields a multilayer stretchable interconnect structure. Design and optimization of the printed meandering interconnects are performed experimentally. The effect of processing steps, area of substrate and encapsulation layers on the electro-mechanical properties of the stretchable interconnects are investigated. Washing endurance of the printed lines is also explored. The meandering stretchable printed line demonstrates stretchability of over 100% strain and fatigue life of 1000 cycles at 20% strain. Washing endurance of 100 cycles is reported. This study presents an inexpensive method of realization of electronics integration on textiles by maintaining textile comfort and wearability.

Introduction

Wearable electronics have been the focus of attention for researchers in the last couple of decades. There is a significant growing interest in this field, ranging from unobtrusive textile integrated bio-sensors [1], to electrochromic displays embedded into textiles [2]. Current research focuses on the use of nanotechnology, organic materials, and innovative fabrication techniques to create flexible electronic devices such as sensors [3], supercapacitors [4], conductive yarns [5], and energy harvesting devices [6]. These flexible devices are designed to bend and flex to form on

curvilinear surfaces, which make them suitable for integration into textiles. The unobtrusive integration of discrete flexible devices into textiles creates a new norm for wearable technology, i.e., a smart garment.

There are key requirements that need to be fulfilled when creating a wearable smart garment. Air and vapor permeability, biocompatibility, comfort, washing and chemical (i.e., detergent) resistance, and ease of deformation (bending, compression, extension etc.) are indispensable necessities. Electro-mechanical durability of the smart garment, when subjected to large strains, is equally critical in determining the endurance of the garment to the dynamic forces of body movement. Prior research has shown that fabrics may experience up to ~20% strain during a set of various physical activities [7], [8]. Electronics positioned various locations of the fabric will undergo this range of deformation from the body's movement. Ideally, this deformation needs to happen through stretchable interconnects between the less resilient, hard electronic components. Therefore, the design of stretchable interconnects is important for maximizing the functionality while at the same time accommodating larger strains without constraining body movement for human comfort.

In order to provide stretchability without diminishing the functionality of electronic devices, various fabrication methods and stretchable material structures have been studied. Fabrication of wavy or buckled single crystal semiconductor nanoribbons [9] or metals [10](e.g., gold) by pre-straining the elastomeric substrate, and mesh-shaped structures [11] yielded electronic device (e.g., thin-film transistors and transistor-based pressure sensors) functionalities up to 25% strain values by undergoing out-of-plane deformation. These techniques have yielded hemispherical electronic eye cameras based on an array of silicon photodetectors [12]. However, the methods require complex component transferring and mechanical pre-straining the polymeric

substrate. A different approach to make stretchable interconnects is to fabricate planar horseshoe-shaped structures by lithographically patterning gold on elastomeric substrates [13]. Failure strain of 54% and cyclic endurance of 200 cycles at 25% strain have been achieved. Moreover, a photoablation method [14] was utilized to fabricate rectilinear and meandering interconnect designs. Its fabrication process used metal layers for polymer masking; therefore, eliminating the alignment process and the use of chemicals for etching. However, the presence of conical defects was stated to have an effect on the stretchability of the meandering lines. A failure strain of 50% with a resistance change ($\Delta R/R$) of 5% was shown. As an alternative method for stretchable interconnects, liquid alloy filled elastomeric microchannels were studied [15]. This technique did not result in a crack formation, which is commonly encountered in metals upon elongation above 1%, due to the presence of alloy metal in liquid form at room temperature. Resistance change (ΔR) of 0.24 Ω with 100% strain was indicated, but lower stretchability ($\sim 30\%$) was observed when active circuit elements were integrated into liquid metal filled micro-channels. Furthermore, an in-plane metal conductor technology for horseshoe-shaped meandering lines was proposed by [16] to pattern copper with a polyimide support underneath. The polyimide support layer increased the fatigue life (3,400 cycles at 10% strain) of the meandering line. The fatigue life was further increased to 40,000 cycles at 30% strain by the addition of a supporting polyimide layer on top of the copper layer [17].

More recently, notable research has been done in nanomaterial research and development to fabricate stretchable interconnects. Carbon nanotubes (CNTs) and carbon black (CB) filled elastomers were developed toward the fabrication of strain gauges [18]. It was shown that CB filled elastomers had $\Delta R/R$ of $\sim 140\%$ at 5% strain because of separation of carbon particles with applied strain, which produced breakage of the conductive pathways. Likewise, serpentine shaped

CNT filled elastomers had a $\Delta R/R$ of $\sim 5\%$ at 15% strain due to rotation and slide of CNTs against each other upon applied strain. In another study [19], silver nanowires (AgNWs) and silver nanoparticles (AgNPs) embedded in an elastomeric matrix had $\Delta R/R$ of ~ 2 after 1,000 cycles with 10% strain, which was attributed to AgNW breakage with a high number of cycles. Even though some of the aforementioned methods and novel materials show excellent stretchability and endurance results, their manufacturing complexity, material cost, and scalability limit their usage in mass production of wearable electronics. For example, the current market price of CNTs and AgNWs is relatively expensive than conductive inks, which limits their usage to only nano-based applications rather than large-scale fabrications.

Other large-scale mass-production techniques such as knitting [20] and weaving [8] have been used in the integration of electronic functionality into smart garments. Knitting polyurethane-covered copper fibers with conventional yarns yielded 1% resistance change up to 300% strain values [21]. Screen-printing of the conductive inks, on the other hand, is an alternative industry scalable technique for the fabrication of inexpensive electronic devices on various substrates (e.g., textiles, polymeric films). It does not involve material extraction and removal steps, as commonly found in semiconductor fabrication processes. Printing of various silver inks has been investigated on polyarylate films [22], woven and knitted fabrics [23], and nonwoven fabrics [24]. However, the electromechanical properties of the printed lines as a function of stretching were not investigated. On the other hand, a brush painting of poly(3,4-ethylenedioxythiophene) :poly(styrene sulfonate) (PEDOT:PSS) conducting polymer on knitted fabrics was studied [25], reporting an elastic stretchability up to 30%. The resistance change after 1000 stretching cycles with 20% strain was about 10%. Screen-printing of horseshoe-shaped silver ink on TPU films was studied in [26], and 7% stretchability value was reported. Finally, another study [27] showed the

development and printing of a new ink material with stretchability of $>93\%$ and endurance of 1,000 cycles at 30% strain. However, the design and optimization of the printed conductive meandering lines on films, its subsequent integration onto textile wearables, and the effect of stretching on the electrical properties of the printed lines were not studied thoroughly before. Addressing these matters will shed light on some of the challenges (e.g., interconnect reliability under large strains, electronics integration, and washability) in textile-based electronics.

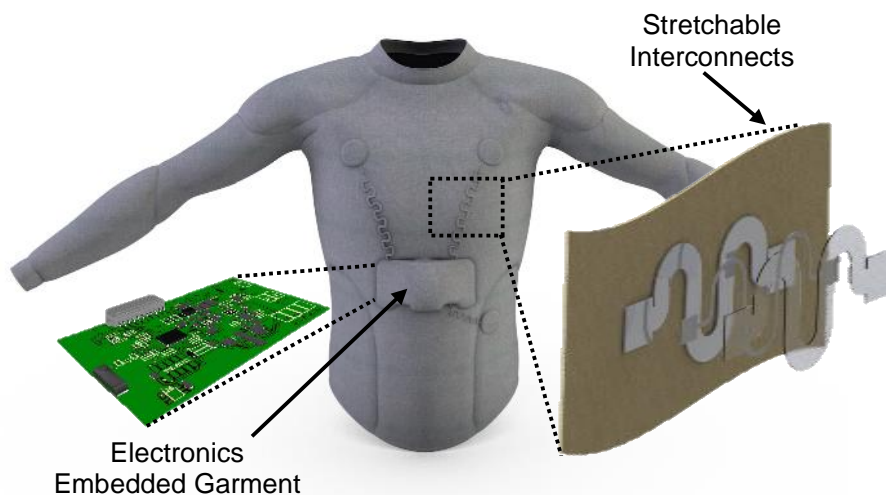


Fig. 1. Stretchable printed interconnect embedded smart garment being developed by ASSIST that incorporates low power electronics, sensors, and energy harvesting devices.

In this study, printed meandering interconnects were fabricated on knit fabrics. Inexpensive and scalable screen printing techniques were utilized to print Ag/AgCl conductive ink on thermoplastic polyurethane (TPU) film. Its heat lamination onto knit fabric and subsequent protective encapsulation layer yielded stretchable interconnects, shown Fig. 1. The printed stretchable interconnects are used in the integration of low power sensors and energy harvesting devices developed by a National Science Foundation Nanosystems Engineering Research Center on Advanced Self-Powered Systems of Integrated Sensors and Technologies (ASSIST). This article focuses on the design and optimization of printed conductive meandering lines, as well as

the effect of the processing steps on the electrical properties of the printed lines. Two demonstrations are provided to exemplify the use of the technique developed in this manuscript. First, a surface mount LED integration onto printed meandering lines as a means of evaluating the application of multi-electrode devices. Second, a shirt is modified with the meandering lines to support a full-signal electrocardiography measurement.

Stretchable Interconnects Fabrication

A. Screen-printing of stretchable interconnects

Stretchable interconnects were printed on both knit fabric and thermoplastic polyurethane film (TPU). The knit fabric, acquired from Hanes Brands Inc., NC, USA, is made of 87% polyester and 13% spandex yarns with a basis weight of 150 g/m². Inclusion of Spandex yarn within fabric construction yields high flexibility and recovery properties to the garment, which are important properties for intimate contact between the fabric and the diverse contours of the human body's surface. The TPU film (TL644), obtained from Bemis Inc., MA, USA, is composed of two layers: a polymer film layer and an adhesive barrier layer. Because of the adhesive layer's low softening point (~80 °C), the TPU film is suitable for heat-sensitive fabrics during heat lamination. The film's ink-receptive surface is suitable for screen-printing processes. It also has high washing resistance up to 60 °C. Creative Materials Ag/AgCl electrically conductive ink (product number: 124-36) was used for printing of stretchable interconnects on the TPU film and the knit fabric. The conductive ink shows excellent adhesion to a variety of substrates and has sufficient resistance to flexing and creasing.

The conductive ink printing was performed by using hand-operated lab-scale screen-printing equipment. A CAD drawn interconnect design was patterned onto a vinyl stencil by using a Silhouette cameo die cutter. The adhesive stencil was then placed onto a 100-mesh size screen-

printing frame, and the ink was transferred onto the substrates by a hand-held squeegee at a 45° angle with operator controlled pressure.

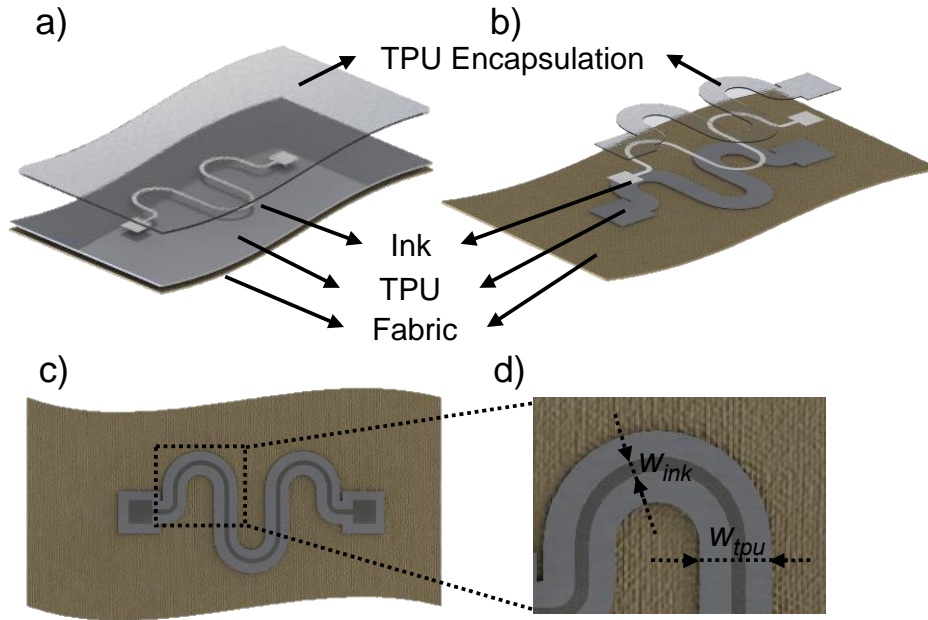


Fig. 2. Multilayer stretchable interconnect concept. (a) Whole area TPU film lamination and TPU film encapsulation, (b) meandering shaped TPU film lamination and TPU film encapsulation, (c) top view of laminated and encapsulated structure, (d) close-up picture of meandering line.

B. Multi-layer Stretchable Interconnects

The presented multilayer stretchable interconnect structure is given in Fig 2. The layered structure is composed of four layers. The knit fabric (thickness: 0.46 mm) lies at the bottom, representing the garment. The TPU film (TL644, thickness: 0.1 mm), the meandering shaped conductive ink layer, and the TPU encapsulation (TL3916, Bemis Inc., thickness: 0.15 mm) are situated on top of the knitted fabric, respectively. The TPU film (TL644) and the TPU encapsulation film (TL3916) will be referred as the printing layer and encapsulation layer, respectively, for the rest of the study. Fig. 2(a) shows the layered structure where the dimensions of the knitted fabric, the printing layer, and the encapsulation layer are similar (6 cm x 16 cm). Whereas, in Fig. 2(b) the printing layer and encapsulation layer are cut to a meandering shape and

then laminated on top of similar size knit fabric. Fig. 2(c) and 2(d) display the top view of the layered structure. The width of printed ink and the encapsulation layer are shown as w_{ink} and w_{tpu} , respectively. The printing layer and the encapsulation layer widths are the same, defined by an offset from the edge of the ink width, $w_{\text{offset}} = (w_{\text{tpu}} - w_{\text{ink}}) / 2$. The stretchable interconnect fabrication steps in Fig. 2(a) are given below.

- 1) Cut a 6 cm x 16 cm knitted fabric in the warp direction.
- 2) Cut a 6 cm x 16 cm TPU film (TL644) for the printing layer.
- 3) Screen-print conductive ink on the printing side (non-adhesive side) of the printing layer (2 passes of conductive ink) and cure at 60 °C for 15 min.
- 4) Laminate conductive ink printed layer onto the knitted fabric with a heat press at 125 °C for 2 min.
- 5) Laminate the encapsulation layer on top of the printed line at 125 °C for 2 min.

The multilayer interconnect structure in Fig. 2(b) was also fabricated by cutting of the printing and encapsulation layers with w_{offset} values of 2 mm and 4 mm. The rest of the procedure is similar as given for Fig. 2(a).

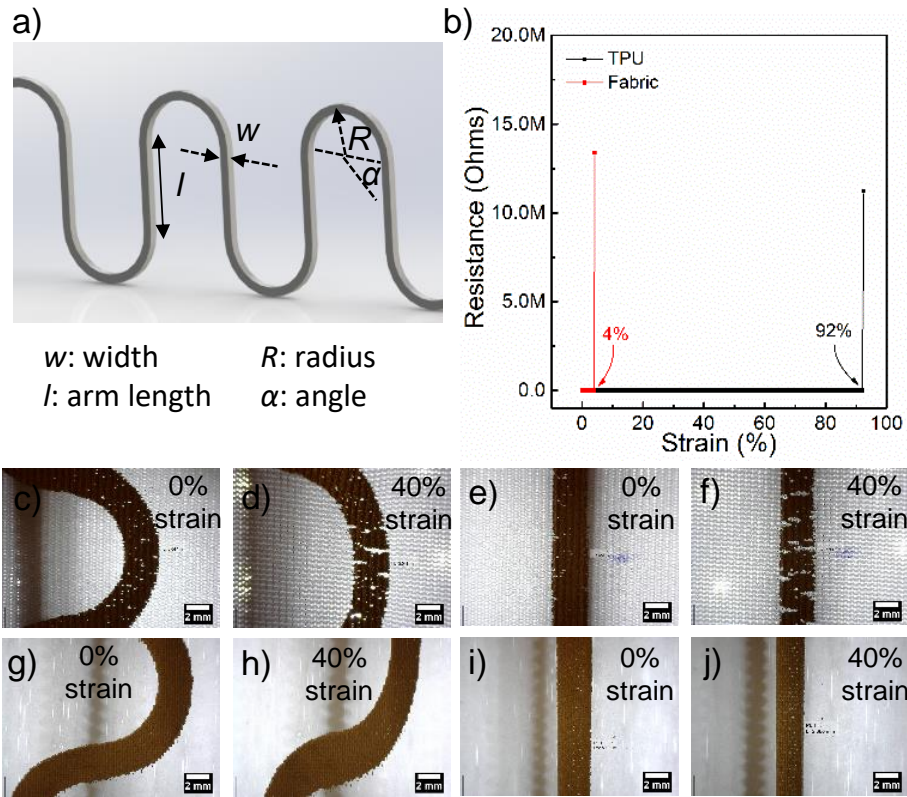


Fig. 3. (a) Meandering line design parameters (w , l , R , α), (b) resistance vs. strain behavior of the printed straight lines (width: 3mm, length: 14cm) on both knit fabric and TPU printing layer, (c), (d), (e), (f) digital microscope pictures of printed meandering and straight lines on knit fabric, (g), (h), (i), (j) digital microscope pictures of printed meandering and straight lines on TPU printing layer.

Results and Discussions

A. Screen-Printing of Conductive Ink on Knitted Fabric and TPU Film

Meandering and straight lines were initially printed on both the knit fabric and the TPU film individually without any lamination and encapsulation steps. The design of the meandering line is given in Fig. 3(a). The design was determined by the parameters: width (w), arm length (l), radius (R), and angle (α). A straight line with a 3 mm width and 14 cm length, and a meandering line ($w=3$ mm, $l=0$ mm, $R=5$ mm, $\alpha=0^\circ$ and total length=13.4 cm) were printed on both substrates. Their surface topology and electromechanical properties were compared. The surface properties of the printed ink were analyzed by Scanning Electron Microscopy (SEM), Optical Microscopy, and Digital Microscope and Atomic Force Microscope (AFM). The in-situ electromechanical

properties of the printed lines were measured with an MTS tensile tester (gauge length: 11.5 cm, crosshead speed: 5 cm/min). Two-probe electrical resistance was simultaneously recorded (2 Hz) with LabVIEW software. Fig. 3(b) shows the resistance change of the printed straight traces on the knit fabric and the TPU film as the samples were elongated. The printed straight lines failed (open electrical resistance) at $2.16\% \pm 2.60\%$ strain on the knit fabric. However, the same printed line on the TPU film could withstand up to $98.60\% \pm 9.02\%$ strain. On the other hand, the meandering lines on the knit fabric and the TPU film were able to be stretched up to $34.85\% \pm 0.64\%$ and $112.84\% \pm 23.67\%$ strains, respectively, without electrical failure. The digital microscopy pictures of the printed meandering and straight lines on the knitted fabric and the TPU film are given in Fig. 3(c)-(f) and Fig. 3(g)-(j). The pictures were taken with a digital microscope situated over a custom-built stretching device strained the sample in discrete strain intervals. The printed straight and meandering lines on the knit fabric showed significant crack formation at 40% strain, relative to that on the TPU film. This result can be attributed to the high surface roughness and surface area of the knit fabric compared to the TPU film. Two passes of conductive ink printing on the knitted fabric created less surface coating due to its high fibrous surface area. Uncoated areas were still visible on the surface of the knitted fabric after the screen-printing process in Fig. 3(c) and 3(e). The printed ink penetrates through the structure of the yarn. It also fills the large gaps that are created by the inter-looped formation during the knitting process. Therefore, the same amount of ink on the knitted fabric yielded less continuous conductive tracks, which made it sensitive to stretching at low strain values. The conductive ink printing on the TPU film yielded had a thickness of 20 micrometers, as shown in Fig 4(b). Inspection did show localized sections of the meandering line to be as high as 50 micrometers. The variability in the thickness of the ink is much lower as compared to ink printed on fabrics. This was due to the TPU film's relatively

smooth surface (Fig. 4(a) and 4(c)) compared to the knitted fabric surface. This was shown with an AFM surface topology picture (Fig. 4(d)). The TPU film had a roughness value of 0.185 micrometers, which yielded a continuous formation of conductive tracks on the TPU surface. Thus, the straight and meandering lines on TPU film at 40% strain had less visible holes and crack formation relative to that on the knit fabric. Due to strain relief property of the meandering line, the maximum stretchability of the meandering line on both substrates was higher than that of the straight line.

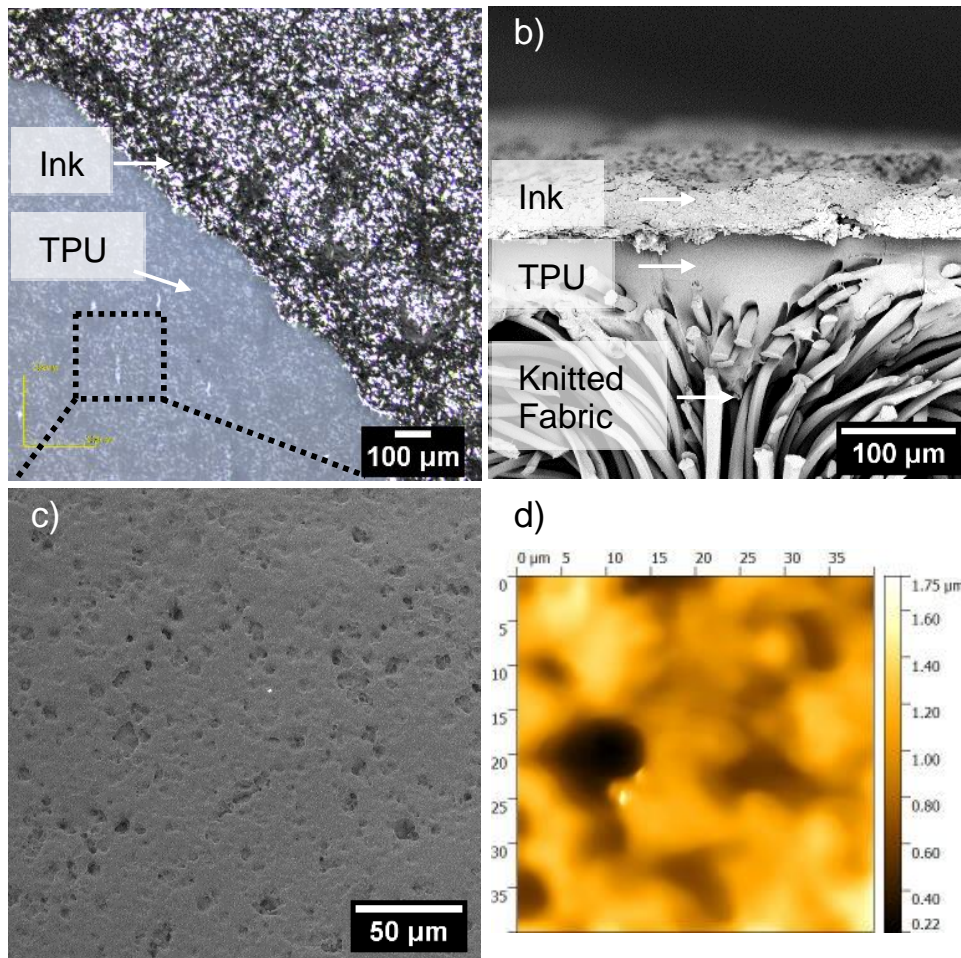


Fig. 4. (a) Optical microscopy picture of the ink on TPU film, (b) SEM cross-sectional picture of the printed conductive ink on TPU film, (c) SEM surface picture of the TPU film, (d) AFM surface topology of the TPU printing layer.

To investigate the relationship of resistance change vs. meandering line design parameters (i.e., width (w), arm length (l), radius (R), angle (α)), different meandering lines were printed on the TPU printing layer (without lamination on the knit fabric and TPU encapsulation), and a final meandering line type was selected in the end to further study in the following sections. The meandering line design parameters along with digital pictures of the printed lines are given in Fig. 1, Fig. 2 and Fig. 3 in the Supplementary Information section. Similar constant strain rate electromechanical tests were performed on the samples, as previously mentioned. The comparison of different meandering line types was made based upon $\Delta R/R$ values at 40% strains, which were obtained as a result of in-situ electromechanical tests. The results are shown in Fig. 5a. The figure shows $\Delta R/R$ vs. strain up to 40% applied strain. Each printed blocks were located on the perimeter of the plot according to decreasing $\Delta R/R$ value. The inner curves correspond to the applied strains of 10, 20, 30, 40%. Blocks A1 through A5 represent $w=1$ to 5 mm, $l=0$ mm, $R=5$ mm, and $\alpha=0^\circ$ (width varies). Blocks B1 through B5 represent $w=1$ to 5 mm, $l=5$ mm, $R=5$ mm, and $\alpha=0^\circ$ (width varies). Blocks C1 through C3 show $w=1$ mm, $l=5, 10, 15$ mm, $R=5$ mm, and $\alpha=0^\circ$ (arm length varies). Blocks D1 through D4 denote $w=1$ mm, $l=0$ mm, $R=5$ mm, and $\alpha=-20, 20, 30, 45^\circ$ (angle varies), and blocks E1 through E3 indicate $w=1$ mm, $l=5$ mm, $R=5$ mm, and $\alpha=-20, 0, 20^\circ$ (angle varies). A total of 20 blocks were printed (three replications for each block). The dimensions of each block were tabulated in the Supplementary Information section. In blocks A1-A5 and B1-B5, increasing the width (w) of the printed line decreased the value of $\Delta R/R$. This might be attributed to crack formation and propagation across the width of the crest region of the meandering line, which might be the predominant effect in meandering lines with small width values. In blocks C1-C3, increasing the arm length (l) decreased the value of $\Delta R/R$. In blocks D1-D4, increasing the angle (α) gave a decreasing trend in $\Delta R/R$. For the blocks E1-E3, decreasing the angle (α) yielded

a decreasing trend in $\Delta R/R$ values. The printed lines (blocks: A5, B3, D3) did not follow the trend, as it can be seen from Fig. 5(a), which may be ascribed to the uneven coating of the TPU film surface due to the variations in the screen-printing process. While finite element analysis (FEA) might be required to validate and compare the induced strain and stress on the printed lines and also the change in $\Delta R/R$ as a function of meandering line parameters, it is noted that a goal in this work is to evaluate the techno-economic performance of the patterned structures, ideally choosing a meandering line design that has a combination of high performance and low cost. The Blocks C2, B3, B5, and C3 had the lowest $\Delta R/R$ among the printed blocks (78.5, 73.1, 69.7, and 64.1 Ω , respectively). Fig. 5(b) shows the price of each printed block per gauge length (11.5 cm) in tensile testing. The equivalent line length for each block type was calculated according to the resistance formula ($R = \rho L/wt$). Averaged measured resistance (R , number of samples=3), resistivity (ρ) of 0.0002 Ω -cm, thickness (t) of 20 μm and printed width (w) were utilized in the calculation. Finally, the printing cost was calculated and plotted by finding the averaged ink amount ($N=3$) for a length of 11.5 cm and then multiplying it with the ink's cost (\$4/g). Localized variation in these dimensions can expect to induce some uncertainty in the cost calculation. These effects would be two-fold. Increasing the thickness of the conductive layer would decrease the resistance of the line due to the addition of more conductive material per unit length. The increased thickness would also increase materials usage and raise the cost of the printing. For the parameters used in this analysis, blocks E4, C2, D2, and D4 had the cheapest printing cost among the printed blocks (6.60, 6.00, 5.95, 5.43 cents, respectively). Block C2 was selected for further testing in the following sections since its cost was much lower than blocks B5 and B3 (20 and 21 cents). Also, block C2 was less wide than the block C3 (22 mm vs. 27 mm). This architecture also occupies less printing space, thus enabling the potential for a higher density of printed interconnects.

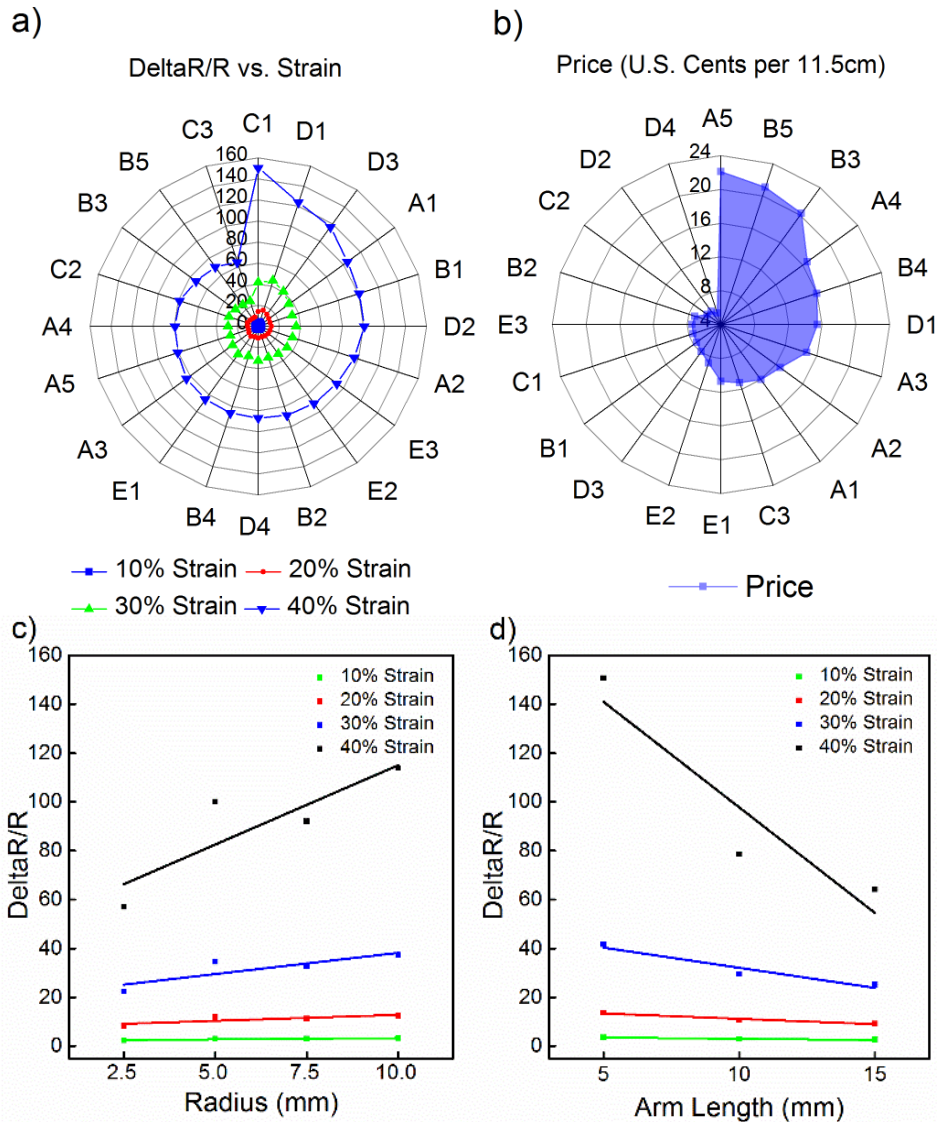


Fig. 5. (a) $\Delta R/R$ vs. strain as a function of printed meandering line parameters (w , l , R , α), (b) price of corresponding printed blocks, (c) $\Delta R/R$ vs. radius of block C2 at different strain values, (d) $\Delta R/R$ vs. arm length of block C2 at different strain values.

B. Lamination of TPU Printing Layer on Knit Fabric and Encapsulation of Conductive Ink

The selected block C2 meandering line shape ($w=1$ mm, $l=5$ mm, $R=5$ mm, $\alpha=0^\circ$) in Section III-A was used in this section. The fabrication procedure in Fig. 2(a) was followed as described in Section II-B. The meandering line was screen-printed onto the TPU printing layer (rectangular, 6 cm x 16 cm). It was then laminated on the knit fabric. Afterward, it was covered with a TPU film encapsulation (rectangular, 6 cm x 16 cm). Heat laminated TPU film layer

provides insulation and protects the printed lines from mechanical and environmental damage as other silicone and acrylic encapsulation coatings [23], [24]. In addition, it eliminates additional screen preparation and cleaning steps in the screen-printing process. Optical microscopy and SEM cross-sectional pictures of the final multilayer structure are given in Fig. 7(a) and 7(b). The mechanical properties of each layer are given in Fig. 6(c) and 6(d). The TPU printing layer, the TPU encapsulation layer, and the knit fabric are denoted as L, E, and KF, respectively. The lamination of the TPU printing layer on knit fabric is denoted as KF+L, and the combination of all of the layers is shown as KF+L+E. Fig. 6(c) shows the stress vs. strain graph of each layer and the final laminated multilayer structure. Young's modulus (modulus=stress/strain, calculated at 10% strain) of the printing layer (L), the encapsulation layer (E), and the knit fabric was calculated as 248, 90, and 1.4 kPa, respectively. The Young's modulus for KF+L and KF+L+E were found as 37 kPa and 52 kPa. The addition of the individual layers created a new multilayer structure whose mechanical properties fall between the mechanical properties of the individual layers. Fig. 6(d) describes how much transverse contraction occurs with an axial strain (i.e., Poisson's ratio=-transverse contraction/axial strain). The Poisson's ratios for L, E, KF+L+E, KF+L, and KF were calculated from the slope of the curves as 0.4, 0.3, 0.22, 0.14, and 0.09, respectively. Similar to the Young's modulus, Poisson's ratio for the multilayer structure falls between Poisson's ratio of the constituent layers.

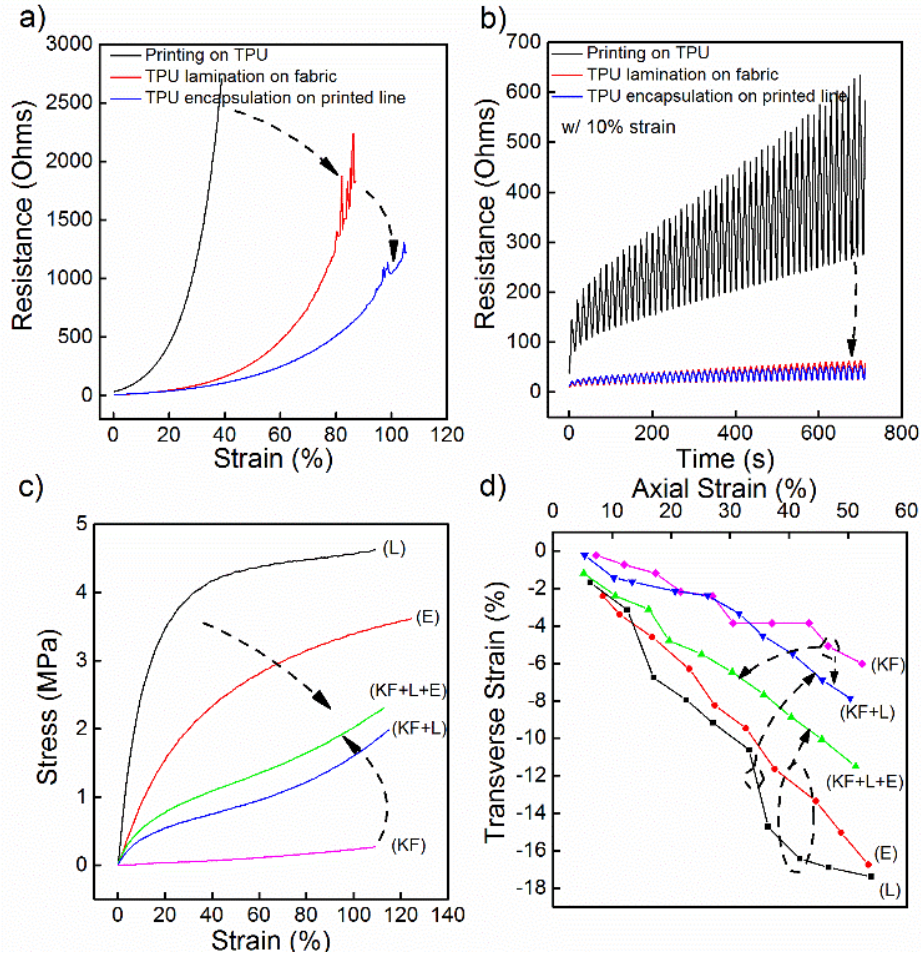


Fig. 6. (a) One-time stretching test of each fabrication step samples (test speed: 5.08 cm/min), (b) cycling test of each fabrication step samples (test speed: 10.16 cm/min), (c) mechanical properties of constituents of multilayer structure, (d) transverse contraction of the constituent layers and the final multilayer structure with axial strain.

To investigate the effect of each step (lamination and encapsulation) on the electrical properties of the printed line, a one-time in-situ stretching tensile test and cyclic tensile test were performed. The results are presented in Fig. 6(a) and 6(b). Fig. 6(a) shows the resistance change vs. strain for the test sample as it goes through each fabrication step. Block C2 printed TPU film had the sharpest strain change with strain, and its electrical failure was at $52.47\% \pm 8.28\%$ strain. When the printed layer was laminated on the knit fabric, the failure strain went up to $78.82\% \pm 11.68\%$. As the TPU encapsulation layer was applied to the rest of the layered structure, the failure strain value went up to $103.91\% \pm 5.31\%$. The cyclic tensile test results (10% strain and 100 cycles)

of each fabrication step are shown in Fig. 6(b). The block C2 printed TPU film had the highest resistance change when the number of cycles increased. The cyclic tensile testing of the multilayer structure before and after the encapsulation layer had a very slight difference. The increase in stretchability in the one-time stretching test and cyclic tensile test was attributed to both lamination temperature and TPU encapsulation. The TPU film lamination and TPU encapsulation process temperatures (125 °C) were higher than the ink curing temperature (60 °C). Thus, this resulted in a resistance drop of about 70% in ink. Since the TPU encapsulation layer enclosed the ink on the topside, an improvement in one time stretching and cyclic tensile testing properties was observed due to the retardation of the deformation of the ink layer. The encapsulation layer inhibited significant crack formation with extension and helped to recover the ink layer to its initial state. Improvement of the results in Fig. 6(a) and 6(b) can be explained by the investigation of the microstructure of the ink as it is strained. Fig. 7(c)-7(f) shows the crack formation on the printed line with strain for the printing layer laminated knit fabric sample. The visible cracks (encircled) were observed on the crest region of the meandering line starting at 20% strain and on. However, no visible cracks were found after TPU film encapsulation on the printed line in Fig. 7(g)-7(j). This explained the early resistance increase in low stain values in Fig. 7(a). When the sample was uniaxially stretched, the width of the arm region of the meandering line increased, and the crest region of the meandering line was narrowed and elongated. In contrast, the length of the crest region of the meandering line extended, and its peak width decreased. To investigate which region of the meandering line (crest vs. arm) had the most effect on the $\Delta R/R$ value, the C2 blocks with various radii ($R=2.5, 5, 7.5,$ and 10 mm) and arm length values ($l=5, 10,$ and 15 mm) were printed on the TPU film. It is helpful to note that an increased radius corresponds to the increased crest length of the printed line (perimeter of crest region= $2\pi R$). The results are given in Fig. 5(c) and

5(d). Fig. 5(c) shows $\Delta R/R$ vs. radius change at different strain values. As the radius of the meandering line was increased, the deformation in the printed line increased. This testing scenario corresponds to the stretched sample conditions in Fig. 7(c)-7(j). The meandering line's crest region length increases with stretching; thus, the deformation ($\Delta R/R$) of the printed line increases. Increasing the arm length decreased the deformation in the meandering line, shown in Fig. 5(d). However, when the sample was stretched in Fig. 7(g)-7(j), the arm length did not change (its width was widened). Therefore, it was concluded that the crest region was the region resulting in a significant resistance increase as the sample was elongated.

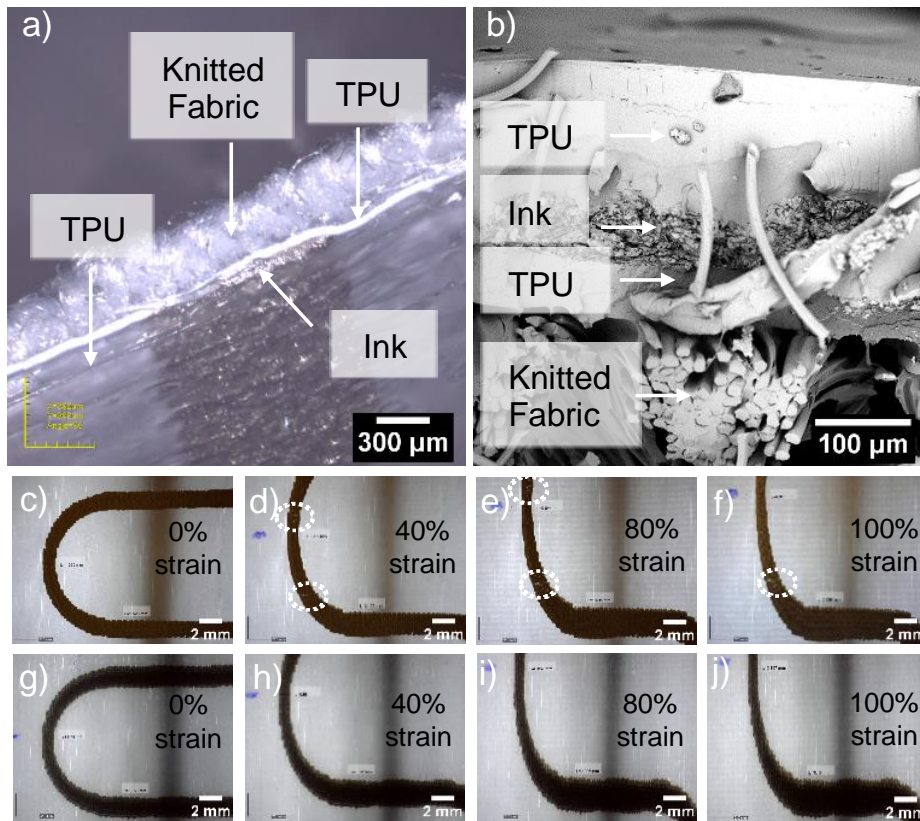


Fig. 7. (a) Optical picture of TPU laminated and encapsulated multilayer stretchable interconnect structure, (b) SEM cross-sectional view of multilayer stretchable interconnect structure, (c)-(d) digital microscope pictures with stretching of TPU film laminated knit fabric, (g)-(j) digital microscope pictures with stretching when TPU encapsulation layer was added on the printed line.

Thus far, only rectangular cut (6 cm x 16 cm) samples of the printing layer and encapsulation layer lamination onto knitted fabric were presented, shown in Fig. 2(a). The effect of removing excess TPU printing layer and encapsulation layer on the electrical properties of the printed interconnects is studied from now on, shown in Fig. 2b. A similar fabrication procedure was followed as described in Section II-B except for the dimensions of the TPU printing layer and TPU encapsulation layers were determined by offsetting the printed Block C2 meandering design by the amount of w_{offset} , as shown in Fig. 2(d). Two offset values (2 mm and 4 mm) were tested. Similar one-time stretching and cyclic tensile tests were performed to explore the effect of removing extra material from the printing and encapsulation layers. Fig. 8(a) and 8(b) shows the cycling testing (10% strain and 100 cycles) results of the whole area (rectangular) vs. 2 mm offset cut (meandering shaped TPU layer) multilayer structure. The latter had only 0.23 Ω resistance change at the end of 100 cycles, whereas, the rectangular cut lamination had a resistance change of 16.37 Ω . The first three oscillation cycles of Fig. 8(a) and 8(b) are given in Fig. 8(c) and 8(d). In Fig. 8(c), an initial straining of the sample by 10% resulted in a resistance increase of 95.96%, and the subsequent second and third cycles had a percent resistance increase of 13.10% and 7.97%. The percent resistance change trend decreased with succeeding stretching cycles (i.e., less deformation in ink with succeeding cycles). In contrast, the percent resistance increase in Fig. 8(d) was only 1.13%, and the following cycles had 0.19% and 0.1% resistance increase. For the meandering shaped multilayer interconnect (Fig. 2(b)), the applied strain resulted in the extension of the knit fabric between the printed meandering lines, where there was no lamination of TPU film. This part of the fabric underwent more straining without imposing more strain on the ink, which produced high flexibility while minimizing resistance change with strain. One-time stretching results are shown in Fig. 9(a) up to 40% strain. The inset image in Fig. 9(a) shows the

pictures of the fabricated samples. The 2 mm offset cut sample showed the smallest resistance change ($\Delta R/R=0.29$) at 40% strain. The 4 mm offset and full area laminated multilayer interconnects had $\Delta R/R$ values of 1.75 and 12.43, respectively. Removing the excess material resulted in less strain in the ink layer, which contributed to smaller resistance change upon elongation. The removal of TPU layers between two subsequent arms of printed meandering lines yielded larger strain values for a constant $\Delta R/R$ value compared to whole area rectangular lamination.

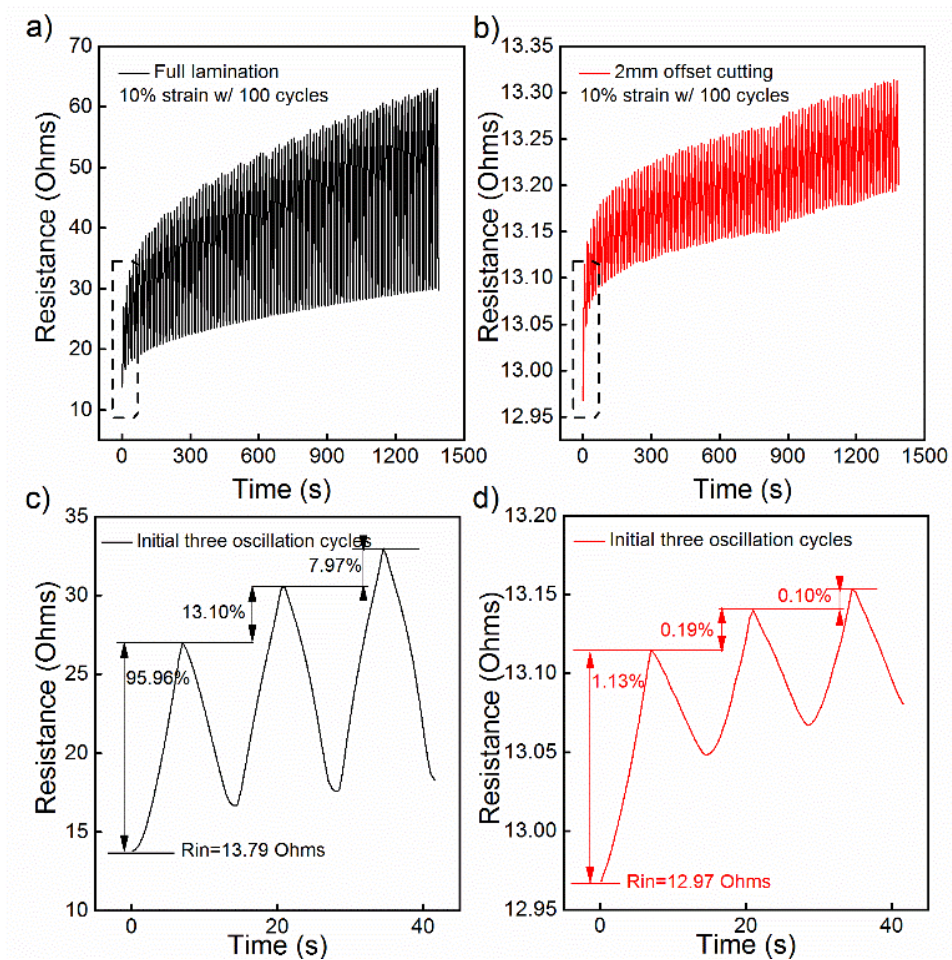


Fig. 8. Cycling test of multilayer interconnect structure (test speed: 10.16 cm/min), (a) Whole area TPU lamination and encapsulation, (b) meandering line shaped (offset-cut) TPU lamination and encapsulation, (c) initial three cycles of Fig. 8(a), (d) initial three cycles of Fig. 8(b).

To simulate the daily use of the garment (i.e., straining during dressing and additional strains due to body movement), the multilayer stretchable printed line structure (Fig. 2(b), $w_{\text{offset}}=2$ mm) was exposed to various pre-strain and cyclic strains in cyclic tensile testing. In other words, the test sample was pre-strained by a certain amount on tensile testing equipment, and then the subsequent 100 cycles were applied with an additional cyclic tensile strain. The pre-strain and cyclic tensile strain values were selected as 5%, 10%, and 20%. The result is given in Fig. 9b. At a constant pre-strain value, increasing the cyclic strain value increased the $\Delta R/R$. A similar increasing trend in $\Delta R/R$ was obtained for increasing pre-strain value at a constant cyclic tensile strain. The lowest $\Delta R/R$ value calculated was with 5% pre-strain + 5% cyclic tensile strain ($\Delta R/R=0.009$). The highest $\Delta R/R$ value was with 20% pre-strain + 20% cyclic strain ($\Delta R/R=0.91$), as expected. Higher total strain (pre-strain + cyclic strain) led to increased deformation in the printed line. To further investigate the electrical properties of the stretchable meandering printed lines, a 1,000 cycles were performed on the cyclic tensile test with a 10% pre-strain + 10% cyclic strain. The results of the test are given in Fig. 9(c) and 9(d). The resistance curve slightly levels off over time in Fig. 9(c). This was attributed to the decreasing percent resistance change of the printed line with an increasing number of cycles, as explained in Fig. 8(d). The printed line resistance changed only by 3.85 Ω at the end of 1,000 cycles, shown in Fig. 9(d). When the tensile tester crosshead was brought down from 10% strain to 0% strain, the recovery in the resistance was 8.8%. At 0% strain, the resistance of the sample decreased exponentially over time due to the recovery of ink and the multilayer substrate. The resistance value was 14.59 Ω after 333 seconds. This value could further decrease over time if the decreasing slope of the resistance was taken into account in the marked rectangular area in Fig. 9(c). It is important to reiterate that the testing in Fig. 9(c) and 9(d) mimics a real human scenario, where the pre-strain is the initial strain generated

on the printed line when a garment is placed on the body. This is followed by a cyclic strain that simulates the daily use of the garment. The self-healing of the resistance at the end of the test replicates the garment removal and storage.

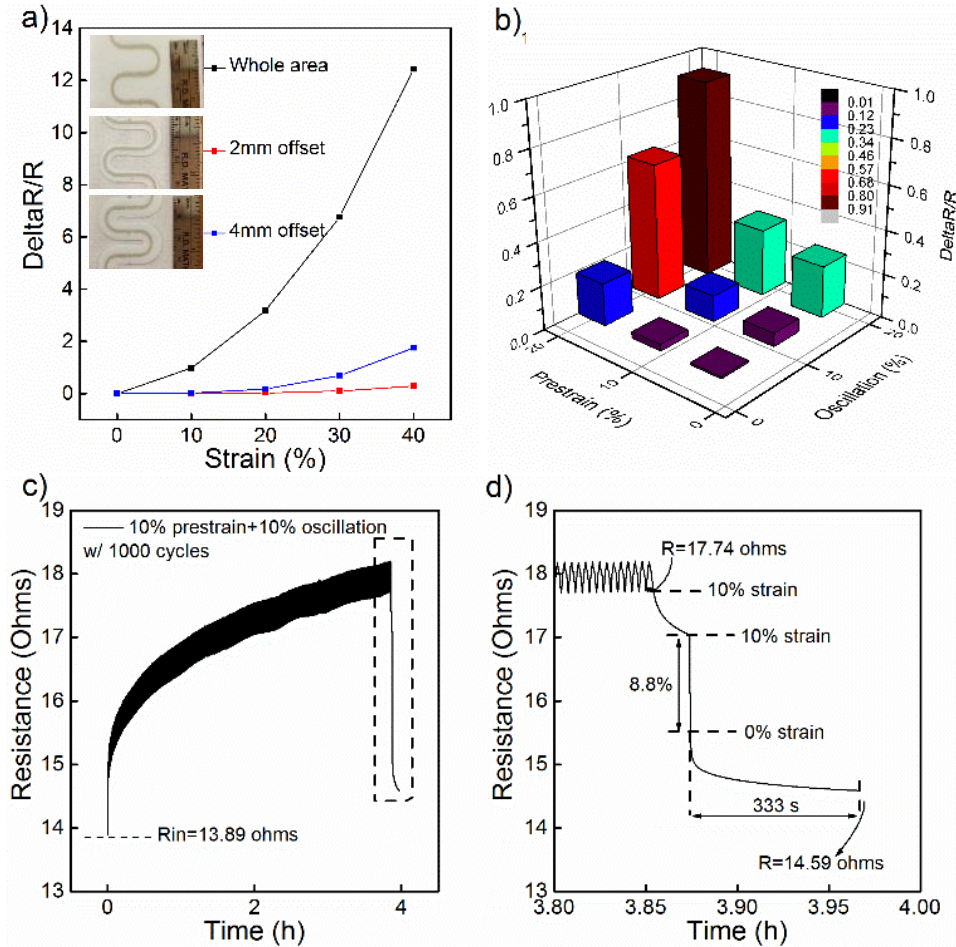


Fig. 9. (a) One-time stretching test of whole area TPU lamination vs. 2 mm and 4mm offset meandering shaped TPU lamination (test speed: 5.08 cm/min), (b) $\Delta R/R$ vs. discrete pre-strain and cyclic tensile strains (test speed: 10.16 cm/min), (c) 1000 cycle cycling test with 10% prestrain and succeeding 10% cycling strain (test speed: 10.16 cm/min), (d) zoom-out region of the marked region in Fig. 9(c).

C. Washing Durability and Stretchable Interconnects Demonstrations

An accelerated wash test (AATCC 61-2a) was performed to examine the effectiveness of the TPU encapsulation on the ink's electrical performance. One accelerated wash test is equivalent to 5 home launderings. A total of six samples with and without TPU encapsulation were fabricated according to the procedure in Fig. 2(a). The samples were placed into metal containers with 50

steel spheres and washed at 49 °C with a powder detergent. The samples without TPU encapsulation were not conductive after the initial 5 home washing cycles. However, the samples with the TPU encapsulation ($R_{\text{initial}}=7.45 \Omega \pm 1.73 \Omega$) were still conductive after 100 washing cycles with a resistance increase of 4.6 Ω .

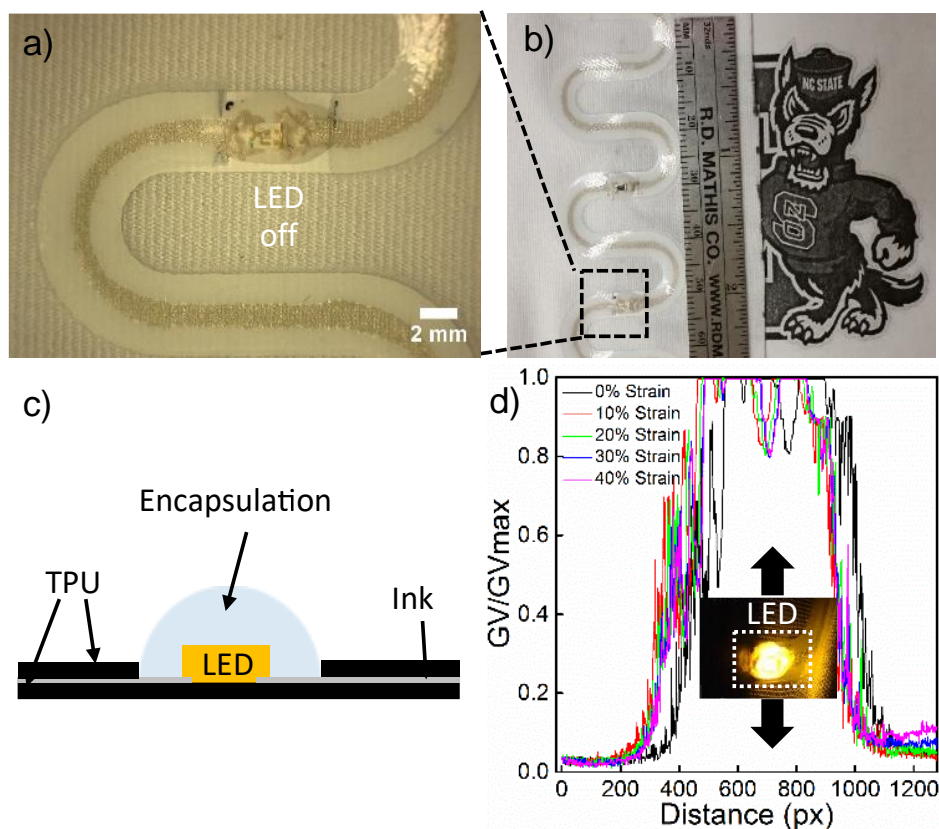


Fig. 10. (a) Close up picture of LED integrated printed stretchable line, (b) LED integrated stretchable line, (c) Cross-sectional view of LED integration, (d) LED intensity with stretching. Inset: Stretched LED integrated printed line.

To demonstrate this technology, a surface mount LED was integrated on the stretchable printed line with a 51 Ω surface mount resistor to show the applicability and use of the proposed stretchable printed meandering lines, shown in Fig. 10(a) and 10(b). The LED was bonded to conductive traces by using silver epoxy (CircuitWorks 2400). It was then encapsulated with UV curable encapsulant (Dymax 9001) to give mechanical stiffening and eliminate the debonding of LED. The cross-sectional image of its integration is shown in Fig. 10(c). The integrated LED was

powered with a 3V coin cell battery. Afterward, the LED integrated printed line was stretched up to 100% strain with a custom-built straining device, and simultaneously the surface picture was taken with a digital microscope in a dark room. The recorded video of the integrated LED was provided in the Supplementary Information section. The LED light turned off above 80% strain due to the resistance increase in the printed line, which decreased the voltage drop across the LED. However, the LED light turned back on with the recovery of the printed line. The LED light intensity up to 40% strain is given in Fig. 10(d). The intensity plot was obtained by image processing of the captured image in MATLAB software. The vertical axis represents a normalized grayscale value (GV/GV_{\max}). It was observed that the light intensity did not change up to 40% strain. However, a horizontal shift was observed in the graph due to the out-of-plane rotation of the LED during stretching.

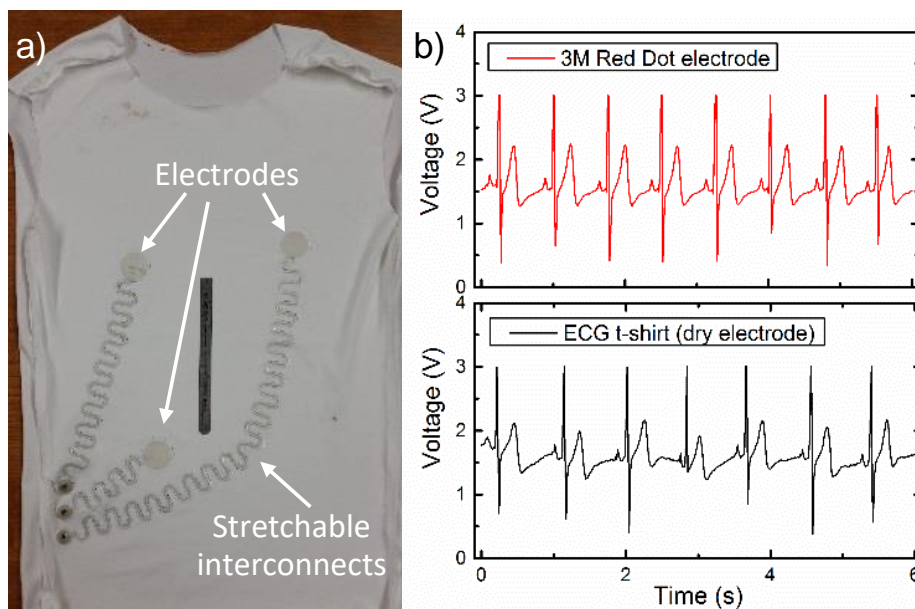


Fig. 11. (a) Inner side of the fabricated ECG t-shirt, (b) recorded ECG signals from 3M Red Dot electrode and ECG t-shirt.

For a second demonstration, an electrocardiography (ECG) shirt was fabricated to show the use of fabricated stretchable printed lines to monitor the electrical activity of the heart. Fig.

11(a) shows the inner side of the t-shirt, where three 30 mm printed dry electrodes [28] were printed along with stretchable meandering lines. The distance between electrode pairs was kept at 13 cm. Lead I of Einthoven's triangle configuration was used to measure the potential difference between electrode pairs. ECG measurement was made with a Vernier ECG signal acquisition device (1 V/1 mV gain, sampling rate: 100 Hz). A healthy male subject wore the fabricated t-shirt, and an ECG measurement was taken while the subject was standing. Fig. 11(b) shows the recorded ECG signals with the 3M Red Dot electrode (as reference) and with the ECG shirt. The acquired ECG signals show comparable ECG signals with characteristic PQRST electrocardiogram peaks.

Conclusion

A multilayer stretchable interconnect design was fabricated by screen-printing Ag/AgCl ink on thermoplastic polyurethane (TPU) film. Its subsequent heat lamination onto a knit fabric, and a TPU encapsulation on the ink layer yielded a novel multilayer stretchable interconnect structure.

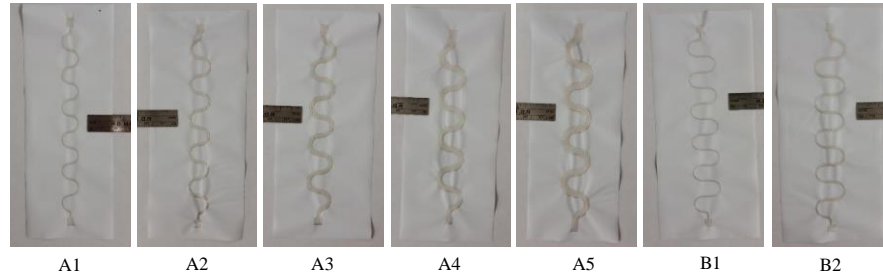
Printing the meandering and straight line on the TPU film layer provided high failure strain values compared to the knit fabric alone. A set of design of experiments was conducted to determine the most suitable meandering line by changing the meandering line parameters (width, arm length, radius, and angle). Block C2 ($w=1$ mm, $l=5$ mm, $R=5$ mm, $\alpha=0^\circ$) was chosen due to its low $\Delta R/R$ value and inexpensive printing cost.

Lamination of the printing layer on the knit fabric and encapsulation of the ink layer with TPU film were explored. The conductive ink printed TPU layer with a knit fabric backing decreased deformation on the ink. Moreover, the TPU film encapsulation on the ink layer prevented the ink from significantly cracking and helped to recover the ink to its initial position.

The effect of decreasing the area and shape of the printing and encapsulation layer was investigated. It was found that the meandering shaped printing and encapsulation layers significantly decreased the resistance change in one time stretching and cycling tests. The multilayer meandering shaped structure was cycled 1,000 times in a simulation of a human use scenario, and only 0.7 Ω resistance change was observed. In our study, the maximum stretchability achieved was about 110% with the 2 mm offset sample. Materials factors of the ink not considered in this work such as chemical and physical properties of the polymer, solvent and surfactant type, and filler type and its concentration provide additional opportunities for improved performance. In addition, synergy of novel elastic ink chemistries with strain-relief printed line designs may yield higher stretchability values.

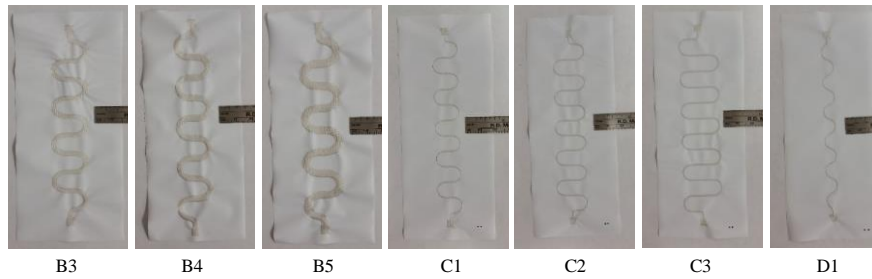
Finally, a surface mount LED integration on stretchable printed lines and an ECG shirt with meandering lines were demonstrated. The integrated LED was resistant to stretching, flexing and twisting, which might be used in wearable optical-based sensors. Moreover, the ECG shirt acquired similar ECG signals compared to the reference electrodes. The proposed inexpensive and washable (100 wash cycles) multilayer interconnects design has the utmost importance in the integration of sensors, antennas, and energy harvesting devices on garments for wearable electronics.

Supplementary Information



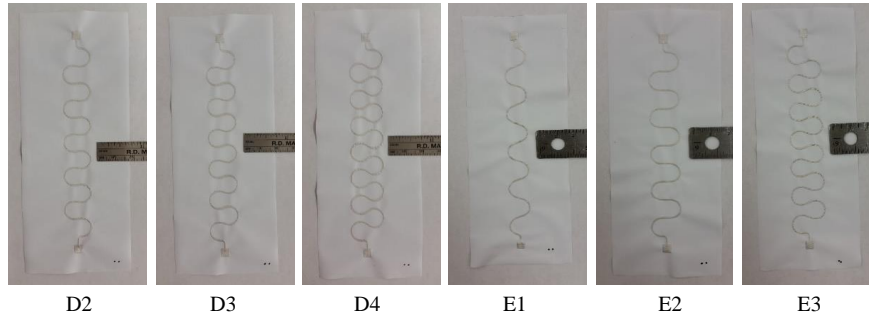
	A1	A2	A3	A4	A4	B1	B2
Length (mm)	140.46	140.25	138.03	133.80	142.56	141	141
Height (mm)	12	14	16	18	20	17	19
α (°)	0	0	0	0	0	0	0
l (mm)	0	0	0	0	0	5	5
w (mm)	1	2	3	4	5	1	2

Supplementary Fig. 1. Block A1-B2 meandering line design parameters.



	B3	B4	B5	C2	C2	C3	D1
Length (mm)	138.97	148.90	143.8	141	141	141	132.20
Height (mm)	21	23	25	17	22	27	8.24
α (°)	0	0	0	0	0	0	-20
l (mm)	5	5	5	5	10	15	0
w (mm)	3	4	5	1	1	1	1

Supplementary Fig. 2. Block B3-D1 meandering line design parameters.



	D2	D3	D4	E1	E2	E3
Length (mm)	134.36	135.71	131.63	139.10	130	133.84
Height (mm)	15.76	17.5	19.78	12.94	17	20.46
α (°)	20	30	45	-20	0	20
l (mm)	0	0	0	5	5	5
w (mm)	1	1	1	1	1	1

Supplementary Fig. 3. Block D2-E3 meandering line design parameters.

References

- [1] M. Ciocchetti, C. Massaroni, P. Saccomandi, M. A. Caponero, A. Polimadei, D. Formica, and E. Schena, "Smart Textile Based on Fiber Bragg Grating Sensors for Respiratory Monitoring: Design and Preliminary Trials," *Biosensors*, vol. 5, no. 3, pp. 602–615, Sep. 2015.
- [2] F. M. Kelly, L. Meunier, C. Cochrane, and V. Koncar, "Polyaniline: Application as solid state electrochromic in a flexible textile display," *Displays*, vol. 34, no. 1, pp. 1–7, Jan. 2013.
- [3] Q. He, Z. Zeng, Z. Yin, H. Li, S. Wu, X. Huang, and H. Zhang, "Fabrication of Flexible MoS₂ Thin-Film Transistor Arrays for Practical Gas-Sensing Applications," *Small*, vol. 8, no. 19, pp. 2994–2999, Oct. 2012.
- [4] Y. He, W. Chen, X. Li, Z. Zhang, J. Fu, C. Zhao, and E. Xie, "Freestanding Three-Dimensional Graphene/MnO₂ Composite Networks As Ultralight and Flexible Supercapacitor Electrodes," *ACS Nano*, vol. 7, no. 1, pp. 174–182, Jan. 2013.
- [5] Y. Cheng, R. Wang, J. Sun, and L. Gao, "Highly Conductive and Ulstretchable Electric Circuits from Covered Yarns and Silver Nanowires," *ACS Nano*, vol. 9, no. 4, pp. 3887–3895, Apr. 2015.
- [6] X. Pu, L. Li, H. Song, C. Du, Z. Zhao, C. Jiang, G. Cao, W. Hu, and Z. L. Wang, "A Self-Charging Power Unit by Integration of a Textile Triboelectric Nanogenerator and a Flexible Lithium-Ion Battery for Wearable Electronics," *Adv. Mater.*, vol. 27, no. 15, pp. 2472–2478, Apr. 2015.
- [7] C. Mattmann, O. Amft, H. Harms, G. Troster, and F. Clemens, "Recognizing Upper Body Postures using Textile Strain Sensors," in *2007 11th IEEE International Symposium on Wearable Computers*, 2007, pp. 29–36.
- [8] K. Cherenack, C. Zysset, T. Kinkeldei, N. Münzenrieder, and G. Tröster, "Woven Electronic Fibers with Sensing and Display Functions for Smart Textiles," *Adv. Mater.*, vol. 22, no. 45, pp. 5178–5182, Dec. 2010.
- [9] Y. Sun and J. A. Rogers, "Structural forms of single crystal semiconductor nanoribbons for high-performance stretchable electronics," *J. Mater. Chem.*, vol. 17, no. 9, pp. 832–840, Feb. 2007.
- [10] S. P. Lacour, S. Wagner, Z. Huang, and Z. Suo, "Stretchable gold conductors on elastomeric substrates," *Appl. Phys. Lett.*, vol. 82, no. 15, pp. 2404–2406, Apr. 2003.
- [11] T. Someya, Y. Kato, T. Sekitani, S. Iba, Y. Noguchi, Y. Murase, H. Kawaguchi, and T. Sakurai, "Conformable, flexible, large-area networks of pressure and thermal sensors with organic transistor active matrixes," *Proc. Natl. Acad. Sci. U. S. A.*, vol. 102, no. 35, pp. 12321–12325, Aug. 2005.
- [12] H. C. Ko, M. P. Stoykovich, J. Song, V. Malyarchuk, W. M. Choi, C.-J. Yu, J. B. Geddes, J. Xiao, S. Wang, Y. Huang, and J. A. Rogers, "A hemispherical electronic eye camera based on compressible silicon optoelectronics," *Nature*, vol. 454, no. 7205, pp. 748–753, Aug. 2008.
- [13] D. S. Gray, J. Tien, and C. S. Chen, "High-Conductivity Elastomeric Electronics," *Adv. Mater.*, vol. 16, no. 5, pp. 393–397, Mar. 2004.
- [14] K. L. Lin and K. Jain, "Design and Fabrication of Stretchable Multilayer Self-Aligned Interconnects for Flexible Electronics and Large-Area Sensor Arrays Using Excimer Laser Photoablation," *IEEE Electron Device Lett.*, vol. 30, no. 1, pp. 14–17, Jan. 2009.

- [15] H.-J. Kim, C. Son, and B. Ziaie, "A multiaxial stretchable interconnect using liquid-alloy-filled elastomeric microchannels," *Appl. Phys. Lett.*, vol. 92, no. 1, p. 011904, Jan. 2008.
- [16] F. Bossuyt, T. Vervust, and J. Vanfleteren, "Stretchable Electronics Technology for Large Area Applications: Fabrication and Mechanical Characterization," *IEEE Trans. Compon. Packag. Manuf. Technol.*, vol. 3, no. 2, pp. 229–235, Feb. 2013.
- [17] Y.-Y. Hsu, M. Gonzalez, F. Bossuyt, J. Vanfleteren, and I. De Wolf, "Polyimide-Enhanced Stretchable Interconnects: Design, Fabrication, and Characterization," *IEEE Trans. Electron Devices*, vol. 58, no. 8, pp. 2680–2688, Aug. 2011.
- [18] N. Lu, C. Lu, S. Yang, and J. Rogers, "Highly Sensitive Skin-Mountable Strain Gauges Based Entirely on Elastomers," *Adv. Funct. Mater.*, vol. 22, no. 19, pp. 4044–4050, Oct. 2012.
- [19] S. Lee, S. Shin, S. Lee, J. Seo, J. Lee, S. Son, H. J. Cho, H. Algadi, S. Al-Sayari, D. E. Kim, and T. Lee, "Ag Nanowire Reinforced Highly Stretchable Conductive Fibers for Wearable Electronics," *Adv. Funct. Mater.*, vol. 25, no. 21, pp. 3114–3121, Jun. 2015.
- [20] Q. Li and X. Tao, "A stretchable knitted interconnect for three-dimensional curvilinear surfaces," *Text. Res. J.*, vol. 81, no. 11, pp. 1171–1182, Jul. 2011.
- [21] Q. Li and X. M. Tao, "Three-dimensionally deformable, highly stretchable, permeable, durable and washable fabric circuit boards," *Proc. R. Soc. Lond. Math. Phys. Eng. Sci.*, vol. 470, no. 2171, p. 20140472, Nov. 2014.
- [22] T. H. J. van Osch, J. Perelaer, A. W. M. de Laat, and U. S. Schubert, "Inkjet Printing of Narrow Conductive Tracks on Untreated Polymeric Substrates," *Adv. Mater.*, vol. 20, no. 2, pp. 343–345, Jan. 2008.
- [23] M. Suh, K. E. Carroll, E. Grant, and W. Oxenham, "Effect of fabric substrate and coating material on the quality of conductive printing," *J. Text. Inst.*, vol. 104, no. 2, pp. 213–222, Feb. 2013.
- [24] B. Karaguzel, C. R. Merritt, T. Kang, J. M. Wilson, H. T. Nagle, E. Grant, and B. Pourdeyhimi, "Flexible, durable printed electrical circuits," *J. Text. Inst.*, vol. 100, no. 1, pp. 1–9, Mar. 2009.
- [25] S. Takamatsu, T. Lonjaret, E. Ismailova, A. Masuda, T. Itoh, and G. G. Malliaras, "Wearable Keyboard Using Conducting Polymer Electrodes on Textiles," *Adv. Mater.*, p. n/a–n/a, Nov. 2015.
- [26] K.-S. Kim, K.-H. Jung, and S.-B. Jung, "Design and fabrication of screen-printed silver circuits for stretchable electronics," *Microelectron. Eng.*, vol. 120, pp. 216–220, May 2014.
- [27] N. Matsuhisa, M. Kaltenbrunner, T. Yokota, H. Jinno, K. Kuribara, T. Sekitani, and T. Someya, "Printable elastic conductors with a high conductivity for electronic textile applications," *Nat. Commun.*, vol. 6, p. 7461, Jun. 2015.
- [28] M. A. Yokus and J. S. Jur, "Fabric-Based Wearable Dry Electrodes for Body Surface Biopotential Recording," *IEEE Trans. Biomed. Eng.*, vol. 63, no. 2, pp. 423–430, Feb. 2016.

Appendix C: Skin Hydration Sensor for Customizable Electronic Textiles

Murat A. Yokus and Michael A. Daniele

*As published in *MRS Advances* (2016)

Abstract

This paper introduces the design and simulated operation of a capacitive hydration sensor for integration into textile-based electronics. The multilayer patch is composed of a textile layer and an attached series of serpentine-interdigitated electrodes. The model used for simulations incorporated this design onto a representative model of skin. The serpentine-interdigitated electrodes are electrodes for the capacitive measurement of skin hydration. In this study, the capacitance change relative to skin hydration was simulated using finite element analysis. The simulation results suggest the fabric layer had little effect on the capacitance of the sensor. Furthermore, the frequency domain simulations indicated that the capacitance of the sensor decreased with increasing frequency, and the decrease in capacitance was more significant for the dry skin compared to the wet skin. Therefore, the variation in the capacitance value of the serpentine-interdigitated electrodes can be employed for continuous skin hydration detection.

Introduction

Hydration plays a significant role in cellular homeostasis and thermoregulation. The human body expels water mainly by discharging urine from kidneys, excreting sweat *via* the skin and exhaling water vapor from the lungs. Water loss from sweating can be between 0.3 L/h – 0.6 L/h, depending on environmental conditions and activity levels. Water loss, as low as 2% of the body mass, leads to dehydration, which manifests as loss in physical and cognitive performance and alterations in kidney, heart, and gastrointestinal functions¹. Therefore, monitoring for dehydration is critical for the determination of the physiological status of people experiencing significant heat

stress or performing strenuous activity, such as emergency operators, athletes, and military personnel.

Electrical methods are the most commonly used techniques for the evaluation of skin hydration. Commercial products, such as Skicon® and Corneometer®, measure skin hydration based on the change in skin conductance and capacitance, respectively². There are at least three major factors affecting the accuracy of measuring skin conductance, including dryness, ion concentration, and measurement frequency³. Electron conduction dominates in dry skin; however, conduction due to the exchange of protons on hydrogen-bonded water molecules dominates in hydrated skin and is a function of water content. Nonetheless, the measurement of skin conductivity may show significant variation dependent on the skin surface (*e.g.*, hair, oil) and skin temperature. Similarly, skin capacitance may change with the distribution of water, ions, and dipoles in the skin, which directly affects the electrical field penetration into skin³. However, capacitive measurement techniques are advantageous over skin conductance measurements because they mitigate surface effects by measuring larger and deeper tissue volumes (*i.e.*, up to 40 μm in depth)².

Alternatives to electrical methods for measuring skin hydration have been developed. Radiofrequency absorptiometry was used to monitor hydration by relating electromagnetic field absorption and reflection parameters to the total weight loss due to sweating⁴. However, location-based RF transmission variation was exhibited due to the change in tissue composition across the skin surface. Optical sweat sensors have been explored which utilize a colorimetric detection scheme to quantify ion concentration in sweat and subsequently infer hydration⁵. A near-infrared (NIR) imaging method was investigated to measure NIR light absorption intensity as a function of the concentration of water in the skin⁶. Although promising such alternative methods for

measuring skin hydration are not yet suitable for integration into wearable sensor systems due to the operational and power requirements of optical systems, or the substantial response variation under mechanical deformation or movement across the skin's surface.

Consequently, many wearable hydration sensors have focused on the miniaturization of electronic systems. Impedance ⁷, capacitance ⁸, and resonance ⁹ based stretchable epidermal sensors are some of the recent techniques utilized in hydration monitoring. Also, wrist-worn wearable sensor arrays ¹⁰ and “tattoo-like” epidermal devices ¹¹ have recently been reported which measure the metabolites and electrolytes in sweat, which can denote hydration level.

Accordingly, we have chosen to begin the investigation into a simple capacitive hydration sensor that can be easily integrated with textile-based systems. Herein, a capacitive hydration sensor for integration with a textile-based system is designed and simulated. The capacitive hydration sensor and measurement concept are illustrated in Figure 1.

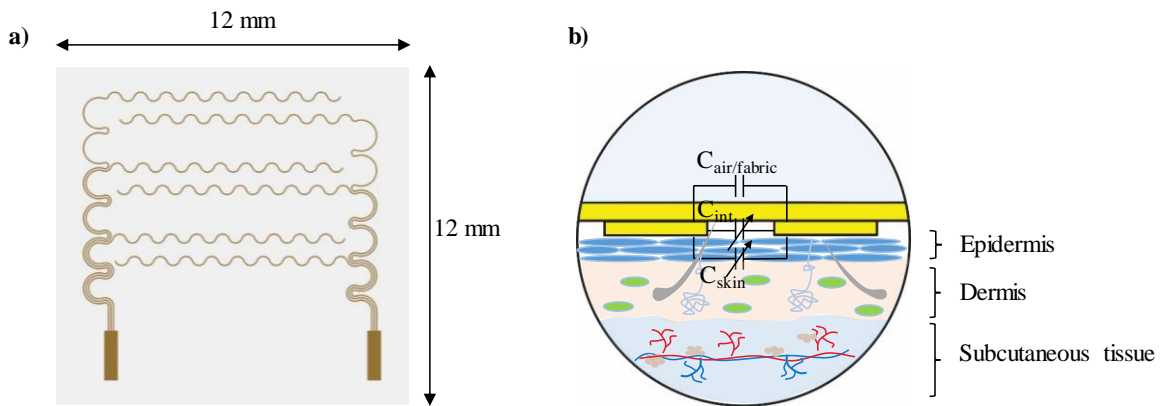


Figure 1. a) Design of capacitance hydration sensor with serpentine-interdigitated electrodes. Electrodes have a width of 50 μm and a separation of 50 μm . A 300 nm gold layer was used as the model for the electrodes. b) A cross-sectional view of the capacitive sensor. $C_{air/fabric}$, C_{int} , and C_{skin} are the capacitances of air/fabric, intermediate layer and underlying skin, respectively.

The proposed capacitive hydration sensor utilizes serpentine-interdigitated electrodes (width of 50 μm). The selected width of the electrodes (50 μm) provides for flexibility and conformal adherence to the skin and textile interfaces; moreover, these electrode dimensions can

be easily fabricated with current photolithography techniques. The serpentine design of the electrodes accommodates for mechanical deformation experienced during use ¹². Increased mechanical compliance of the electrodes is advantageous for the integration of the sensor on a flexible and stretchable textile system. Electrodes are encapsulated in polyimide (1 μm top and 1 μm bottom, $\epsilon_r=3.4$) to improve endurance under cyclic tensile loading. Only the individual electrodes are encapsulated, which provides for a minimally occlusive patch when applied to the textile or skin. The serpentine-shaped electrodes can be easily integrated onto wearables such as on a knit fabric to realize a wearable or skin mounted patches. In the model, textile lies at the top of the multilayer structure and facilitates the air and vapor permeability to the skin. Fig. 1(b) illustrates the capacitive sensing mechanism of the patch, where $C_{\text{air/fabric}}$, C_{int} , and C_{skin} are capacitances due to air/fabric, intermediate layer, and underlying skin. The skin capacitance (C_{skin}) and the intermediate layer capacitance (C_{int}) vary with hydration of the skin as the dielectric constant of the medium changes; therefore, the capacitive sensor patch could give a feedback to the user regarding hydration.

Experimental

The operation of the capacitive hydration sensor was modeled in COMSOL Multiphysics® software. The 3D simulations were performed with Electrostatics and Electric Current Models. Under static conditions, the Electrostatic Model solves Maxwell's equations, Eqn. 1-2, for electric potential, where D , ρ_v , E , and V are electric flux density (C/m^2), electric charge density (C/m^3), electric field intensity (V/m), and electric potential (V), respectively ¹³. Divergence and gradient operators are shown as $(\nabla \cdot)$ and (∇) .

$$\nabla \cdot \mathbf{D} = \rho_v \quad (1)$$

$$\mathbf{E} = -\nabla V \quad (2)$$

Similarly, the Electric Current Model utilizes the Maxwell's equations in Eqn. 2-4 in the frequency domain, where \mathbf{J} , Q_j , σ , \mathbf{J}_e are current density (A/m^2), current source (A/m^3), electrical conductivity (S/m), and externally generated current density (A/m^2).

$$\nabla \cdot \mathbf{J} = Q_j \quad (3)$$

$$\mathbf{J} = \sigma \mathbf{E} + j\omega \mathbf{D} + \mathbf{J}_e \quad (4)$$

The Stationary Electrostatic Model was used to compute the electric field, potential distribution, and capacitance; whereas, the Electric Current Model was utilized to compute the value of capacitance in frequency-domain from 10 Hz to 0.1 MHz. The applied voltage amplitude was kept constant for both simulations (1 V). The relative tolerance for the stationary and frequency-domain studies was set to 0.001. Partitioned boundary boxes (width: 20 mm, depth: 20 mm, height: 20mm) were used at the top and bottom of the patch to model the dielectric properties of air, fabric, and skin. To simulate the effect of the fabric on top of the capacitive sensor, a dielectric permittivity sweep from 1 to 10 was performed in the Stationary Electrostatic Model and the corresponding capacitance values were calculated.

Discussion

The capacitance of the interdigitated structure as a function of its geometrical parameters has been reported ¹⁴⁻¹⁵; hence, the proposed geometry (Fig. 1a) was selected as a practical design for both simulation and future fabrication. As reported by Wang ¹⁴, the capacitance of the interdigitated electrodes is proportional to an increase in electrode thickness, electrode width, electrode overlap, number of electrodes, and dielectric constant of the medium, and inversely proportional to electrode spacing.

The capacitance of the sensor with respect to the change of the top dielectric layer's relative permittivity (ϵ_r) value is shown in Figure 2a. The capacitance was calculated by incorporating the

relative permittivity of the dry and wet skin into the model, which were reported for 10 Hz¹⁶⁻¹⁷. In the model, it is assumed that the relative permittivity of the skin does not change significantly from 10 Hz to DC. The sensor on the wet skin showed a larger capacitance compared to the dry skin. This was attributed to the change in the dielectric constant of the skin with hydration. The capacitance in the air medium ($\epsilon_r=1$) on dry skin was computed as 29.3 pF. The dielectric constants of commonly used textiles (*e.g.* polyester, polyamide etc.) fall in the range of the hatch area in Fig. 2(a). The addition of a textile layer ($\epsilon_r=4$) on top of the capacitive sensor in the model increased the capacitance by 1.2 and 1.8 pF for dry and wet skin, respectively. It is important to note that the textile layer is not modeled as a porous media. Future models may incorporate the significant porosity of advanced textiles, which would decrease the effective permittivity of the medium, resulting in a decrease in total capacitance. Further increases in the permittivity of the textile layer increased the capacitance value for both wet and dry skin models. This could be an indication of the absorbency and wetting effects of the textile under perspiring conditions.

The electric field and potential distribution of the capacitive sensor are shown in Fig. 2(b) and (d), respectively. There was a strong capacitive coupling between the serpentine inner interdigitated fingers separated by 0.4 and 1.5 mm in Fig. 2(b). Fig. 2(c) shows the cross-sectional potential distribution of the capacitive sensor on the dry skin with a textile layer ($\epsilon_r=2$). The cross-sectional image was obtained by using a vertical cut plane in Fig. 1(a). It was shown that the field penetrated more into the textile and dielectric layer than the skin due to the higher dielectric constant of the skin relative to the air.

The capacitance change as a function of frequency is shown in Figure 3. The equivalent circuitry of the capacitive sensor can be written as a parallel combination of a capacitor and a

resistor. The complex admittance of the RC circuit is given as in Eqn. 5, where Y , G , ω , and C are used for admittance, conductance, radial frequency, and capacitance.

$$Y = G + j\omega C \quad (5)$$

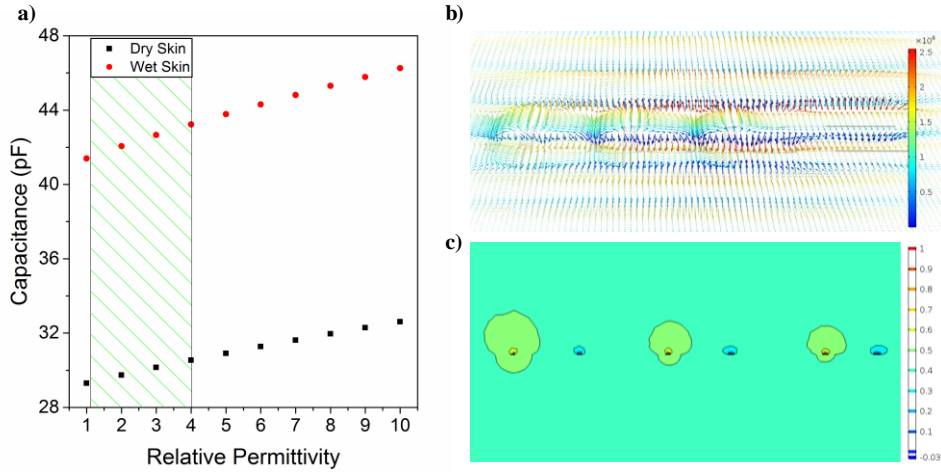


Figure 2. a) Capacitance change as a function of the textile layer’s relative permittivity for dry and wet skin models. The hatch area indicates the relative permittivity range for common textile materials. b) Side view electric field distribution of capacitive sensor on the dry skin with a fabric layer ($\epsilon_r=2$). c) Cross-sectional view of the electrical potential distribution of the serpentine capacitive sensor on the dry skin.

The admittance of the capacitive hydration sensor was calculated. Subsequently, the capacitance value of the serpentine-interdigitated electrodes was calculated from the imaginary part of the admittance. The decrease in the dielectric constant and the increase in the conductivity with increasing frequency (*i.e.*, the dispersion effects), which corresponds to previous reports¹⁶⁻¹⁷, were included in the model. The simulation determined the capacitance of the sensor decreased with increasing frequency for the dry and wet skin. This is a result, in part, of the decrease in the dielectric constant with respect to increasing frequency. The decrease in the capacitance also may be attributed to the increasing electrical conductivity of the skin with respect to increasing frequency, which results in an increase in the real part (*i.e.*, conductance) of the admittance. The capacitance decreases as radial frequency (ω) increases, and the decrease in the capacitance was much smaller for the wet skin model with increasing frequency. Ultimately, the capacitive

response of the serpentine-interdigitated electrodes at high frequencies can be used to assess skin hydration.

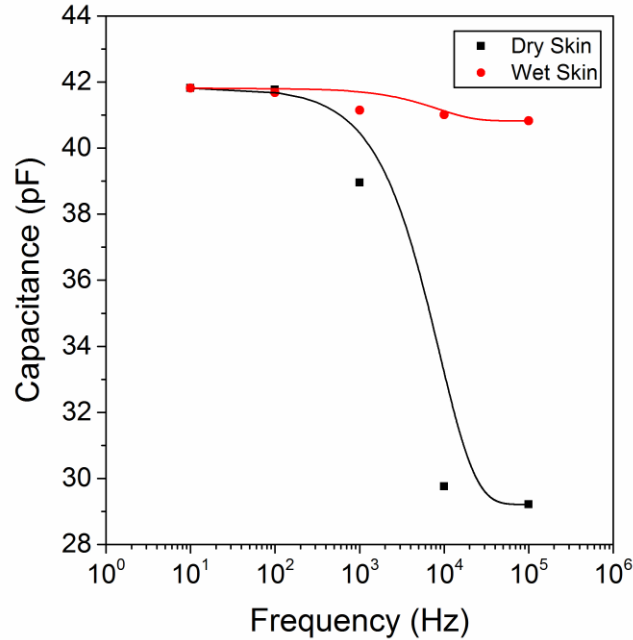


Figure 3. Capacitance change as a function of frequency for dry and wet skin models.

Conclusion

Design and simulation of a capacitive sensor were studied for potential use in skin hydration or sweat monitors to be integrated onto textile systems. The capacitance change of the serpentine-interdigitated electrodes was modeled as a device at the skin-textile interface. The electrical properties of the sensor were simulated with models of hydrated and dehydrated skin. The capacitance of the sensor increased as a function of skin hydration. We also note that the addition of the textile layer to the model did not raise the capacitance significantly. The simulation results also suggest that higher frequencies are more sensitive to changes in hydration.

Continued modeling efforts will explore the change in capacitance with dynamic conditions, where the sensor itself undergoes mechanical stress and deformation as a result of a wearer's movements. Future experimental work will include fabrication, *in vitro* characterization

(linearity, response time, and sensitivity), and *in vivo* operation of the capacitive hydration sensor integrated into a textile system.

References

1. Popkin, B. M.; D'Anci, K. E.; Rosenberg, I. H., Water, hydration, and health. *Nutr Rev* **2010**, *68* (8), 439-458.
2. Clarys, P.; Clijsen, R.; Taeymans, J.; Barel, A. O., Hydration measurements of the stratum corneum: comparison between the capacitance method (digital version of the Corneometer CM 825 (R)) and the impedance method (Skicon-200EX (R)). *Skin Res Technol* **2012**, *18* (3), 316-323.
3. Berardesca, E.; Cosmetics, E. G. f. E. M. o.; Products, O. T., EEMCO guidance for the assessment of stratum corneum hydration: electrical methods. *Skin Res Technol* **1997**, *3* (2), 126-132.
4. Moran, D. S.; Heled, Y.; Margaliot, M.; Shani, Y.; Laor, A.; Margaliot, S.; Bickels, E. E.; Shapiro, Y., Hydration status measurement by radio frequency absorptiometry in young athletes - a new method and preliminary results. *Physiol. Meas.* **2004**, *25* (1), 51-59.
5. Al-omari, M.; Liu, G.; Mueller, A.; Mock, A.; Ghosh, R. N.; Smith, K.; Kaya, T., A portable optical human sweat sensor. *J. Appl. Phys.* **2014**, *116* (18), 183102.
6. Zhang, S.; Meyers, C. L.; Subramanyan, K.; Hancewicz, T., Near infrared imaging for measuring and visualizing skin hydration. A comparison with visual assessment and electrical methods. *J. Biomed. Opt.* **2005**, *10* (3), 031107.
7. Huang, X.; Yeo, W.-H.; Liu, Y.; Rogers, J. A., Epidermal differential impedance sensor for conformal skin hydration monitoring. *Biointerphases* **2012**, *7* (1), 52.
8. Wei, P. H.; Morey, B.; Dyson, T.; McMahon, N.; Hsu, Y. Y.; Gazman, S.; Klinker, L.; Ives, B.; Dowling, K.; Rafferty, C., A Conformal Sensor for Wireless Sweat Level Monitoring. *2013 Ieee Sensors* **2013**, 991-994.
9. Huang, X.; Liu, Y. H.; Cheng, H. Y.; Shin, W. J.; Fan, J. A.; Liu, Z. J.; Lu, C. J.; Kong, G. W.; Chen, K.; Patnaik, D.; Lee, S. H.; Hage-Ali, S.; Huang, Y. G.; Rogers, J. A., Materials and Designs for Wireless Epidermal Sensors of Hydration and Strain. *Adv. Funct. Mater.* **2014**, *24* (25), 3846-3854.
10. Gao, W.; Emaminejad, S.; Nyein, H. Y. Y.; Challa, S.; Chen, K.; Peck, A.; Fahad, H. M.; Ota, H.; Shiraki, H.; Kiriya, D.; Lien, D.-H.; Brooks, G. A.; Davis, R. W.; Javey, A., Fully integrated wearable sensor arrays for multiplexed in situ perspiration analysis. *Nature* **2016**, *529* (7587), 509-514.
11. Bhandodkar, A. J.; Molinnus, D.; Mirza, O.; Guinovart, T.; Windmiller, J. R.; Valdes-Ramirez, G.; Andrade, F. J.; Schoning, M. J.; Wang, J., Epidermal tattoo potentiometric sodium sensors with wireless signal transduction for continuous non-invasive sweat monitoring. *Biosens Bioelectron* **2014**, *54*, 603-609.
12. Gray, D. S.; Tien, J.; Chen, C. S., High-conductivity elastomeric electronics. *Adv. Mater.* **2004**, *16* (5), 393-+.
13. COMSOL AC/DC Module User's Guide, Version 5.2.
14. Wang, Y.; Chong, N.; Cheng, Y. L.; Chan, H. L. W.; Choy, C. L., Dependence of capacitance on electrode configuration for ferroelectric films with interdigital electrodes. *Microelectron. Eng.* **2003**, *66* (1-4), 880-886.
15. Gevorgian, S. S.; Martinsson, T.; Linner, P. L. J.; Kollberg, E. L., CAD models for multilayered substrate interdigital capacitors. *IEEE Trans. Microwave Theory Tech.* **1996**, *44* (6), 896-904.

16. Miklavčič, D.; Pavšelj, N.; Hart, F. X., Electric properties of tissues. *Wiley encyclopedia of biomedical engineering* **2006**.
17. Gabriel, S.; Lau, R.; Gabriel, C., The dielectric properties of biological tissues: III. Parametric models for the dielectric spectrum of tissues. *Physics in medicine & biology* **1996**, *41* (11), 2271.

Appendix D: Towards a Wearable Perspiration Sensor

Murat A. Yokus, Cheyanne Hass, Talha Agcayazi, Alper Bozkurt and Michael A. Daniele

*As published in *IEEE Sensors Conference* (2017)

Abstract

There has been a growing interest in sweat-based sensors in the past several decades as eccrine sweat contains many metabolites of physiological significance. In particular, perspiration sensing is important not only for wellness monitoring and performance analysis, but also replenishment of metabolically significant ions and metabolites such as Na^+ , Cl^- , K^+ , and glucose. This study aims to develop a technology for a miniaturized and wearable system for perspiration monitoring by integrating serpentine-shaped interdigitated electrodes as an impedance sensor interfaced with a flexible low-power circuit system. In this paper, we demonstrated that the wearable perspiration system could track the changes of impedance of a simulated sweat solution as close to a benchtop potentiostat. This wearable system holds a significant potential for performance, wellness, and health tracking.

Introduction

Sweating plays an important role in thermal regulation of the human body by cooling off the skin surface when a person is exposed to heat, mental stimuli or muscular exercise. In contrast to its assistance in keeping the body temperature constant, sweating in large quantities disrupts the tonicity and volumes of the body fluid compartments and may lead to impaired circulation, diminished heat dissipation, nausea, fatigue, and heatstroke¹. Therefore, perspiration, as the product of sweating mechanism, has the utmost importance in monitoring the performance of athletes, firefighters, and military personnel when they undergo strenuous activities in addition to the detection of medical problems such as cystic fibrosis. Moreover, if the perspiration is sampled

in a collective fashion, it can act as a “biochemical memory card” by continuously storing physiologically relevant analytes (e.g., Na^+ , Cl^- and K^+) and metabolites (e.g., glucose, lactate and urea); hence it can be ultimately used as a prolonged measurement of human biochemistry ¹.

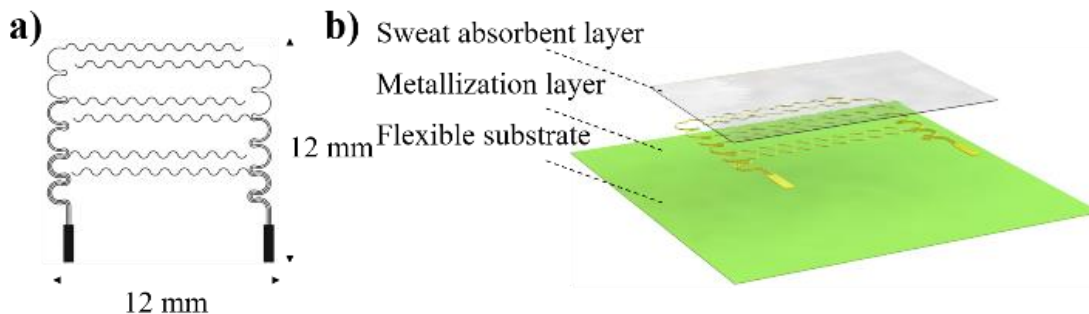


Fig. 1. a) Serpentine-interdigitated electrodes. b) Conceptual design of a multilayer perspiration sensor.

One of the most common ways of measuring perspiration is to assess the bare weight of a person before and after exercise ². This method lacks a measurement of instantaneous or real-time perspiration and may not be able to monitor a sudden change in physiology due to excessive sweat loss or physical exhaustion. Various other techniques (e.g., colorimetric, direct observation of sweat drops with a CCD camera, thermal conductivity, and capacitance) were proposed in the past for perspiration monitoring ³. Bulky equipment sizes, high cost, and environmental interference hinder the use of these techniques as real-time wearable perspiration monitors during physical activity. Conductivity-based sweat analysis is a fast and inexpensive method. It has been used for the detection of cystic fibrosis ⁴, measurement of electrolyte activity in tears ⁵, and evaluation of sweat ion concentration during exercise ⁶. There have been a few studies recently on wearable conductivity-based sweat sensors ⁷, but still, continuous measurement of the sweat rate in wearable form is not reported yet.

Herein, we report the development of a flexible and miniaturized impedance-based perspiration sensor. The system is small ($35 \times 50 \text{ mm}^2$) and mechanically compliant to conform to

the skin surface. We designed the system by using commercial-off-the-shelf (COTS) components on a flexible Kapton[®] film. We validated the system by measuring the impedance of different concentrations of NaCl solutions as Na⁺ and Cl⁻ ions are the most abundant ions in sweat and determine the overall conductance properties of sweat. We compared the performance of our system to a benchtop impedance measurement equipment. We showed a comparable performance, but in a more functional and inexpensive manner.

Materials and Methods

A. Fabrication of Perspiration Sensors

We started the fabrication of the perspiration sensors by DC sputtering a 100 nm aluminum layer on a glass wafer. Subsequently, the glass wafer underwent photolithography and Al wet etching processes to obtain a serpentine-shaped interdigitated pattern (Fig. 1a). We selected the serpentine-shaped interdigitated pattern because it would provide flexibility to the system while maintaining its functionality under dynamic body movements. While the sensing part is currently fabricated on a glass wafer, the next iteration will utilize a flexible substrate (e.g., polyimide). Three different sizes of perspiration sensors were fabricated (i.e., small, medium, and large). The sensing areas of electrodes were around 0.09, 0.21, and 0.37 cm², respectively.

B. In-vitro Characterization

We carried out the impedance measurements with a conventional benchtop potentiostat (Reference 600+, Warminster, PA USA). Electrochemical impedance spectroscopy measurements were performed from 10 Hz to 5 MHz with a 10 mV applied AC potential. A filter paper (10 mm x 15 mm) was placed on top of electrodes during impedance measurements for fluid absorption (Fig. 1b). For each measurement, the filter paper was submerged into different NaCl solutions, and then placed onto the serpentine-shaped perspiration sensor to mimic sweat generation. This method

was selected because it was shown that the concentration of Na^+ and Cl^- ions in sweat rises with increasing sweat rate, which changes its conductivity⁸⁻¹¹.

The simulation of generation of sweat with various rates and volumes was performed with a syringe pump (Model 11 Plus, Harvard Apparatus, MA, USA) along with the perspiration sensor system. 55 mM NaCl solution was pumped to the center of the filter paper to test the effect of flow rate (i.e., simulating sweat rate) and volume on the measured impedance.

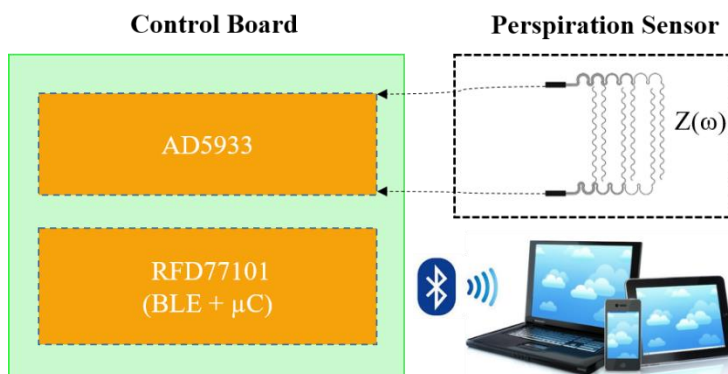


Fig. 2. Block diagram of the perspiration sensor system

C. Flexible Circuit System

We fabricated a custom-made impedance measurement circuit on a 75 μm thick Kapton[®] film with 18 μm laminated copper. The conductive traces were created by etching the unprotected copper in a mixture of hydrochloric acid and hydrogen peroxide solution. The flexible circuit system (Fig. 2) consists of an impedance converter (AD5933) and Simblee[™] RFD77101 system-on-chip, which includes a BLE transceiver and built-in ARM Cortex M0 microcontroller. The system operates with a 50 mAh, 3.7 V lithium-ion battery. We made the connection to the perspiration sensors on the glass wafer via flexible copper interconnects. The acquired data was transferred to a computer via USB cable.

Results and Discussions

The impedance of perspiration sensors was initially tested with a benchtop potentiostat by varying the NaCl concentrations (DI water, 10 mM, 100 mM and 1 M NaCl). The results are given in Fig. 3 for various sensor sizes and NaCl concentrations. The impedance decreased a function of frequency and flattened out at higher frequencies. The decreasing trend of the impedance curve is due to the capacitive effect of the total complex impedance. The flat region of each curve at high frequencies can be attributed to the solution resistance of the NaCl solutions. Increasing the NaCl concentration from 0 mM to 1 M decreases the total impedance due to increased ion concentrations. This flat region (> 10 kHz) later on was used to differentiate the variations of conductance of different NaCl solutions in our wearable perspiration sensing system.

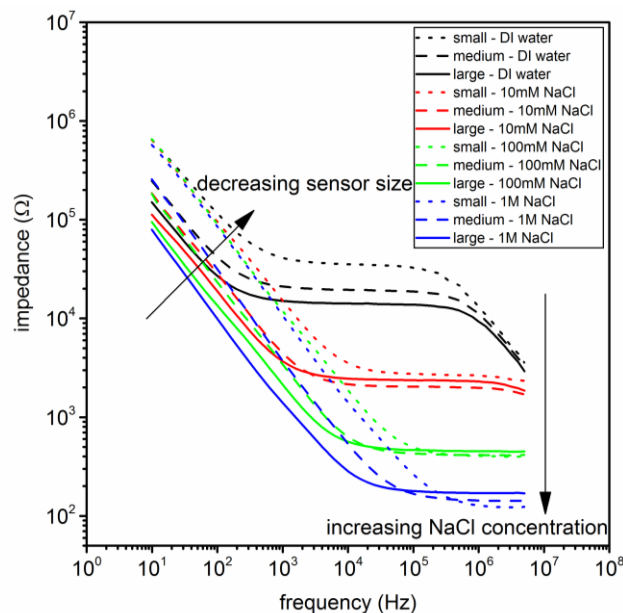


Fig. 3. Impedance vs. frequency graph of all sensor sizes with varying NaCl concentration. Dotted, dashed and straight line indicate small, medium and large sensor sizes, respectively. Each curve is average of three measurements on a given sample.

The sensor size and the total impedance had an inverse relation at low frequencies (Fig. 3). Larger sensor sizes yielded smaller impedance values due to increased capacitance of the electrodes because the capacitance of the electrodes is directly proportional to the surface area of

electrodes. The effect of electrode area on impedance diminishes at higher frequencies because of reduced capacitive effects. Therefore, the small sensor size was selected in the following measurements due to its form factor.

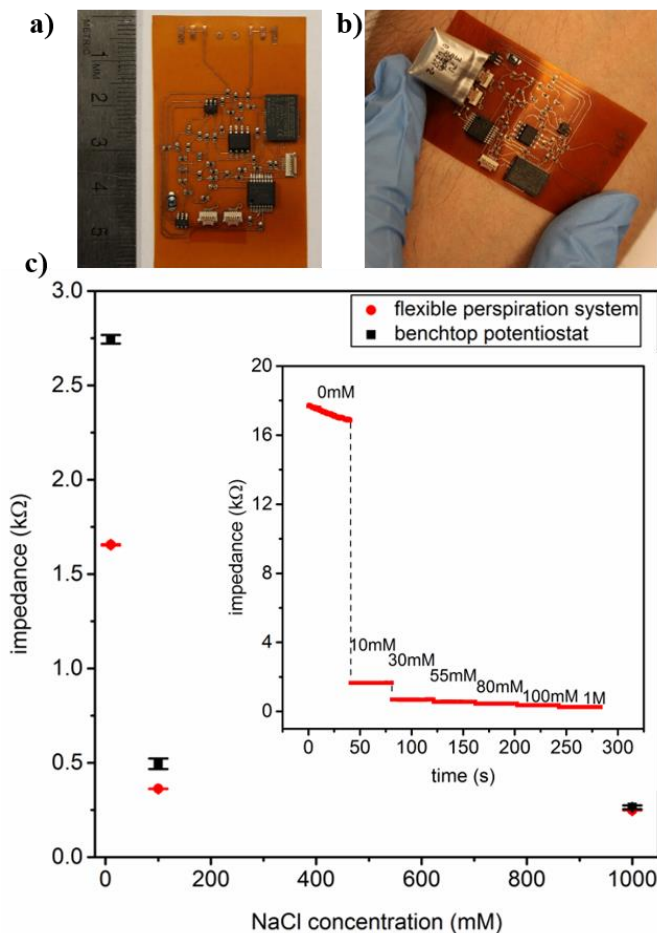


Fig. 4. a) Top view of flexible circuit system for perspiration monitoring. b) Perspiration sensor on forearm. c) Impedance vs. time graph of small sensor with varying NaCl concentration. Inset: Impedance vs. NaCl concentration graph of flexible perspiration system.

The fabricated perspiration system was shown in Fig. 4a and 4b. Single frequency (100 kHz) impedance measurements were carried out with this system by using a small size serpentine-shaped sensor. A comparison of the impedance measurements with the perspiration system and the benchtop potentiostat are shown in Fig. 4c. The miniaturized system was sensitive to variations in NaCl concentrations. At low NaCl concentrations (10 mM), the flexible system had smaller

impedance values compared to the benchtop system, which was due to the small calibration resistance ($R_{cal}=470 \Omega$) used in the AD5933 impedance converter. The difference in impedance values decreased as the impedance of NaCl solution approaches to the impedance of the calibration resistor. The inset figure in Fig. 4c shows the impedance measurements with the flexible perspiration system. The system was able to measure the differences in NaCl concentration in physiological Na^+ or Cl^- concentrations in sweat (10 mM to 100 mM).

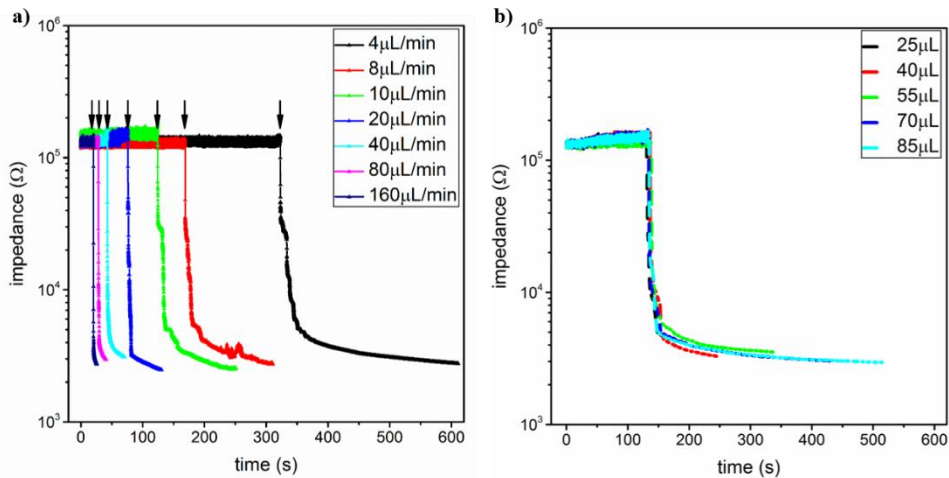


Fig. 5. a) Effect of flow rate on impedance. 40 μL of 55 mM NaCl was used for all flow rates. b) Effect of NaCl volume on impedance. 55 mM NaCl solution was used for all fluid volumes.

Fig. 5a and 5b show the impedance vs. time graphs for varying flow rate and volume of the NaCl solutions, respectively. A significant drop in the impedance values was observed upon the detection of the fluid (indicated with arrows in Fig. 5a). The time that this drastic impedance change occurred was different for each flow rate. Detection of the NaCl solution under low flow rate (4 $\mu\text{L}/\text{min}$; 342.5 ± 17 s) took much longer duration than the high flow rates (160 $\mu\text{L}/\text{min}$; 18.75 ± 1.69 s). This can be attributed to the slow diffusion and absorption of NaCl solution by the filter paper. High flow rate of NaCl solution resulted in a steep decrease of the impedance in a short time due to the fast wetting of the filter paper. The drop in the impedance levels occurred at $\sim 22 \mu\text{L}$ for all flow rates. Therefore, we tested NaCl solution volumes above this limit, see Fig.

5b. The NaCl solutions with various volumes followed a similar decreasing trend independent of the fluid volume. The deviation from the trend was due to the differences in the impedance drop times (134.75 ± 2.6 s) for varying fluid volumes.

Conclusion

In this study, we fabricated perspirations sensors with various form factors and performed *in vitro* characterizations in various NaCl solutions. Additionally, we coupled this with low-cost and miniaturized sensors with a flexible and wearable perspiration monitoring system. We have shown that the perspiration sensing system could detect variations in NaCl concentrations at physiological levels (10 mM-100 mM). This wearable perspiration system has an utmost importance in continuous sweat rate measurement. When combined with other electrochemical sensors, this sweat-based sensing system can provide a wealth of information about biochemical and physiological information of the human body. Future work will include human subject trials of wearable perspiration sensors.

References

1. Robinson, S.; Robinson, A. H., Chemical Composition of Sweat. *Physiol. Rev.* **1954**, *34* (2), 202-220.
2. Armstrong, L. E., Assessing hydration status: the elusive gold standard. *J. Am. Coll. Nutr.* **2007**, *26* (5), 575s-584s.
3. Toshio, O.; Masao, S.; Takao, T., Human perspiration measurement. *Physiol. Meas.* **1998**, *19* (4), 449.
4. Fouke, J. M.; Wolin, A. D.; Saunders, K. G.; Neuman, M. R.; Mcfadden, E. R., Sensor for Measuring Surface Fluid Conductivity In vivo. *IEEE Trans. Biomed. Eng.* **1988**, *35* (10), 877-881.
5. Mitsubayashi, K.; Yokoyama, K.; Takeuchi, T.; Tamiya, E.; Karube, I., Flexible Conductimetric Sensor. *Anal. Chem.* **1993**, *65* (24), 3586-3590.
6. Tronstad, C.; Gjein, G. E.; Grimnes, S.; Martinsen, O. G.; Krogstad, A. L.; Fosse, E., Electrical measurement of sweat activity. *Physiol. Meas.* **2008**, *29* (6), S407-S415.
7. Liu, G.; Hob, C.; Slaphey, N.; Zhou, Z.; Snelgrove, S. E.; Brown, M.; Grabinski, A.; Guo, X.; Chen, D. Y.; Miller, K.; Edwards, J.; Kaya, T., A wearable conductivity sensor for wireless real-time sweat monitoring. *Sensor Actuat B-Chem* **2016**, *227*, 35-42.
8. Dill, D. B.; Hall, F. G.; Van Beaumont, W., Sweat chloride concentration: sweat rate, metabolic rate, skin temperature, and age. *J. Appl. Physiol.* **1966**, *21*, 99-106.
9. Buono, M. J.; Ball, K. D.; Kolkhorst, F. W., Sodium ion concentration vs. sweat rate relationship in humans. *J. Appl. Physiol.* **2007**, *103* (3), 990-994.
10. Boisvert, P.; Candas, V., Validity of the Wescor's sweat conductivity analyzer for the assessment of sweat electrolyte concentrations. *Eur J Appl Physiol O* **1994**, *69* (2), 176-178.
11. Shamsuddin, A. K. M.; Tatsuo, T., Continuous monitoring of sweating by electrical conductivity measurement. *Physiol. Meas.* **1998**, *19* (3), 375.

Appendix E: Towards Wearable Electrochemical Lactate Sensing using Osmotic-Capillary

Microfluidic Pumping

Murat A. Yokus, Tamoghna Saha, Jennifer Fang, Michael D. Dickey, Orlin D. Velev and Michael A. Daniele

*As published in *IEEE Sensors Conference* (2019)

Abstract

Sweat analysis has received significant attention recently because the collection of sweat is minimally-invasive, and it contains a panel of physiologically relevant biomarkers. While there is significant progress in engineering sensor systems for sweat analysis, a few major challenges remain unaddressed, *e.g.* contamination due to the skin surface, old sweat mixing with new sweat, loss of sweat due to evaporation, and dilution of analytes on excessive sweating. To address some of these challenges, we present a wearable biosensor patch for biofluid extraction, sampling, and quantitative sensing. The wearable biosensor patch consists of (1) a hydrogel and paper-based microfluidic device for combined osmotic and capillary pumping of sweat coupled with (2) screen-printed electrodes for analysis of lactate concentration in sweat. In this report, we present our benchtop characterization of the proposed device towards the development of a continuous and wearable lactate monitoring system. This wearable biosensor patch advances the continuous, non-invasive monitoring of human biochemistry at low sweat rates.

Introduction

Wearable health monitoring devices have received significant attention recently as they have a great potential to diminish the perpetual challenges associated with the healthcare industry (*e.g.*, high healthcare expenditures and frequent hospital visits). These devices give users the opportunity to monitor their physical, emotional, and mental status (*e.g.*, calories burned, body temperature, skin conductance, ECG, EEG, blood pressure etc.) to make smart decisions towards

a healthy lifestyle. Such user-controlled devices lack monitoring biochemical markers. Biofluids, such as sweat, saliva, or urine, contain important biochemical information which can be collected noninvasively and analyzed for specific biomarkers of interest in contrast to invasive capillary or venous blood analyses. Sweat, more specifically, contains electrolytes (*e.g.*, Na⁺, Cl⁻, K⁺), metabolites (*e.g.*, glucose and lactate), and hormones (*e.g.*, cortisol) that can be used for continuous and pain-free monitoring of human health. Various research groups have reported skin-attachable and miniaturized sensors for the measurement of glucose, lactate, ethanol, and electrolytes in sweat¹⁻³. The challenges related to sweat-based sensing⁴, such as sweat contamination, mixing of perfused sweat with the old sweat on the skin surface, low sweat volumes due to evaporation and dilution of analytes with excessive sweating, have still not yet been adequately addressed. Therefore, an ideal wearable sweat-monitoring device must incorporate components for extracting information at low sweat rates, effective transport of small volume of sweat to sensing sites, and long-term continuous monitoring of analytes of interest.

Paper-based microfluidic devices are potential candidates for wearable sensing applications as they are inexpensive, scalable, easily disposable, provide capillary transport of small fluid volumes, and do not require complex fabrication steps. Many paper-based sensors have been designed for point-of-care, food, and environmental sensing applications⁵⁻⁶. Paper-based sweat sensors have also been reported for monitoring of lactate, Na⁺, pH, and temperature⁷. Yet, these devices require frequent replacement of the paper microfluidic channel, do not provide a long-term measurement of sweat biomarkers, and most importantly, they function under active sweat generation (*i.e.*, reverse iontophoresis or exercise). Improved sweat sensing devices are required with capabilities of extracting sweat at low sweat rates (*i.e.*, sedentary subjects and low

humid surroundings), efficient transport of sweat to the sensing sites without fluid loss, and long-term sensing with minimal contamination due to skin.

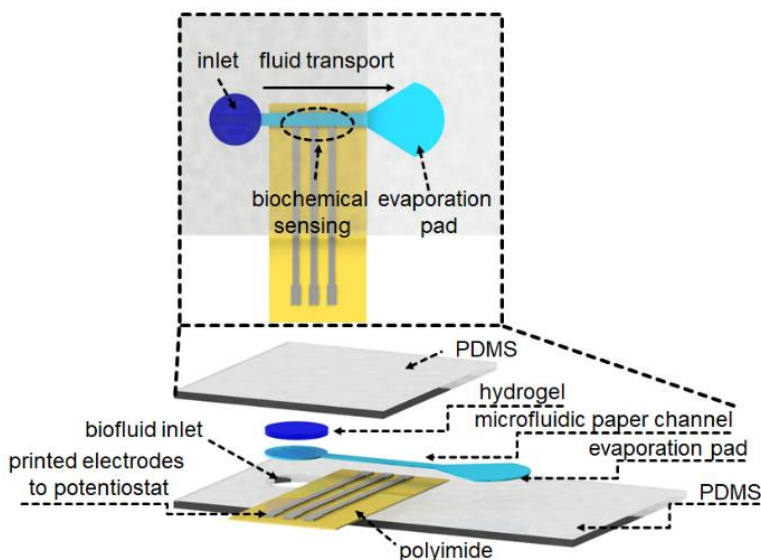


Fig. 1. Top and side exploded view of the microfluidic patch. The patch consists of a hydrogel, a paper-based channel with an evaporation pad, and a screen-printed sensor for lactate sensing.

Herein, we report an integrated patch for continuous lactate monitoring. Lactate is a byproduct of cellular anaerobic activity and an indicator for human muscle performance⁸⁻⁹. The microfluidic component (Fig. 1) consists of a hydrogel, a paper-based fluid wicking channel with an additional site for evaporation at the end (evaporation pad), and printed electrodes for electrochemical quantification of lactate. The hydrogel is engineered to have a higher chemical potential than sweat, which enables continuous extraction of fluid from the skin surface due to osmosis, once interfaced¹⁰. The paper-based channel transports the extracted fluid to the evaporation pad through capillary wicking. Continuous evaporation from the pad sustains the capillary pressure inside the channel, which facilitates more fluid and biomarker collection over time. The electrochemical sensor is then coupled to the paper-based channel for enzymatic detection of lactate on the working electrode. In this study, we initially illustrate the potential of hydrogel assisted paper-based microfluidics to sense lactate using commercial colorimetric assays,

followed by the benchtop electrochemical characterization of the printed lactate sensors. Finally, we demonstrate a fully-integrated patch for continuous monitoring of lactate from a model skin.

Materials and Methods

A. Materials

Whatman filter paper (Grade 542, GE Healthcare Life Sciences); Sylgard 184 elastomer (Dow Corning); phosphate buffer saline (PBS), lactic acid, Regenerated cellulose dialysis tubing (21-152-16) (Fisher Scientific); acrylamide, N-N' methylenebisacrylamide, 2-hydroxy-4'-(2-hydroxyethoxy)-2-methylpropiophenone, D-glucose, Nafion® (~5%), graphite (<20 μm), gelatin type A (~300 g Bloom) (Sigma-Aldrich); L-lactic acid test strips (QQLAC10, BioAssay Systems); stabilized lactate oxidase (10kU, E2030703P1, Sun Chemical, UK); Ag/AgCl ink (C2130809D5, Gwent) graphite paste (C2070424P2, Gwent), carbon paste (C2050106P7, Gwent).

B. Fabrication and Testing of Osmotic-Capillary Pump

1) *Hydrogel*: The hydrogels were fabricated with acrylamide as the monomer, N-N' methylenebisacrylamide as the crosslinker and 2-hydroxy-4'-(2-hydroxyethoxy)-2-methylpropiophenone as the photo-initiator. The monomer solution contained 22% (w/w) acrylamide, 0.48% (w/w) crosslinker and 0.15% (w/w) photo-initiator. The solution was cured inside a circular petri dish (47 mm diameter) under a $175 \text{ mW}\cdot\text{cm}^{-2}$ UV lamp (Sunray 400-SM) for 3 minutes. Disks of 8 mm diameter were punched out and equilibrated in 4M Glucose solution for 24 hours. After 24 hours, the disks were transferred and stored in a fresh glucose solution until further usage.

2) *Paper microfluidic patch fabrication*: Sylgard 184 silicone elastomer and its curing agent are mixed in 10:1 ratio and cured for 12 hours at 70°C for PDMS. The patch is prepared using two PDMS sheets – $38 \text{ mm} \times 15 \text{ mm} \times 2 \text{ mm}$ (bottom) and $30 \text{ mm} \times 15 \text{ mm} \times 1 \text{ mm}$ (top). A single

hole of 8 mm diameter was punched on the bottom sheet on one of its ends, which served the spot for embedding the hydrogel disk. A shape similar to Fig. 1 was cut out from Whatman filter paper using a laser cutter (Universal Laser Systems VLS 3.5) and was sandwiched between the top and bottom sheets. Both the sheets were glued using the PDMS precursor. The patch was then kept inside an oven at 40°C overnight to establish strong bonding between the sheets.

3) *Fabrication of model skin*: PBS was initially heated to ~80°C. 13% (w/w) gelatin type-A solution was prepared in 6 mL PBS solution and continuously stirred until it was fully dissolved. 5 mL of each 25, 50, 75, and 100 mM lactic acid in PBS were prepared and added to gelatin-PBS mixture and mixed well. This gelatin-lactic acid-PBS mixture was transferred to a mold and was refrigerated for 18 hours to obtain our model skin.

4) *Colorimetric quantification of lactate on the evaporation pad*: A 1.2 cm x 1.2 cm x 0.5 cm section was cut from the cured model skin and was placed inside a PDMS mold. A thin layer of cellulose dialysis membrane was placed on top of the model skin to act as the semi-permeable barrier of the stratum corneum interfacing the model skin on one side and the osmotic patch on the other. The osmotic-capillary pump was placed on the dialysis membrane for various times. After a set time, the evaporation pad on the paper microfluidic channel was separated, wet with 10 µL of DI water, and analyzed with the L-Lactic Acid Test Strips after 5 minutes. This waiting period was to ensure the collected lactate was dissolved completely into the added water. L-Lactic Acid Test Strips were rubbed on the wet evaporation pad and were run through the commercial lactic acid assay to obtain a color change. Images of these strips were taken using a camera (Canon EOS Mark5 DSLR), surrounded by a dark background. The images were processed in MATLAB (R2018b) to estimate the cumulative intensity of greyscale color change in the strips over time, which proportionally indicated the net lactic acid collection on the evaporation pad.

C. Lactate Sensing and Electrochemical Measurements

The lactate sensor was fabricated on a 50 μm thick polyimide film. Working electrode (WE, carbon ink with Prussian blue mediator), reference electrode (RE, Ag/AgCl), and counter electrode (CE, carbon ink) were screen-printed on the film with a 230 mesh size mask. The dimensions of the all electrodes were 1.5 mm x 2 mm. 15 $\text{mg}\cdot\text{mL}^{-1}$ graphene stock solution was prepared in 1xPBS and sonicated in the ultrasonic bath for 30min. 5 μL of a aqueous mixture (50 $\text{mg}\cdot\text{mL}^{-1}$ LO_x and 5 $\text{mg}\cdot\text{mL}^{-1}$ graphene in 1xPBS) was drop-casted on the WE and dried at room temperature for 1h. 0.5 wt% Nafion was drop-casted on the WE and dried at room temperature for 1h. Chronoamperometric tests were performed with a benchtop Gamry 600+ potentiostat at -0.2 V with respect to the RE.

Results and Discussion

A. Characterization of Paper-Based Microfluidic Patch

A calibration curve was prepared for the commercial L-lactic acid strips based on greyscale intensity for each concentration (Fig. 2a). A linear trend in the intensity was observed up to 6 mM lactic acid (Fig. 2b). This calibration curve was used to quantify lactate levels in the colorimetric tests in Fig. 2c and 2d.

Net lactate collection on the evaporation pad was quantified. A linear increase in net lactate was observed over 3 hours when the patch interfaced the model skin containing 39 mM lactic acid (Fig. 2c), demonstrating the potential of the osmotic-capillary pump to extract and transport lactate solutions. Chemical potential difference between the model skin and hydrogel in the patch produces extraction of fluid, which wicks through the paper and eventually reaches the evaporation pad. Continuous evaporation from the pad sustains the capillary pressure inside the paper channel which facilitates the accumulation of lactate over time.

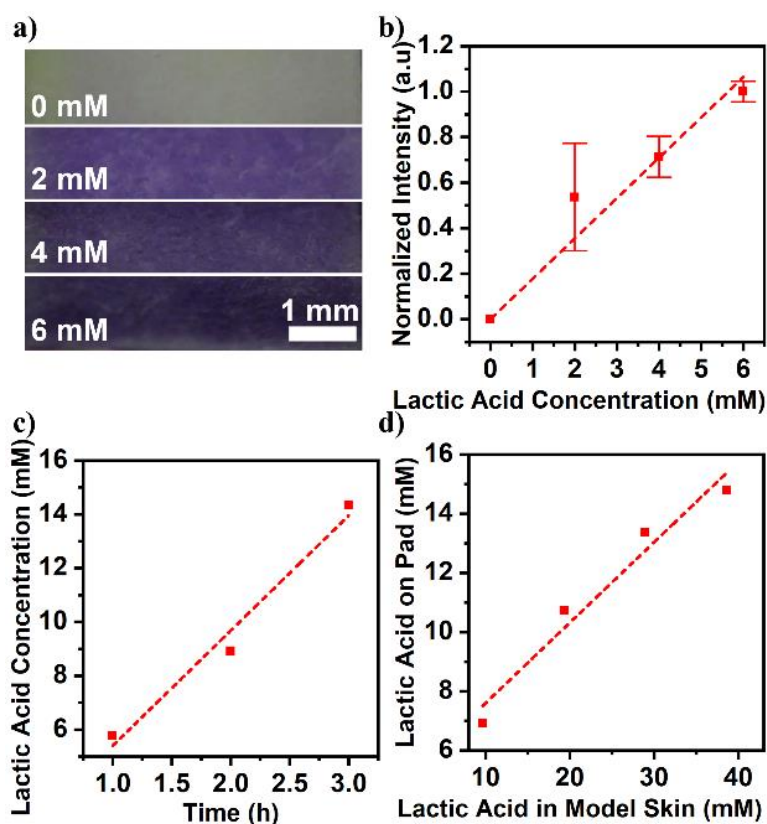


Fig. 2. (a) Color change of colorimetric lactate assay with 0, 2, 4, and 6 mM lactic acid concentrations in DI water. (b) Calibration curve of the colorimetric lactate assay. (c) Lactic acid concentration in the evaporation pad at discrete times (1h, 2 h, and 3 h) when the patch interfaced the model skin with 39 mM lactic acid. (d) Model skin lactic acid concentration vs. lactic acid concentration at the evaporation pad after 3 hours of collection.

The lactate content in the model skin itself was varied, and lactate collections on the evaporation pad were quantified after collecting for three hours. A linear increase was observed in the amount of collected lactate on the evaporation pad (Fig. 2d). The lactic acid concentration in the pad was found to be less than that in the model skin throughout the test. This difference may be due to the adsorption of lactate molecules inside the paper matrix during the continuous flow. It might also depend on the amount of lesser freely available lactate molecules for flow through the paper channel due to binding with gelatin in the model skin. Overall, the relative amount of lactate collected correlates well with the concentration of lactate in the model skin (Fig. 2d). The correlation between starting lactate concentration and accumulated concentration will be evaluated in future efforts.

B. Chronoamperometric Measurement of Lactate

Chronoamperometry was performed to characterize the printed lactate sensors (Fig. 3a inset) in 1X PBS (0.1 M, pH = 7.4). The current response of the lactate sensors was assessed over a lactate concentration range of 0-40 mM (Fig. 3a). An increase in the cathodic current with respect to an increase of lactic acid concentration was observed (Fig. 3a and 3b). The sensitivity of the sensor was measured using a linear fitting method in the range of 5 mM to 20 mM. The sensitivity of the sensor was $0.03 \mu\text{A}\cdot\text{mM}^{-1}\cdot\text{mm}^{-2}$.

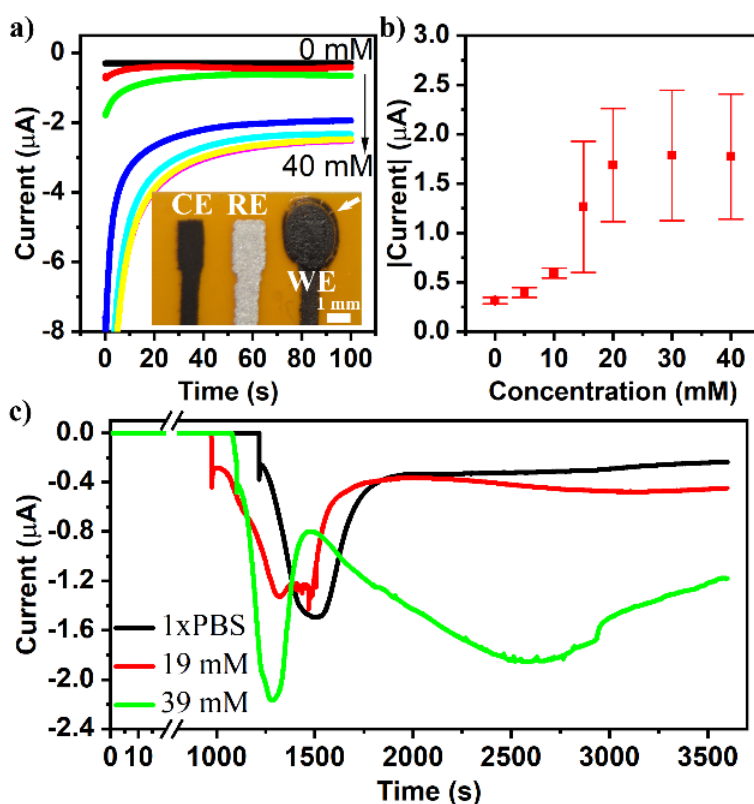


Fig. 3. (a) Chronoamperometry in 1X PBS solution for varying lactic acid concentrations (0, 5, 10, 15, 20, 30, 40 mM). Inset: Screen-printed electrochemical sensors on the polyimide film. The arrow in the inset shows the functionalization of the WE. (b) Calibration curve of the lactate sensor ($N=3$, $R^2=0.96$). (c) Continuous measurement of lactate from the model skin with the fully integrated microfluidic device for 1 h.

We tested the functionality of the fully-integrated patch (*i.e.*, hydrogel, paper microfluidic, and lactate sensor) as illustrated in Fig. 1. The amperometric response of the system was tested at -0.2 V for various lactic acid concentrations (0, 19, and 39 mM in the model skin) for an hour.

Model skin with 1X PBS was used for the 0 mM lactic acid measurement. For all tests, a complete wetting of the printed electrodes and closed cell—observed as a sharp drop in the cathodic current—occurred between 16 and 20 min (Fig. 3c). This current drop peaked and then returned to a steady current. The response of the lactate sensor to 1X PBS solution leveled out over time (black line). The current increased over time (red and green lines) with increasing lactic acid in the model skin (19 mM and 39 mM), indicating successful wicking, transport, and sensing of the lactic acid over a 1 hour period. The current vs. concentration response of the patch (Fig. 3b) correlated well with the electrochemical lactate sensing from the model skin (Fig. 3c).

Conclusion

In this report, we demonstrate the *in vitro* operation of an integrated patch for the pumping and analyses of lactate in sweat. The combination of the osmotic pump and paper microfluidics extracts and delivers model sweat samples to a screen-printed electrochemical cell for lactate measurement. This microfluidic device with unique extraction and sensing platform can have a significant impact on non-invasive, continuous and long-term wearable biochemical sensing which can also be applicable for sensing other biomarkers of interest in sweat and other biofluids.

References

1. Rose, D. P.; Ratterman, M. E.; Griffin, D. K.; Hou, L.; Kelley-Loughnane, N.; Naik, R. R.; Hagen, J. A.; Papautsky, I.; Heikenfeld, J. C., Adhesive RFID Sensor Patch for Monitoring of Sweat Electrolytes. *IEEE Trans. Biomed. Eng.* **2015**, *62* (6), 1457-1465.
2. Kim, J.; Jeerapan, I.; Imani, S.; Cho, T. N.; Bandodkar, A.; Cinti, S.; Mercier, P. P.; Wang, J., Noninvasive Alcohol Monitoring Using a Wearable Tattoo-Based Iontophoretic-Biosensing System. *ACS Sensors* **2016**, *1* (8), 1011-1019.
3. Gao, W.; Emaminejad, S.; Nyein, H. Y. Y.; Challa, S.; Chen, K.; Peck, A.; Fahad, H. M.; Ota, H.; Shiraki, H.; Kiriya, D.; Lien, D.-H.; Brooks, G. A.; Davis, R. W.; Javey, A., Fully integrated wearable sensor arrays for multiplexed in situ perspiration analysis. *Nature* **2016**, *529* (7587), 509-514.
4. Heikenfeld, J., Non-invasive Analyte Access and Sensing through Eccrine Sweat: Challenges and Outlook circa 2016. *Electroanal* **2016**, *28* (6), 1242-1249.
5. Dungchai, W.; Chailapakul, O.; Henry, C. S., Electrochemical Detection for Paper-Based Microfluidics. *Anal. Chem.* **2009**, *81* (14), 5821-5826.
6. Nie, Z.; Nijhuis, C. A.; Gong, J.; Chen, X.; Kumachev, A.; Martinez, A. W.; Narovlyansky, M.; Whitesides, G. M., Electrochemical sensing in paper-based microfluidic devices. *Lab Chip* **2010**, *10* (4), 477-483.
7. Anastasova, S.; Crewther, B.; Bemnowicz, P.; Curto, V.; Ip, H. M. D.; Rosa, B.; Yang, G.-Z., A wearable multisensing patch for continuous sweat monitoring. *Biosens. Bioelectron.* **2017**, *93*, 139-145.
8. Billat, L. V., Use of Blood Lactate Measurements for Prediction of Exercise Performance and for Control of Training. *Sports Med* **1996**, *22* (3), 157-175.
9. Rassaei, L.; Olthuis, W.; Tsujimura, S.; Sudhölter, E. J. R.; van den Berg, A., Lactate biosensors: current status and outlook. *Anal. Bioanal. Chem.* **2014**, *406* (1), 123-137.
10. Shay, T.; Dickey, M. D.; Velev, O. D., Hydrogel-enabled osmotic pumping for microfluidics: towards wearable human-device interfaces. *Lab Chip* **2017**, *17* (4), 710-716.

Appendix F: Wearable Sweat Rate Sensors

Murat A. Yokus, Talha Agcayazi, Matt Traenkle, Alper Bozkurt and Michael A. Daniele

*Submitted to *IEEE Sensors Conference* (under review)

Abstract

Sweat plays a significant role in human homeostasis by regulating the body temperature via evaporative cooling under heat or work stress. Water and electrolytes (mainly sodium and chloride) constitute almost 99% of the sweat composition. Excessive sweat loss disturbs the human homeostasis, impairs circulation, and impedes heat dissipation. Some of the limitations of the conventional sweat loss measurement techniques lie in their wearability, sweat sampling, analyte contamination from skin, and evaporation. To overcome these limitations, we have developed a wearable sensor for continuous sweat rate measurement in wearable form factors. The wearable sensor consists of low-cost printed interdigitated electrodes for impedance sensing, a serpentine shaped paper-based microfluidic channel, and a polyurethane encapsulation layer. In this report, we present the benchtop characterization of the proposed sensor's capability to track sweat rate. The microfluidics can hold sweat volumes up to 82 μL and enables the detection of sweat rates on various locations of the body for extended periods.

Introduction

Sweating occurs due to the activation of eccrine glands by temperature, emotion, stress, gustation, or medical illnesses ¹. Elevated body temperature is the primary cause of sweat generation, which holds a vital role in thermoregulation of the body ². The eccrine glands are widely distributed across the body (1.6 to 4 million) and show a regional density variation, with the highest gland density on volar surfaces of fingers (530 glands cm^{-2}) ³⁻⁴. Taking into account the spreading and density of the sweat glands, a prolonged workout in extreme climatic conditions

may cause whole-body sweat loss as much as 16 L or 20 nL min⁻¹ gland⁻¹ ^{3,5}. The body cannot sustain the high sweating rates for extended periods as it may cause loss of essential electrolytes (e.g., sodium and chloride), which are necessary for maintaining homeostasis within the body. For instance, during an exercise, failing to restore the fluid-need will increase the chances of dehydration which may lead to elevation of core body temperature and heart rate, hypertonicity of body fluids as well as impairment of blood flow ⁶. Exercise-induced dehydration may lead to life-threatening conditions such as heat stroke, rhabdomyolysis, muscle cramps, hypernatremia, as well as a decrease in mental and cognitive performance ⁷. Thus, tracking real-time sweat rate values would enable users or athletes to achieve their optimum performance and obviate the potential health complications.

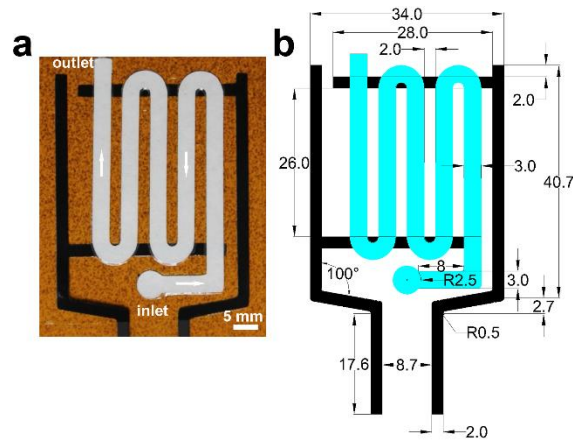


Fig. 1. a) A picture of the fabricated sweat rate sensor, consisting of printed carbon interdigitated electrodes, a paper-based microfluidic layer, and a transparent and waterproof polyurethane encapsulation layer. b) Schematic of the fabricated sensors. Unit: mm.

Conventional measurements of sweat rate or total sweat loss include whole-body wash-down technique and sweat collection with plastic bags, absorbent patches, and Macroduct ⁸. These methods are carried out in controlled lab settings, require complicated steps and trainers, and are sensitive to analyte degradation and skin contamination. Untraditional sweat rate monitoring methods have also been developed, measuring impedance, optical reflectance, or water vapor in a

microfluidic channel, swellable hydrogel, or in a sealed chamber, respectively⁹⁻¹¹. These methods enable continuous sampling and real-time analysis of sweat loss with minimal sweat evaporation.

Herein, we demonstrate a printed impedance sensor with integrated paper-based microfluidics for sweat rate monitoring (Fig. 1). This study is an improved and low-cost version of our previous work on interdigitated impedance-based sweat rate sensing¹². The proposed work incorporates paper-based microfluidics because of their low-cost, ease of fabrication, and continuous fluid wicking properties¹³. Their PDMS counterparts require sophisticated microfabrication techniques, hydrophilic microchannels, as well as optimization of channel dimensions for attaining optimum bursting pressures¹⁴. The sensor utilizes a similar impedance sensing approach that was presented in^{10,15}.

Materials and Methods

A. Materials

The used materials include Whatman filter paper (Grade 541, thickness: 155 μm , VWR LLC, USA); phosphate buffer saline (1X PBS); carbon paste (C2050106P7, Gwent Ltd, UK); TegadermTM (3M Co., USA).

B. Fabrication of Sweat Rate Sensors

We designed the sweat rate sensor with interdigitated electrodes in AutoCAD and fabricated by screen printing carbon ink on a 50 μm thick polyimide film using a 230 mesh size frame (Fig. 1b). We cured the printed sensor at 80°C for 15 min. A serpentine-shaped paper channel with a 3 mm channel width was cut from a 155 μm thick filter paper using Silhouette Cutter. The microfluidic paper channel was placed onto the printed electrodes and encapsulated with a polyurethane Tegaderm layer. We created an inlet opening with $\sim 20 \text{ mm}^2$ on the

encapsulation layer. We, then, made an outlet opening with 14 mm^2 on the polyimide layer facing the backside of the sensor to ensure continuous fluid flow.

C. Microfluidic and Electrical Characterization

We used $200 \text{ }\mu\text{L}$ of 1X PBS solution as an artificial sweat solution and drop-cased to the inlet of the microfluidic channel for microfluidic characterization of the paper-based channel. The fluid flow was recorded continuously using a digital camera. We measured the electrical impedance between the interdigitated electrodes simultaneously using a Gamry reference 600+ potentiostat. The recorded video was used for calculation of the fluid velocity and time-dependent filling of the paper-based channel. We used Electrochemical Impedance Spectroscopy (EIS) (100 kHz , $V_{AC} = 10 \text{ mV}$, and $V_{dc} = 0 \text{ V}$) for measuring the impedance between the electrodes as the fluid slowly filled the microfluidic channel.

Results and Discussions

The fabricated sweat rate sensor was shown in Fig. 1a. It is a printed and flexible sensor offering a low-cost approach for continuous quantification of the sweat rate or sweat loss. The sensor consists of three layers: a flexible polyimide film with printed interdigitated electrodes, a paper-based microfluidic channel for collection and continuous transport of the fluid, and a polyurethane cover layer for encapsulation of the microfluidic channel to prevent fluid evaporation.

The capillary pressure-driven transport of 1X PBS solution across the paper microfluidic channel is shown in Fig. 2a. The distance traveled by the fluid in a porous media slowed down over time because of a decrease in fluid velocity. As the fluid is transported throughout the paper microfluidic channel, the capillary pressure decreases, leading to a decrease in the fluid velocity, according to Darcy's law¹⁶. Because of the square root dependence of the distance (*i.e.*, visible

wetted front of the paper) to time (t) (Lucas-Washburn equation), the distance taken by the fluid slows down over time¹⁷. Overall, the paper-based microfluidic channel can hold 82 μL of fluid in approx. 30 min fill time, corresponding to approx. 15 μL of fluid collection per the microfluidic channel length between each electrode fingers (Fig. 2b).

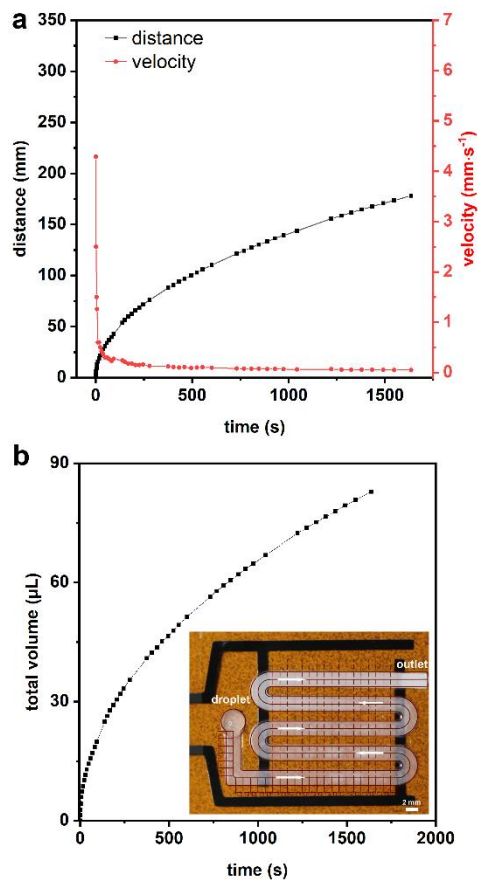


Fig. 2. **a)** Fluid velocity and distance traveled by the fluid over the course of testing. **b)** Filling of the microfluidic channel as a function of time. Inset: Sweat rate sensor with 1X PBS filled microfluidic channel.

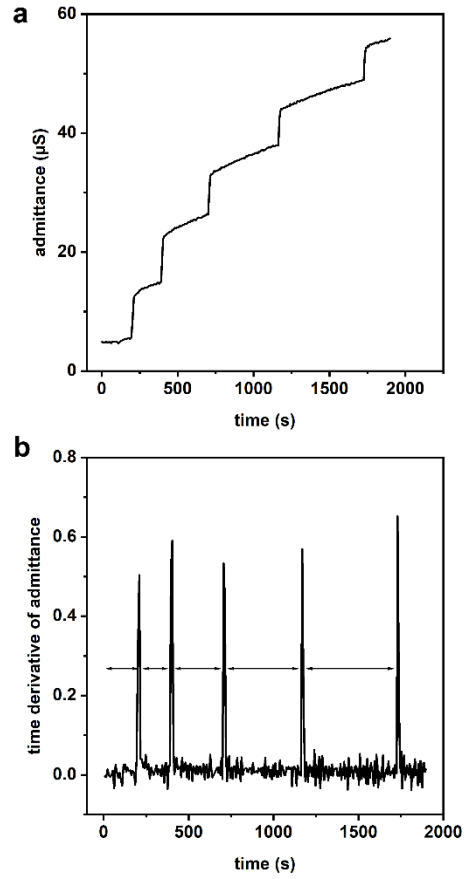


Fig. 3. **a)** Admittance change of the sweat rate sensor as 1X PBS solution travels throughout the paper microfluidic channel and crosses subsequent electrode fingers. Crossing a new electrode results in a jump in admittance. **b)** Time derivation of the admittance data in (a). The distinct peaks correspond to the admittance steps in (a).

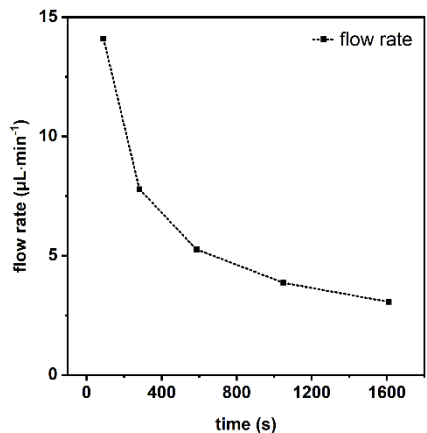


Fig. 4. Demonstration of a continuous flow rate measurement. The flow rate will be altered based on the perspiration rate on the skin surface.

In addition to the fluid volume per serpentine line, real-time monitoring of sweat rate also requires the assessment of the time points at which the fluid crosses the fingers of the interdigitated electrodes. This was achieved by monitoring the admittance between the electrode fingers as the fluid traveled on the serpentine-shaped microfluidic channel. When the fluid crossed a new electrode pair, a sharp increase in the admittance plot was observed (Fig. 3a). The step size in the admittance curve is determined by the conductivity of the solution and the contact area between the paper microfluidic channel and the printed electrodes. Fig. 3b shows the time derivation of the admittance plot in Fig. 3a. The location of the distinct peaks corresponds to the increase in admittance every time when the fluid passes an electrode pair. The time interval between each peak extended over time, which was attributed to the decrease in fluid velocity as the fluid got closer to the outlet of the microfluidic channel. The flow rate was calculated using the volume of fluid collection per serpentine line and the locations (time points) of the admittance peaks (Fig. 4). When the sweat rate sensor is worn on the skin surface, the flow rate graph would be modified in line with the rate of perspiration on the skin surface. Considering the maximum sweat rate as $20 \text{ nL}\cdot\text{min}^{-1}\cdot\text{gland}^{-1}$, average sweat gland density as $150 \text{ glands}\cdot\text{cm}^{-2}$, and $\sim 0.2 \text{ cm}^2$ inlet area, the sweat generation per this area would be $0.6 \text{ }\mu\text{L}\cdot\text{min}^{-1}$. This number indicates that the starting flow

rate of the fabricated sensor will not be a limiting factor for continuous wicking of the perspired sweat on the skin surface for real-time sweat rate assessment. At this flow rate, the total time required to fill out the microfluidic paper channel (82 μL) would be over 2 hours. Further modifications to the inlet area and the width of the microfluidic channel can be made for the collection of increased sweat volumes.

Conclusion and Future Work

In this study, we demonstrate the *in vitro* operation of an inexpensive and flexible patch for continuous sweat rate monitoring. Facile integration of a paper-based microfluidic channel with printed interdigitated electrodes provides a passive sweat transport platform for prolonged sweat rate monitoring. The integration of this sensor with other biochemical sensors will enable real-time sweat analysis and the correlation of sweat-rate dependent biomarkers. Future work will involve *in situ* testing of the proposed sensor when the human subjects undergo active exercise conditions.

References

1. Schlereth, T.; Dieterich; Birklein, Hyperhidrosis-Causes and Treatment of Enhanced Sweating. *Dtsch Arztebl Int* **2009**, *106* (3), 32-Ii.
2. Nadel, E. R.; Bullard, R. W.; Stolwijk, J. A., Importance of skin temperature in the regulation of sweating. *J. Appl. Physiol.* **1971**, *31* (1), 80-7.
3. Taylor, N. A. S.; Machado-Moreira, C. A., Regional variations in transepidermal water loss, eccrine sweat gland density, sweat secretion rates and electrolyte composition in resting and exercising humans. *Extreme Physiol. Med.* **2013**, *2*, 4-4.
4. Sato, K.; Kang, W. H.; Saga, K.; Sato, K. T., Biology of Sweat Glands and Their Disorders .1. Normal Sweat Gland-Function. *J Am Acad Dermatol* **1989**, *20* (4), 537-563.
5. Sato, K.; Sato, F., Individual Variations in Structure and Function of Human Eccrine Sweat Gland. *Am. J. Physiol.* **1983**, *245* (2), R203-R208.
6. Convertino, V. A.; Armstrong, L. E.; Coyle, E. F.; Mack, G. W.; Sawka, M. N.; Senay, L. C.; Sherman, W. M., American College of Sports Medicine position stand - Exercise and fluid replacement. *Med. Sci. Sports Exercise* **1996**, *28* (1), R1-R7.
7. Sawka, M. N.; Burke, L. M.; Eichner, E. R.; Maughan, R. J.; Montain, S. J.; Stachenfeld, N. S., Exercise and fluid replacement. *Med. Sci. Sports Exercise* **2007**, *39* (2), 377-390.
8. Liu, C. H.; Xu, T. L.; Wang, D. D.; Zhang, X. J., The role of sampling in wearable sweat sensors. *Talanta* **2020**, *212*.
9. Zhao, F. J.; Bonmarin, M.; Chen, Z. C.; Larson, M.; Fay, D.; Runnoe, D.; Heikenfeld, J., Ultra-simple wearable local sweat volume monitoring patch based on swellable hydrogels. *Lab Chip* **2020**, *20* (1), 168-174.
10. Kim, S. B.; Lee, K.; Raj, M. S.; Lee, B.; Reeder, J. T.; Koo, J.; Hourlier-Fargette, A.; Bandodkar, A. J.; Won, S. M.; Sekine, Y.; Choi, J.; Zhang, Y.; Yoon, J.; Kim, B. H.; Yun, Y.; Lee, S.; Shin, J.; Kim, J.; Ghaffari, R.; Rogers, J. A., Soft, Skin-Interfaced Microfluidic Systems with Wireless, Battery-Free Electronics for Digital, Real-Time Tracking of Sweat Loss and Electrolyte Composition. *Small* **2018**, *14* (45).
11. Salvo, P.; Pingitore, A.; Barbini, A.; Di Francesco, F., A wearable sweat rate sensor to monitor the athletes' performance during training. *Sci. Sports* **2018**, *33* (2), e51-e58.
12. Yokus, M. A.; Hass, C.; Agcayazi, T.; Bozkurt, A.; Daniele, M. A., Towards a Wearable Perspiration Sensor. *2017 Ieee Sensors* **2017**, 1260-1262.
13. Yokus, M. A.; Saha, T.; Fang, J.; Dickey, M. D.; Velez, O. D.; Daniele, M. A. In *Towards Wearable Electrochemical Lactate Sensing using Osmotic-Capillary Microfluidic Pumping*, 2019 IEEE SENSORS, 27-30 Oct. 2019; 2019; pp 1-4.
14. Choi, J.; Xue, Y. G.; Xia, W.; Ray, T. R.; Reeder, J. T.; Bandodkar, A. J.; Kang, D.; Xu, S.; Huang, Y. G.; Rogers, J. A., Soft, skin-mounted microfluidic systems for measuring secretory fluidic pressures generated at the surface of the skin by eccrine sweat glands. *Lab Chip* **2017**, *17* (15), 2572-2580.
15. Yuan, Z.; Hou, L.; Bariya, M.; Nyein, H. Y. Y.; Tai, L. C.; Ji, W. B.; Liabc, L.; Javey, A., A multi-modal sweat sensing patch for cross-verification of sweat rate, total ionic charge, and Na⁺ concentration. *Lab Chip* **2019**, *19* (19), 3179-3189.
16. Masoodi, R.; Pillai, K. M., Darcy's Law-Based Model for Wicking in Paper-Like Swelling Porous Media. *AlChE J.* **2010**, *56* (9), 2257-2267.

17. Cummins, B. M.; Chinthapatla, R.; Ligler, F. S.; Walker, G. M., Time-Dependent Model for Fluid Flow in Porous Materials with Multiple Pore Sizes. *Anal. Chem.* **2017**, *89* (8), 4377-4381.

Appendix G: IRB Human Trials Document: Analysis of Sweat and Measurement of Local Tissue Oxygenation with a Wearable Device

i. Foreword

This study has not undergone a scientific review elsewhere (e.g., at NSF or NC State) before submitting for review at UNC.

Principle investigator (Dr. Michael Daniele) has a joint appointment in the Joint Department of Biomedical Engineering between UNC-Chapel Hill and NC State. This study is being submitted for IRB review at UNC-Chapel Hill per the agreement of the Joint Biomedical Engineering program. Research team includes graduate students from Electrical Engineering and Chemical Engineering at NC State. The work for this study will be conducted on NC State campus.

ii. Objective

Purpose: To measure lactate in sweat and local tissue oxygenation using a conformable wearable device.

The aim of this study is to **(1)** measure the concentration of lactate in sweat under resting and exercising conditions. The lactate sensors with or without a sweat collection patch will be interfaced with the skin. The lactate sensors with the sweat collection patch will enable sweat extraction and transportation under low sweat rate conditions due to its engineered interface. Our goal is to explore the lactate levels in sweat with a custom designed wearable device. We will compare the concentration of lactate in sweat to the concentration of lactate in capillary blood.

Additional exploratory aim is to **(2)** measure tissue oxygenation levels of the skin where the perspiration occurs. This will be achieved by interfacing noninvasive optical sensors to the skin for continuous measurement of the local tissue oxygenation.

(3) We plan to evaluate the placement of devices on the forearm, forehead, and calf. Based on aim 1 and 2, we will be able to choose the best locations (maximum amount of sweat generation and quality of optical signal) for the future studies.

No medical diagnostic data will be evaluated using this device. This study will not be used to evaluate efficacy or safety of the device for commercial distribution.

Participants: 75 participants from 18 to 35 years old.

Procedures: Subjects will arrive to NC State's Centennial Campus and provide informed consent before beginning the study. Participants will be seated for the testing. Staff will attach the wearable device to various locations on the participants' body to record sweat lactate and tissue oxygenation levels under resting and exercise conditions. Capillary blood lactate measurements will be recorded throughout the protocol via finger pricking. In addition, a commercial finger pulse oximeter will be used on the participants for heart rate calculation. Before completing the study, the participants will fill out an exit survey (sample survey attached).

iii. Background rationale

Prevalent use of wearable devices has recently increased significantly as they decrease the patient dependence on bulky medical equipment. These devices can be used in various areas such as remote health monitoring, early detection of diseases, post-surgery health monitoring, and physical performance monitoring. To meet this need, wearable electronics market has been dominated by various body-worn physiological sensors such as electrocardiography (ECG), electroencephalography (EEG), plethysmography (PPG), electromyography (EMG), pulse oximetry, skin temperature, and respiration. However, the current wearables market is still in shortage of health monitoring devices for detection of other physiologically relevant biomarkers.

The lack of such health monitoring devices limits the type and number of health conditions that can be monitored with the wearable devices we have access today.

Development of wearables for detection of analytes from noninvasive biofluids such as sweat enables monitoring of biomarkers of human biochemistry. Sweat, when extracted iontophoretically or via active sweating, can provide an overall picture of human physiology as it contains electrolytes (Na^+ , Cl^- , K^+ , and NH_4^+), small molecules (e.g., ethanol, glucose, lactate, and urea), and small proteins. For example, the concentration of chloride in sweat is used for diagnosis of cystic fibrosis in newborns. The concentration of ammonium and urea in sweat can provide information about metabolic disorders related to liver and kidney.

Continuous monitoring of lactate in sweat and local tissue oxygenation is the prime focus of this study. Lactate is the biomarker of human exertion and related to oxygen through metabolic pathways in the cells. Under physical exercise, the cells surrounding the eccrine sweat glands generate sweat, which is then transferred to the skin surface via dermal ducts. When the sweat is collected from the skin and further analyzed with sensors, the concentration of lactate can be quantified. Similarly, utilization of oxygen is a part of the energy metabolism and required for survival of the cells. The energy production mechanism is altered from aerobic to anaerobic respiration in absence of oxygen, resulting in generation of lactate in cells, which constitutes the fundamental rationale behind this study. The relationship between venous lactate concentration and blood oxygenation levels was well studied in the past. Yet, there is not an exploratory study for understanding the dependency of sweat lactate levels to oxygen levels in arteries and its surrounding tissue. If such a correlation is established, it would eliminate the need for a blood lactate analysis for human performance monitoring in sports medicine.

The goal of our research is to monitor lactate in sweat along with local tissue oxygenation levels. Electrochemical lactate sensing and continuous wave near infrared spectroscopy (cw-NIRS) techniques will be used for noninvasive monitoring of both the biomarkers. NIRS is a commonly used optical sensing method for measurement of relative changes of oxygenated hemoglobin (ΔHbO_2), deoxygenated hemoglobin (ΔHb) in arteries, and local tissue oxygenation. Electrochemical sensing along with biorecognition elements is also a commonly used technique for quantification of electro-active biomarkers in biofluids, such as sweat or blood. Utilization of both the techniques in wearables will help us to understand the correlation between the lactate levels in sweat and tissue oxygenation levels. Additional information collected during this study regarding the wearability and user comfort will be used to guide the development of such related future devices for long-term health monitoring.

iv. Design

Investigator experience

Michael Daniele (PI) currently works at the Department of Biomedical Engineering as an Assistant Professor. Dr. Daniele has been involved with human studies and projects working towards development of wearable biosensors. Alper Bozkurt is an associate professor in the Department of Electrical and Computer Engineering at NC State University. He has been involved in human and animal studies and projects evaluating a variety of wearable health monitoring devices. Murat Yokus and Tanner Songkakul are graduate students in Department of Electrical and Computer Engineering at NC State. Tamoghna Saha is also a graduate student in Department of Chemical and Biomolecular Engineering.

IRB Approval

This study (#19-3065), *Analysis of Sweat and Measurement of Local Tissue Oxygenation with a Wearable Device*, will be reviewed by the Institutional Review Board, University of North Carolina at Chapel Hill.

Ethics training

The University of North Carolina requires all persons engaged in research involving human subjects to complete training in the ethical conduct of research and protection of human subjects. Data collectors will be required to have completed the Collaborative IRB training initiative (CITI) web-based training course before data collection. North Carolina State University requires all persons engaged in research involving human subjects to complete training in the ethical conduct of research and protection of human subjects. Data collectors will be required to have completed the Collaborative IRB training initiative (CITI) web-based training course before data collection. All members of the research team carrying out the protocol have completed the CITI Training for Human Subjects Research requirements for UNC-CH and NC State.

Confidentiality Assurance.

We are committed to protecting the rights and privacy of study participants. As a data collector, you must maintain confidentiality regarding any information pertaining to this study. This confidentiality assurance includes all information provided about participants that would allow her or him to be personally identified. Verbal and written communication provided by or about a subject, as well as any information that would lead to identification of names, telephone number, or address must remain confidential. As part of our commitment to upholding confidentiality, all data collectors will be required to sign a confidentiality agreement.

Consent.

The research assistant will go over **Consent** with the participant. Although it is not necessary to read every line, you should cover these main points:

1. Purpose of study
2. What the participant will be asked to do
3. How long participation will last
4. Bad and good things that might happen
5. Incentives
6. Participants don't have to do anything they don't want to!
7. If you have questions, you can always call the project contact person [show Michael Daniele's name and number (919.513.2654)]

Ask:

Do you want me to read through the whole paper with you? Do you have any questions? Are you willing to participate?

- What if the participant is not sure if she or he wants to participate?

If a participant is not sure that she/he wants to participate, you can say:

- All information collected as part of the study will be kept in a secure location.
- Is there something that you are concerned about?
- [If they really seem hesitant or want to talk about it with family members] Would you like to think about it for a few days and have someone give you a call to see if you are interested?

IF A PARTICIPANT REFUSES: It is considered a refusal. Thank the participant for their time and try to elicit reason for refusal from those who are unwilling to participate. Research assistant should record refusal and notify the PI, Michael Daniele.

IF THE PARTICIPANT AGREES TO PARTICIPATE: After answering all questions, the research assistant will say the following to the participant:

If you don't have any more questions, please print and sign your first and last name on the last page and write in today's date [SAY DATE]. This duplicate copy is for you to keep.

- The research staff member should sign the duplicate copies of the informed consent and provide it to the participant.

Device

Our custom wearable device consists of four main components, as demonstrated in Fig. 1: a 3.7V lithium-polymer battery, a FR-4 main board, an optical, and an electrochemical sensing platform. The battery is commercially available and presents minimal risk in this experiment; also, it will be on top of the main board and not in contact with the skin. The main board is fabricated on a green-colored FR-4. It contains nearly all electronic components for NIRS and electrochemical sensing, including the microcontroller with Bluetooth antenna and analog-to-digital converter. The dimensions of the main board is 38 mm × 24 mm. The main board will be placed on top of a fabric during the exercise and not in contact with the skin. The flexible optical platform (~ 41 mm × 15 mm) is made of a polyimide film, light emitting diodes (LEDs) and a photodetector. The wavelengths of the LEDs will be in range of 630 nm to 940 nm. The electrochemical platform (~38 mm × 8 mm) has electrodes for both lactate and pH sensing. This platform can function with and without the presence of a sweat collection patch. The details of the sweat collection patch are provided below.

The main board will be wrapped with 3M Tegaderm bandage to secure the FR-4 board to the underlying fabric. Two slits will be created on the fabric to connect the optical and electrochemical platforms to the main board. Only the optical and the electrochemical platforms will be facing the skin directly. The platforms will be connected to the main board through the slits created on the fabric.

Device will be controlled from a laptop via Bluetooth and data will be recorded on the laptop. Data recording and collection will be performed with a custom Python software.

A commercially available optical heart rate measuring device will be used to monitor the heart rate of the subjects during the test.

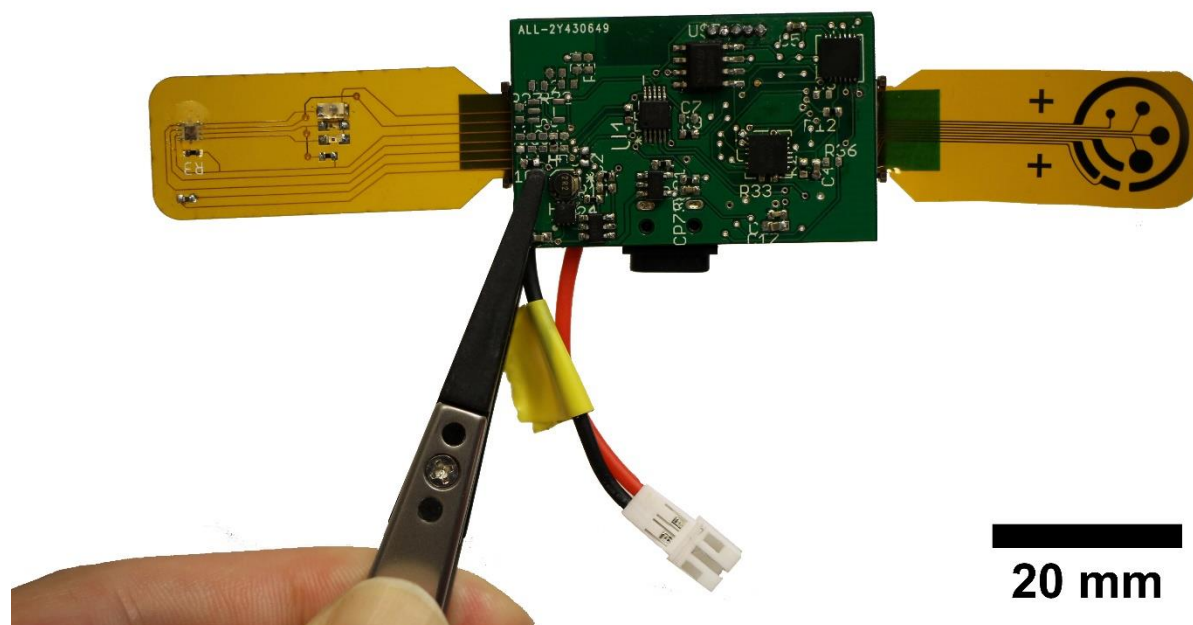


Fig. 1. Custom wearable device to measure sweat lactate and local tissue oxygenation levels. The device comprises a lithium-polymer battery, a FR-4 main board, an optical (left), and an electrochemical sensing platform (right). The optical platform hosts a temperature sensor, LEDs for illuminating the skin and a photodetector for light detection. The electrochemical platform includes sensors for lactate and pH measurements in sweat.

Sweat Collection Patch

The sweat collection patch consists of three main components, as demonstrated in Fig. 2: a hydrogel, a paper-based fluidic wicking channel with an additional site for evaporation at the end (evaporation pad), and printed electrodes for electrochemical quantification of lactate (lactate sensors). The hydrogel is engineered to have a lower chemical potential than sweat, which enables it to continuously extract fluid from the skin surface due to osmosis, once interfaced. The paper-based channel transports the extracted fluid to the evaporation pad through capillary wicking. Continuous evaporation from the pad sustains the capillary pressure inside the channel, which facilitates more fluid and biomarker collection over time. The electrochemical sensors are placed underneath the paper-based channel for enzymatic detection of lactate. The other end of the electrochemical sensors is connected to the FR-4 main board for data processing and transmission.

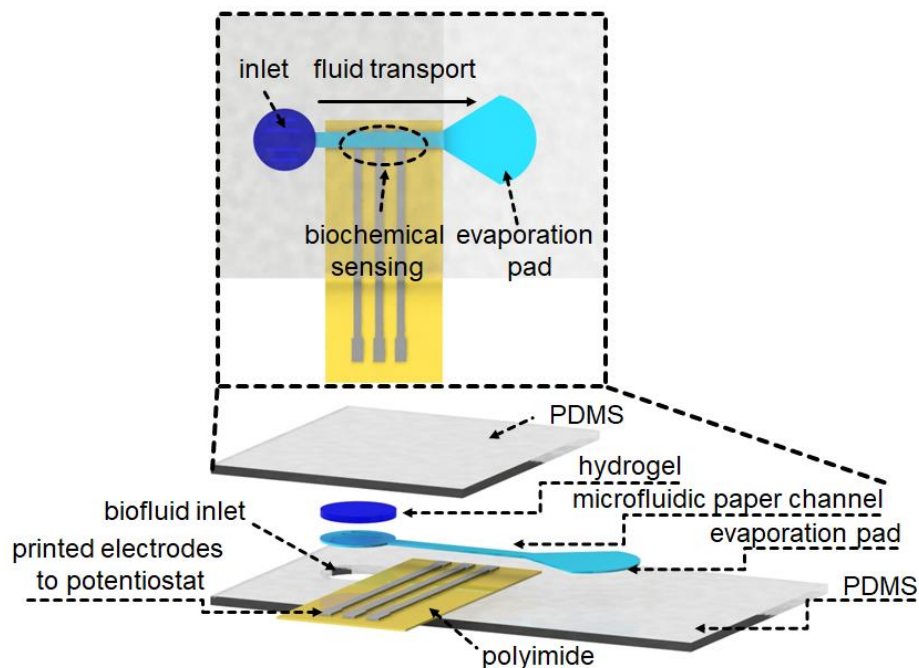


Fig. 2. Sweat collection patch with an integrated electrochemical lactate sensor. The microfluidic patch is made up of a hydrogel, a paper-based fluidic channel with an evaporation pad at the end, and printed electrodes for lactate sensing. Hydrogel extracts the sweat from the skin under low sweat rate conditions. The paper-based channel transports the extracted sweat to the evaporation pad. Continuous evaporation from the pad facilitates more sweat transport and collection over time. The lactate sensors are placed beneath the paper-based channel. As the sweat flows through the paper-based channel, the concentration of the lactate is quantified with electrochemical lactate sensors.

Photography

Research assistants will photograph the wearable device at every test site on the participant. The purpose of these images is to record the conformability of the device on the skin, and elucidate any abnormality in the generated data, or document any skin reaction to the devices. For example, presence of hair between the optical patch and the skin will reduce the optical signal due to scattering. These images will be de-identified as described later.

Technical Protocol

The sensors with and without the sweat collection patch will be tested on human subjects individually at three different locations (forehead, forearm, calf), under three different conditions – resting (no exercise), low exercising intensity, and high exercising intensity. The subjects will be accepted if they consent to participate in multiple tests.

a. Protocol for resting

Participants will be asked about any known skin reactions before participation to determine device compatibility. Confirm that the participant does not have any objections to sensor application before starting. If participant has objections with the application site, select the next one.

Test anatomic sites in the following order: A = forehead, B = forearm, C = calf. The location of the patch will be entered in the custom Python program at the time of data capture and saved using a specific naming convention described later.

- The test with the device will be carried out on the test locations of every individual.
- The participant will be seated throughout the testing.
- First, the selected skin area will be cleaned with alcohol wipes and DI water to get rid of the excess epithelial matter and residual lactate from the skin surface.

- An optical heart rate monitor will be placed on the finger of the participant.
- The Bluetooth connection will be verified between the devices and the laptop.
- Let the participant rest for 5 min.
- A plain paper strip (similar to the paper channel being used in the device) will be initially rubbed on the skin surface and be tested for the presence of lactate. The purpose of this test will be to confirm the absence of any residual lactate on the skin surface prior beginning the test with the device.
- The device with the sweat collection patch will be interfaced to the skin for 2 hours.
- For the testing of the device with the sweat collection patch, a hydrogel disk along with a paper channel will be directly interfacing the pre-washed testing location on the skin surface.
- A strap will be used to wrap around the device and adjusted to ensure firm contact with the skin.
- Participants will remain in the test room while pictures of the sweat collection patch will be taken every 20 minutes till 2 hours of testing.
- Once the test with the patches are over on sedentary subjects, it will be taken out and disposed.
- Now, the blood lactate levels will be measured on the same subject.
 - For capillary sampling of blood, alcohol will initially be applied to the lancet entry site and will be left to air dry. It will be used to puncture the skin.
 - The first drop of blood will be wiped away as it may be contaminated with tissue fluid or debris.

- A conventional, commercial lancet will then be placed on the side of the participants finger and deployed. The pricked finger will be lightly squeezed until a drop of blood forms. The drop of blood will be applied to a test strip inserted into the lactate meter (<http://www.novabio.us/lactate-plus/>).
 - The site of the finger stick will then be wiped with an alcohol wipe and a sterile bandage will be applied. The lactate reading will be recorded and compared with the lactate reading of the custom wearable device.
- The application site will be finally washed with soap and water.
 - Upon completion, the participants will be requested to complete a survey.
 - Thank participant for their participation and time.

b. Protocol for low exercising intensity

Participants will be asked about any known skin reactions before participation to determine device compatibility. Confirm that the participant does not have any objections to sensor application before starting. If participant has objections with the application site, select the next one.

Test anatomic sites in the following order: A = forehead, B = forearm, C = calf. The location of the patch will be entered in the custom Python program at the time of data capture and saved using a specific naming convention described later.

Subjects undergoing testing under low exercising conditions will be asked to ride a bike by complying with the following procedures:

- The test with the device will be carried out on the test locations of every individual.
- First, the selected skin area will be cleaned with alcohol wipes and DI water to get rid of the excess epithelial matter and residual lactate from the skin surface.

- Participants will be seated on a bike.
- An optical heart rate monitor will be placed on the finger of the participant.
- The Bluetooth connection will be verified between the devices and the laptop.
- Let the participant rest for 5 min.
- Blood lactate will be measured by following the same procedure as mentioned in the resting protocol.
- Let the participant exercise for 5 min at the starting intensity level with 60 rpm (warm up at 40-50 W output).
- Increase the exercise intensity to the next level (>75 rpm at 75-100 W output).
- Participant exercises for 20 min at this new exercise intensity level.
- Rest for 5 minutes (0 rpm).
- Exercise for 5 min at the starting intensity level with 60 rpm (warm up at 40-50 W output).
- Increase the exercise intensity to the next level (>75 rpm at 75-100 W output) and exercise for 20 minutes.
- Let the participant exercise for 5 min at the starting intensity level with 60 rpm (40-50 W output).
- The participant will use an optical heart rate monitor on the finger to measure the heart rate simultaneously.
- After exercising, the device will still be in contact with the skin surface.
- Blood lactate reading will be taken after exercise, following the same procedures as mentioned previously.
- Photographs of the device will be taken every 10 minutes during the total 1-hour time interval of sweat collection.

- Participants will then rest for 1 hour.
- At the end of the resting period, blood lactate reading will be taken.
- The application site will be finally washed with soap and water.
- Upon completion, the participants will be requested to complete the survey.
- Thank participant for their participation and time.

c. Protocol for high exercising intensity

Participants will be asked about any known skin reactions before participation to determine device compatibility. Confirm that the participant does not have any objections to sensor application before starting. If participant has objections with the application site, select the next one.

Test anatomic sites in the following order: A = forehead, B = forearm, C = calf. The location of the patch will be entered in the custom Python program at the time of data capture and saved using a specific naming convention described later.

- The test with the device will be carried out on the test locations of every individual.
- First, the selected skin area will be cleaned with alcohol wipes and DI water to get rid of the excess epithelial matter and residual lactate from the skin surface.
- Photographs of the device on the testing site will be taken.
- The participant will be seated on a bike.
- An optical heart rate monitor will be placed on the finger of the participant.
- The Bluetooth connection will be verified between the devices and the laptop.
- Adjust the seat of the bike. Let the participant rest for 5 min.
- The blood lactate level will be measured as described previously.
- Let the participant exercise for 5 min at the intensity level of 50 W with 60 rpm.

- Increase the exercise intensity to 100 W and let the participant exercise for 5 min with 75 rpm. Measure the blood lactate level.
- Increase the exercise intensity to 100-150 W and let the participant exercise for 15-20 min with 75 rpm. Measure the blood lactate level.
- Increase the exercise intensity to 200 W for 5 mins.
- Let the participant rest for 10 min and measure the blood lactate level.
- When testing of the device is complete, the device will be removed and the application site will be washed with soap and water.
- Upon completion, the participants will be requested to complete the survey.
- Thank participant for their participation and time.

Information on missing data or unsuccessful optical and/or electrochemical data recordings should be recorded for each subject.

Data Collection Naming Procedure

Upon consent, participants will be assigned a 6 character randomly generated alphanumeric identifier. This identifier will be used to code all data, photographs, and surveys.

The data sets will be labeled as follows: [*Participant ID*]-[*Device Location*]-[*Device Configuration*]-[*Exercise Type*] [DATE]

Example: e3wg8d-A-WOSCP-HE 100619

- **Device location:** A = forehead, B = forearm, C = calf
- **Device configuration:** WOSCP = without sweat collection patch; WSCP =with sweat collection patch
- **Exercise type:** LE = Low Exercise Intensity, HE = High Exercise Intensity, R = Resting

➤ **Date:** MMDDYY

Photographs of the working device will be labeled as follows: [*Participant ID*]-[*Device Location*]-[*Device Configuration*]-[*Exercise Type*] [DATE]

Example: e3wg8d-A-WOSCP-HE 100619.jpg

Data Analysis and Data Monitoring

De-identifiable data will be reported in aggregate form at the completion of all tests. Data will be reported in the form of charts, graphs, or tables once all tests are completed.

Photographs of devices on skin will be de-identified by covering any identifying marks or features (i.e., tattoos, scars, iris, facial features, and fingerprint) with black or randomly-pixelated polygons. These polygons will be oversized to cover the identifying marks by a 5 - 10 mm border (not constant). In the case of multiple identifying marks, additional random polygons of similar shape will be added, per equation:

$$1 \leq m \leq \sqrt{n} \qquad \text{for } n > 2$$

, where n is the number of polygons required to cover identifiers, and m is the number of polygons to be used to de-identify the de-identifying data.

Data Storage and Confidentiality

Data will be recorded on site and analyzed at a later point. Participant names will not be used during the data collection. All pieces of information regarding the participant and data collected during the test will be confidentially kept in the office of the research staff on a password-protected computer and hard copies kept in a locked filing cabinet. The password-protected computer access and key to the filing cabinet will only be given to the research staff.

Setting

Testing will be performed in the ASSIST physiology lab, which is located in Room 454 of the Monteith Research Center (MRC) on NC State's Centennial Campus. During these tests, participants will be in MRC 454 from 2 - 3 hours.

Estimated Period of Time to Complete the Study.

Participant recruitment: 3 months

Enrollment and data collection: 6 months

Data analysis: 1 month

After completion of the data analysis, findings of the study will be submitted for publication in a journal determined suitable by the PI.

v. Eligibility criteria

Research team members will attempt to recruit 75 participants who are able to give informed consent. This estimated test population is based on an initial guess, attrition rate and a protocol incompleteness rate of approximately 20%. There are no age, gender or race biases in this study.

The subjects will predominantly be recruited from the student, faculty, staff and visitor population of NC State University. The research team will be responsible for conveying the research study information to potential subjects via word of mouth, handouts or posted flyers. The potential subjects will then be given the research staff's e-mail in order to schedule a testing time if the subject does decide to become a participant. In addition, participants will be instructed to arrive for testing with an attire that would allow their forearms and calves to not be obstructed by clothing (e.g., short sleeve and shorts).

Eligibility criteria:

- are between 18 and 35 years of age
- can speak and write in English
- are not pregnant (women who self-report being pregnant will be excluded since they may have physical performance standards different than the general population)
- do not have psoriasis, dermatitis, or other skin conditions that would interfere with the ability to wear the device.
- do not have preexisting cardiac/heart conditions, epilepsy, diabetes, cystic fibrosis, and do not possess tattoos, eczema or additional skin conditions on patch application site (forehead, forearm, and calf). In addition, we will exclude subjects with hypertension, diabetes, or known metal allergies.
- are not UNC-CH students
- are not students enrolled in Prof. Daniele's or Prof. Bozkurt's courses
- do not have a history of skin reaction to adhesive substances
- do not have a known skin sensitivity (e.g., allergy to tape or 3M Tegaderm)

Subject contact

1. Participants will reach out to research staff based on recruitment materials.
 2. Initial telephone or e-mail exchange about eligibility and any questions.
 3. Response from the participant to confirm eligibility and time availability
- (2. and 3. may repeat due to scheduling difficulties or additional questions from participant)
4. Enrollment and consent meeting. A valid driver's license or other form of identification that clearly displays the subject's date of birth will be used to confirm age requirements before participation in the study. Verbal confirmation will be given by the subject to

validate that the subject does not possess one of the skin conditions to interfere with the testing, to the best of her or his knowledge, which would exclude her/him from the study. The application sites will be visually inspected for redness, abrasion, wounds or other skin conditions.

5. Study participation

vi. Outcome characteristics and endpoint definitions

Primary endpoints

- Mean sweat and blood lactate levels, ranges, and fluctuations during the sensor integration period after placement and over the study period.
- Mean sweat and blood lactate levels, ranges, and fluctuations during rest and activity periods.
- Mean sweat lactate levels, ranges, and fluctuations over time for various anatomical locations (forehead, forearm, and calf).
- Exploratory goal: Measure changes in sweat lactate and local tissue oxygenation levels.
- Comfort level of the custom device on various anatomical locations (forehead, forearm, and calf).

vii. Statistical analysis

Two sample paired t-test will be used to evaluate the null hypothesis (the mean difference between the blood and sweat lactate levels is zero). To accomplish this:

- Mean and standard deviations of blood and sweat lactate will be calculated.
- Mean concentration difference between sweat and blood lactate will be calculated.
- T-statistic will be calculated and then p-value for the paired t-test will be obtained.
- If the p-value is less than the alpha level ($p < 0.05$), the null hypothesis will be rejected.

As an exploratory research, the correlation between blood and sweat lactate with the tissue oxygenation levels will be assessed using Pearson's correlation coefficient (r).

viii. Sample size justification

The blood lactate levels range from 0.4 to 5 mM during exercise. Desired margin of error is 0.3 mM. According to the manufacturer, the commercial blood lactate analyzer has a standard deviation of 0.7 mM at 5 mM blood lactate level. For a 90% confidence level, the sample size should be 15 { $(1.645 * 0.7/0.3)^2 = 14.73$ }.

The sweat lactate level ranges from 5 to 60 mM during exercise. Desired margin of error is 3 mM. Based on our lab results, the electrochemical lactate sensing platform has a standard deviation of 8 mM in 15 mM lactate test solution. For a 90% confidence level, the sample size should be 20 { $(1.645 * 8/3)^2 = 19.24$ }.

The sample size for blood and sweat lactate measurements were determined based on the standard deviations of the sensors at high lactate concentrations. According to the manufacturer of the commercial lactate meter and our lab results, the standard deviation of the sensors are low at lower lactate levels, which corresponds to a lower sample size. This means that the calculated sample sizes are the maximum values that will be statistically required for the testing.

This study will recruit 25 participants per exercise type, assuming a 20% drop-out or early termination rate. The total number of the participants for the whole test will be 75.

ix. Data management

Because we are only detecting participants' lactate and tissue oxygenation, we do not anticipate any data safety concerns. However, the PI will monitor the study progress, ensure subject safety, and the accuracy and security of the data. While some tasks may be delegated, the PI retains full

responsibility. The PI will monitor the study progress, ensure subject safety, and the accuracy and security of the data.

Data will be de-identified and reported in aggregate form at the completion of all tests. Study ID numbers will be used to label data sets collected during the study. This will ensure that the data remains confidential. Photographs of the device on the body will serve as a record of device placement and will be de-identified by hiding any identifying marks (iris, identifying features, tattoos, fingerprints, etc.) with black or randomly pixelated polygons.

All data will be collected at the College of Engineering at NC State, so there is no need to transmit data among research team members during the data collection phase. Data will be collected on password-protected laptop secured by the Department of Electrical and Computer Engineering at NC State. Some of the analysis may be carried out on desktops in Engineering Building II (also, secured by the ECE Department). USB drive will be used to transfer data between the computers. After transfer, data will be deleted and shredded from the USB drive. No data will be stored on USB.

x. Safety management plan

We will describe the study procedures to the participants during the consent process. If we find that a participant is unable to comply with the procedures, then he/she will be withdrawn from the study. In addition, if participants are discovered to have any known skin reactions to device materials or interfering skin condition, he/she will be withdrawn from the study. Although unlikely, we will also withdraw individuals if they present with a serious allergic reaction to the applied device, and have them contact their medical provider. Research participants will monitor their skin condition for any reaction throughout the testing, including different devices and anatomic locations.

There are no noted potential social risks, such as stigma, associated with this study. Any potential social risk due to breach of confidentiality will be minimized. Records of participants in this study will be secured and encrypted, and only access is provided to the PI and named study personnel. All data sets will be de-identified at completion of the subjects' participation.

Some potential adverse events have been identified from past and similar studies:

Rare and mild: Skin irritation from the placement of the device on the skin.

Participants will be asked about any known skin reactions before study participation to determine device compatibility. At the first signs of irritation, testing will be stopped. Exposed skin areas will be flushed with cold water for 15 minutes and washed with soap and water. If irritation persists research staff will aid the participant to seek medical attention at NC State health center. Research staff will also follow-up with the participant in 2 to 3 days regarding the irritation.

Rare and mild: Skin irritation due to the contact of the hydrogel, paper, glucose, and silicone.

The skin will be exposed to glycerin, polyacrylamide hydrogel, filter paper, silicone, glucose and NaCl. All materials have been selected based on prior use in commercial products or foods with direct physical contact with skin. According to materials safety data sheets polyacrylamide gel and silicone are not expected to cause skin irritation or any other adverse effect when in contact with skin. Both polyacrylamide gels and silicone are components of FDA approved medical devices and commercial cosmetic products. According to materials safety data sheets, glucose is not expected to cause skin irritation or any other adverse effect when in contact with skin. All materials used fall within safe limits as per GRAS and SDS guidelines. All skin contact irritation or staining is suggested to be treated by flushing with water and washing with soap and water.

Rare and mild: Skin irritation from light excitation by 630 to 940 nm LEDs.

Testing will be stopped upon any sensation of discomfort. Exposed areas will be flushed with cold water for 15 minutes. If discomfort persists, research staff will aid the participant to seek medical attention at NC State health center. Research staff will also follow-up with the participant in 2 to 3 days regarding the irritation.

Rare and mild: Skin irritation due to heating of LEDs in operation.

The temperature of LEDs increases with operation and such close proximity to the skin could increase the skin temperature. LEDs will be operated in pulsed mode with most of the time spent in “off” mode to reduce heating. In the unlikely case of irritation, testing will be stopped.

Rare and mild: Electric shock from the 3.7V battery in case of catastrophic failure.

The severity associated with this failure is minimal due the high skin impedance and would be at the worst equivalent to placing 3.7V battery terminals to the skin. To minimize this risk, the device will not be in contact with the skin. The devices will be tested before placement on participants. In the unlikely case of electric shock, testing will be stopped. If participants require medical attention, research staff will assist them in getting it. In addition, research staff will follow-up in 2 to 3 days with the participant.

Rare and mild: Discomfort, lightheadedness, and infection during or after finger pricking. To minimize the discomfort and lightheadedness, a lower setting on the lancing device will be used. To minimize the infection, the sampling site will be cleaned with an alcohol swab. The lancet will not be reused between the subjects. A new lancet will be used for each subject.

The PI will be present or on-call at all times during testing. If a subject begins to experience discomfort the PI will be immediately notified and the study team will document the site of irritation and terminate the study. The research staffs will be present during the whole testing and

will monitor for unanticipated events. In case of an emergency or severe risk situation, testing will be stopped and 911 or campus police (919.515.300) will be contacted for assistance. If we find that subjects are in the need of a medical follow-up, we will have the participants contact their medical provider.

xi. Abbreviations/Acronyms

ASSIST	Engineering Research Center at NC State
FR-4	reinforced epoxy laminate material
LED	light emitting diode
MRC	Monteith Research Center on NC State Centennial Campus
PI	principle investigator (Dr. Daniele in this study)

Appendix H: List of Publications

Journal Articles

1. **Yokus, M. A.**; Songkakul, T.; Bozkurt, A.; Daniele, M. A., Wearable System for Continuous Monitoring of Metabolites in Sweat and Local Tissue Oxygenation (*in preparation*).
2. **Yokus, M. A.**; Songkakul, T.; Pozdin, V. A.; Bozkurt, A.; Daniele, M. A., Wearable multiplexed biosensor system toward continuous monitoring of metabolites. *Biosens. Bioelectron.* **2020**, *153*, 112038.
3. **Yokus, M. A.**; Jur, J. S., Fabric-Based Wearable Dry Electrodes for Body Surface Biopotential Recording. *IEEE Trans. Biomed. Eng.* **2016**, *63* (2), 423-430.
4. **Yokus, M. A.**; Foote, R.; Jur, J. S., Printed Stretchable Interconnects for Smart Garments: Design, Fabrication, and Characterization. *IEEE Sens. J.* **2016**, *16* (22), 7967-7976.

Conference Papers

1. **Yokus, M. A.**; Agcayazi, T.; Traenkle, M.; Bozkurt, A.; Daniele, M. A. In *Wearable Sweat Rate Sensors*, **2020** IEEE Sensors (*submitted*)
2. **Yokus, M. A.**; Saha, T.; Fang, J.; Dickey, M. D.; Velev, O. D.; Daniele, M. A. In *Towards Wearable Electrochemical Lactate Sensing using Osmotic-Capillary Microfluidic Pumping*, 2019 IEEE SENSORS, 27-30 Oct. 2019; **2019**; pp 1-4.
3. Songkakul, T.; Bhushan, P.; Umasankar, Y.; **Yokus, M.**; Daniele, M. A.; Bhansali, S.; Bozkurt, A. In *Towards a Long-Term Multi-Site Electrochemical Wound Monitoring System*, 2019 IEEE SENSORS, 27-30 Oct. 2019; **2019**; pp 1-4.
4. **Yokus, M. A.**; Hass, C.; Agcayazi, T.; Bozkurt, A.; Daniele, M. A., Towards a Wearable Perspiration Sensor. *2017 Ieee Sensors* **2017**, 1260-1262.
5. Pozdin, V. A.; **Yokus, M. A.**; Sotory, P.; Wisniewski, N.; Bozkurt, A.; Daniele, M. A., Low-cost Flexible Inorganic Optical Devices for Flexible Sensors. *2017 Ieee Sensors* **2017**, 1449-1451.
6. Pozdin, V. A.; **Yokus, M. A.**; Daniele, M. A., Strain Sensors on Thermoplastic Polyurethane Films for Lightweight Epidermal Sensing. *2017 Ieee Sensors* **2017**, 675-677.

7. Pozdin, V. A.; Dieffenderfer, J.; Williams, E.; Sotory, P.; **Yokus, M. A.**; Bozkurt, A.; Daniele, M. A., Modular Design for Epidermal Temperature Sensing. *2017 Ieee Sensors* **2017**, 328-330.
8. Agcayazi, T.; **Yokus, M. A.**; Gordon, M.; Ghosh, T.; Bozkurt, A., A Stitched Textile-based Capacitive Respiration Sensor. *2017 Ieee Sensors* **2017**, 1074-1076.
9. **Yokus, M. A.**; Daniele, M. A., Skin Hydration Sensor for Customizable Electronic Textiles. *MRS Adv.* **2016**, *1* (38), 2671-2676.
10. Dieffenderfer, J. P.; Goodell, H.; Bent, B.; Beppler, E.; Jayakumar, R.; **Yokus, M.**; Jur, J. S.; Bozkurt, A.; Peden, D., Wearable Wireless Sensors for Chronic Respiratory Disease Monitoring. *2015 Ieee 12th International Conference on Wearable and Implantable Body Sensor Networks (Bsn)* **2015**.

Issued Patents

1. Jur, J. S.; **Yokus, M.**; Foote, R.; Myers, A. C.; Bhakta, R. P. Flexible Interconnects, Systems, And Uses Thereof. US20160358849A1, **2018**.

Review Papers

1. **Yokus, M. A.**; Daniele, M. A., Integrated Biochemical and Biophysical Sensing Systems for Health and Performance Monitoring: A Systems Perspective. *Proceedings of the IEEE* **2020** (*submitted*).
2. Rivera, K. R.; **Yokus, M. A.**; Erb, P. D.; Pozdin, V. A.; Daniele, M., Measuring and regulating oxygen levels in microphysiological systems: design, material, and sensor considerations. *Analyst* **2019**, *144* (10), 3190-3215.